frontiers | Research Topics

Advanced biomaterials and technologies for oral and maxillofacial regeneration

Edited by
Xin Liu, Jianmin Han, Si Chen and Juncen Zhou

Published in
Frontiers in Bioengineering and Biotechnology

ISSN 1664-8714
ISBN 978-2-8325-4921-6
DOI 10.3389/978-2-8325-4921-6

About Frontiers

Frontiers is more than just an open access publisher of scholarly articles: it is a pioneering approach to the world of academia, radically improving the way scholarly research is managed. The grand vision of Frontiers is a world where all people have an equal opportunity to seek, share and generate knowledge. Frontiers provides immediate and permanent online open access to all its publications, but this alone is not enough to realize our grand goals.

Frontiers journal series

The Frontiers journal series is a multi-tier and interdisciplinary set of open-access, online journals, promising a paradigm shift from the current review, selection and dissemination processes in academic publishing. All Frontiers journals are driven by researchers for researchers; therefore, they constitute a service to the scholarly community. At the same time, the *Frontiers journal series* operates on a revolutionary invention, the tiered publishing system, initially addressing specific communities of scholars, and gradually climbing up to broader public understanding, thus serving the interests of the lay society, too.

Dedication to quality

Each Frontiers article is a landmark of the highest quality, thanks to genuinely collaborative interactions between authors and review editors, who include some of the world's best academicians. Research must be certified by peers before entering a stream of knowledge that may eventually reach the public - and shape society; therefore, Frontiers only applies the most rigorous and unbiased reviews. Frontiers revolutionizes research publishing by freely delivering the most outstanding research, evaluated with no bias from both the academic and social point of view. By applying the most advanced information technologies, Frontiers is catapulting scholarly publishing into a new generation.

What are Frontiers Research Topics?

Frontiers Research Topics are very popular trademarks of the *Frontiers journals series*: they are collections of at least ten articles, all centered on a particular subject. With their unique mix of varied contributions from Original Research to Review Articles, Frontiers Research Topics unify the most influential researchers, the latest key findings and historical advances in a hot research area.

Find out more on how to host your own Frontiers Research Topic or contribute to one as an author by contacting the Frontiers editorial office: frontiersin.org/about/contact

Advanced biomaterials and technologies for oral and maxillofacial regeneration

Topic editors

Xin Liu — Shanghai Jiao Tong University School of Medicine, China
Jianmin Han — Peking University People's Hospital, China
Si Chen — Alexander Dubcek University in Trencin, Slovakia
Juncen Zhou — Stony Brook University, United States

Citation

Liu, X., Han, J., Chen, S., Zhou, J., eds. (2024). *Advanced biomaterials and technologies for oral and maxillofacial regeneration*. Lausanne: Frontiers Media SA. doi: 10.3389/978-2-8325-4921-6

Table of contents

frontiers | Frontiers in Bioengineering and Biotechnology

TYPE Original Research
PUBLISHED 26 January 2023
DOI 10.3389/fbioe.2023.1124107

OPEN ACCESS

EDITED BY
Juncen Zhou,
Stony Brook University, United States

REVIEWED BY
Zhiyi Shan,
The University of Hong Kong, Hong Kong SAR, China
Xiong Lu,
Southwest Jiaotong University, China

*CORRESPONDENCE
Shuli Liu,
liushuli@shsmu.edu.cn
Shichong Qiao,
shichong_qiao@hotmail.com
Hongchang Lai,
lhc9hospital@163.com

†These authors have contributed equally to this work

SPECIALTY SECTION
This article was submitted to Biomaterials, a section of the journal Frontiers in Bioengineering and Biotechnology

RECEIVED 14 December 2022
ACCEPTED 17 January 2023
PUBLISHED 26 January 2023

CITATION
Zhu Y, Zhi Q, Zhang C, Gu Y, Liu S, Qiao S and Lai H (2023), Debridement of contaminated implants using air-polishing coupled with pH-responsive maximin H5-embedded metal-organic frameworks. *Front. Bioeng. Biotechnol.* 11:1124107. doi: 10.3389/fbioe.2023.1124107

Debridement of contaminated implants using air-polishing coupled with pH-responsive maximin H5-embedded metal-organic frameworks

Yu Zhu[1,2,3†], Qiang Zhi[1,2,3†], Chunan Zhang[1,2,3], Yingxin Gu[1,2,3], Shuli Liu[2,3,4*], Shichong Qiao[1,2,3*] and Hongchang Lai[1,2,3*]

[1]Department of Implant Dentistry, Shanghai Ninth People's Hospital, College of Stomatology, Shanghai Jiao Tong University School of Medicine, Shanghai, China, [2]National Clinical Research Center for Oral Diseases, Shanghai, China, [3]Shanghai Key Laboratory of Stomatology and Shanghai Research Institute of Stomatology, Shanghai, China, [4]Department of Oral and Maxillofacial-Head and Neck Oncology, Shanghai Ninth People's Hospital, College of Stomatology, Shanghai Jiao Tong University School of Medicine, Shanghai, China

The primary goal of peri-implantitis treatments remains the decontamination of implant surfaces exposed to polymicrobial biofilms and renders biocompatibility. In this study, we reported a synergistic strategy for the debridement and re-osteogenesis of contaminated titanium by using erythritol air abrasion (AA) coupled with an as-synthesized pH-responsive antimicrobial agent. Here, the anionic antibacterial peptide Maximin H5 C-terminally deaminated isoform (MH5C) was introduced into the Zeolitic Imidazolate Frameworks (ZIF-8) *via* a one-pot synthesis process. The formed MH5C@ZIF-8 nanoparticles (NPs) not only possessed suitable stability, but also guarantee the slow-release effect of MH5C. Antibacterial experiments revealed that MH5C@ZIF-8 NPs exhibited excellent antimicrobial abilities toward pathogenic bacteria of peri-implantitis, confirming ZIF-8 NPs as efficient nanoplatforms for delivering antibacterial peptide. To evaluate the comprehensive debridement efficiency, single-species as well as mixed-species biofilms were successively established on commercially used titanium surfaces and decontaminated with different methods: removed only by erythritol air abrasion, treated merely with MH5C@ZIF-8 NPs, or received both managements. The results demonstrated that only erythritol air abrasion accompanied with MH5C@ZIF-8 NPs at high concentrations eliminated almost all retained bacteria and impeded biofilm rehabilitation, while neither erythritol air abrasion nor MH5C@ZIF-8 NPs alone could achieve this. Subsequently, we evaluated the re-osteogenesis on previously contaminated surfaces which were treated with different debridement methods afterwards. We found that cell growth and osteogenic differentiation of bone marrow–derived mesenchymal stem cells (BMSCs) in the group received both treatments (AA + MH5C@ZIF-8) were higher than those in other groups. Our work emphasized the great potential of the synergistic therapy as a credible alternative for removing microorganisms and rendering re-osseointegration on contaminated implant surfaces, boding well for the comprehensive applications in peri-implantitis treatments.

KEYWORDS

peri-implantitis, decontamination, air-polishing, antimicrobial agents, metal-organic frameworks

1 Introduction

Peri-implantitis has been defined as inflammatory reactions occurring in tissues around dental implants characterized by suppuration, bleeding, and bone loss, which ultimately lead to implant failures (Schwarz et al., 2018). The prevalence of peri-implantitis varied between 17% and 22% of patients and between 9.25% and 12.8% of the implant sites (Munoz et al., 2018). The main cause associated with peri-implantitis is the polymicrobial biofilms development owing to the settlement and expansion of pathogenic bacteria, including *F. nucleatum*, *P. gingivalis*, and *S. mutans* (Munoz et al., 2018). Therefore, the basic cause-related intervention for peri-implantitis remains the decontamination of implant surfaces exposed to bacterial biofilms and renders biocompatibility, with re-osseointegration as the ultimate objective. The screw-shaped designing and the microstructure surface of titanium implants may hinder the access of debridement instruments and limit the cleansing efficacy (Louropoulou et al., 2015). To date, no recognized gold standards for surface decontamination during peri-implantitis treatments have been suggested.

Mechanical decontamination involves scaling and polishing of implant surfaces. Treatment modalities such as polishing brushes and rubber cups fail to remove plaques from the depth of threads due to limited flexibilities (Louropoulou et al., 2015). Debridement managements such as curettes and ultrasonic scalers cause detrimental surface alterations and deposit residual fragments (Park et al., 2015). Promising results for air abrasion (AA) were concluded in a review and the authors demonstrated that "the cleaning efficiency of air abrasion on titanium strips, discs or implants is outstanding" (Park et al., 2015). The suspension of the air-powder system, made up of air abrasive powders and pressurized water-air mixture, is sprayed from the subgingival nozzles to implant surfaces, which would remove the plaque due to friction (Matsubara et al., 2020). The powder particles could be reflected in an angulation vertically to their angle of incidence, indicating that powders would reach these highly recessed areas (Keim et al., 2019). Compared with the classical glycine powders (25 μm) and sodium bicarbonate powders (40–65 μm), the erythritol powders (14 μm) were gentler to implant surface with no damage to the surface integrity (Matsubara et al., 2020). Moreover, the erythritol-based powders have higher dissolution potentials and more rapid degradation by the organisms (Drago et al., 2014). Nevertheless, merely mechanical decontamination with air-polishing remains a difficult task and depends mainly on the operator's experiences.

Chemotherapeutic agents act as an adjunct to mechanical debridement, which weaken biofilms, facilitate its removal, and kill remaining bacteria. However, organic chemical agents including chlorhexidine (CHX) and hydrogen peroxide (H_2O_2) suffer from high toxicity and rapid release rate (Kotsakis et al., 2016). Local antibiotics including minocycline and tetracycline paste fail to decrease microorganisms compatible with peri-implant health and cause drug resistance (Ntrouka et al., 2011). Antimicrobial peptides (AMPs) which are ancient and effective antimicrobials of innate immune systems maybe an intelligent strategy (Dennison et al., 2018). The majority of AMPs are cationic, but a growing number of anionic AMPs (AAMPs) have attracted attentions (Dennison et al., 2018). The Maximin H5 (MH5) existing abundantly in the brain and the skin of the Chinese frog Bombina maxima is an AAMP with attractive characteristics (Dennison et al., 2016). MH5 owns membranolytic abilities, which mainly involves the bilayer insertion of the hydrophobic N-terminal region (Dennison et al., 2016). MH5 uses lipid interactions of the α-helical structure and exhibits antibacterial activities by the membranolytic method compared with the specific "Carpet" mechanisms (Dennison et al., 2015). There is strong evidence to suggest that MH5 kills gram-positive bacteria through the pH dependent membranolytic mode (Dennison et al., 2015). Nevertheless, MH5 exhibited limited activities against gram-negative bacteria (Dennison et al., 2015). Researches on AAMPs have demonstrated that C-terminal deamidation would strengthen the antibacterial effectiveness without enhancing the lyric capacity, hence promoting the therapeutic ability of the antimicrobial peptide (Ortiz-Gomez et al., 2020). Dennison et al. have described the effect of C-terminal deamidation on the antibacterial abilities of the peptide, and found that MH5 with the structure ILGPVLGLVSDTLDDVLGIL-COOH (MH5C) gained antibacterial abilities against those gram-negative bacteria (Dennison et al., 2015). These increased antimicrobial activities might be associated with hydrogen-bonding interactions occurring between the C-terminal amide structure of the peptide MH5C and the membrane surface of gram-negative bacteria (Dennison et al., 2015). Still, it is necessary to draw up a green and powerful nanoplatform to deliver the specific antibacterial peptide MH5C.

Metal–organic frameworks (MOFs) have attracted attentions in drug delivery due to porous structures, simple preparations, and multifunctional features (Karami et al., 2021; Li et al., 2022b). Among MOFs, zeotlitic imidazolate framework-8 (ZIF-8) constructed by zinc ions and 2-methylimidazole, serves as container of antibacterial metal ions and possesses the tailorable pore size for loading antimicrobial agents (Karami et al., 2021; Xia et al., 2022). It was found that ZIF-8 exhibited >99.9999% inactivation efficiency against gram-negative bacteria in saline under 2 h of simulated solar irradiation (Li et al., 2019). Another study demonstrated that ZIF-8 outperformed the extensively used antibacterial ZnO (Ahmed et al., 2019). The photoelectrons trapped within the zinc ions of ZIF-8 are responsible for ROS production inducing cell deformation and cytoplasm leakage of bacteria (Ahmed et al., 2019; Li et al., 2022a; Yu et al., 2022). It is noteworthy that the ZIF-8 crystal exhibits excellent capabilities for drug delivery because the ZIF-8 is stable in neutral or alkaline aqueous medium but break down rapidly in acidic medium (Liu et al., 2020a). The accumulating acetic acid and lactic acid in the inflammatory site cause low pH value, which was beneficial for specific release of ZIF-8 (Liu et al., 2020a). Previously the ZIF-8 was made in the dimethylformamide solution *via* the solvothermal process, but the dimethylformamide may be deposited within the pore space (Zou et al., 2020). Kida et al. Have mentioned the synthesis of the ZIF-8 crystal without by-products in pure water under room temperature *via* the one-pot method (Zou et al., 2020). The green synthesis method makes the ZIF-8 nanoparticles (NPs) appealing for the encapsulation of the fragile biomacromolecules including peptides, proteins, and enzymes. The peptide addition can modulate the shape and size of ZIF-8 crystals, which mainly depended on the molecular concentrations, biomolecule charges, and amino acid sequences. Some studies have affirmed that only negatively charged biomolecules with low isoelectric point (PI) would form biomolecules@ZIF-8, while biomolecules with neutral or positive charge would induce the development of a totally new phase *dia-Zn*$(HmIm)_2$ (Carraro et al., 2020; Xuan et al., 2020). Thus the anionic

antimicrobial peptides MH5C with negative charge (PI = 6.5) would make MH5C@ZIFs crystals frequently, boding well for its applications in chemical debridement.

In this work, we reported a synergistic strategy for the debridement and re-osteogenesis of contaminated titanium by using erythritol AA coupled with an as-synthesized pH-responsive antimicrobial agent. Our work not only highlights the great potential of applying ZIF-8 NPs as a green and robust nanoplatform to deliver antibacterial peptide in chemical decontamination, but also bring a new insight into the synergistic therapy for better managements of the contaminated dental implant surfaces during peri-implantitis treatments.

2 Materials and methods

2.1 Preparation of MH5C@ZIF-8

The MH5C-terminally deaminated isoform (MH5C) (ILGPVLGLVSDTLDDVLGIL-COOH, 95% purity) was synthesized by Top-peptide Co. (Shanghai, China). MH5C@ZIF-8 NPs and ZIF-8 NPs were conducted by the one-pot method at room temperature in water as previous studies (Li et al., 2018). As for the ZIF-8 NPs, dissolve zinc nitrate hexahydrate and 2-methylimidazole in deionized water, respectively. Then quickly add zinc nitrate solution into imidazole solution under the condition of stirring at room temperature. After complete crystallization (up to 12 h), a centrifuge (14,000 rpm, 10 min) was used to separate the solid and liquid of the solution. As for the MH5@ZIF-8 NPs, the aqueous solutions of MH5C and 2-methylimidazole was blended with the zinc nitrate aqueous solution through vigorous stirring. After completing crystallization (up to 12 h), the synthesized MH5C@ZIF-8 NPs were washed by the deionized water and then purified *via* centrifugation (14,000 rpm, 10 min). The purified MH5C@ZIF-8 and ZIF-8 NPs were completely freeze dried and kept at −20°C for the further experiments. Based on the equation that drug loading content (DLC, %) = (weight of loaded drug)/(weight of drug loaded nanoparticles) × 100% while drug loading efficiency (DLE, %) = (weight of loaded drug)/(weight of drug in feed) × 100%, the DLC and DLE of MH5C@ZIF-8 NPs was 9.8% and 33.2%, respectively.

2.2 Characterization of MH5C@ZIF-8

The scanning electron microscopy (SEM, Hitachi S-4800, Japan) and transmission electron microscopy (TEM, Tecnai G2, United States) were utilized to characterize the morphology. The dynamic light scattering (DLS, Nicomp 380, United States) was utilized to measure the size distributions. The powder X-ray diffraction (XRD, D8 Advance A25, United States) was utilized to characterize the crystalline structure. The fourier transform infrared (FTIR, Nicoletteis50, United States) was utilized to explore the chemical structure. The thermogravimetric analyzer (TGA, Mettler Toledo, Switzerland) was utilized to complete the thermogravimetric study from 20°C to 820°C under air atmosphere. The Malvern Zeta Sizer-Nano ZS90 instrument was utilized to measure the zeta potential. As for the release of MH5C, the BCA reagents (Beyotime, China) was utilized to determine the peptide concentration and the release behavior of MH5C@ZIF-8 was accomplished in both PBS buffer at pH 7.4 and MES buffer at pH 5.5.

2.3 Microbial and cellular culture

The bacterial strains *F. nucleatum* (ATCC10953), *P. gingivalis* (ATCC 33277), and *S. mutans* (UA 159) were acquired from the Shanghai Key Laboratory of Stomatology, Ninth People's Hospital, affiliated with Shanghai Jiao Tong University, School of Medicine. Bacteria were seeded on the brain heart infusion (BHI) agar in the presence or absence of sterile sheep blood. After gram staining routinely, the single colony was chosen and cultured in the BHI broth. All species were culture in an anaerobic incubator. The bacteria of the log phase with vigorous activities were applied for further use.

The single-species and mixed-species biofilms was developed directly on the 24-well culture plate or on the surface of sandblasted, large-grit and acid-etched (SLA) titanium discs (15 mm in diameter, 1 mm in thickness). The bacterial suspensions containing 10^4 colony-forming units (CFU)/mL for *F. nucleatum*, 10^6 CFU/mL for *P. gingivalis*, and 10^5 CFU/mL for *S. mutans* were utilized separately or all together to provide the single-species and mixed-species biofilms. The above plates or titanium disks were cultured for two consecutive days to develop biofilms as previous studies (Qin et al., 2020).

The 4-week-old SD rats were utilized to acquire rat bone marrow–derived mesenchymal stem cells (rBMSCs), which was approved by the Animal Care and Experiment Committee of Shanghai Ninth People's Hospital affiliated to Shanghai Jiao Tong University (Protocol Number: SH9H-2020-A612-1). After separating both ends of the femora, the marrow was flushed out. The isolated cells were cultured with DMEM with 10% FBS in an incubator. Then 72 h later, non-adherent BMSCs were removed by utilizing the PBS buffer. Once reaching 80%–90% confluence, cells were sub-cultured to 2-3 dishes. The 2–3 passages of BMSCs were adopted for the following experiments.

2.4 Antibacterial activity of MH5C@ZIF-8

The growth curve indicating the bacterial growth in different systems was drawn up *via* the record of the OD value for different bacteria suspensions with time. Here, the bacterial concentration of *F. nucleatum*, *P. gingivalis* and *S. mutans* was initially set at approximately 10^8 CFU/mL, corresponding to the OD value at 0. 135–0150 for these three species. To study the slow-release sterilization ability of MH5C@ZIF-8 NPs, pure MH5C and MH5C@ZIF-8 with the same peptide concentration were added into the bacterial solutions. As for pure MH5C, the MH5C concentrations were 31.25, 62.5, 125, and 250 μg/mL. As for MH5C@ZIF-8 NPs, the final equivalent concentration of peptide MH5C varied from 31.25 to 250 μg/mL. The bacterial suspension without antibacterial systems was applied as the control. The OD values at 600 nm within both antibacterial materials were recorded at regular time interval, until the growth curve of the specific bacterial species have reached the plateau.

The 3-(4,5-dimethylthiazol-2-yl)-2,5-diphenyl tetrazolium bromide (MTT) assay was used to evaluate the relative bacterial viability. In brief, the mixed-species biofilms were developed directly on the conventional 24-well culture plate instead of titanium discs. The bacterial suspensions were discarded and the retained biofilms were treated with pure MH5C or MH5C@ZIF-

8 for 12 h and 24 h. Then the previous liquid was discarded and the MTT (Beyotime, China) solution was added. After 2 h in the dark, the unreacted MTT was removed and dimethyl sulfoxide (DMSO) was utilized for dissolving the formazan crystal. Afterwards, the above solution was transferred to the 96-well plate and OD at 490 nm was recorded through the BioTek instrument.

The biomasses of the bacterial biofilms were determined *via* the crystal violet (CV) staining assay. In brief, the mixed-species biofilms were developed directly on the culture plate and the biofilms were treated with pure MH5C or MH5C@ZIF-8 for 12 h and 24 h. Then the previous liquid was discarded and 100 μL of 0.01% (v/v) CV (Sigma, United States) solution was added to each well for 15 min. After washed with PBS, each well was added with ethanol. Afterwards, the above solution was transferred to the 96-well plate and OD at 595 nm was recorded through the BioTek instrument.

2.5 Cleaning capacity of mechanical-chemical synergistic treatments

To evaluate the decontamination effects of the synergistic therapy, we designed four experimental groups: group AA, biofilms removed with erythritol air abrasion (AA); group MH5C@ZIF-8, biofilms dealt with high concentrations of MH5C@ZIF-8 (125 μg/mL) for 24 h; group AA + MH5C@ZIF-8, biofilms treated with MH5C@ZIF-8 (125 μg/mL) for 24 h followed by erythritol AA; and the control group, untreated biofilms. Specifically, the single-species and mixed-species biofilms were developed directly on the SLA titanium discs. After washed with PBS to eliminate the unattached bacteria, the contaminated titanium discs were transferred to the 24-well culture plate. Then the fresh BHI medium with (group MH5C@ZIF-8 and AA + MH5C@ZIF-8) or without (groups Control and AA) the MH5C@ZIF-8 solution (125 μg/mL) was introduced into each well. After 24 h, for groups AA and AA + MH5C@ZIF-8, the biofilms on titanium discs in group AA and AA + MH5C@ZIF-8 were cleaned by the AA device (EL-308/C, EMS Nyon, Switzerland) with erythritol powders (particle size ≈14 mm) under the static pressure (7 bar) for totally 1 min, perpendicular to titanium discs, at a distance of 10 mm. Here, all discs have received treatments by being continuously rotated opposing the subgingival nozzles from center to periphery in four different circular motions. After air abrasions, all discs were dried by the compressed air for nearly 10 s for removing the retained powders. All air abrasions were finished by the same experienced operator. Afterwards, the titanium plates in each group were washed by PBS, transferred to the new 24-well plate, and received the subsequent antimicrobial assessments.

The single-species biofilm integrity after decontamination methods was detected by SEM examinations (JSM-7600F, Japan). In detail, samples were rinsed by PBS and fixed by using glutaraldehyde at room temperature for 2 h. Then samples were dehydrated by the ethanol concentration gradient, ending with the 100% ethanol for 30 min. Before visualization, each sample was dried and sputter coated with gold. SEM images were taken at different locations on each sample.

The single-species biofilm bioactivity after decontamination methods was detected by the live/dead fluorescence staining. The staining solution included 2.5 mM SYTO9 and 2.5 mM propidium iodide. The intact bacteria were stained with SYTO9 emitting the green fluorescence, and the membrane-compromised bacteria were stained with propidium iodide emitting the red fluorescence. After staining in the dark for 15 min, fluorescence images on each sample were collected with the CLSM (Olympus FV1000, Japan).

The bacterial viability and biomasses of the mixed-species biofilms after decontamination methods were determined by the MTT assay and the CV staining assay, respectively. Here, the mixed-species biofilms were developed directly on the SLA titanium discs. After different debridement, the remaining biofilms in each group were assessed by the MTT assay and the CV staining assay according to the methods mentioned above.

2.6 Biofilm removal assessment using implant models

Six cylindric tissue-level titanium implants with SLA surfaces (3.3 mm in diameter, 12 mm in height) were allocated to two groups. The mixed-species biofilms were produced on implant surfaces by immersing implants into mixed bacterial suspensions. The group AA + MH5C@ZIF-8 received the MH5C@ZIF-8 (125 μg/mL) pre-treatment for 24 h, whereas the group AA was merely immersed into the fresh BHI medium. Subsequently, each implant was evenly coated by an intact layer of bacterial indicator for recognition of the aggregated plaque following the manufacture's recommendations. Afterwards, all implants received the identical erythritol air abrasion treatment by the same experienced clinician *via* the AA device with subgingival nozzles (EMS, Switzerland) (Sahrmann et al., 2015; Matsubara et al., 2020). The distance was set to 10 mm, the static pressure was set at 7 bar, and the processing time was set to totally 1 min. After air abrasions, all discs were dried by the compressed air for nearly 10 s for removing the retained powders.

As for biofilm removal assessment, the standard digital photographs of dental implants were taken with the digital SLR camera (Canon digital SLR). Here, the shutter speed was set at 1/4,000 and the aperture was set at F32. These photos have been compounded so as to build the panoramic images of dental implants. With the aid of the color analysis software (Photoshop CC, United States), the pixel percentages of retained plaque indicators were assessed and the corresponding percentage of biofilm removal was then calculated. As for the implant surfaces analysis, the area roughness (Sa) of implant surfaces was measured by the optical profilometry analysis through the TrueSurface Microscopy (WITec Alpha 300, Germany). Specifically, the Sa value was obtained *via* the evaluations of change in height on implant surfaces across numerous individual points.

2.7 Re-osseointegration potential after debridement

To evaluate the re-osseointegration potentials of the contaminated titanium surface after debridement, five experimental groups were designed for further cellular experiments: group AA, biofilms removed with erythritol air abrasion (AA); group MH5C@ZIF-8, biofilms dealt with high concentrations of MH5C@ZIF-8 (125 μg/mL) for 24 h; group AA + MH5C@ZIF-8, biofilms treated with MH5C@ZIF-8 (125 μg/mL) for 24 h followed by erythritol AA; the control group, untreated biofilms; and the clean group, totally intact titanium discs without biofilms and never contaminated by bacteria suspensions.

TABLE 1 Primer pairs used in real-time PCR analysis.

Gene	Primers (F = forward, R = reverse)
ALP	F: TCCGTGGGTCGGATTCCT
	R: GCCGGCCCAAGAGAGAA
OPN	F: TCCAAGGAGTATAAGCAGCGGGCCA
	R: CTCTTAGGGTCTAGGACTAGCTTCT
RUNX2	F: ACCAGCAGCACTCCATATCTCTAC
	R: CTTCCATCAGCGTCAACACCATC
OCN	F: ATTGTGACGAGCTAGCGGAC
	R: GCAACACATGCCCTAAACGG
β-actin	F: CACCCGCGAGTACAACCTTC
	R: CCCATACCCACCATCACACC

Before subsequent experiments, all titanium discs were sterilized by the ethylene oxide sterilizer. Hence merely dead biofilms or bacteria were retained on titanium surfaces.

As for cell adhesions, cell suspensions with the cell density at 1×10^4 cell/mL was transferred to each sample. After cultured for 24 h, rBMSCs were fixed in paraformaldehyde for 10 min and then permeabilized by 0.5% Triton X-100 for nearly 5 min. Afterwards, each sample was firstly stained by fluorescein isothiocyanate-phalloidin (FITC, Sigma-Aldrich, United States) for 30 min and further stained by the 4′,6-diamidino-2-phenylindole dihydrochloride (DAPI, Sigma-Aldrich, United States) for 5 min in the dark. The fluorescence images were obtained *via* the inverted fluorescence microscope (IX70, Olympus Corporation, Japan).

As for cell proliferation, cell suspensions with the cell density at 1×10^4 cell/mL was transferred to each sample initially. Then the rBMSCs viability was evaluated by the cell counting kit (CCK)-8 assay (AbD Serotec, UK) at 1, 3, and 7 days. Specifically, CCK-8 solution was transferred to different samples and cultured for totally 2 h, and the absorbance at 450 nm was recorded by the BioTek instrument.

As for cell osteogenic differentiations, cell suspensions with the cell density at 4×10^4 cell/mL was transferred to each sample initially. After 24 h, the previous culture medium was changed to the differentiation medium containing DMEM supplemented with dexamethasone, sodium β-glycerophosphate and ascorbic acid-2-phosphate (Thermo Fisher Scientific, United States). The staining of alkaline phosphatase (ALP) was carried out at 4, 7, and 14 days. In brief, samples were fixed in paraformaldehyde and stained by using the BCIP/NBT ALP Color Development Kit (Beyotime, China). Total RNA of rBMSCs at 7 and 14 days was extracted by the TRIzol reagent (Thermo Fisher Scientific, United States) and then reverse transcribed into cDNA by the Primescript RT Reagent Kit (TakaraBio Inc., Japan). Then the expressions of the osteogenesis-related genes were determined by the reverse transcription-polymerase chain reaction (RT-PCR) (LightCycler 480, Switzerland) *via* the QuantiTest SYBR Green Kit (Takara, Japan). Here, β-actin was used as an internal control. The relative ratios were analyzed by the relative expression analysis ($2^{-\Delta\Delta CT}$). The primer sequences were displayed in Table 1.

2.8 Statistical analysis

Each experiment was performed in triplicates, and the data was expressed as means ± standard deviations. The one-way analysis of variation coupled with the Student–Newman–Keuls *post-hoc* tests was utilized to assess the level of significance. The significance level was set at $^*p < 0.05$.

3 Results and discussion

3.1 Synthesis and characterization of nanoparticles

The native structure of antimicrobial peptide MH5 was ILGPVLGLVSDTLDDVLGIL-NH2 (MH5N) (Ortiz-Gomez et al., 2020). The peptide MH5C (ILGPVLGLVSDTLDDVLGIL-COOH), the C-terminally deamidated isoform of MH5, was a hydrophobic anionic molecule with 20 amino acids (Ortiz-Gomez et al., 2020). Dennison et al. (2015) have demonstrated the significant effects of C-terminal deamidation on the antibacterial activities of peptide MH5 against gram-negative bacteria. During the typical biomimetic mineralization, biomolecules (including antimicrobial peptide) were trapped into ZIF-8 NPs, formed by the self-assembly of organic linkers and metal ions through the facile one-pot water phase method (Abdelhamid, 2021). The synthetic procedure of ZIF-8 and MH5C@ZIF-8 NPs were schematically illustrated in Figure 1A. Specifically, an aqueous solution containing the target antimicrobial peptide MH5C together with 2-methylimidazole was blended with the aqueous solution of the zinc nitrate. It is worth mentioning that the synthetic procedure here was green, simple, and rapid. In the synthesis processes, the synergistic interactions between biomolecules and precursors were extremely crucial to the nucleation and growth process (Xuan et al., 2020; Zou et al., 2020; Han et al., 2022). Previous studies have also found that only biomolecules with negative charge or with low isoelectric point (PI) would form biomolecules@ZIF-8 (Fan et al., 2018; Maddigan et al., 2018; He et al., 2019). In this study, the MH5C with the PI of 6.5, which exhibited negative charge at the neutral pH, has been utilized for the formation of biomimetically mineralized ZIF-8. During mineralization, the initial indication for nanoparticles formations was the transformation of transparent solutions containing reactants into turbid solutions following vigorous stirrings (Xuan et al., 2020; Zou et al., 2020). As expected, the biomineralization process of MH5C under the specific reaction conditions was very quick (within several minutes). Based on these, it was estimated that the negatively charged peptide MH5C posed specific affinities to the specific ZIF-8 precursor owing to electrostatic attractions, which would finally induce the rapid form of MH5C@ZIF-8 NPs.

In order to gain a deeper understanding of the microstructure of MH5C@ZIF-8 NPs and its ZIF-8 NPs control, samples were observed by SEM, which revealed that both monodisperse particles possessed a regular rhomboidal dodecahedron shape accompanied with a relatively smooth surface (Figure 2A). The TEM images depicted the macroscopic state of nanoparticles in water. The ZIF-8 NPs exhibited the rhombic dodecahedron structures accompanied by the sharp edge as well as the uniform particle sizes, whereas encapsulation of MH5C into ZIF-8 seemed to slightly smooth edge sharpness of these dodecahedrons and increase the diameters of these

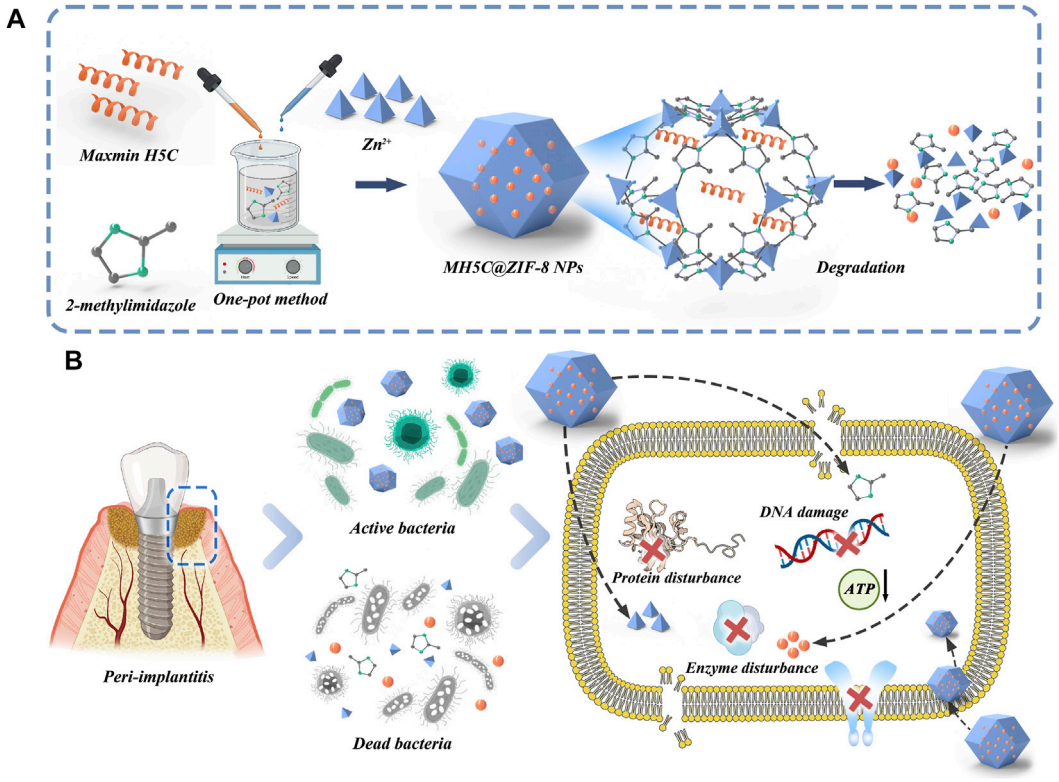

FIGURE 1
(A) Schematic illustration of the fabrication of MH5C@ZIF-8 NPs and degradation route after entering bacteria. **(B)** Potential antimicrobial mechanisms involved in this chemical decontamination strategy.

nanoparticles fractionally (Figure 2A). It is presumed that the loading of MH5C did not affect the shape of ZIF-8 NPs, indicating that MH5C were confined in the interior micropore or entrapped on the surface of ZIF-8 frameworks (Wen et al., 2021). Based on the DLS analysis, the hydrodynamic diameter of MH5C@ZIF-8 NPs displayed the relative narrow size distributions (124.6 ± 4.7 nm) that was slightly larger than that of the ZIF-8 control (107.8 ± 5.1 nm), indicating that the growth process of ZIF-8 was scarcely influenced by the incorporation of MH5C (Figure 2B). Overall, as compared with ZIF-8 NPs, no significant differences were observed in the size and morphology of MH5C@ZIF-8 NPs, suggesting that ZIF-8 would be employed as the promising nanocarrier in the delivery of the antimicrobial peptide MH5C.

The crystalline structure of MH5C@ZIF-8 and pure ZIF-8 NPs was assessed by the XRD measurement. The XRD pattern of the ZIF-8 control here was identical to the simulated one, verifying the smooth formation of the crystal structure (Figure 2C). Specifically, the diffraction peaks at 7.3°, 10.7°, 12.7°, 14.6°, 16.4°, 18.0°, 22.1°, 24.5°, and 26.7° of ZIF-8 control were corresponded to the lattice planes of ZIF-8 [(011), (002), (112), (022), (013), (222)), (114), (233) and (134)] (Yang K. et al., 2022). After the loading of MH5C, it is worth noting that the XRD patterns of MH5@ZIF-8 NPs coincided with those of pure ZIF-8 NPs, suggesting that the crystalline structures of ZIF-8 were not influenced by the encapsulation processes of the MH5C, which was in consistency with the results of electron microscopy (Figure 2C). The chemical structure and functional group of MH5C@ZIF-8 and ZIF-8 NPs were explored by FTIR spectrum. For the ZIF-8 control, the characteristic peaks at 1,585 and 420 cm^{-1} were ascribed to the C=N bond and Zn-N stretching, while the peaks at 1,500–1,350, 1,350–900 and 900–650 cm^{-1} were attributed to the entire ring stretching, in-plane- and out-plane-bending of the ring, which belonged to the pure ZIF-8 (Figure 2D) (Xu et al., 2020; Wen et al., 2021; Yang K. et al., 2022). After the loading of the peptide MH5C, the new absorption bond at 1,652 cm^{-1} agreeing with carbonyls groups of MH5C was observed in the MH5C@ZIF-8 FTIR spectrum, verifying the existence of MH5C within the nanoparticles (Figure 2D) (Li et al., 2018). The TGA was utilized to evaluate the thermal characteristics and loading contents. From the TGA curve under air atmosphere, the minimal weight loss occurred initially at approximately 100°C–200°C, mainly originating from the removals of inorganic salts, water, and the small guest molecule (Figure 2E) (Hao et al., 2022). The subsequent weight loss stage appeared in the temperature of 400°C, and the weight loss became more notable with the increase of temperature, illustrating the gradual destroy of the ZIF-8 skeletons (Hao et al., 2022). The decomposition lasted until reaching approximately 500°C when ZIF-8 has been almost completely degraded, and the remaining materials was carbon and zinc oxide (Hao et al., 2022). The TGA curves of MH5C@ZIF-8 were similar to that of pure ZIF-8, but the weight loss extent of MH5C@ZIF-8 was more notable and the difference was calculated as approximately 13.1 wt%, which resulted from the decompositions of the peptide MH5C embedded within nanoparticles (Figure 2E). As shown in Figure 2F, the surface zeta potential value of pure ZIF-8 and MH5C@ZIF-8 NPs are +13.5 ± 0.77 mV and +15.5 ± 0.81 mV,

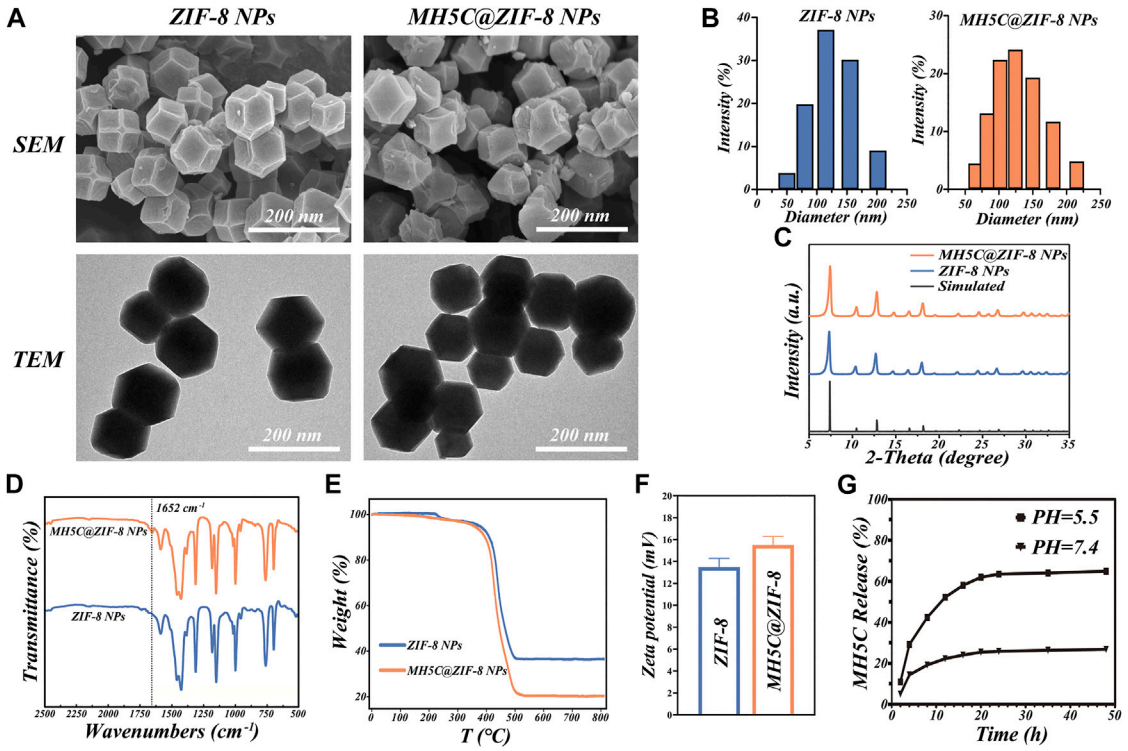

FIGURE 2
Basic properties of MH5C@ZIF-8 NPs. **(A)** SEM and TEM images of MH5C@ZIF-8 NPs and ZIF-8 NPs. **(B)** Particle size distribution of MH5C@ZIF-8 NPs and ZIF-8 NPs dispersed in water. **(C)** XRD patterns of MH5C@ZIF-8 NPs, ZIF-8 NPs and simulated ZIF-8. **(D)** FTIR spectra of MH5C@ZIF-8 NPs and ZIF-8 NPs. **(E)** TGA curves of MH5C@ZIF-8 NPs and ZIF-8 NPs. **(F)** Zeta potential of ZIF-8 NPs and MLT@ZIF-8 NPs. **(G)** MH5C release profiles from MH5C@ZIF-8 in PBS solution (pH = 5.5 and 7.4).

respectively, verifying that the vast majority of the peptide MH5C might be embedded into the frameworks of ZIF-8 (Li et al., 2018). The slight increase in zeta potential might be due to the normally restricted part of electronegative MH5C absorbed onto the external surface of crystal structures (Li et al., 2018; Hao et al., 2022).

It is widely assumed that coordination between 2-methylimidazolate and zinc ions was acid-sensitive, ZIF-8 NPs were stable under neutral conditions but degrade rapidly in the acidic environment (Yu et al., 2021). To demonstrate the potentials of MH5C@ZIF-8 NPs as a pH-responsive delivering nano-systems of antimicrobial peptide, the release study of MH5C was completed in both PBS buffer at pH 7.4 and MES buffer at pH 5.5. The releases of MH5C from MH5C@ZIF-8 NPs were inefficient and the release rate accounted for about 25% in the PBS within 24 h, indicating the stability in the normal physiological environment and the specific property would inhibit the early leakage of peptide during circulations (Figure 2G) (Meng et al., 2022). In contrast, MH5C released rapidly from MH5C@ZIF-8 and the release rate accounted for as over 65% at PH 5.5 within 24 h, indicating that the peptide could be released more rapidly in the low pH conditions similar to inflammatory reactions environments in our bodies (Figure 2G) (Meng et al., 2022). The release of peptide from MH5C@ZIF-8 in a low pH environment was related to the decompositions of ZIF-8 skeletons through the breakages of the coordinate bonds between imidazolate and zinc ions. Hence, it was speculated that the MH5C@ZIF-8 particle was a quite promising pH-sensitive delivering nano-system of peptide for treatments of bacterial infection around dental implants due to the acidic environment.

3.2 Antibacterial activity of nanoparticles

Oral microbes related to peri-implantitis were variable, and most of the time, dominated by the gram-negative anaerobic bacterium, involving *F. nucleatum* and *P. gingivalis* (Zhu et al., 2017). In addition, gram-positive *S. mutans* showed high affinity to the titanium surface (Zhu et al., 2017). Previous studies have reported that *P. gingivalis* bound with *S. mutans* through the incorporations of *F. nucleatum*, which generated the polymicrobial biofilm mimicking the peri-implantitis conditions (Guo et al., 2017; Qin et al., 2020). Figure 3A showed the gram staining of bacteria from the three single specie or the polymicrobial biofilm: the gram-positive *S. mutans* were the purple cocci in chains; the gram-negative *P. gingivalis* were the red cocci; and the gram-negative *F. nucleatum* were the red rod-shaped cells.

In most cases, bacteria would experience four stages, comprising lag phase, log phase, stationary phase, and death phase (Qin et al., 2020). According to the growth curve of the three bacterial strains, bacteria would reach the log phase after about 12 h for *F. nucleatum*, 24 h for *P. gingivalis*, and 6 h for *S. mutans* (Figure 3B). The three strains were harvested when they reached the log phase, because bacteria at this phase were in an optimal growth state corresponding to highly proliferative capabilities for the formation of mature biofilms (Lu et al., 2014; Cao et al., 2020). Here, the antibacterial abilities of the peptide MH5C were reflected by the time spent to enter the specific log phase. The growth curves of three bacterial strains cultured in a series of concentrations of MH5C solutions were shown in Figure 3B. As

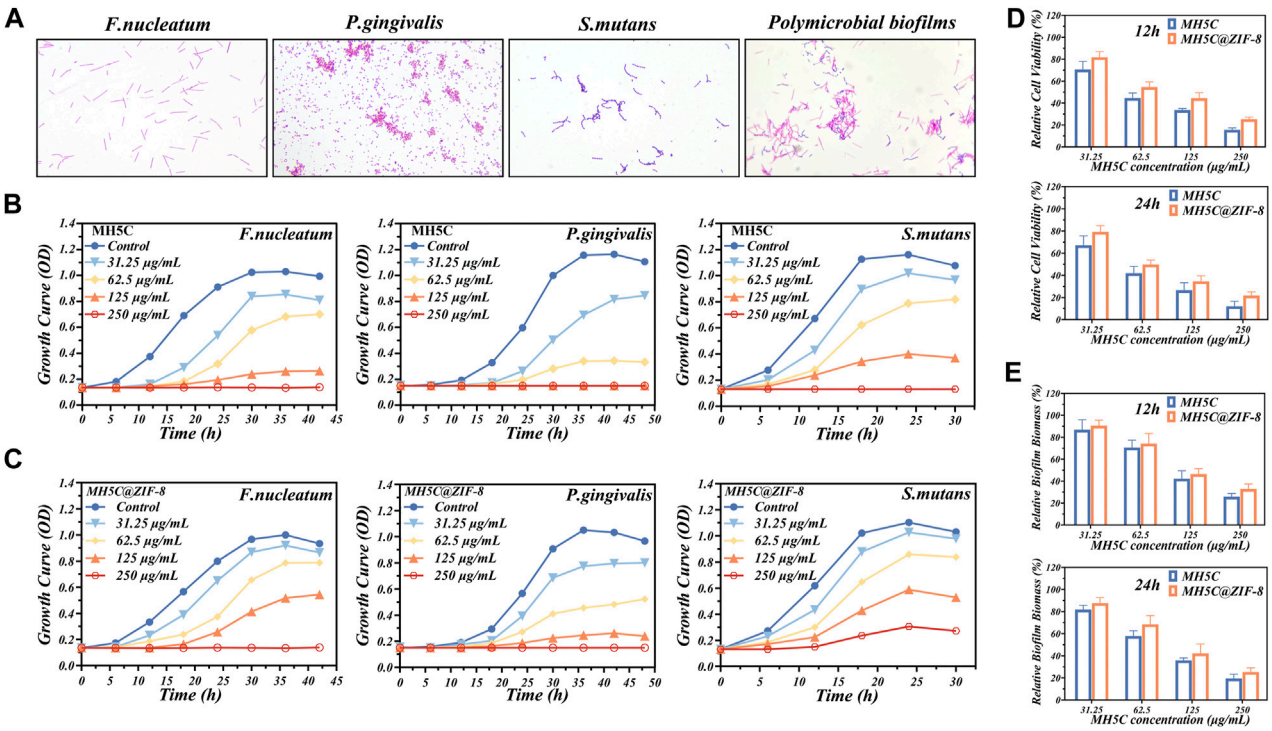

FIGURE 3
Antibacterial properties of MH5C@ZIF-8 NPs. **(A)** Gram staining of *F. nucleatum*, *P. gingivalis*, *S. mutans*, and polymicrobial biofilm. **(B)** Growth curves of the three species of bacteria in free MH5C with different concentrations. **(C)** Growth curves of the three species of bacteria in MH5C@ZIF-8 NPs with different concentrations. **(D)** Bacterial activity in the presence of free MH5C and MH5C@ZIF-8 NPs with different concentrations after 12 h and 24 h. **(E)** Biofilm biomass in the presence of free MH5C and MH5C@ZIF-8 NPs with different concentrations after 12 h and 24 h.

expected, the growth of *F. nucleatum* slowed down and the amount of *F. nucleatum* during the stationary phase were decreased obviously with the increase of the MH5C concentration. Especially, when the concentration of MH5C reached 125 μg/mL, the OD values of *F. nucleatum* remained unchanged across the testing periods from beginning to end, suggesting that almost all bacteria were killed during the lag stage. Moreover, after the stationary stage, the amount of *F. nucleatum* reduced gradually, which resulted from the facts that nutrient in MH5C-contained medium could not sustain the life of bacteria any longer. The overall growth trends of *P. gingivalis* as well as *S. mutans* were similar to that of *F. nucleatum*, and the time to enter the log phase was highly associated with the peptide concentration (Figure 3B). These phenomena indicated the concentration-dependent antibacterial activities of MH5C, which were consistent with previous studies (Dennison et al., 2015; Ortiz-Gomez et al., 2020).

To assess the slow-release sterilization properties of MH5C@ZIF-8 nano-systems, the MH5C@ZIF-8 NPs with specific concentrations of MH5C were added to the culture medium. The growth curves of three bacterial strains cultured in a series of concentrations of MH5C@ZIF-8 solutions were shown in Figure 3C. As compared to the blank culture medium, bacteria in solutions containing ZIF-8 NPs were decreased slightly, confirming the fact that pure ZIF-8 NPs inhibited the growth of *P. gingivalis*, *F. nucleatum*, and *S. mutans* (Figure 3C). Previous studies have shown that photoelectrons trapped at the center of zinc ions were responsible for the production of reactive oxygen species *via* ligand to metal charge transfer, finally inducing cell deformations, cell wall ruptures and cytoplasm leakages (Ahmed et al., 2019; Taheri and Tsuzuki, 2021). In comparison with pure MH5C, the antimicrobial activities of MH5C@ZIF-8 against three bacteria strains were more or less weakened (Figure 3C). These results might be ascribed to the slow-release rates of MH5C in the MH5C@ZIF-8 nano-systems and the maximum utilizations of antimicrobial capacities of MH5C@ZIF-8 NPs (Cao et al., 2020). In detail, quite a limited part of the MH5C was released to the solutions in the beginning, for the released antibacterial peptide in the first 24 h accounted for merely 25% of the total released antibacterial peptide. Nevertheless, the amounts of MH5C from MH5C@ZIF-8 were relatively enough to prevent the bacteria growth during the initial period (Figure 3C). Besides, the MH5C encapsulated in the ZIF-8 framework might have longer sterilization time than pure MH5C in the liquid phase, in other words, the MH5C@ZIF-8 might possess controllable antibacterial activity against the three bacteria stains (Cao et al., 2020). After comparing Figures 3B, C, the order of the three species easy to be killed by both pure MH5C and MH5C@ZIF-8 was *P. gingivalis*, *F. nucleatum*, and *S. mutans*. The increased antimicrobial activities against gram-negative pathogens might be owing to the direct hydrogen-bonding interaction occurring between the bacteria membranes of gram-negative bacteria and the C-terminal amide groups of the peptide MH5C (Dennison et al., 2015; Ortiz-Gomez et al., 2020).

After cultivation for 2 days, the polymicrobial biofilms were formed on the surface of culture plates. To evaluate the antimicrobial effects of pure MH5C and MH5C@ZIF-8 NPs on polymicrobial biofilms, the MTT assay and the CV staining assay were used to evaluate the biofilm biomass and cell the viability,

respectively. After 12 h, the relative cell viability in group MH5C with MH5C concentrations of 31.25, 62.5, 125, and 250 μg/mL was 70.57% ± 7.45%, 44.57% ± 4.67%, 33.63% ± 1.43%, and 15.60% ± 1.68%, whereas that in group MH5C@ZIF-8 was 81.82% ± 5.02%, 54.60% ± 4.65%, 44.46% ± 5.04%, and 25.31% ± 1.90% (Figure 3D). After 24 h, the relative cell viability in group MH5C was 67.15% ± 8.45%, 41.98% ± 6.11%, 26.61% ± 6.75%, and 12.09% ± 4.43%, whereas that in group MH5C@ZIF-8 was 79.23% ± 5.68%, 49.76% ± 4.01%, 34.61% ± 5.03%, and 21.76% ± 3.37% (Figure 3D). After 12 h, the relative biofilm biomass in group MH5C was 86.87% ± 9.11%, 70.65% ± 6.68%, 42.24% ± 717%, and 25.83% ± 2.93%, whereas that in group MH5C@ZIF-8 was 90.56% ± 5.11%, 74.25% ± 9.21%, 46.45% ± 4.84%, and 32.87% ± 4.58% (Figure 3E). After 24 h, the relative biofilm biomass in group MH5C was 81.78% ± 3.97%, 57.86% ± 4.81%, 35.87% ± 2.19%, and 19.46% ± 3.83%, whereas that in group MH5C@ZIF-8 was 87.65% ± 4.96%, 68.47% ± 7.90%, 42.13% ± 8.49%, and 25.35% ± 3.75% (Figure 3E). These antibiofilm results demonstrated that the bacterial viabilities and the biofilm biomass decreased as the MH5C concentrations increased, confirming that the antibiofilm property of MH5C was concentration dependent. Moreover, antibiofilm results quantitatively demonstrated that the biofilm destruction efficiencies were slightly decreased as MH5C encapsulated into the ZIF-8 crystals, partly due to the gradual degradation of ZIF-8 and the sustained-release of MH5C (Yu et al., 2021). The slow-release sterilization abilities were mainly associated with degradation of MOFs, further determined by the chemical stability and the structural characteristic of MOFs (Cao et al., 2020). It is widely accepted that too strong stabilities made it tough to release antibacterial peptides, whereas too weak stabilities caused rapid release rates and underutilizations of antibacterial peptides (Yang M. et al., 2022). Our results showed that the structural stability of as-synthesized MH5C@ZIF-8 nanoparticles was appropriate.

The antimicrobial activities of MH5C@ZIF-8 NPs primarily depended on the antibacterial peptides and zinc ions released to inflammation sites along with the hydrolysis and collapses of the whole frameworks (Ju et al., 2021; Wan et al., 2021). In detail, with the help of sustained released peptides and metal ions, the cell membranes, the membrane potentials, and the ion homeostasis were initially interrupted, causing obvious membrane dyshomeostasis, membrane permeability, and leakages of the cell component (Figure 1B) (Wen et al., 2021; Han et al., 2022). Afterwards, ions or peptides passed through the cell membranes to damage the intracellular nucleic acid, hamper the protein formations, block the ATP synthesis and inhibit the enzyme activity (Figure 1B) (Hou et al., 2021; Li et al., 2021). Additionally, the imidazole ring released from ZIF-8 might exhibit antibacterial effects as well by the disruption of the liposome composed of phospholipid containing the unsaturated fatty acid (Wan et al., 2021). As a consequence, *F. nucleatum*, *P. gingivalis*, and *S. mutans* would be almost all inactivated during these courses.

3.3 Cleaning capacity of mechanical-chemical synergistic treatments

SEM observations were used to observe the morphologies and membrane integrities of three single-species biofilms. In the control group, the biofilms with the firm and dense cluster of internal bacteria were clearly visible (Figure 4A). Most bacteria in the control exhibited smooth and intact cell structures with abundant intracellular materials. In the group AA, structures of biofilms were disrupted into the disordered cluster, and the amounts of bacteria were evidently reduced, which might ultimately facilitate the transport and application of antimicrobial agents (Figure 4A). Accordingly, it was partly proved that the mechanical removals of biofilms remained the essential step to clean the infected surface during peri-implantitis treatments. In the MH5C@ZIF-8 group, most bacteria were distributed across the pores and merely the small piles instead of a whole piece of aggregated colony were observed (Figure 4A). Here, the cell wall of MH5C@ZIF-8-treated bacteria appeared dis-continuous and even collapsed. In the group AA + MH5C@ZIF-8, the pore on surfaces of titanium discs was exposed again and almost all the bacteria were collapsed, partially indicating that the strong clean capacities of the synergistic therapy (Figure 4A). Based on these, the air abrasion would disrupt the biofilm structures and remove the absorbed extracellular polymeric substances (EPSs) (Qin et al., 2020). During microbial biofilms formations, the secreted EPSs would ensure mechanical stabilities, form the three-dimensional scaffolds and facilitate bacteria adhesions (Wan et al., 2021; Yu et al., 2021). Hence MH5C@ZIF-8 NPs alone even at the high concentration of 125 μg/mL could not diffuse through the EPSs to kill the internal bacteria within polymicrobial biofilms. However, MH5C@ZIF-8 NPs could act as the adjunct to air abrasion successfully, which weakened the biofilms and killed the rest bacteria.

The typical three-dimensional images of live/dead staining for *F. nucleatum*, *P. gingivalis*, and *S. mutans* biofilms were depicted in Figure 4B, where red and green stained areas represented dead and live bacteria, respectively. In the control group, the majority emitted fluorescence while the minority emitted red fluorescence, suggesting that the excellent growth trends of internal bacteria (Figure 4B). In the group AA, a part of bacteria was dyed red, but lots of green fluorescence were still observed, indicating that antibacterial abilities of air abrasion on rough surfaces were relatively limited (Figure 4B). In the MH5C@ZIF-8 group, some dead bacteria were found, indicating that MH5C@ZIF-8 exhibited antibacterial properties against all three pathogenic bacteria (Figure 4B). In sharp contrast, in the group AA + MH5C@ZIF-8, only spotted and scattered red fluorescence has been observed, further verifying that the enhanced bactericidal activities of the synergistic therapy (Figure 4B). The antibacterial capabilities of most antimicrobial agents including MH5C@ZIF-8 alone were less effective against the mature biofilms (Kanwar et al., 2017; Renvert and Polyzois, 2018). For the above reason, the initial mechanical debridement for destroying the intact biofilms was quite essential (Qin et al., 2020). In this study, the pretreatment MH5C@ZIF-8 (125 μg/mL) followed by the air abrasion could fully break up the EPSs, efficiently penetrate the biofilms, and eventually eliminate the residual bacteria, thus the synergistic treatment might be an ideal way to manage biofilms around rough surfaces.

To evaluate the antimicrobial effects of the synergistic therapy on the mature polymicrobial biofilms formed on commercially used SLA titanium surfaces, we used the MTT assay and the CV staining assay to evaluate the relative biofilm biomass and the relative cell viability after different debridement. The relative cell viability after 12 h in groups MH5C@ZIF-8, AA and AA + MH5C@ZIF-8 was decreased to 80.31% ± 10.17%, 29.01% ± 5.67%, and 13.87% ± 1.98% (Figure 4C). The relative cell viability after 24 h in groups MH5C@ZIF-8, AA and AA + MH5C@ZIF-8 was decreased to 69.01% ± 5.74%,

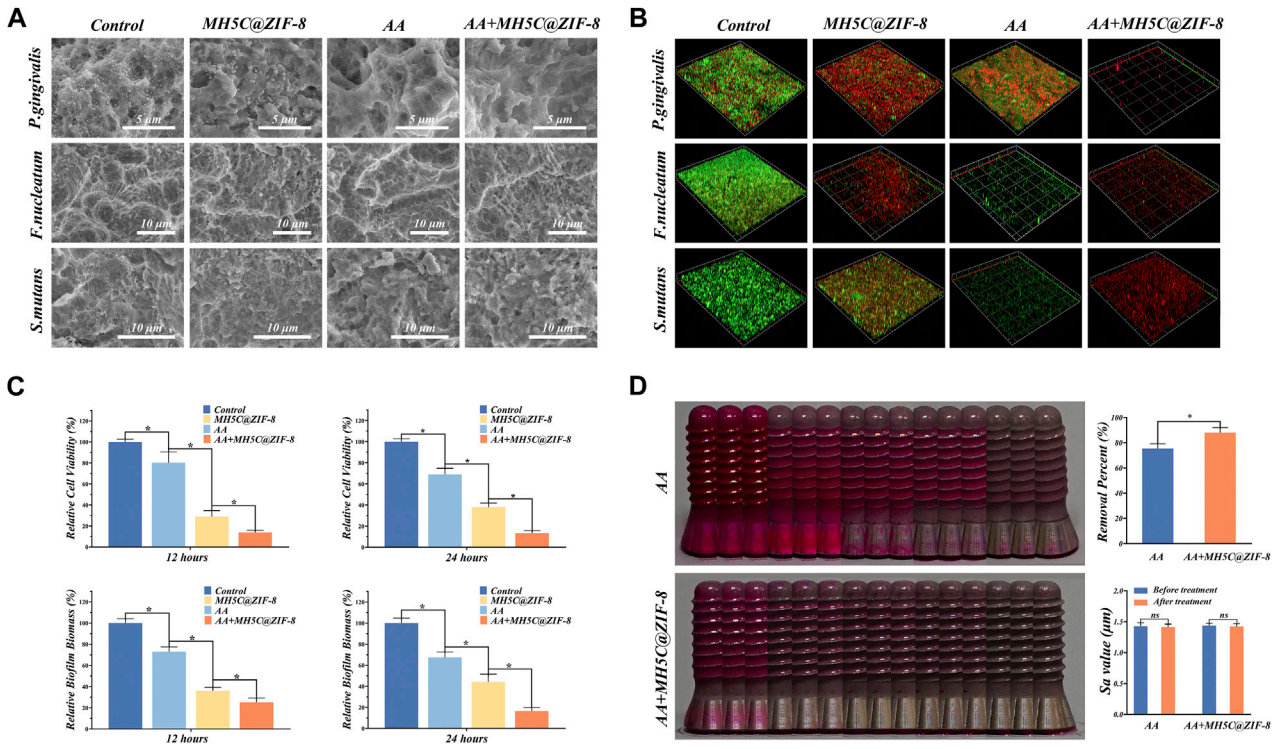

FIGURE 4
Decontamination efficiencies of the synergistic therapy using erythritol air-polishing coupled with MH5C@ZIF-8 NPs. **(A)** SEM morphologies of *F. nucleatum*, *P. gingivalis*, and *S. mutans* after different debridement. **(B)** Representative 3D live/dead images of single-species biofilms in different groups. **(C)** Bacterial activity and biofilm biomass in each group with different treatments. **(D)** Assessment of the residual stains from digital photo as well as the surface roughness after 60 s of air abrasion with or without the pre-treatment of MH5C@ZIF-8 NPs.

38.07% ± 3.71%, and 13.24% ± 2.43% (Figure 4C). The relative biofilm biomass after 12 h in groups MH5C@ZIF-8, AA and AA + MH5C@ZIF-8 was decreased to 73.02% ± 4.54%, 36.02% ± 3.43%, and 25.12% ± 4.21% (Figure 4C). The relative biofilm biomass after 24 h in groups MH5C@ZIF-8, AA and AA + MH5C@ZIF-8 was decreased to 67.50% ± 5.01%, 44.21% ± 7.24%, and 16.59% ± 3.14% (Figure 4C). Air abrasion could destroy the structures of mature bacterial membranes, but it could not effectively kill internal bacteria in inaccessible areas (Louropoulou et al., 2014). Chemical decontaminations could kill individual bacteria, but it could not effectively penetrate the interior of mature polymicrobial biofilms (Ntrouka et al., 2011). Based our findings, MH5C@ZIF-8 at high concentrations (125 μg/mL) coupled with air abrasion effectively eliminated the polymicrobial biofilms remaining on previously contaminated implant surfaces.

3.4 Biofilm removal assessment using implant models

Mechanical debridement remained the gold standard in treatments of peri-implantitis (Sahrmann et al., 2015). Air abrasion employing erythritol powders exhibited excellent cleaning potentials on screw-shaped implants with rough surfaces in comparison with the manual or ultrasonic instrument (Al-Hashedi et al., 2017). Small particles like erythritol powders would reach the area inaccessible by large particles, and gain high solubility potentials that could reduce the amounts of the undissolved particle within the water-air mixtures, which finally might contribute to surface abrasions (Sahrmann et al., 2015; Tong et al., 2021). However, based on the digital photography, complete biofilm removals were not fulfilled on SLA surfaces even by air abrasion (Figure 4D). In other words, due to the complex and rough surfaces, mechanical decontaminations of these areas remained the challenging task in the managements of peri-implantitis. Quantitative data of the visual color analysis suggested significant biofilm removal differences between group AA + MH5C@ZIF-8 and group AA (Figure 4D). Here, with the pretreatment of MH5C@ZIF-8 (125 μg/mL), the biofilm removal percent was increased from 75.33% ± 3.78% to 88.01% ± 4.12% (Figure 4D). Previous studies have shown that the additions of antibacterial agents to small AA particles not only promoted the removals mature biofilms, but also decreased the likelihoods of the biofilm-associated infection in the future (Drago et al., 2017). Another study has demonstrated that chlorhexidine contained erythritol powders was quite effective to reduce bacterial viabilities on the infected titanium disc (Mensi et al., 2018). In this study, the surface roughness was not altered by the erythritol AA treatments with or without MH5C@ZIF-8 (Figure 4D). Hence it was safe to apply the synergistic therapy using erythritol AA coupled with MH5C@ZIF-8 NPs as it caused minimal changes in the surface roughness. Besides, glycine could be easily degradable by our body, so the presences of glycine particles seemed quite unproblematic. Therefore, the air abrasion associated with antimicrobial agents MH5C@ZIF-8 NPs favored the prognosis of peri-implantitis treatments.

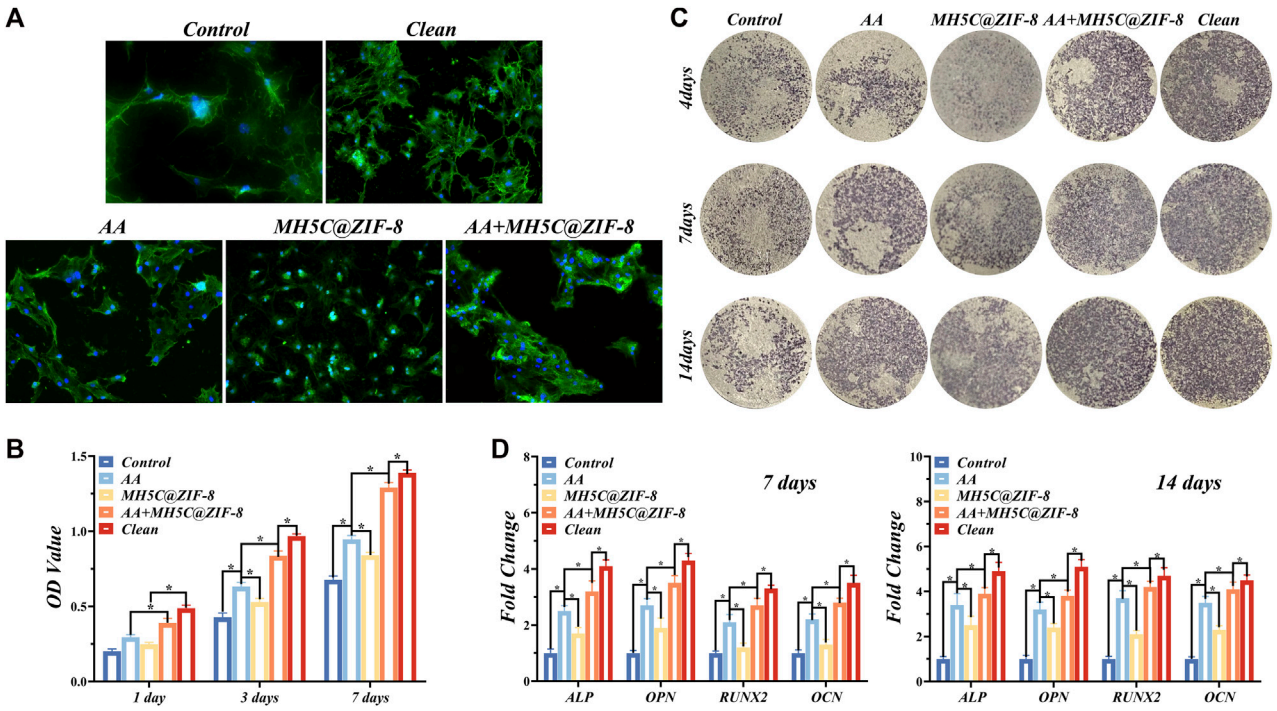

FIGURE 5
Re-osseointegration on contaminated titanium plates treated with erythritol air-polishing coupled with MH5C@ZIF-8 NPs. **(A)** Fluorescent images of BMSCs cultured on contaminated titanium plates after different treatments. **(B)** Cell proliferation assay of BMSCs cultured on contaminated titanium plates after different treatments. **(C)** ALP staining of BMSCs cultured on contaminated titanium plates after different treatments. **(D)** Osteogenic-related gene expression after culturing for 7 and 14 days.

3.5 Re-osseointegration potential after debridement

The initial cell adhesions were observed by staining by DAPI and FITC for the visualization of the nuclei and F-actin. The spherical morphology of BMSCs was observed on groups control, AA and MH5C@ZIF-8 owing to a lack of the filopodia extension (Figure 5A). The expression of F-actin in the group AA + MH5C@ZIF-8 was more obvious and lots of filopodia were detected accordingly (Figure 5A). The BMSCs on these totally clean surfaces demonstrated the well-organized cytoskeleton structure, the multipolar spindle morphologies, and a lot of lamellipodia as well as filopodia (Figure 5A). The results of CCK-8 assay were remarkably consistent with the adhesive results. The BMSC viabilities in groups clean and AA + MH5C@ZIF-8 were significantly higher than in other groups at all timepoints (Figure 5B). The average OD value increased along with the culture time suggesting the continuous cell proliferations in the group AA + MH5C@ZIF-8 (Figure 5B). The cell adhesion and cell proliferation experiments consistently indicated that the AA + MH5C@ZIF-8 would debride most of the biofilms and the potential residual particles showed no apparent cytotoxicity to the proliferation of BMSCs. Here, to evaluate the effects of contaminated surfaces after debridement on cell behaviors, we maintained surface morphologies of contaminated surfaces by sterilization before cellular studies, which have been performed by other researchers before (John et al., 2014; Qin et al., 2020). The ultimate fates of titanium implants depended on outcomes of the so-called "race for the surface" between the oral pathogen and the host cell (Zhu et al., 2017). Implant surface contaminations mainly caused two corruptive effects, one was the facilitated recolonizations of pathogenic bacteria, and the other was the reduced cytocompatibilities of eucaryotic cells involved in healing processes (Sahrmann et al., 2015). Here, after incubations with these three bacteria species for 2 days, the original microscopic pore on SLA surfaces was totally covered with numerous bacteria as well as EPSs, thus establishing mature multispecies biofilms. After debridement, pores on contaminated surfaces were distinguished again, which facilitated the adhesion of osteogenic cells. Our results showed that BMSCs acclimated and grew rapidly in the AA + MH5C@ZIF-8 group, which indicated that the retained biofilms after the synergistic therapy did no harm to the initial adhesions and proliferations of BMSCs. This might be due to high clean capacities of the synergistic therapy and the residual particles would not inhibit normal cell functions.

The ALP staining images of BMSCs in different groups were displayed in Figure 5C. The previously contaminated discs in groups AA or MH5C@ ZIF-8 exhibited increased ALP expressions as compared to the control group (Figure 5C). Among all groups, expression of ALP was highest in the clean group, followed by the Group AA + MH5C@ZIF-8 (Figure 5C). Furthermore, RT-PCR results showed that after culturing for 7 and 14 days, obvious increased mRNA levels of ALP, OPN, RUNX2, and OCN were observed in the groups AA or MH5C@ ZIF-8 as compared with the control (Figure 5D). It was also noted that BMSC osteogenesis in group AA + MH5C@ZIF-8 was similar to those on intact clean titanium surface (Figure 5D). These results might be ascribed to the destructions and removals of the biofilms and the subsequent

re-exposures of the micropores on SLA surfaces in the group AA + MH5C@ZIF-8, which improved the osteogenic differentiation of BMSCs. These findings also suggested that the residual biofilm after the sterilization in the group AA + MH5C@ZIF-8 caused no adverse effects on the cell behaviors. Moreover, the enhanced BMSCs osteogenic differentiations observed in the group AA + MH5C@ZIF-8 might be owing to the formations and precipitations of zinc ions from ZIF-8 nanoparticles (Hoseinpour and Shariatinia, 2021). Here, ZIF-8 NPs in the culture medium agglomerated and precipitated frequently on the SLA surfaces after the pretreatment of MH5C@ZIF-8 for 24 h, which was somewhat similar to ZIF-8 coatings on titanium surfaces (Liu et al., 2020b). Previous studies exhibited that the functionalized ZIF-8 coatings deposited on titanium promoted the viabilities and the osteogenic property of osteogenic cells (Sandomierski et al., 2022). Another study also demonstrated that ZIF-8-coated titanium surfaces enhanced the osteogenesis of the osteoblast and promoted new bone formations (Zhang et al., 2017). Nevertheless, too high concentrations of ZIF-8 still might bring up somewhat toxic effects to cells. Therefore, our findings emphasized the great potential of the synergistic therapy as a credible alternative for improving the biocompatibility and rendering the re-osseointegration on contaminated implant surfaces, boding well for the comprehensive applications in peri-implantitis treatments.

However, our study is preliminary. First, the specific antibacterial mechanisms of MH5C@ZIF-8 NPs retained indistinct and further molecular mechanism experiments are still needed. Second, during cellular experiments, only dead biofilms were maintained on titanium surfaces and these circumstances did not reflect the condition occurring clinically. Further animal experiments should be designed to evaluate re-osteogenesis effects of the synergistic therapy.

4 Conclusion

To summarize, an effective and mild method to synthesis the antibacterial agent MH5C@ZIF-8 NPs has been established. The formed MH5C@ZIF-8 NPs possessed nanoscale sizes as well as robust stabilities, and effectively protected MH5C from rapid release. The MH5C@ZIF-8 NPs not only possessed slow-release abilities, but also exhibited excellent antibacterial abilities against pathogenic bacteria. Here, the air abrasion with erythritol powders was safe to use on implant surfaces as it resulted in obvious biofilm destructions and minimal surface roughness changes. Moreover, their cleaning capacities was significantly increased with the pretreatment of MH5C@ZIF-8 NPs. However, none of MH5C@ZIF-8 NPs nor erythritol air abrasion alone was able to completely remove the stained biofilms on titanium. In contrast, the synergistic strategy using erythritol air abrasion coupled with an as-synthesized pH-responsive antimicrobial agent MH5C@ZIF-8 NPs demonstrated excellent debridement and re-osteogenesis properties. In other words, notwithstanding the limitations of our study, MH5C@ZIF-8 NPs at high concentrations combined with air abrasion significantly removed polymicrobial biofilms that remained on previously contaminated titanium surfaces. The osteogenic potentials of BMSC were also regained on titanium surfaces treated by the synergistic therapy *in vitro*, which might provide a new idea for the treatments of peri-implantitis.

Data availability statement

The original contributions presented in the study are included in the article/Supplementary Material, further inquiries can be directed to the corresponding authors.

Author contributions

YZ and QZ contributed equally to this work. YZ and QZ conceived, designed and conducted the experiments. YZ, CZ, and YG conducted the data analyses. YZ and QZ wrote the manuscripts. HL, SQ, and SL oversaw the completion of this study and edited the manuscript.

Funding

This work was supported by the Research Discipline Fund (No. KQYJXK2020) from Ninth People's Hospital, Shanghai Jiao Tong University School of Medicine, and College of Stomatology, Shanghai Jiao Tong University. This work was also supported by the Innovative Research Team of High-Level Local Universities in Shanghai (SHSMU-ZDCX20212500).

Conflict of interest

The authors declare that the research was conducted in the absence of any commercial or financial relationships that could be construed as a potential conflict of interest.

Publisher's note

References

Abdelhamid, H. N. (2021). Zeolitic imidazolate frameworks (zif-8) for biomedical applications: A review. *Curr. Med. Chem.* 28 (34), 7023–7075. doi:10.2174/0929867328666210608143703

Ahmed, S. A., Bagchi, D., Katouah, H. A., Hasan, M. N., Altass, H. M., and Pal, S. K. (2019). Enhanced water stability and photoresponsivity in metal-organic framework (mof): A potential tool to combat drug-resistant bacteria. *Sci. Rep.* 9 (1), 19372. doi:10.1038/s41598-019-55542-8

Al-Hashedi, A. A., Laurenti, M., Benhamou, V., and Tamimi, F. (2017). Decontamination of titanium implants using physical methods. *Clin. Oral Implants Res.* 28 (8), 1013–1021. doi:10.1111/clr.12914

Cao, P., Wu, X., Zhang, W., Zhao, L., Sun, W., and Tang, Z. (2020). Killing oral bacteria using metal–organic frameworks. *Industrial Eng. Chem. Res.* 59 (4), 1559–1567. doi:10.1021/acs.iecr.9b05659

Carraro, F., Velasquez-Hernandez, M. J., Astria, E., Liang, W., Twight, L., Parise, C., et al. (2020). Phase dependent encapsulation and release profile of zif-based biocomposites. *Chem. Sci.* 11 (13), 3397–3404. doi:10.1039/c9sc05433b

Dennison, S. R., Harris, F., Mura, M., and Phoenix, D. A. (2018). An atlas of anionic antimicrobial peptides from amphibians. *Curr. Protein Pept. Sci.* 19 (8), 823–838. doi:10.2174/1389203719666180226155035

Dennison, S. R., Morton, L. H. G., Harris, F., and Phoenix, D. A. (2016). Low ph enhances the action of maximin h5 against staphylococcus aureus and helps mediate lysylated phosphatidylglycerol-induced resistance. *Biochemistry* 55 (27), 3735–3751. doi:10.1021/acs.biochem.6b00101

Dennison, S. R., Mura, M., Harris, F., Morton, L. H., Zvelindovsky, A., and Phoenix, D. A. (2015). The role of c-terminal amidation in the membrane interactions of the anionic antimicrobial peptide, maximin h5. *Biochim. Biophys. Acta* 1848 (5), 1111–1118. doi:10.1016/j.bbamem.2015.01.014

Drago, L., Bortolin, M., Taschieri, S., De Vecchi, E., Agrappi, S., Del Fabbro, M., et al. (2017). Erythritol/chlorhexidine combination reduces microbial biofilm and prevents its formation on titanium surfaces *in vitro*. *J. Oral Pathol. Med.* 46 (8), 625–631. doi:10.1111/jop.12536

Drago, L., Del Fabbro, M., Bortolin, M., Vassena, C., De Vecchi, E., and Taschieri, S. (2014). Biofilm removal and antimicrobial activity of two different air-polishing powders: An *in vitro* study. *J. Periodontol.* 85 (11), e363–e369. doi:10.1902/jop.2014.140134

Fan, G., Dundas, C. M., Zhang, C., Lynd, N. A., and Keitz, B. K. (2018). Sequence-dependent peptide surface functionalization of metal-organic frameworks. *ACS Appl. Mater Interfaces* 10 (22), 18601–18609. doi:10.1021/acsami.8b05148

Guo, L., Shokeen, B., He, X., Shi, W., and Lux, R. (2017). *Streptococcus mutans*SpaP binds to RadD of*Fusobacterium nucleatums*sp.*polymorphum*. *Polymorphum. Mol. Oral Microbiol.* 32 (5), 355–364. doi:10.1111/omi.12177

Han, D. L., Liu, X. M., and Wu, S. L. (2022). Metal organic framework-based antibacterial agents and their underlying mechanisms. *Chem. Soc. Rev.* 51 (16), 7138–7169. doi:10.1039/d2cs00460g

Hao, Y., Deng, S., Wang, R., Xia, Q., Zhang, K., Wang, X., et al. (2022). Development of dual-enhancer biocatalyst with photothermal property for the degradation of cephalosporin. *J. Hazard Mater* 429, 12294. doi:10.1016/j.jhazmat.2022.128294

He, J., Sun, S., Lu, M., Yuan, Q., Liu, Y., and Liang, H. (2019). Metal-nucleobase hybrid nanoparticles for enhancing the activity and stability of metal-activated enzymes. *Chem. Commun. (Camb)* 55 (44), 6293–6296. doi:10.1039/c9cc03155c

Hoseinpour, V., and Shariatinia, Z. (2021). Applications of zeolitic imidazolate framework-8 (zif-8) in bone tissue engineering: A review. *Tissue Cell* 72, 101588. doi:10.1016/j.tice.2021.101588

Hou, X., Shi, J., Zhang, J., Wang, Z., Zhang, S., Li, R., et al. (2021). Treatment of acute kidney injury using a dual enzyme embedded zeolitic imidazolate frameworks cascade that catalyzes *in vivo* reactive oxygen species scavenging. *Front. Bioeng. Biotechnol.* 9, 800428. doi:10.3389/fbioe.2021.800428

John, G., Becker, J., and Schwarz, F. (2014). Rotating titanium brush for plaque removal from rough titanium surfaces--an *in vitro* study. *Clin. Oral Implants Res.* 25 (7), 838–842. doi:10.1111/clr.12147

Ju, G., Liu, B., Ji, M., Jin, R., Xu, X., Xiao, Y., et al. (2021). Folic acid-modified mir-491-5p-loaded zif-8 nanoparticles inhibit castration-resistant prostate cancer by regulating the expression of ephx1. *Front. Bioeng. Biotechnol.* 9, 706536. doi:10.3389/fbioe.2021.706536

Kanwar, I., Sah, A. K., and Suresh, P. K. (2017). Biofilm-mediated antibiotic-resistant oral bacterial infections: Mechanism and combat strategies. *Curr. Pharm. Des.* 23 (14), 2084–2095. doi:10.2174/1381612822666161124154549

Karami, A., Mohamed, O., Ahmed, A., Husseini, G. A., and Sabouni, R. (2021). Recent advances in metal-organic frameworks as anticancer drug delivery systems: A review. *Anti-Cancer Agents Med. Chem.* 21 (18), 2487–2504. doi:10.2174/1871520621666210119093844

Keim, D., Nickles, K., Dannewitz, B., Ratka, C., Eickholz, P., and Petsos, H. (2019). *In vitro* efficacy of three different implant surface decontamination methods in three different defect configurations. *Clin. Oral Implants Res.* 30 (6), 550–558. doi:10.1111/clr.13441

Kotsakis, G. A., Lan, C., Barbosa, J., Lill, K., Chen, R., Rudney, J., et al. (2016). Antimicrobial agents used in the treatment of peri-implantitis alter the physicochemistry and cytocompatibility of titanium surfaces. *J. Periodontol.* 87 (7), 809–819. doi:10.1902/jop.2016.150684

Li, P., Li, J., Feng, X., Li, J., Hao, Y., Zhang, J., et al. (2019). Metal-organic frameworks with photocatalytic bactericidal activity for integrated air cleaning. *Nat. Commun.* 10 (1), 2177. doi:10.1038/s41467-019-10218-9

Li, Q., Feng, R., Chang, Z., Liu, X., Tang, H., and Bai, Q. (2022a). Hybrid biomimetic assembly enzymes based on zif-8 as "intracellular scavenger" mitigating neuronal damage caused by oxidative stress. *Front. Bioeng. Biotechnol.* 10, 991949. doi:10.3389/fbioe.2022.991949

Li, Q., Guo, Y., Xu, C., Sun, J., Zeng, F., Lin, S., et al. (2022b). Therapy of spinal cord injury by folic acid polyethylene glycol amine-modified zeolitic imidazole framework-8 nanoparticles targeted activated m/ms. *Front. Bioeng. Biotechnol.* 10, 959324. doi:10.3389/fbioe.2022.959324

Li, R., Chen, T., and Pan, X. (2021). Metal-organic-framework-based materials for antimicrobial applications. *ACS Nano* 15 (3), 3808–3848. doi:10.1021/acsnano.0c09617

Li, Y., Xu, N., Zhu, W., Wang, L., Liu, B., Zhang, J., et al. (2018). Nanoscale melittin@ zeolitic imidazolate frameworks for enhanced anticancer activity and mechanism analysis. *ACS Appl. Mater Interfaces* 10 (27), 22974–22984. doi:10.1021/acsami.8b06125

Liu, Y., Li, Z., Zou, S., Lu, C., Xiao, Y., Bai, H., et al. (2020a). Hyaluronic acid-coated zif-8 for the treatment of pneumonia caused by methicillin-resistant staphylococcus aureus. *Int. J. Biol. Macromol.* 155, 103–109. doi:10.1016/j.ijbiomac.2020.03.187

Liu, Y., Zhu, Z., Pei, X., Zhang, X., Cheng, X., Hu, S., et al. (2020b). Zif-8-modified multifunctional bone-adhesive hydrogels promoting angiogenesis and osteogenesis for bone regeneration. *ACS Appl. Mater Interfaces* 12 (33), 36978–36995. doi:10.1021/acsami.0c12090

Louropoulou, A., Slot, D. E., and Van der Weijden, F. (2015). Influence of mechanical instruments on the biocompatibility of titanium dental implants surfaces: A systematic review. *Clin. Oral Implants Res.* 26 (7), 841–850. doi:10.1111/clr.12365

Louropoulou, A., Slot, D. E., and Van der Weijden, F. (2014). The effects of mechanical instruments on contaminated titanium dental implant surfaces: A systematic review. *Clin. Oral Implants Res.* 25 (10), 1149–1160. doi:10.1111/clr.12224

Lu, X. Y., Ye, J. W., Zhang, D. K., Xie, R. X., Bogale, R. F., Sun, Y., et al. (2014). Silver carboxylate metal-organic frameworks with highly antibacterial activity and biocompatibility. *J. Inorg. Biochem.* 138, 114–121. doi:10.1016/j.jinorgbio.2014.05.005

Maddigan, N. K., Tarzia, A., Huang, D. M., Sumby, C. J., Bell, S. G., Falcaro, P., et al. (2018). Protein surface functionalisation as a general strategy for facilitating biomimetic mineralisation of zif-8. *Chem. Sci.* 9 (18), 4217–4223. doi:10.1039/c8sc00825f

Matsubara, V. H., Leong, B. W., Leong, M. J. L., Lawrence, Z., Becker, T., and Quaranta, A. (2020). Cleaning potential of different air abrasive powders and their impact on implant surface roughness. *Clin. Implant Dent. Relat. Res.* 22 (1), 96–104. doi:10.1111/cid.12875

Meng, X., Guan, J., Lai, S., Fang, L., and Su, J. (2022). Ph-responsive curcumin-based nanoscale zif-8 combining chemophotodynamic therapy for excellent antibacterial activity. *RSC Adv.* 12 (16), 10005–10013. doi:10.1039/d1ra09450e

Mensi, M., Cochis, A., Sordillo, A., Uberti, F., and Rimondini, L. (2018). Biofilm removal and bacterial re-colonization inhibition of a novel erythritol/chlorhexidine air-polishing powder on titanium disks. *Mater. (Basel)* 11 (9), 1510. doi:10.3390/ma11091510

Munoz, V., Duque, A., Giraldo, A., and Manrique, R. (2018). Prevalence of peri-implant disease according to periodontal probing depth and bleeding on probing: A systematic review and meta-analysis. *Int. J. Oral Maxillofac. Implants* 33 (4), e89–e105. doi:10.11607/jomi.5940

Ntrouka, V. I., Slot, D. E., Louropoulou, A., and Van der Weijden, F. (2011). The effect of chemotherapeutic agents on contaminated titanium surfaces: A systematic review. *Clin. Oral Implants Res.* 22 (7), 681–690. doi:10.1111/j.1600-0501.2010.02037.x

Ortiz-Gomez, V., Rodriguez-Ramos, V. D., Maldonado-Hernandez, R., Gonzalez-Feliciano, J. A., and Nicolau, E. (2020). Antimicrobial polymer-peptide conjugates based on maximin h5 and peg to prevent biofouling of e. Coli and p. Aeruginosa. *ACS Appl. Mater Interfaces* 12 (41), 46991–47001. doi:10.1021/acsami.0c13492

Park, J. B., Jeon, Y., and Ko, Y. (2015). Effects of titanium brush on machined and sand-blasted/acid-etched titanium disc using confocal microscopy and contact profilometry. *Clin. Oral Implants Res.* 26 (2), 130–136. doi:10.1111/clr.12302

Qin, W., Wang, C., Jiang, C., Sun, J., Yu, C., and Jiao, T. (2020). Graphene oxide enables the reosteogenesis of previously contaminated titanium *in vitro*. *J. Dent. Res.* 99 (8), 922–929. doi:10.1177/0022034520913873

Renvert, S., and Polyzois, I. (2018). Treatment of pathologic peri-implant pockets. *Periodontol* 76 (1), 180–190. doi:10.1111/prd.12149

Sahrmann, P., Ronay, V., Hofer, D., Attin, T., Jung, R. E., and Schmidlin, P. R. (2015). *In vitro* cleaning potential of three different implant debridement methods. *Clin. Oral Implants Res.* 26 (3), 314–319. doi:10.1111/clr.12322

Sandomierski, M., Jakubowski, M., Ratajczak, M., and Voelkel, A. (2022). Zeolitic imidazolate framework-8 (zif-8) modified titanium alloy for controlled release of drugs for osteoporosis. *Sci. Rep.* 12 (1), 9103. doi:10.1038/s41598-022-13187-0

Schwarz, F., Derks, J., Monje, A., and Wang, H. L. (2018). Peri-implantitis. *J. Periodontol.* 89, S267–S290. doi:10.1002/JPER.16-0350

Taheri, M., and Tsuzuki, T. (2021). Photo-accelerated hydrolysis of metal organic framework zif-8. *ACS Mater. Lett.* 3 (2), 255–260. doi:10.1021/acsmaterialslett.0c00522

Tong, Z., Fu, R., Zhu, W., Shi, J., Yu, M., and Si, M. (2021). Changes in the surface topography and element proportion of clinically failed sla implants after *in vitro* debridement by different methods. *Clin. Oral Implants Res.* 32 (3), 263–273. doi:10.1111/clr.13697

Wan, Y., Fang, J., Wang, Y., Sun, J., Sun, Y., Sun, X., et al. (2021). Antibacterial zeolite imidazole frameworks with manganese doping for immunomodulation to accelerate infected wound healing. *Adv. Healthc. Mater* 10 (22), e2101515. doi:10.1002/adhm.202101515

Wen, T., Lin, Z., Zhao, Y., Zhou, Y., Niu, B., Shi, C., et al. (2021). Bioresponsive nanoarchitectonics-integrated microneedles for amplified chemo-photodynamic therapy against acne vulgaris. *ACS Appl. Mater Interfaces* 13 (41), 48433–48448. doi:10.1021/acsami.1c15673

Xia, X., Song, X., Li, Y., Hou, W., Lv, H., Li, F., et al. (2022). Antibacterial and anti-inflammatory zif-8@rutin nanocomposite as an efficient agent for accelerating infected wound healing. *Front. Bioeng. Biotechnol.* 10, 1026743. doi:10.3389/fbioe.2022.1026743

Xu, M., Hu, Y., Ding, W., Li, F., Lin, J., Wu, M., et al. (2020). Rationally designed rapamycin-encapsulated zif-8 nanosystem for overcoming chemotherapy resistance. *Biomaterials* 258, 120308. doi:10.1016/j.biomaterials.2020.120308

Xuan, J., Liu, Y., Xu, X., Ding, Z., Zhuang, Z., Zhang, Y., et al. (2020). Peptide-mediated synthesis of zeolitic imidazolate framework-8 with controllable morphology and size. *Langmuir* 36 (46), 13981–13988. doi:10.1021/acs.langmuir.0c02496

Yang, K., Jia, P., Hou, J., Zhao, S., and Wang, L. (2022). An ingenious turn-on ratiometric fluorescence sensor for sensitive and visual detection of tetracyclines. *Food Chem.* 396, 133693. doi:10.1016/j.foodchem.2022.133693

Yang, M., Zhang, J., Wei, Y., Zhang, J., and Tao, C. (2022). Recent advances in metal-organic framework-based materials for anti-staphylococcus aureus infection. *Nano Res.* 15 (7), 6220–6242. doi:10.1007/s12274-022-4302-x

Yu, M., Zhang, G., Li, P., Lu, H., Tang, W., Yang, X., et al. (2021). Acid-activated ros generator with folic acid targeting for bacterial biofilm elimination. *Mater Sci. Eng. C Mater Biol. Appl.* 127, 112225. doi:10.1016/j.msec.2021.112225

Yu, Z., Cao, W., Han, C., Wang, Z., Qiu, Y., Wang, J., et al. (2022). Biomimetic metal-organic framework nanoparticles for synergistic combining of sdt-chemotherapy induce pyroptosis in gastric cancer. *Front. Bioeng. Biotechnol.* 10, 796820. doi:10.3389/fbioe.2022.796820

Zhang, X., Chen, J., Pei, X., Wang, J., Wan, Q., Jiang, S., et al. (2017). Enhanced osseointegration of porous titanium modified with zeolitic imidazolate framework-8. *ACS Appl. Mater Interfaces* 9 (30), 25171–25183. doi:10.1021/acsami.7b07800

Zhu, Y., Gu, Y., Qiao, S., Zhou, L., Shi, J., and Lai, H. (2017). Bacterial and mammalian cells adhesion to tantalum-decorated micro-/nano-structured titanium. *J. Biomed. Mater Res. A* 105 (3), 871–878. doi:10.1002/jbm.a.35953

Zou, D., Yu, L., Sun, Q., Hui, Y., Tengjisi, Liu, Y., et al. (2020). A general approach for biomimetic mineralization of mof particles using biomolecules. *Colloids Surf. B Biointerfaces* 193, 111108. doi:10.1016/j.colsurfb.2020.111108

frontiers | Frontiers in Bioengineering and Biotechnology

TYPE Brief Research Report
PUBLISHED 28 February 2023
DOI 10.3389/fbioe.2023.1153631

OPEN ACCESS

EDITED BY
Juncen Zhou,
Stony Brook University, United States

REVIEWED BY
Kakyung Kim,
Stony Brook University, United States
Yuyun Yang,
Harbin Engineering University, China

*CORRESPONDENCE
Antonio López-Valverde,
alopezvalverde@usal.es

†These authors have contributed equally to this work

SPECIALTY SECTION
This article was submitted to Biomaterials, a section of the journal Frontiers in Bioengineering and Biotechnology

RECEIVED 29 January 2023
ACCEPTED 20 February 2023
PUBLISHED 28 February 2023

CITATION
López-Valverde N, Aragoneses J, López-Valverde A, Rodríguez C and Aragoneses JM (2023), Role of BMP-7 on biological parameters osseointegration of dental implants: Preliminary results of a preclinical study.
Front. Bioeng. Biotechnol. 11:1153631.
doi: 10.3389/fbioe.2023.1153631

Role of BMP-7 on biological parameters osseointegration of dental implants: Preliminary results of a preclinical study

Nansi López-Valverde[1†], Javier Aragoneses[1†], Antonio López-Valverde[2*], Cinthia Rodríguez[3] and Juan Manuel Aragoneses[4]

[1]Department of Medicine and Medical Specialties, Faculty of Health Sciences, Universidad Alcalá de Henares, Madrid, Spain, [2]Department of Surgery, Instituto de Investigación Biomédica de Salamanca (IBSAL), University of Salamanca, Salamanca, Spain, [3]Department of Dentistry, Universidad Federico Henríquez y Carvajal, Santo Domingo, Dominican Republic, [4]Faculty of Dentistry, Universidad Alfonso X El Sabio, Madrid, Spain

The aim of this work was to analyze and compare the effect of bone morphogenetic protein-7 on biological parameters related to implant osseointegration in an experimental animal model. Sixteen dental implants were placed in the tibias of four randomly selected minipigs for the following dental implant surface treatments: Group A: conventional treatment of the dental implant surface by SLA (n = 8) and Group B: treatment of the dental implant surface with carboxyethylphosphonic acid and bone morphogenetic protein-7 (n = 8). The animals were sacrificed one month after dental implants placement and a histomorphometric study was performed for the evaluation of bone-to-implant contact, corrected bone-to-implant contact, new bone formation, interthread bone density and peri-implant density using Student's t-test and the non-parametric Mann-Whitney test. The histomorphometric parameters bone-to-implant contact and corrected bone-to-implant contact showed statistically significant differences between the study groups; 34.00% ± 9.92% and 50.02% ± 10.94%, respectively (p = 0.004) for SLA and 43.08% ± 10.76% and 63.30% ± 11.30%, respectively (p = 0.003) for BMP-7. The parameters new bone formation, interthread bone density and peri-implant density did not show statistically significant differences between the study groups (p = 0.951, p = 0.967 and p = 0.894, respectively). Dental implant surfaces treated with carboxyethylphosphonic acid and BMP-7 improve the biological response of dental implants to osseointegration.

KEYWORDS

dental implants, biological parameters, BMP-7, osseointegration, minipig model

1 Introduction

Currently, dental implant placement is considered a predictable treatment option to restore partially or fully edentulous patients; however, despite high success rates, early failures occur, usually attributable to insufficient osseointegration in the early stages of osseointegration, surgical trauma, and infections (Esposito et al., 1998; Sakka et al., 2012; Alghamdi and Jansen, 2020).

In recent years, research has focused on surface treatment procedures for titanium (Ti) alloy dental implants to enhance their biological response during the osseointegration process and prevent the development of peri-implant diseases (Ferraris et al., 2011). Titanium-aluminum-vanadium alloy (Ti-6Al-4V), in addition to having superior strength, provides biocompatibility and mechanical properties to dental implants (Kaur and Singh, 2019) and this, together with surface treatment techniques, modifying the roughness, topography, chemistry and electrical charge of dental implants, would promote an increase in the biological response of the surrounding peri-implant tissues, and of the microscopic contact surface, which would improve the histological reaction at the bone-implant interface (Gittens et al., 2014; Jemat et al., 2015).

Therefore, manufacturers have subjected dental implants to different technical approaches, based on etching, blasting or a combination of both (Khang et al., 2001; Fini et al., 2003; Szmukler-Moncler et al., 2004; Le Guéhennec et al., 2007; Wennerberg and Albrektsson, 2009; Leon-Ramos et al., 2019) with the aim of increasing the surface roughness and, consequently, the success rate of osseointegration. In particular, it has been described that the application of carboxyethylphosphonic acid (CEPA), enhances the osseointegration process, improving protein adhesion, after generating a physicochemical layer of Al_2O_3 or TiO_2 (Aragoneses et al., 2021). On the other hand, conventional surface treatments (Sandblasted Large-Grit Acid-Etched, SLA type) have shown enhanced osseointegrative power when combined with surface bioactivation, based on the immobilization of proteins, enzymes or peptides, which could induce a specific cellular response in peri-implant tissues in the early stages of osseointegration (López-Valverde et al., 2020). Moreover, in order to promote histological performance, some organic substrates have been used to induce bioactivation; in particular, the osteogenic capacity of bone morphogenetic proteins has been demonstrated "*in vivo*" to induce ectopic bone formation by stimulating bone remodeling (Kim et al., 2017). The latest advances are focused on bioactive surfaces, which endow the mechanical properties of implants with osteoinductive properties, by functionalizing the surface, providing a synergistic effect on osteogenesis through molecular recognition events, determining, in a short period of time, the type of tissue that will develop at the bone-implant interface (Rupp et al., 2018).

Bone morphogenetic proteins (BMPs) are osteoinductive proteins belonging to the transforming growth factor beta (TGF-β) family with the ability to stimulate the differentiation of pluripotential cells towards different cell lineages and promote osseointegration of dental implants (López-Valverde et al., 2022).

Silanization has long been considered, the gold standard coating method for adding organic components to Ti oxide; however, siloxane products can be hydrolytically unstable, which may result in a decrease in the concentration of organic components on the implant surface when the silanized surface is exposed to an aqueous medium (Matinlinna et al., 2013). For this reason, new modifying coatings for implant surfaces have been proposed, through the application of organic acids such as phosphates or carbonates, which, in addition to interacting strongly with Ti oxide, allow the formation of stable surfaces, which bind biomolecules, such as BMPs on the metal oxide, creating a true chemical bond between bone tissue and the implant surface, with absence of fibrous tissue at the bone-implant interface (Liu et al., 2004; Hall et al., 2007; Liu et al., 2007).

The aim of our work was to analyze and compare the effect of BMP-7 on biological parameters related to implant osseointegration in an experimental animal model, with a null hypothesis (H_0) stating that there were no differences in these biological parameters, between dental implants treated and not treated superficially with BMP-7.

2 Materials and methods

2.1 Study design

Four ($n = 4$) female minipigs of the Landrace Large White race of 25 kg of weight were selected for this study, according to the European Committee for Standardization guidelines for bone tissue testing. Each animal randomly (Epidat 4.1, Galicia, Spain) received two ($n = 2$) dental implants (grade IV titanium (90 Ti, 6 Al and 4 wt%) 4.0 mm diameter and 10 mm length with an internal taper and conical wall connection (Surgimplant IPX, Galimplant, Sarria, Lugo, Spain) randomly selected (Epidat 4.1, Galicia, Spain) of the following dental implant surface treatments: Group A: conventional dental implant surface treatment through SLA (Galimplant, Sarria, Lugo, Spain) ($n = 8$) and Group B: dental implant surface treatment with CEPA and BMP-7 (Galimplant, Sarria, Lugo, Spain) ($n = 8$). The randomized, triple blinded, and prospective experimental research was approved on 19 March 2013 by the Ethics Committee in Animal Experimentation (ECAE) of the Puerta de Hierro University Hospital (Madrid, Spain) (ECAE Code: 017/2013). In addition, the study was conducted in accordance with the ethical principles of the ARRIVE guidelines, Royal Decree 1,201/2005 of October 10 (86/609/CEE and ETS 123) on the protection of animals used in experimentation and for other scientific purposes, as well as Council Directive 86/609/EEC of 24 November 1986 and were carried out in accordance with the United Kingdom. Animals (Scientific Procedures) Act 1986, the associated guidelines, and EU Directive 2010/63/EU for animal experiments. The randomized experimental research was performed at the Getafe University Hospital/European University of Madrid (Madrid, Spain) between November 2021 and April 2022. Sample size was determined with a confidence level of 95% ($Z\alpha/2 = 1.96$), a significance level of 5% (Error $\alpha = 0.05$) and a power of 80% (Error $\beta = 0.20$; Power = 0.80) using the GRANMO sample size calculator; subsequently, a sample size of 8 dental implants was stablished in each study group.

2.2 Conditioning of implant surfaces

The surface of the dental implants ($n = 16$) (Surgimplant IPX, Galimplant, Sarria, Lugo, Spain) were submitted to a dilution of 50 mL tetrahydrofuran (THF) (Uvasol®, Madrid, Spain) and 55 mg CEPA for one day at 76°C. Afterwards, the CEPA was activated with a solution of 5 mL distilled water, 175 mL of ethyl-3-(3-dimethylaminopropyl) carboxyamide (EDC) and 54 mg of N-hydroxysulfamide (NHS) for 15 min at room temperature. The stability of the pH was checked (pH 7) using a pH-meter (MP230, Mettler Toledo®, Barcelona, Spain) during the full process. EDC

activates carboxyl groups and amines by reacting with a carboxyl group to form an O-acylisourea intermediate; however, if it does not react with the amine, it hydrolyzes and regenerates the carboxyl group, thus incorporating the NHS. In the presence of N-hydroxysulfamide, EDC can be used to convert carboxyl groups to amine-reactive N-hydroxysulfamide esters, activating the CEPA with EDC and NHS to react with the amino groups of BMP-7. Once the carboxyl groups were activated, 20 mg of BMP-7 was incubated for 1 h at 37°C.

Finally, the dental implants were exposed to ultrasonic waves to remove impurities, packed in laminar flow cabinets under a sterile atmosphere and sterilized by gamma radiation at 25 KGy. Moreover, the dental implants were blinded to the operator by covering packing.

2.3 Experimental procedure

Veterinary assistance was given throughout the study. General anesthesia was induced with intravenous injected propofol 0.2–0.4 mg/kg (Diprivan®, AstraZeneca, Cambridge, United Kingdom) using a 20 G needle (BD Microlance®, Becton Dickinson, Franklin Lakes, NJ, United States) and epidural anesthesia by injecting bupivacaine (Bupinex®, Richmond Vet Pharma, Buenos Aires, Argentina) and fentanyl (Fentanilo®, Kilab, Buenos Aires, Argentina). Additionally, local anesthesia was also infiltrated with articaine 4% and 1:200,000 epinephrine (Ultracain®, Normon, Madrid, Spain). One N°7 endotracheal tube with a balloon cuff was placed and connected to a circular anesthesia circuit (Leon Plus, Heinen&Löwenstein, Bad Ems, Germany). Multimodal analgesia was used during the study, including medetomidine 0.01 mg/kg (Medetor®, Virbac, Carros, France), ketamine 5.0 mg/kg (Ketonal 50®, Richmond Vet Pharma, Buenos Aires, Argentina), midazolam 0.2 mg/kg (Dormicum®, Roche S.A., Basilea, Switzerland) and atropine 0.02 mg/kg (Atropina®, Pharmavet, Bogotá, Colombia). Then, a drilling sequence was performed following the manufacturer´s recommendations using a micromotor (AM-25 E RM, W&H, Bürmoos, Austria) and a contra-angle (WS-75 LG, W&H, Bürmoos, Austria) at 20: 1 reduction with profuse saline serum (Vitulia® 0.9%, Barcelona, Spain), after performing an incisión on the tibia. Subsequently, four dental implants (Surgimplant IPX, Galimplant, Sarria, Lugo, Spain) were placed on one tibia of each animal at 40 N torque. Afterwards, multimodal analgesia was administered by a transdermal patch of buprenorphine 0.3 mg/kg (Buprex®, Quintiles, Danbury, CT, United States) and meloxicam (Kern Pharma, Madrid, Spain) or buprenorphine 0.05–2 mg/kg (Buprex®, Quintiles, Danbury, CT, United States) if neccessary. Moreover, antibiotic therapy of amoxicilin 1.5 g (Clamoxyl®, Pfizer, New York, NY, United States) was also administered intramuscularly.

2.4 Euthanasia procedure

Animals were randomly (Epidat 4.1, Galicia, Spain) euthanized by an overdose of sodium pentobarbital, under a premedication with Zolacepam-Tiletamina-Medetomidina (Zoletil 5 mg/kg, medetomidine 0.1 mg/kg) administered intramuscularly, four weeks after the surgical intervention.

2.5 Histomorphometric analysis

The four tibias were fixed in 10% buffered formalin solution for two weeks to allow histomorphometric processing at the Department of Veterinary Clinical Sciences of University Veterinary Hospital Rof Codina (Lugo, Spain). The dental implants (Surgimplant IPX, Galimplant, Sarria, Lugo, Spain) and bone fragments were then individually extracted with an oscillating autopsy saw (Exakt, Kulzer, Germany) in 16 mm thick sagittal serial sections and dehydrated in semi-liquid alcoholic solutions (80, 96, 100 and 100%) for three days. The samples were embedded in glycolmethacrylate (GMA; 2-hydroxyethyl methacrylate, HEMA, JB-4; JB-4 Plus) (Technovit 7200 VLC, Heraeus Kulzer, Wehrheim, Germany). Finally, the samples were sectioned into 50 µm thick slices (Exakt Aparatebau GMBH, Hamburg, Germany) and stained with the Levai Laczko staining technique and examined with light optical microscopy (BX51, Olympus, Tokyo, Japan) by an experienced pathologist who was unaware of the randomization of the study groups. In addition, images from histological analysis were processed using Adobe Photoshop CS3 (San Jose, CA, United States), digitized (Intuos 4 large, Wacom, Saitama, Japan) and loaded into the Cell Sens Dimensions software, Olympus (Tokyo, Japan) (Balik et al., 2019) in order to evaluate the following variables in an isolated 5 mm × 5 mm area.

- Bone-implant contact (BIC), described as the percentage of the dental implant surface in contact with the surrounding bone.
- Corrected bone-implant contact (BICc), described as the length of bone in contact with the dental implant surface excluding regions non-covered by bone.
- New bone formation (BV/TV), described as the area of new bone formed after placing the dental implant.
- Interthread bone density (BAI/TA), described as the area of threads covered by the surrounding bone.
- Peri-implant bone density (BAP/TA), described as the area of bone that grows along the length of the implant.

All these values were expressed as percentages.

2.6 Statistical tests

Statistical analysis of all variables was carried out using SAS 9.4 (SAS Institute Inc., Cary, NC, United State). Descriptive statistics were expressed as means, medians, and standard deviations (SD) for quantitative variables. Comparative analysis was performed by comparing the BIC (%), BICc (%), BV/TV (%), BAI/TA (%) and BAP/TA (%) histomorphometric parameters between the SLA and BMP-7 study groups, using the Student's t-test and the Mann-Whitney non-parametric test. The statistical significance was set at $p < 0.05$.

3 Results

3.1 Histomorphometry

Figure 1 shows the longitudinal section of the specimen before being processed by the software for data extraction. The second

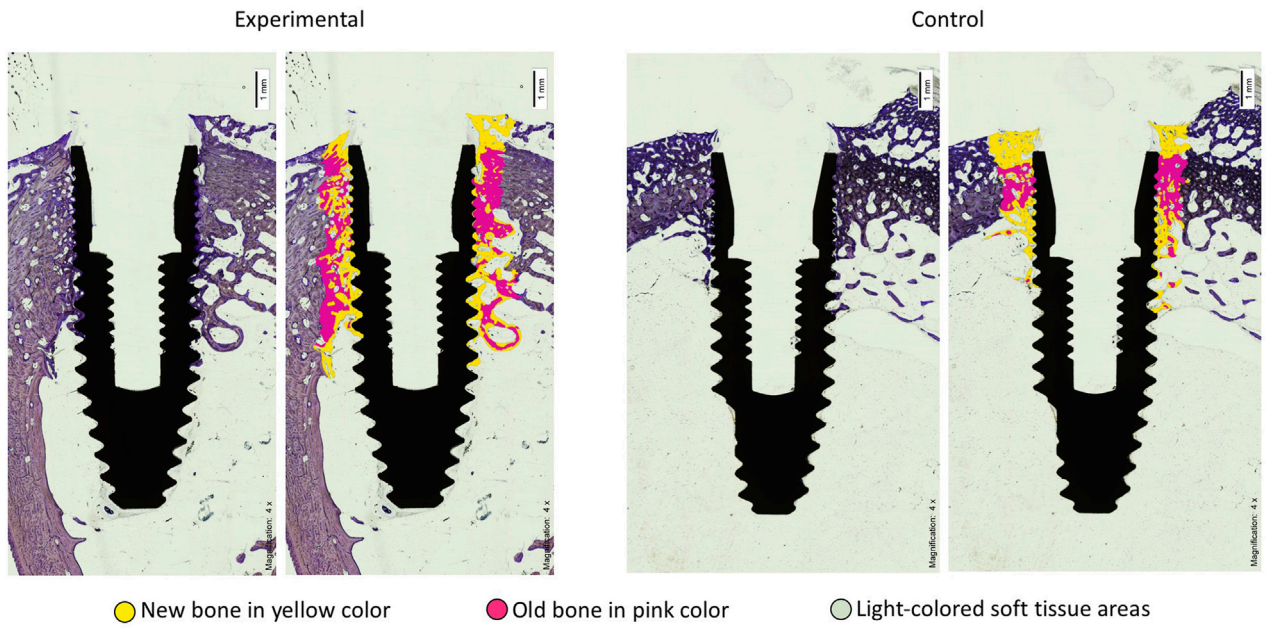

FIGURE 1
Histomorphometric section images of the BIC of implants in the Acid-BMP-7 (experimental) and SLA (control) groups after four weeks. The yellow color is new bone, more abundant and with greater contact with the implant surface in the experimental group compared to the control group.

TABLE 1 Descriptive statistics of the BIC (%) histomorphometric parameters.

BIC (%)	*n*	Mean	Median	SD	Minimum	Maximum
SLA	8	34.00[a]	33.17	9.92	21.91	46.47
BMP-7	8	52.02[b]	51.34	10.94	38.88	66.34

a, b different superscripts mean statistically significant differences between groups ($p < 0.05$).

image of each frame shows, by means of the software, the areas of old bone in pink, the areas of new bone in yellow and the areas of soft tissue in light color. The amount of soft tissue is much more abundant in the control group. The bone-implant contact line is much more extensive in the experimental group.

3.2 Statistical results

The means, medians and SD values for BIC (%) histomorphometric parameter of the study groups are displayed in Table 1 and Table 2 and Figure 2.

Student's t-test revealed statistically significant differences in histomorphometric parameters BIC and BICc between the experimental and control groups ($p = 0.004$ and $p = 0.003$, respectively). No statistical significance was found between the groups for the other parameters studied; the BAI/TA group obtained values of 32.71 ± 10.87 for the experimental group versus 32.91 ± 7.76 for the control group ($p = 0.967$); the BAP/TA group, 45.47 ± 11.07 for the experimental group versus 44.79 ± 8.67 for the control group ($p = 0.894$) and the BV/TV group, 27.01 ± 6.00 for the experimental group versus 26.63 ± 7.90 for the control group ($p = 0.951$).

4 Discussion

Early osseointegration has been shown to be influenced by both the roughness and surface coatings of Ti (Le Guéhennec et al., 2007; Sakka et al., 2012).

Organic coatings on inorganic surfaces, such as Ti, have been widely used to improve their biocompatibility and induce a specific biological response and different *in vivo* investigations demonstrated increased adhesion and proliferation of osteoblastic cells with BMP-2 based coatings (Schliephake et al., 2005; Schliephake et al., 2009).

BMPs act as potent regulators during bone and cartilage formation and repair and both recombinant human BMP-2 and BMP-7 have been approved for clinical use in bone regeneration, fracture healing and spinal fusion (Carreira et al., 2014). Although BMP-2 has been the most studied, certain studies have demonstrated *in vitro* the potential of BMP-7 as a stimulator of

TABLE 2 Descriptive statistics of the BICc (%) histomorphometric parameters.

BICc (%)	*n*	Mean	Median	SD	Minimum	Maximum
SLA	8	43.08[a]	43.13	10.76	24.81	55.37
BMP-7	8	63.30[b]	67.00	11.30	45.13	76.27

a, b different superscripts mean statistically significant differences between groups ($p < 0.05$).

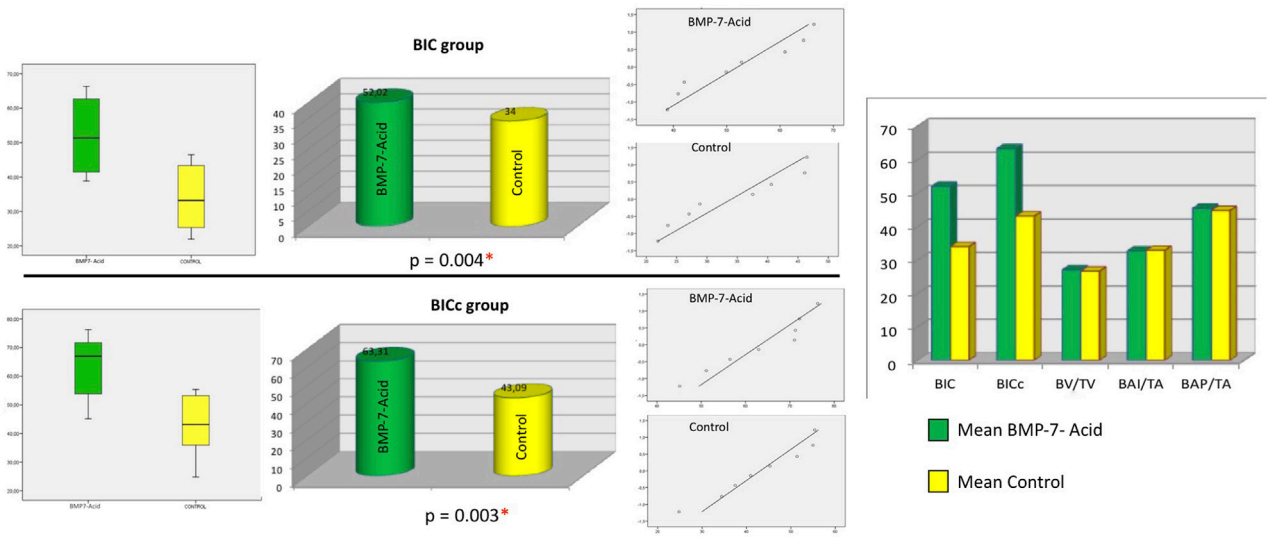

FIGURE 2
For both BIC and BICc, the box plot shows that the mean value of the BMP7-acid group (test group) was higher than that of the control group. In the Q-Q plots, the points are within the confidence interval and are randomly distributed on both sides of the axis, indicating that the distribution is normal for each group and variable. The bar chart shows the means of the compared groups (statistically significant for the variables BIC and BICc). * Statistical significance.

bone regeneration (Zhang et al., 2012), it has also been documented that BMP-7 stimulates the maturation of osteoblastic progenitors and induces the differentiation of undifferentiated non-osteogenic cells to osteoblasts (Shen et al., 2010). Busuttil Naudi et al. reported bone regeneration in critical rabbit mandibular defects using beta-tricalcium phosphate (β-TCP) scaffolds and recombinant human bone morphogenetic protein 7 (rhBMP-7) (Busuttil Naudi et al., 2012).

Currently, biomimetic coatings have been developed to induce the formation of a biologically active surface layer of apatite on the implant surface, by developing various techniques capable of creating functional groups (-OH, -COOH, -CH = CH2, etc.). Liu et al. (2002) suggested that pre-deposition of hydroxyapatite (HA) on functionalized self-assembled monolayer surfaces, could be an efficient and fast way to prepare biomimetic apatite coatings on surgical implants. On the other hand, it has been described that the use of acids for peptide anchoring further stimulates the activity of the implant surface, increasing its initial osseointegration; Aresti et al. (2021) demonstrated that the treatment of the surface with CEPA provides functional anchoring groups such as carboxyl groups, and increases the roughness of the dental implant surface, due to the corrosive action of the acid, which causes structural modifications on the surface as a result of the erosive action of the acid, thus showing a more complex surface structure, which induces a greater surface hydrophilicity, which would guarantee a greater affinity for the adhesion and proliferation of osteoblasts to the implant surface. These results would coincide with those found in our study, in which the parameters BIC and BICc were statistically significant between the groups experimental and control.

Other studies reported on the immobilization of BMP-2 after using 11-(hydroxydecyl) phosphonic acid and 12-(carboxydecyl) phosphonic acid to evaluate the reactivity of different surfaces using trifluoroethylamine hydrochloride, since these reactive molecules, can immobilize on the implant surface under the same conditions as a protein, demonstrating a higher covalent immobilization of fluorine molecules in the -COOH group with respect to the -OH group (Adden et al., 2006).

The inducing effect of BMPs on the differentiation of mesenchymal stem cells into osteoblasts has also been demonstrated, which would lead to an improvement in local bone growth, in addition to stimulating the formation of calcium deposits (Hoffmann et al., 2001; Karageorgiou et al., 2004); therefore, these molecules have been extensively studied in dental

implantology, in particular BMP-2 (Sykaras et al., 2001; Stadlinger et al., 2008; Wölfle et al., 2014), mainly for their ability to improve osseointegration of dental implants, since BMP-2, BMP-4 and BMP-7 appear to induce comparable levels of bone augmentation (Kirkwood et al., 2003; Leknes et al., 2008; Susin et al., 2010) and in recent years several studies have focused on the role of BMPs in osteoblastic differentiation and their inducing function in collagenous and non-collagenous protein synthesis (Constantinescu-Bercu et al., 2022), however, few studies have focused on analyzing BMP-derived peptides for their osteogenic capacity; Kirkwook et al. (2003), analyzed *in vitro* the minimal bioactive sequences of BMP-7, to evaluate its potential for biomaterial immobilization and its use in controlling osteoblast functions, demonstrating the potential of this molecule to induce osteoblast-specific genes associated with non-collagenous matrix formation and mineralization, along with gene expression, which would suggest some role of BMP-7 in mineralization.

However, there are no uniform results regarding the osteogenic power of BMP-7-functionalized Ti; an *in vitro* study by Togashi et al. (2009) found no effect of the addition of rhBMP-7 to the culture medium on the viability, proliferation, or differentiation of osteoblast-like cells, whereas others have found superior osteogenic power of samples with BMP-7 (Cirano et al., 2014). Zuardi et al. (2022) in a recent study, demonstrated that the effects of BMP-7 on osteogenic differentiation *in vitro*, would be conditioned by the topography of the surface on which the cell cultures are grown, the concentration of the growth factor in the culture medium and the stage of differentiation of the osteoblastic cells. Chen et al. (2013) developed a BMP-7-activated Ti gene delivery system for *in vitro* osteoblast culture and found enhanced differentiation capacity. This demonstrates that strategies for the development of metallic implants functionalized with BMP-7 (and probably with other bioactive molecules) should take into account the release profile during the repair process, depending on the concentration used for functionalization, and the physicochemical characteristics of the implant surface, all with the aim of guaranteeing a specific cellular behavior and/or generating an appropriate tissue phenotype. Nemcakova et al. (2022) in a combined *in vitro* and *in vivo* study found, after 4 and 12 weeks, a more pronounced osteogenic cell maturation and increased mineralization of the extracellular matrix around Ti6Al4V implants functionalized with BMP-7; in contrast, in our study we found no statistical significance in the BAI/TA and BAP/TA parameters. These results coincided with those obtained by Stenport et al. (2003) who, in a study in rabbit tibiae and femurs, found more areas of osteoid-like tissue in implants treated with BMP-7. Susin et al. (2010), Leknes et al. (2008) attribute the results to the concentration of rhBMP-7 used and agree that the observed bone remodeling would be proportional to higher doses of rhBMP-7. Leknes et al. (2008) are in agreement with our study and show robust bone formation after 4 weeks and remodeling of newly formed bone with characteristics similar to those of old bone. As in our study, Hunziker et al. (2021) in an experimental osteoporotic model, found at the third postoperative week, a significantly higher BIC value in the BMP-7 group compared to the Ti metal surface only control group.

Finally, it should be noted that the potential of rhBMP-7 to promote bone formation has been evaluated in a wide variety of large preclinical animal models (Phillips et al., 2006; Hunziker et al., 2021; Schierano et al., 2021) and in our study we used an experimental model with comparable bone anatomy and healing to humans and which has been used extensively in research related to maxillofacial surgery and dental implants. The anatomic and physiologic similarities of the pig to humans in terms of size, physiology, and bone biology have contributed to the successful use of this animal to understand and treat various bone situations and our experimental design was based on previous studies with this animal model, which considered the anatomical characteristics of the tibia to be similar to those of the human mandibular bone in terms of cortical/cancellous ratio and bone quality (Okubo et al., 2002; Mardas et al., 2014).

Our results rejected H_0 and demonstrated that Ti dental implants exposed to CEPA and coated with BMP-7 exhibit a favorable biological response prone to osseointegration.

Further preclinical studies are needed to investigate the beneficial effects of BMP-7 on bone repair in contact with biomaterials (Senna et al., 2021).

Data availability statement

The original contributions presented in the study are included in the article/Supplementary Material, further inquiries can be directed to the corresponding author.

Ethics statement

The animal study was reviewed and approved by Ethics Committee in Animal Experimentation (ECAE) of the Puerta de Hierro University Hospital (Madrid, Spain) (ECAE Code: 017/2013).

Author contributions

Conceptualization, NL-V and JA; methodology, JA and NL-V; software, CR; validation, JMA and AL-V; investigation, NL-V and JA; data curation, CR; writing—original draft preparation, AL-V; writing—review and editing, JA; supervision, JA. All authors have read and agreed to the published version of the manuscript.

Conflict of interest

The authors declare that the research was conducted in the absence of any commercial or financial relationships that could be construed as a potential conflict of interest.

Publisher's note

References

Adden, N., Gamble, L. J., Castner, D. G., Hoffmann, A., Gross, G., and Menzel, H. (2006). Phosphonic acid monolayers for binding of bioactive molecules to titanium surfaces. *Langmuir* 22, 8197–8204. doi:10.1021/la060754c

Alghamdi, H. S., and Jansen, J. A. (2020). The development and future of dental implants. *Dent. Mater J.* 39, 167–172. doi:10.4012/dmj.2019-140

Aragoneses, J., Suárez, A., López-Valverde, N., Martínez-Martínez, F., and Aragoneses, J. M. (2021). Assessment of the tissue response to modification of the surface of dental implants with carboxyethylphosphonic acid and basic fibroblastic growth factor immobilization (Fgf-2): An experimental study on minipigs. *Biol. (Basel)* 10, 358. doi:10.3390/biology10050358

Aresti, A., Aragoneses, J., López-Valverde, N., Suárez, A., and Aragoneses, J. M. (2021). Effectiveness of biofunctionalization of titanium surfaces with phosphonic acid. *Biomedicines* 9, 1663. doi:10.3390/biomedicines9111663

Balik, V., Uberall, I., Sulla, I., Ehrmann, J., Kato, Y., Sulla, I. J., et al. (2019). Variability in wall thickness and related structures of major dural sinuses in posterior cranial fossa: A microscopic anatomical study and clinical implications. *Oper. Neurosurg. Hagerst.* 17, 88–96. doi:10.1093/ons/opy287

Busuttil Naudi, K., Ayoub, A., McMahon, J., Di Silvio, L., Lappin, D., Hunter, K. D., et al. (2012). Mandibular reconstruction in the rabbit using beta-tricalcium phosphate (β-TCP) scaffolding and recombinant bone morphogenetic protein 7 (rhBMP-7) - histological, radiographic and mechanical evaluations. *J. Craniomaxillofac Surg.* 40, e461-e469. doi:10.1016/j.jcms.2012.03.005

Carreira, A. C., Lojudice, F. H., Halcsik, E., Navarro, R. D., Sogayar, M. C., and Granjeiro, J. M. (2014). Bone morphogenetic proteins: Facts, challenges, and future perspectives. *J. Dent. Res.* 93, 335–345. doi:10.1177/0022034513518561

Chen, S., Yang, J., Wang, H., Chao, Y., Zhang, C., Shen, J., et al. (2013). Adenovirus encoding BMP-7 immobilized on titanium surface exhibits local delivery ability and regulates osteoblast differentiation *in vitro*. *Arch. Oral Biol.* 58, 1225–1231. doi:10.1016/j.archoralbio.2013.03.019

Cirano, F. R., Togashi, A. Y., Marques, M. M., Pustiglioni, F. E., and Lima, L. A. (2014). Role of rhBMP-2 and rhBMP-7 in the metabolism and differentiation of osteoblast-like cells cultured on chemically modified titanium surfaces. *J. Oral Implant.* 40, 655. doi:10.1563/aaid-joi-d-12-00071

Constantinescu-Bercu, A., Wang, Y. A., Woollard, K. J., Mangin, P., Vanhoorelbeke, K., Crawley, J. T. B., et al. (2022). The GPIbα intracellular tail - role in transducing VWF- and collagen/GPVI-mediated signaling. *Haematologica* 107, 933–946. doi:10.3324/haematol.2020.278242

Esposito, M., Hirsch, J. M., Lekholm, U., and Thomsen, P. (1998). Biological factors contributing to failures of osseointegrated oral implants. (I). Success criteria and epidemiology. *Eur. J. Oral Sci.* 106, 527–551. doi:10.1046/j.0909-8836.t01-2-.x

Ferraris, S., Spriano, S., Pan, G., Venturello, A., Bianchi, C. L., Chiesa, R., et al. (2011). Surface modification of Ti-6Al-4V alloy for biomineralization and specific biological response: Part I, inorganic modification. *J. Mater Sci. Mater Med.* 22, 533–545. doi:10.1007/s10856-011-4246-2

Fini, M., Savarino, L., Nicoli Aldini, N., Martini, L., Giavaresi, G., Rizzi, G., et al. (2003). Biomechanical and histomorphometric investigations on two morphologically differing titanium surfaces with and without fluorohydroxyapatite coating: An experimental study in sheep tibiae. *Biomaterials* 24, 3183–3192. doi:10.1016/s0142-9612(03)00164-9

Gittens, R. A., Scheideler, L., Rupp, F., Hyzy, S. L., Geis-Gerstorfer, J., Schwartz, Z., et al. (2014). A review on the wettability of dental implant surfaces II: Biological and clinical aspects. *Acta Biomater.* 10, 2907–2918. doi:10.1016/j.actbio.2014.03.032

Hall, J., Sorensen, R. G., Wozney, J. M., and Wikesjö, U. M. (2007). Bone formation at rhBMP-2-coated titanium implants in the rat ectopic model. *J. Clin. Periodontol.* 34, 444–451. doi:10.1111/j.1600-051X.2007.01064.x

Hoffmann, A., Weich, H. A., Gross, G., and Hillmann, G. (2001). Perspectives in the biological function, the technical and therapeutic application of bone morphogenetic proteins. *Appl. Microbiol. Biotechnol.* 57, 294–308. doi:10.1007/s002530100746

Hunziker, E. B., Liu, Y., Muff, M., Haegi, T., Shintani, N., and Lippuner, K. (2021). The slow release of BMP-7 at a low dose accelerates dental implant healing in an osteopenic environment. *Eur. Cell Mater* 41, 170–183. doi:10.22203/eCM.v041a12

Jemat, A., Ghazali, M. J., Razali, M., and Otsuka, Y. (2015). Surface modifications and their effects on titanium dental implants. *Biomed. Res. Int.* 2015, 1–11. doi:10.1155/2015/791725

Karageorgiou, V., Meinel, L., Hofmann, S., Malhotra, A., Volloch, V., and Kaplan, D. (2004). Bone morphogenetic protein-2 decorated silk fibroin films induce osteogenic differentiation of human bone marrow stromal cells. *J. Biomed. Mater Res. A* 71, 528–537. doi:10.1002/jbm.a.30186

Kaur, M., and Singh, K. (2019). Review on titanium and titanium-based alloys as biomaterials for orthopaedic applications. *Mater Sci. Eng. C Mater Biol. Appl.* 102, 844–862. doi:10.1016/j.msec.2019.04.064

Khang, W., Feldman, S., Hawley, C. E., and Gunsolley, J. (2001). A multi-center study comparing dual acid-etched and machined-surfaced implants in various bone qualities. *J. Periodontol.* 72, 1384–1390. doi:10.1902/jop.2001.72.10.1384

Kim, S., Park, C., Moon, B. S., Kim, H. E., and Jang, T. S. (2017). Enhancement of osseointegration by direct coating of rhBMP-2 on target-ion induced plasma sputtering treated SLA surface for dental application. *J. Biomater. Appl.* 31, 807–818.doi:10.1177/0885328216679761

Kirkwood, K., Rheude, B., Kim, Y. J., White, K., and Dee, K. C. (2003). *In vitro* mineralization studies with substrate-immobilized bone morphogenetic protein peptides. *J. Oral Implantol.* 29, 57–65. doi:10.1563/1548-1336(2003)029<0057:IVMSWS>2.3.CO;2

Le Guéhennec, L., Soueidan, A., Layrolle, P., and Amouriq, Y. (2007). Surface treatments of titanium dental implants for rapid osseointegration. *Dent. Mater* 23, 844–854. doi:10.1016/j.dental.2006.06.025

Leknes, K. N., Yang, J., Qahash, M., Polimeni, G., Susin, C., and Wikesjö, U. M. (2008). Alveolar ridge augmentation using implants coated with recombinant human bone morphogenetic protein-7 (rhBMP-7/rhOP-1): Radiographic observations. *J. Clin. Periodontol.* 35, 914–919. doi:10.1111/j.1600-051X.2008.01308.x

Leon-Ramos, J. R., Diosdado-Cano, J. M., López-Santos, C., Barranco, A., Torres-Lagares, D., and Serrera-Figallo, M. Á. (2019). Influence of titanium oxide pillar array nanometric structures and ultraviolet irradiation on the properties of the surface of dental implants-A pilot study. *Nanomater. (Basel).* 9, 1458. doi:10.3390/nano9101458

Liu, Q., Ding, J., Mante, F. K., Wunder, S. L., and Baran, G. R. (2002). The role of surface functional groups in calcium phosphate nucleation on titanium foil: A self-assembled monolayer technique. *Biomaterials* 23, 3103–3111. doi:10.1016/s0142-9612(02)00050-9

Liu, Y., Hunziker, E. B., Layrolle, P., De Bruijn, J. D., and De Groot, K. (2004). Bone morphogenetic protein 2 incorporated into biomimetic coatings retains its biological activity. *Tissue Eng.* 10, 101–108. doi:10.1089/107632704322791745

Liu, Y., Huse, R. O., de Groot, K., Buser, D., and Hunziker, E. B. (2007). Delivery mode and efficacy of BMP-2 in association with implants. *J. Dent. Res.* 86, 84–89. doi:10.1177/154405910708600114

López-Valverde, N., Aragoneses, J., López-Valverde, A., Quispe-López, N., Rodríguez, C., and Aragoneses, J. M. (2022). Effectiveness of biomolecule-based bioactive surfaces, on osseointegration of titanium dental implants: A systematic review and meta-analysis of *in vivo* studies. *Front. Bioeng. Biotechnol.* 10, 986112. doi:10.3389/fbioe.2022.986112

López-Valverde, N., Flores-Fraile, J., Ramírez, J. M., Sousa, B. M., Herrero-Hernández, S., and López-Valverde, A. (2020). Bioactive surfaces vs. Conventional surfaces in titanium dental implants: A comparative systematic review. *J. Clin. Med.* 9, 2047. doi:10.3390/jcm9072047

Mardas, N., Dereka, X., Donos, N., and Dard, M. (2014). Experimental model for bone regeneration in oral and cranio-maxillo-facial surgery. *J. Invest. Surg.* 27, 32–49. doi:10.3109/08941939.2013.817628

Matinlinna, J. P., Tsoi, J. K., de Vries, J., and Busscher, H. J. (2013). Characterization of novel silane coatings on titanium implant surfaces. *Clin. Oral Implants Res.* 24, 688–697. doi:10.1111/j.1600-0501.2012.02504.x

Nemcakova, I., Litvinec, A., Mandys, V., Potocky, S., Plencner, M., Doubkova, M., et al. (2022). Coating Ti6Al4V implants with nanocrystalline diamond functionalized with BMP-7 promotes extracellular matrix mineralization *in vitro* and faster osseointegration *in vivo*. *Sci. Rep.* 28, 5264. doi:10.1038/s41598-022-09183-z

Okubo, Y., Bessho, K., Fujimura, K., Kusumoto, K., Ogawa, Y., and Iizuka, T. (2002). Expression of bone morphogenetic protein in the course of osteoinduction by recombinant human bone morphogenetic protein-2. *Clin. Oral Implants Res.* 13, 80–85. doi:10.1034/j.1600-0501.2002.130110.x

Phillips, F. M., Turner, A. S., Seim, H. B., 3rd., MacLeay, J., Toth, C. A., Pierce, A. R., et al. (2006). *In vivo* BMP-7 (OP-1) enhancement of osteoporotic vertebral bodies in an ovine model. *Spine J.* 6, 500–506. doi:10.1016/j.spinee.2006.01.014

Rupp, F., Liang, L., Geis-Gerstorfer, J., Scheideler, L., and Hüttig, F. (2018). Surface characteristics of dental implants: A review. *Dent. Mater* 34, 40–57. doi:10.1016/j.dental.2017.09.007

Sakka, S., Baroudi, K., and Nassani, M. Z. (2012). Factors associated with early and late failure of dental implants. *J. Investig. Clin. Dent.* 3, 258–261. doi:10.1111/j.2041-1626.2012.00162.x

Schierano, G., Canuto, R. A., Mauthe von Degerfeld, M., Navone, R., Peirone, B., Preti, G., et al. (2021). Role of rhBMP-7, fibronectin, and type I collagen in dental implant osseointegration process: An initial pilot study on minipig animals. *Mater. (Basel)* 14, 2185. doi:10.3390/ma14092185

Schliephake, H., Aref, A., Scharnweber, D., Bierbaum, S., Roessler, S., and Sewing, A. (2005). Effect of immobilized bone morphogenic protein 2 coating of titanium implants on peri-implant bone formation. *Clin. Oral Implants Res.* 16, 563–569. doi:10.1111/j.1600-0501.2005.01143.x

Schliephake, H., Aref, A., Scharnweber, D., Bierbaum, S., and Sewing, A. (2009). Effect of modifications of dual acid-etched implant surfaces on peri-implant bone formation. Part I: Organic coatings. *Clin. Oral Implants Res.* 20, 31–37. doi:10.1111/j.1600-0501.2008.01603.x

Senna, P. M., de Almeida Barros Mourão, C. F., Mello-Machado, R. C., Javid, K., Montemezzi, P., Del Bel Cury, A. A., et al. (2021). Silane-coating strategy for titanium functionalization does not impair osteogenesis *in vivo*. *Mater. (Basel).* 14, 1814. doi:10.3390/ma14071814

Shen, B., Wei, A., Whittaker, S., Williams, L. A., Tao, H., Ma, D. D., et al. (2010). The role of BMP-7 in chondrogenic and osteogenic differentiation of human bone marrow multipotent mesenchymal stromal cells *in vitro*. *J. Cell Biochem.* 109, 406–416. doi:10.1002/jcb.22412

Stadlinger, B., Pilling, E., Huhle, M., Mai, R., Bierbaum, S., Scharnweber, D., et al. (2008). Evaluation of osseointegration of dental implants coated with collagen, chondroitin sulphate and BMP-4: An animal study. *Int. J. Oral Maxillofac. Surg.* 37, 54–59. doi:10.1016/j.ijom.2007.05.024

Stenport, V. F., Johansson, C., Heo, S. J., Aspenberg, P., and Albrektsson, T. (2003). Titanium implants and BMP-7 in bone: An experimental model in the rabbit. *J. Mater Sci. Mater Med.* 14, 247–254. doi:10.1023/a:1022884724059

Susin, C., Qahash, M., Polimeni, G., Lu, P. H., Prasad, H. S., Rohrer, M. D., et al. (2010). Alveolar ridge augmentation using implants coated with recombinant human bone morphogenetic protein-7 (rhBMP-7/rhOP-1): Histological observations. *J. Clin. Periodontol.* 37, 574–581. doi:10.1111/j.1600-051X.2010.01554.x

Sykaras, N., Triplett, R. G., Nunn, M. E., Iacopino, A. M., and Opperman, L. A. (2001). Effect of recombinant human bone morphogenetic protein-2 on bone regeneration and osseointegration of dental implants. *Clin. Oral Implants Res.* 12, 339–349. doi:10.1034/j.1600-0501.2001.012004339.x

Szmukler-Moncler, S., Perrin, D., Ahossi, V., Magnin, G., and Bernard, J. P. (2004). Biological properties of acid etched titanium implants: Effect of sandblasting on bone anchorage. *J. Biomed. Mater Res. B Appl. Biomater.* 68, 149–159. doi:10.1002/jbm.b.20003

Togashi, A. Y., Cirano, F. R., Marques, M. M., Pustiglioni, F. E., Lang, N. P., and Lima, L. A. (2009). Effect of recombinant human bone morphogenetic protein-7 (rhBMP-7) on the viability, proliferation and differentiation of osteoblast-like cells cultured on a chemically modified titanium surface. *Clin. Oral Implants Res.* 20, 452–457. doi:10.1111/j.1600-0501.2008.01669.x

Wennerberg, A., and Albrektsson, T. (2009). Effects of titanium surface topography on bone integration: A systematic review. *Clin. Oral Implants Res.* 20, 172–184. doi:10.1111/j.1600-0501.2009.01775.x

Wölfle, J. V., Fiedler, J., Dürselen, L., Reichert, J., Scharnweber, D., Förster, A., et al. (2014). Improved anchorage of Ti6Al4V orthopaedic bone implants through oligonucleotide mediated immobilization of BMP-2 in osteoporotic rats. *PLoS One* 9, e86151. doi:10.1371/journal.pone.0086151

Zhang, F., Ren, L. F., Lin, H. S., Yin, M. N., Tong, Y. Q., and Shi, G. S. (2012). The optimal dose of recombinant human osteogenic protein-1 enhances differentiation of mouse osteoblast-like cells: An *in vitro* study. *Arch. Oral Biol.* 57, 460–468. doi:10.1016/j.archoralbio.2011.10.008

Zuardi, L. R., de Oliveira, F. S., Fernandes, R. R., Gomes, M. P. O., Spriano, S., Nanci, A., et al. (2022). Effects of rmBMP-7 on osteoblastic cells grown on a nanostructured titanium surface. *Biomimetics (Basel).* 7, 136. doi:10.3390/biomimetics7030136

frontiers | Frontiers in Bioengineering and Biotechnology

TYPE Original Research
PUBLISHED 02 March 2023
DOI 10.3389/fbioe.2023.1160509

OPEN ACCESS

EDITED BY
Xin Liu,
Shanghai Jiao Tong University School of Medicine, China

REVIEWED BY
Peiyuan Wang,
Fujian Institute of Research on the Structure of Matter (CAS), China
Benhao Li,
National University of Singapore, Singapore
Anjaneyulu Dirisala,
Innovation Centre of NanoMedicine (iCONM), Japan
Yong Fan,
Fudan University, China

*CORRESPONDENCE
Jianjun Zhang,
zhangjianjun0221@126.com
Kang He,
hekang929@163.com
Qiang Xia,
xiaqiang@shsmu.edu.cn

SPECIALTY SECTION
This article was submitted to Biomaterials, a section of the journal Frontiers in Bioengineering and Biotechnology

RECEIVED 07 February 2023
ACCEPTED 20 February 2023
PUBLISHED 02 March 2023

CITATION
Yang T, Xia L, Li G, Zhao J, Li J, Ge J, Yuan Q, Zhang J, He K and Xia Q (2023), Novel bionic inspired nanosystem construction for precise delivery of mRNA.
Front. Bioeng. Biotechnol. 11:1160509.
doi: 10.3389/fbioe.2023.1160509

Novel bionic inspired nanosystem construction for precise delivery of mRNA

Taihua Yang[1], Lei Xia[1], Gen Li[2], Jie Zhao[1], Jie Li[1], Jiahao Ge[1], Qinggong Yuan[3], Jianjun Zhang[1]*, Kang He[1]* and Qiang Xia[1,4,5]*

[1]Department of Liver Surgery, Renji Hospital, School of Medicine, Shanghai Jiao Tong University, Shanghai, China, [2]Department of Orthopedics, Ruijin Hospital, Shanghai Jiaotong University School of Medicine, Shanghai, China, [3]Department of Gastroenterology, Hepatology and Endocrinology, Hannover Medical School, Hannover, Germany, [4]Shanghai Engineering Research Center of Transplantation and Immunology, Shanghai, China, [5]Shanghai Institute of Transplantation, Shanghai, China

The intracellular delivery of messenger (m)RNA holds great potential for the discovery and development of vaccines and therapeutics. Yet, in many applications, a major obstacle to clinical translation of mRNA therapy is the lack of efficient strategy to precisely deliver RNA sequence to liver tissues and cells. In this study, we synthesized virus-like mesoporous silica (V-SiO_2) nanoparticles for effectively deliver the therapeutic RNA. Then, the cationic polymer polyethylenimine (PEI) was included for the further silica surface modification (V-SiO_2-P). Negatively charged mRNA motifs were successfully linked on the surface of V-SiO_2 through electrostatic interactions with PEI (m@V-SiO_2-P). Finally, the supported lipid bilayer (LB) was completely wrapped on the bionic inspired surface of the nanoparticles (m@V-SiO_2-P/LB). Importantly, we found that, compared with traditional liposomes with mRNA loading (m@LNPs), the V-SiO_2-P/LB bionic-like morphology effectively enhanced mRNA delivery effect to hepatocytes both *in vitro* and *in vivo*, and PEI modification concurrently promoted mRNA binding and intracellular lysosomal escape. Furthermore, m@V-SiO_2-P increased the blood circulation time ($t_{1/2}$ = 7 h) to be much longer than that of the m@LNPs (4.2 h). Understanding intracellular delivery mediated by the V-SiO_2-P/LB nanosystem will inspire the next-generation of highly efficient and effective mRNA therapies. In addition, the nanosystem can also be applied to the oral cavity, forehead, face and other orthotopic injections.

KEYWORDS

virus-like mesoporous silica, bionic inspired nanosystem, precise delivery of mRNA, liver target, oral *in Situ* injection

1 Introduction

mRNA has demonstrated great potential in biomedical applications such as oral and frontal diseases, immunotherapy, regenerative medicine, vaccines, and genetic diseases (Guan and Rosenecker, 2017; Kowalski et al., 2019; Wang and Yu, 2020; Shuai et al., 2021; Xiao et al., 2022). By functioning through translation directly in the cytosol, mRNA achieves higher gene expression efficiency than its counterpart DNA and thus does not carry the risk of DNA-related insertional translation (Granot-Matok et al., 2019). However, exogenous mRNA itself has difficulty penetrating the cytomembranes due to the nature of these negatively charged macromolecules. Moreover, mRNA degrades in seconds when applied alone *in vivo* (Wang HX et al., 2017). mRNA is still subjected to ribonuclease-

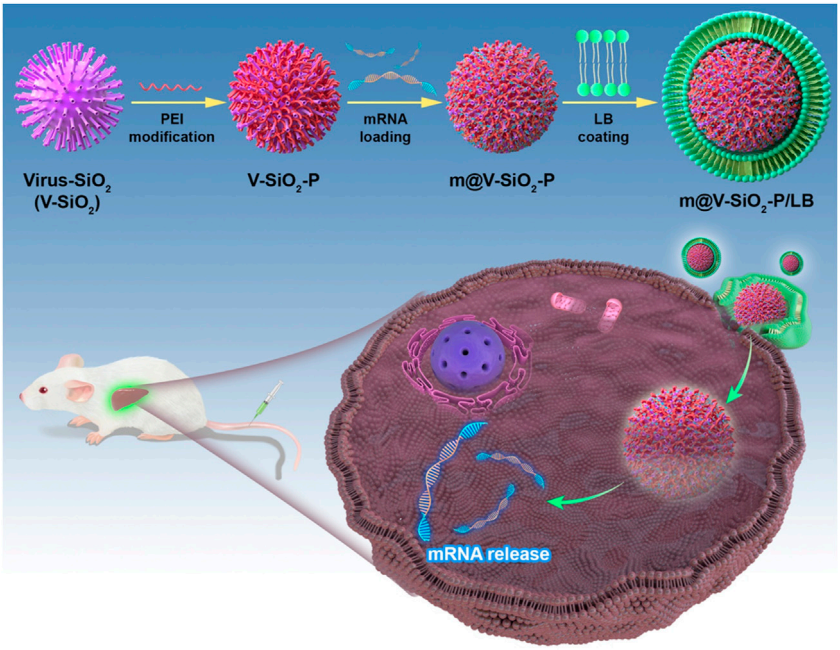

FIGURE 1
Schematic illustration. Novel bionic inspired nanosystem construction m@V-SiO_2-P/LB nanosystem for Precise Delivery.

mediated degradation even though packaged within the nanoparticles (Yen et al., 2018; Dirisala et al., 2019; Dirisala et al., 2022; Lin et al., 2022) Hence, developing an efficient platform to deliver mRNA into target cells for effective translation is very important for the development of mRNA-based therapeutics.

To date, various nanomaterials with different compositions, such as lipid/lipid-like materials, polymers, inorganic materials, and hybrid systems, have been developed for mRNA delivery (Guan and Rosenecker, 2017; Kowalski et al., 2019; Shuai et al., 2021; Xiao et al., 2022). In particular, one of the most developed nanomaterials for mRNA delivery is lipid nanoparticles (LNPs), which have been thoroughly explored. Among these, two have been authorized and successfully applied in the clinic for the delivery of mRNA-based COVID-19 vaccines, mRNA-1273 and BNT162b21 (Anderson et al., 2020; Polack et al., 2020; Baden et al., 2021). Although LNPs are an effective platform for mRNA delivery, the interactions between certain chemical functionalities during storage, such as oxidation, hydrolysis, or transesterification, can lead to the loss of mRNA activity (Fenton et al., 2016; Packer et al., 2021). In addition, physiological barriers confronted by LNPs, such as reaching the target tissues and escaping from endosomes to enter the cytoplasm to further increase the *in vivo* translation efficiency of mRNA molecules, should be overcome (Hou et al., 2021).

Hybrid nanoparticles integrating the advantages of its individual components, such as lipid hybrid nanoparticles, can improve the delivery efficacy of mRNA. For instance, Riley and coauthors developed a library of ionizable polyamine-lipid nanoparticles for *in utero* mRNA delivery to mouse foetuses. These LNPs demonstrate higher efficiency and safety compared to benchmark delivery systems, dilinoleylmethyl-4-dimethylaminobutyrate (DLin-MC3-DMA) and jetPEI, in terms of mRNA delivery to foetal livers, lungs, and intestines (Riley et al., 2021). Virus-like mesoporous silica nanoparticles (MSNs) have shown superior cellular uptake and longer blood circulation times compared with those of conventional MSNs due to their biomimetic morphology (Wang W et al., 2017). Moreover, the surface spikes of virus-like MSNs can provide a continuous open space to bind nucleic acids *via* multivalent interactions and protect them from nuclease degradation, which is beneficial for mRNA delivery (Song et al., 2017; Wang et al., 2018).

To improve the precise mRNA delivery efficiency, herein, we constructed a mRNA delivery nanoplatform based on virus-like MSNs with surface coating of lipid bilayer (LB). As shown in Figure 1, the described nanosystem (m@V-SiO_2-P/LB) was successfully constructed by binding HNF4α mRNA onto polyethylenimine (PEI)-modified virus-like MSNs followed by surface coating with a LB. m@V-SiO_2-P/LB nanoparticles combine the advantages of LNPs, PEI, and virus-like MSNs. First, PEI conjugation contributes to improved mRNA binding and promotes endosome escape (Xia et al., 2009; Wang et al., 2018). Second, their biomimetic morphology enhances gene delivery efficiency both *in vitro* and *in vivo*. Finally, a supported LB coating maintains colloidal stability and effectively prevents mRNA degradation (Noureddine et al., 2020; Gao et al., 2021; Riley et al., 2021; Li et al., 2022). Using green fluorescence protein (GFP)-expressing mRNA as a model, the intracellular delivery and transfection efficiency of m@V-SiO_2-P/LB nanoparticles were demonstrated to be much higher than that of the benchmark LNPs loaded with mRNA (m@LNPs). Furthermore, *in vivo* fluorescent images demonstrated that more m@V-SiO_2-P/LB nanoparticles specifically accumulated in the liver, thereby delivering more mRNA to this organ. These findings revealed the

improved mRNA delivery performance of the m@V-SiO_2-P/LB nanoparticles both *in vitro* and *in vivo* compared to LNPs, which could be used in efficient mRNA therapeutics for liver disease treatment.

2 Materials and methods

2.1 Materials

Hexadecyltrimethylammonium bromide (CTAB), decahydronaphthalene, 1-octadecene (ODE), PEI (branched, M_W 1000), dipalmitoylphosphatidylcholine (DPPC), cholesterol, and 1,2-distearoyl-sn-glycero-3-phosphoethanolamine (DSPE)-PEG were provided by Sigma-Aldrich. NaOH, cyclohexane, NH_4NO_3, ammonia aqueous solution (28 wt%), tetraethyl orthosilicate (TEOS), (3-aminopropyl) triethoxysilane (APTES), triethanolamine (TEA), sodium 3-(trihydroxysilyl) propylmethylphosphonate (THPMP), and decahydronaphthalene (98%) were obtained from Macklin Industrial, Inc. LNPs were purchased from Jiliang Pharmaceutical Engineering Co., Ltd. (Shanghai).

2.2 Methods

2.1.1 Virus-like MSN (V-SiO_2) synthesis

V-SiO_2 was synthesized according to a previous study (Wang W et al., 2017). Briefly, 1.0 g of CTAB was dissolved in 50 ml of water followed by the addition of NaOH (0.1 M, 0.8 ml), and the solution was stirred gently at 60°C. After 2 h, 20 ml of TEOS in cyclohexane (20 v/v %) was added to the mixture with continuous stirring for 48 h. The products were collected by centrifugation, washed with water and ethanol several times, and refluxed in 50 ml of acetone at 50°C overnight to remove the CTAB templates. Then, virus-like MSNs were obtained after centrifugation, washing with ethanol, and drying under vacuum.

2.1.2 PEI modification of V-SiO_2 (V-SiO_2-P)

V-SiO_2-P was prepared according to a previously reported method (Wang et al., 2018). To modify the surface of V-SiO_2 with PEI, the nanoparticle surface was first modified with phosphonate groups. Typically, 0.1 g of MSNs was dispersed into 30 ml of NaOH solution (pH = 10), and then 40 ml of 60 mM THPMP solution was added before the solution was stirred at 40°C for 2 h. Phosphonate group-modified V-SiO_2 was obtained by centrifugation and thorough washing, and then the sample was resuspended in 50 ml of carbonate buffer solution (100 mM, pH = 9.6). Next, 150 mg of PEI was added to the solution, which was stirred for 4 h. V-SiO_2-P was collected by high-speed centrifugation, washed with water, and dried under vacuum.

2.1.3 m@V-SiO_2-P and m@LNPs preparation and loading efficiency

One microgram of mRNA was mixed with V-SiO_2-P or LNPs at various weight ratios (V-SiO_2-P/mRNA = 0, 10, 20, 40, 60, 80) in 0.01 M PBS at 4°C for 30 min. Then, 2 μl of sample was removed for the agarose gel electrophoresis assay (1%, stained with gel safe) at 80 V for 50 min and visualized using a UV transilluminator 2000 (Bio-Rad, Hercules, CA, United States). The rest of each sample was centrifuged at 15,000 rpm for 10 min, from which 2 μl of the supernatant was removed to determine the mRNA content with a Nanodrop 1000 spectrophotometer (Thermo Scientific, Waltham, MA, United States). PBS was used as the blank, and the LNPs were used as controls. Specific information on mRNA and synthesis m@LNPs is further referred to our previous studies (Yang et al., 2022).

2.1.4 LB-coated m@V-SiO_2-P (m@V-SiO_2-P/LB) preparation

m@V-SiO_2-P was prepared at a weight ratio of 10:1 (V-SiO_2-P:mRNA), and LB coating was added based on a previously published protocol (Meng et al., 2015). A combination of DPPC/cholesterol/DSPE-PEG at a molar ratio of 77.5:20:2.5 was used as the LB layer. The DPPC/cholesterol/DSPE-PEG mixture was suspended in chloroform at a concentration of 10 mg/ml, and the solvent was evaporated using a rotary evaporator to obtain a lipid film. For the LB coating, m@V-SiO_2-P nanoparticles:LB weight ratio of 1:1.5 (w/w) was selected. Then, the lipid film was added to 0.5 ml of m@V-SiO_2-P suspension followed by probe sonication for 20 min with a 20/20 s on/off working cycle at a power output of 32.5 W. m@V-SiO_2-P/LB nanoparticles were collected by centrifugation at 15 000 rpm for 30 min and washed with saline.

2.3 Characterization

The morphologies of the m@V-SiO2-P/LB and m@V-SiO2-P nanoparticles were observed *via* transmission electron microscopy (TEM) and scanning electron microscopy (SEM). For TEM observations, samples were suspended in water, dried on a carbon film-supported copper grid, and observed using a JEOL 1010 instrument (JEOL, Tokyo, Japan) operated at 100 kV. For SEM measurements, samples were dropped onto silicon wafers, dried, and characterized using field-emission scanning electron microscopy (FE-SEM) with a JEOL JSM 7800 microscope (JEOL, Tokyo, Japan). The particle size and zeta potential were measured using dynamic light scattering (DLS) with a Zetasizer Nano-ZS instrument.

2.1.5 mRNA release profile from m@LNPs and m@V-SiO_2-P/LB nanoparticles

The release of mRNA from m@LNPs and m@V-SiO_2-P/LB nanoparticles was studied by dispersing m@LNPs and m@V-SiO_2-P/LB nanoparticles (containing 5 μg of mRNA) in 1 ml of 0.01 M PBS (pH = 7.4) at 37°C with shaking at 50 rpm. At predetermined time intervals, samples were centrifuged, and 0.5 ml of supernatant was removed, followed by the addition of the same volume of fresh PBS immediately after sampling. The amount of mRNA released was measured using a Nanodrop.

2.1.6 Cell culture and animals

Human liver L02 cells and human hepatic carcinoma HepG2 cells were provided by ATCC and cultured in high glucose Dulbecco's modified Eagle's medium (DMEM) containing 10% foetal bovine serum, streptomycin (100 U ml−1) and penicillin (100 U ml−1) (Invitrogen, CA, United States) in a

37°C incubator with 5% CO_2 and 95% humidity. Female BALB/c mice (9 weeks old) from Beijing Vital River Laboratory Animal Technology Co. (Beijing, China) were housed in a controlled environment (temperature, 22°C–24°C; humidity, 60%) under a 12-h light-dark cycle. All animal experiments were performed in accordance with the Guide for the Care and Use of Laboratory Animals and approved by the Experimental Animal Ethics Committee in Renji Hospital, School of Medicine, Shanghai Jiao Tong University.

2.1.7 Cellular uptake assay

The cellular uptake efficiency of LNPs and V-SiO_2-P/LB nanoparticles was studied in L02 (human normal liver) cells. Briefly, L02 cells were seeded in 6-well culture plates at a density of 1×10^5 cells per well and cultured for 24 h. Then, 20 μl of FITC-labelled LNPs or V-SiO_2-P/LB nanoparticles (100 ng per well) was added to each well for another 3 h of culture. Afterwards, the cells were washed with PBS, stained with DAPI and observed by confocal laser scanning microscopy (Leica HCS A, Leica, Wetzlar, Germany).

2.1.8 mRNA template construction and synthesis

To construct mRNA generation template, GFP sequence was codon optimized and clone into T7 promoter and polyA encoded plasmid. After template linearization, GFP mRNA was generated through *in vitro* transcription kit (Promega) and Cleancap reagent (TriLink). The High performance Liquid Chromatography (HPLC, Agilent 1100, Agilent Technologies, Santa Clara, CA, United States) was applied for mRNA purification. All mRNAs were checked *via* agarose gel electrophoresis and stored frozen at −80°C.

2.1.9 *In vitro* GFP mRNA transfection

The intracellular delivery efficacy of GFP mRNA by the V-SiO_2-P/LB nanoparticles was evaluated in L02 cells. The L02 cells were seeded in a 12-well plate at the density of 1×10^5 cells per well and cultured for 24 h. One hundred nanograms of free GFP mRNA, GFP mRNA-loaded LNPs or V-SiO_2-P/LB nanoparticles in PBS was added to each well, and the cells were cultured for 3 h. The cells were then stained with DAPI and subsequently subjected to CLSM observation. For flow cytometry analysis, cells treated with free GFP mRNA, GFP mRNA-loaded LNPs or V-SiO_2-P/LB nanoparticles were collected after 3 h of incubation, and intracellular green fluorescent protein expression was analysed by flow cytometry (Millipore Guava EasyCyte 5, Millipore, France).

2.1.10 Cytotoxicity and live/dead staining

CCK-8 assays were carried out to evaluate the toxicity of LNPs or V-SiO_2-P/LB nanoparticles to L02 cells. Briefly, L02 cells were seeded on 96-well plates and incubated with various concentrations of LNPs or V-SiO_2-P/LB nanoparticles for 24 h. Afterwards, the cell viability was determined *via* a standard CCK-8 protocol.

2.1.11 *In vivo* fluorescence imaging

To investigate the *in vivo* distribution of LNPs or V-SiO_2-P/LB nanoparticles, mice were intravenously injected with indocyanine green (ICG)-loaded LNPs or V-SiO_2-P/LB nanoparticles. One, 12, 24, and 48 h after tail vein injection, mice were euthanized and imaged by an *in vivo* imaging system (Xenogen IVIS kinetic, Caliper Life Sciences, United States). Simultaneously, the region of interest (ROI) in each image was analysed by Living Image software 3.2.

2.1.12 *In vivo* mRNA transfection

BALB/c mice were injected with GFP mRNA-loaded LNPs or V-SiO_2-P/LB nanoparticles *via* the tail vein at a total dose of 1 mg/kg of mRNA per mouse. After 72 h, mice were sacrificed, and liver tissues were cut on ice, stained with DAPI, and evaluated for immunofluorescence.

2.1.13 Acute toxicity test and histopathological examinations

BALB/c mice were randomly divided into three groups (n = 3) and intravenously injected with PBS, LNPs, or V-SiO_2-P/LB nanoparticles (3 mg/kg, 200 μl) and saline (200 μl) once daily for 7 days. After 7 days of observation, the mice were sacrificed, and the blood and vital organs were collected. Serum was separated from the blood samples, and the levels of cytokines and chemokines, including TNF-α, TNF-γ, IL-1b, IL-2, IL-3, IL-4, IL-10, IL-12p70, IL-13, and IL-17, were determined by a multiplex protein array kit according to the manufacturer's protocols (Bio-Rad Laboratories, CA). All cytokines and chemokine levels were corrected according to our previously reported method (Yang et al., 2021). Vital organs were fixed, embedded in paraffin, sectioned, and stained with haematoxylin and eosin (H&E). The H&E-stained sections were observed under a light microscope (LeicaDMi8M, Leica, Wetzlar, Germany) for histopathological examination.

2.1.14 Pharmacokinetic analysis

BALB/c mice were injected with ICG-labelled LNPs or V-SiO_2-P/LB (4 mg/kg, i. v.). Blood was collected from the ocular vein at 5 min, 1, 2, 4, 8, 12, and 24 h after injection, and the fluorescence intensity at 780 nm was detected by a multifunctional microplate reader (SpectraMax M5, Molecular Devices, United States).

2.1.15 Statistical analysis

Statistical analyses were carried out using two-sided Student's t test for unpaired comparisons with GraphPad Prism. Statistical significance is depicted with error bars representing ±SD. A p-value <0.05 was considered significant.

3 Results and discussion

3.1 The optimal design and characterization of the m@V-SiO_2-P/LB nanoparticles

According to our design, the stepwise procedure for the fabrication of the m@V-SiO_2-P/LB nanoparticles is illustrated in Figure 2A. Virus-like mesoporous silica nanoparticles (V-SiO_2) were synthesized in a two-phase reaction system (water/cyclohexane) with a low template concentration (CTAB) (Wang W et al., 2017). The scanning electron microscopy (SEM) and transmission electron microscopy (TEM) images of the V-SiO_2 show that they had a one-of-a kind bionic inspired morphology, all nanoparticles were well dispersed, and presented with a uniform size distribution that can be determined as approximately −115 nm (Figure 2B, top). Simultaneously, hydration radius was further confirmed by dynamic light scattering (DLS), which was slightly

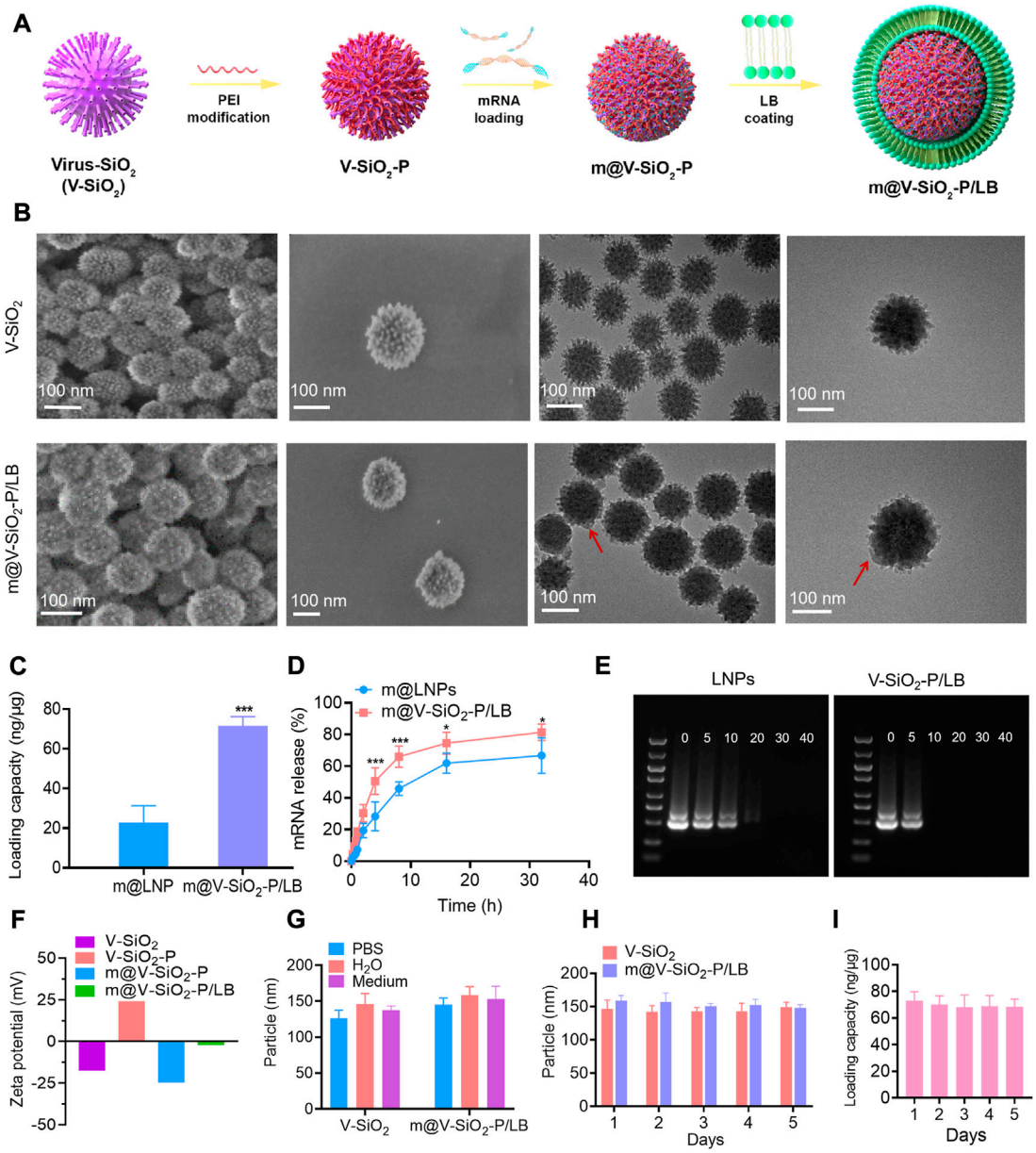

FIGURE 2
The optimal design and characterization of m@V-SiO_2-P/LB nanoparticles. **(A)** An illustration of the V-SiO_2-P/LB nanotopography for precise mRNA delivery. **(B)** Structural characterization of V-SiO_2 and m@V-SiO_2-P/LB by SEM and TEM. **(C)** GFP mRNA loading capacities of LNPs and V-SiO_2-P/LB nanoparticles. **(D)** Cumulative release of GFP mRNA from LNPs and V-SiO_2-P/LB nanoparticles at pH 7.4. *$p < 0.05$, **$p < 0.001$. **(E)** Agarose gel electrophoresis of the GFP mRNA-LNPs and GFP m@V-SiO_2-P/LB complexes, respectively. The amounts of LNPs and V-SiO_2-P/LB varied from 0 to 40 μg, while the amount of mRNA was kept at a constant (0.5 μg). **(F)** Zeta potentials of V-SiO_2 and PEI-V-SiO_2 (V-SiO_2-P), GFP mRNA loading, and LB coating. **(G)** Size distribution analysis of V-SiO_2 and m@V-SiO_2-P/LB nanoparticles dispersed in water, PBS and cell culture medium for 24 h. **(H)** Particle size distribution curves of V-SiO_2 and V-SiO_2-P/LB nanoparticles after suspension in PBS for 1, 2, 3, 4, and 5 days measured by DLS. **(I)** mRNA loading by m@V-SiO_2-P/LB nanoparticles after suspension in PBS for 1, 2, 3, 4 and 5 days.

increased to 120 nm (Supplementary Figure S1A). The prepared SiO_2 nanoparticles were immediately modified with PEI (V-SiO_2-P), mRNA loading followed by the addition of a complete LB coating (V-SiO_2-P/LB; The thickness of LB is 7–10 nm; Red arrow). The two steps of PEI and LB modifications could improve the mRNA binding efficiency, facilitate lysosomal escape, and maintain colloidal stability that is capable of effectively avoiding mRNA degradation (Wang et al., 2018) (Noureddine et al., 2020) (Xia et al., 2009; Wang et al., 2018) (Noureddine et al., 2020; Gao et al., 2021; Riley et al., 2021; Li et al., 2022). At present, there are few studies on mRNA delivery by inorganic nanomaterials, and LNPs have been an effective mRNA delivery (Meng et al., 2015). Therefore, subsequently, we chose commercial LNPs that have been previously reported as a control (Akinc and Battaglia, 2013; Turnbull et al., 2016) to compare mRNA loading and release. The mRNA loading into the LNPs was calculated as 22.74 ng/μg, remarkably lower than that of the m@V-SiO_2-P/LB

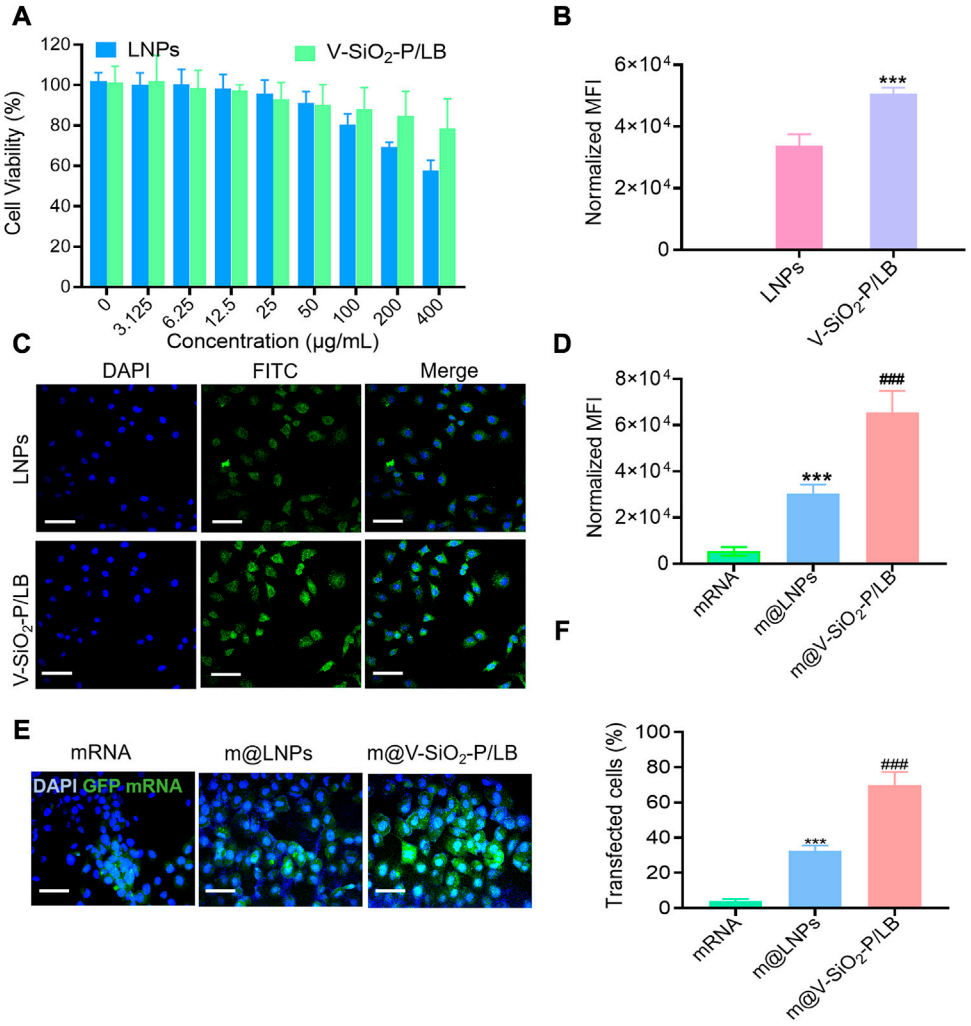

FIGURE 3
***In vitro* cellular internalization and GFP mRNA transfection. (A)** Viability of L02 cells treated with LNPs or V-SiO_2-P/LB nanoparticles at concentrations ranging from 0 to 800 μg/mL for 24 h. **(B)** Quantification of FITC fluorescence in L02 cells treated with FITC-labelled NP or V-SiO_2-P/LB nanoparticles (100 ng per well, 3 h, $n = 3$). ***$p < 0.001$. **(C)** Confocal laser scanning microscopy (CLSM) observations of L02 cells after incubation with LNPs and V-SiO_2-P/LB nanoparticles for 6 h. Scale bar: 50 μm. **(D)** Quantification of green fluorescence intensity (indicating GFP expression level) in L02 cells treated with free GFP mRNA, m@LNPs, m@V-SiO_2-P/LB nanoparticles (100 ng per well, 3 h, $n = 3$). ***$p < 0.001$ vs. mRNA, ###$p < 0.001$ vs. m@LNPs. **(E)** CLSM confocal microscopy images of GFP expression in L02 cells treated with free GFP mRNA, m@LNPs, m@V-SiO_2-P/LB. **(F)** The effect of LNPs and V-SiO_2-P/LB nanoparticles on the transfection of GFP detected by flow cytometry.

which was determined as 71.52 ng/μg (Figure 2C). The low mRNA loading efficiency of LNPs may be due to the low concentration of phospholipid, but high concentration of phospholipid will lead to poor morphology and stability of LNPs (Robinson et al., 2018). We then performed further mRNA release efficiency of the two nanocarriers at pH 7.4. In Figure 2D, at 8 h, the mRNA release rate in the m@V-SiO_2-P/LB group was 65.94%, significantly higher than that of m@LNPs group (45.77%). The mRNA release rate in the m@V-SiO_2-P/LB group was 81.4% at 32 h, while it was 66.72% in the m@LNPs group at the same time point. All these results suggest that the V-SiO_2-P/LB nanoparticles increased mRNA loading efficiency due to their bionic inspired nanospikes and PEI modification, but the release trend of mRNA was identical with LNPs. To further investigate the binding affinity of mRNA to the LNPs or V-SiO_2-P/LB nanoparticles, gel retardation experiments were then performed (Figure 2E). The doses of LNPs and V-SiO_2-P/LB were ranged from 0 to 40 μg, and the concentration of mRNA was kept constant (0.5 μg). In the LNPs group, the intensity of the offset mRNA bands decreased with increasing LNPs concentration. When the LNPs concentration was 5 μg, the LNPs bands were still brighter than that of V-SiO_2-P/LB, further indicating that the mRNA was completely bound to the V-SiO_2-P/LB nanoparticles.

Then m@V-SiO_2-P/LB were observed under both SEM and TEM. As displayed in Figure 2B (bottom), uniform coating of the surfaces with an intact LB can be successfully found. Furthermore, the changes in zeta potential were used to characterize the success of PEI modification, mRNA loading and LB coating. As shown in Figure 2F, the original charge of V-SiO_2 was determined as −17.4 mV, and after PEI modification, V-SiO_2-P exhibited a surface charge of +24 mV, indicating that PEI was

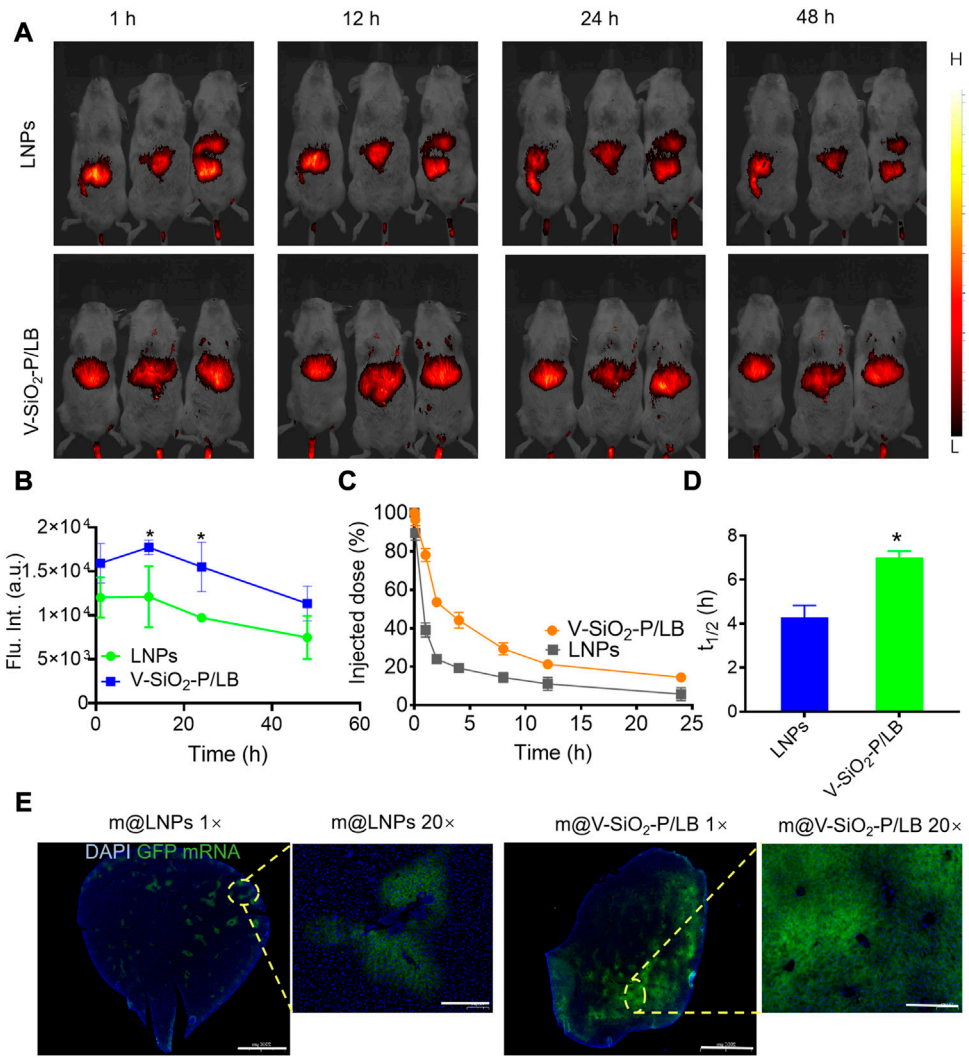

FIGURE 4
V-SiO_2-P/LB nanoparticles contribute to precise mRNA delivery to the liver *in vivo*. **(A)** Bioluminescence analyses at 1 h, 12 h, 24 h, 48 h and 72 h in BALB/c mice (n = 3 mice per group) injected **(I)**. v. with ICG-labelled LNPs or V-SiO_2-P/LB nanoparticles. **(B)** Quantification of light intensity over time. **(C)** Time-dependent blood levels of ICG-labelled LNPs and V-SiO_2-P/LB nanoparticles after tail vein injection, calculated as the percentage of injected dose remaining in the blood. **(D)** Blood circulation half-lives ($t_{1/2}$) of LNPs and V-SiO_2-P/LB nanoparticles (n = 3 mice per group). *$p < 0.05$. **(E)** GFP mRNA expression levels in liver tissue after m@LNPs or m@v-SiO2-P/LB treatment under different magnification.

successfully bound to the bionic inspired surface. After anchoring the negatively charged exogenous GFP mRNA, the zeta potential of V-SiO_2-P reversed to approximately −12 mV, indicating that the mRNA was mostly covered on the rough surface of the Si based nanoparticles. Finally, the zeta potential became electrically neutral (−2 mV) after LB coating, primarily demonstrating the successful wrapping of lipid layer. Moreover, the particle sizes of V-SiO_2, V-SiO_2-P, m@V-SiO_2-P and m@V-SiO_2-P/LB and their stability in different media were further analysed by DLS. As shown in Supplementary Figure S1, the particle size after PEI modification, mRNA loading and LB coating increased from 120 to 122 nm, 124, and 132 nm, respectively. The particle size distributions are similar after dispersed V-SiO_2 or m@V-SiO_2-P/LB in water, PBS and cell culture medium (Figure 2G). In addition, V-SiO_2 and m@V-SiO_2-P/LB suspensions were stored in PBS for 1, 2, 3, 4, and 5 d. As shown in Figure 2H, and all size distributions have no significant changes even after 5 d incubation. Meanwhile, no obvious aggregation or sedimentation was observed, indicating that the fabricated m@V-SiO_2-P/LB had exceptional stability. As expected, the amount of loaded mRNA did not change after 5 days (Figure 2H). Meng et al. also confirmed by repeated experiments that there was no leakage, and the nanoparticles remained intact for at least 1 month after LB coating (Meng et al., 2015).

3.2*In vitro* cytotoxicity assay, cellular internalization, and GFP mRNA transfection

An ideal intracellular mRNA delivery nanocarriers must present outstanding biocompatibility. Advancedly, the cytotoxicity of the LNPs and V-SiO_2-P/LB was determined by CCK-8 assay after co-incubated with L02 cells (normal human

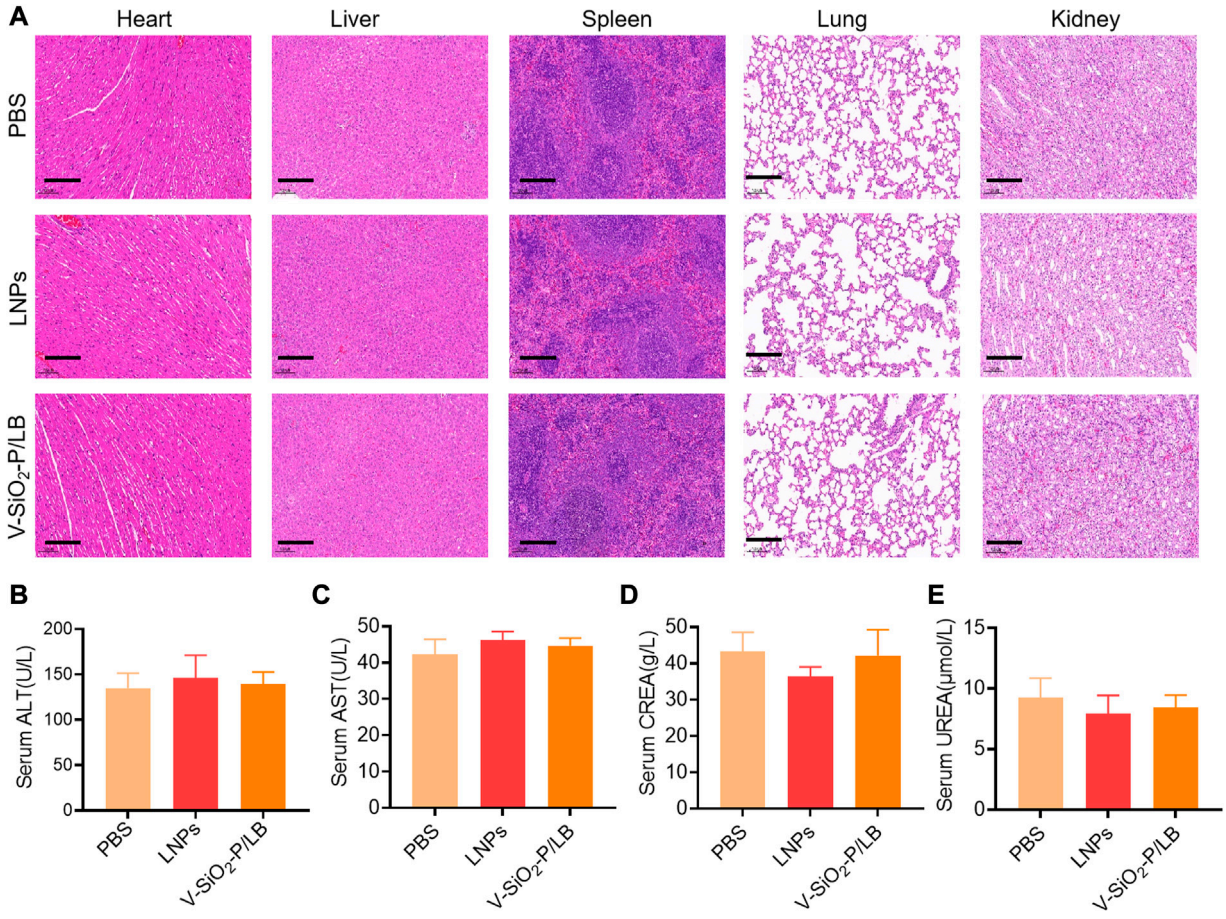

FIGURE 5
Biosafety of V-SiO_2-P/LB nanoparticles *in vivo*. (A) Histopathological examination of vital organ tissues after intravenous injection of PBS, LNPs, and V-SiO_2-P/LB nanoparticles (3 mg/kg, 200 μL) and saline (200 μL) once daily for 7 days by H&E staining. Scale bars, 200 μm. n = 3 mice per group. Detection of serum **(B)** ALT, **(C)** AST, **(D)** CREA and **(E)** UREA levels after the acute toxicity test. n = 3 mice per group.

liver cells) for 6h, respectively. Figure 3A shows that both the LNPs and V-SiO_2-P/LB nanoparticles exhibit dose-dependent cytotoxic behaviour toward L02 cells. The cell mortality rate was less than 20% when the concentration of V-SiO_2-P/LB nanoparticles ranged from 5 to 400 μg/ml. Exhilaratingly, when the concentration of LNPs reached 400 μg/ml, cell viability was only calculated as 57%, further verifying the advantageous of our bionic inspired nanoparticles. In addition to exceptional biocompatibility, an optimal mRNA delivery nanovector needs to precisely deliver mRNA motifs into living cells and achieve high transfection efficiency. Therefore, endocytosis effect of L02 cells toward FITC-labelled LNPs and V-SiO_2-P/LB nanoparticles along with nuclear staining with DAPI was carefully studied. The confocal laser scanning microscopy (CLSM) results displayed that the relative cellular uptake rates of the LNPs and V-SiO_2-P/LB nanoparticles were very different (Figure 3C). After 3 h of incubation, both the LNPs and V-SiO_2-P/LB nanoparticles were able to penetrate the cell membrane and accumulate in the cytoplasm. Satisfactorily, the cellular uptake rate of the V-SiO_2-P/LB nanoparticles was obviously higher than that of the LNPs. The same trend was also observed by quantitative analysis of the median fluorescence intensity (MFI) by flow cytometry (Figure 3B). This is mainly due to the rough virus-like morphology promotes cellular uptake and has a unique internalization pathway (Niu et al., 2013; Wang W et al., 2017). Finally, the expression level of GFP was also observed by CLSM with fluorescein-labelled mRNA. L02 cells were incubated with m@LNPs or m@V-SiO_2-P/LB nanoparticles for 24 h, and free mRNA was used as a control. The results are shown in Figure 3E, where the intensity of green fluorescence, indicating the GFP expression level, was weak in the free mRNA group, while the intensity of green fluorescence was stronger in m@V-SiO_2-P/LB nanoparticle group. The quantified flow cytometry results were consistent with the CLSM data (Figure 3D), with the m@V-SiO_2-P/LB nanoparticles showing the highest MFI; this was due to its strong binding affinity and high cellular uptake, benefiting from the PEI modification and rough virus-like morphology, respectively. In the meantime, the transfection efficiency in the m@V-SiO_2-P/LB nanoparticle group was 69.97%, which was relatively higher than that in the LNPs group (32.61%). In brief, our LB coated bionic inspired nanocarriers have superior capabilities of precise mRNA delivery toward liver cells and excellent mRNA transfection effect.

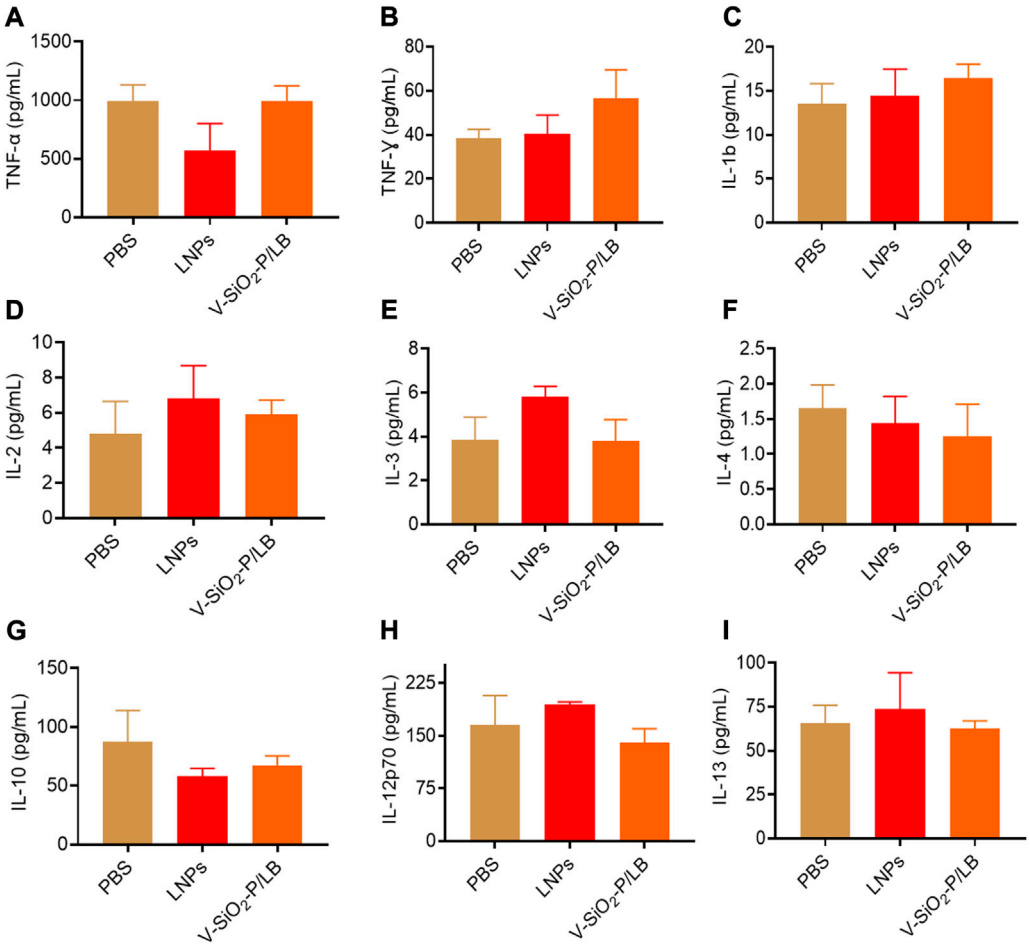

FIGURE 6
The cytokines and chemokines of V-SiO_2-P/LB nanoparticles *in vivo*. The levels of the cytokines and chemokines **(A)** TNF-α, **(B)** TNF-γ, **(C)** IL-1b, **(D)** IL-2, **(E)** IL-3, **(F)** IL-4, **(G)** IL-10, **(H)** IL-12p70, and **(I)** IL-13 determined by a multiplex protein array kit.

3.3V-SiO_2-P/LB nanoparticles contribute to effective mRNA delivery to the liver *in vivo*

After demonstrating the high efficiency of mRNA delivery by the V-SiO_2-P/LB nanoparticles to liver cells *in vitro*, we were encouraged to investigate the efficacy of the V-SiO_2-P/LB nanoparticles to deliver mRNA to the liver and their biosafety *in vivo*. First, the biodistribution (liver-targeting ability) of LNPs and V-SiO_2-P/LB nanoparticles was performed using fluorescence imaging system. Indocyanine green (ICG)-labelled LNPs and V-SiO_2-P/LB nanoparticles were injected into BALB/c mice through the tail vein, and fluorescence images were collected at different time points (1, 12, 24, and 48 h). As expected, fluorescence signals were detected in the livers in both the LNP- and V-SiO_2-P/LB nanoparticle-treated groups 1 h after injection (Figures 4A, B; Supplementary Figure S2). It is worth noting that the fluorescence in the LNP and V-SiO_2-P/LB groups peaked at 12 h after injection. Apparently, the liver fluorescence signal in the V-SiO_2-P/LB group was prominently higher than that in the LNP group at all time points (Figure 4B). Additionally, long blood circulation is particularly important for mRNA delivery *in vivo*. Compared with the blood circulation half-life ($t_{1/2}$) of the LNPs with only 4.2 h, that of the V-SiO_2-P/LB nanoparticles was lengthened to 7 h (Figures 4C, D). The prolonged blood circulation of the V-SiO_2-P/LB nanoparticles may promote the partial mRNA transport period and aggregation duration in the liver, probably due to its special surface morphology and outstanding stability in serum, which is consistent with previous reports (Hu et al., 2013).

Immediately, m@LNPs and m@V-SiO_2-P/LB nanoparticles were injected into healthy BALB/c mice *via* the tail vein, and the livers were removed 12 h later for sectioning (in the dark on ice) and DAPI staining. A tissue immunofluorescence scan was used to observe the expression level of GFP. As shown in Figure 4E, the livers tissue in the m@LNP group showed faint green fluorescence, while the livers tissue of the mice after the m@V-SiO_2-P/LB treatment presented large areas of green fluorescence with prominently higher signal intensity. These results also confirmed that the V-SiO_2-P/LB nanoparticles can efficiently delivered mRNA to the liver tissue.

3.4 Biosafety of V-SiO_2-P/LB nanoparticles

Before the potential clinical translation, we examined the acute toxicity of a high dose (3 mg/kg) of V-SiO_2-P/LB nanoparticles in mice after intravenous administration once daily for 7 days. Fortunately, no death or severe weight loss were observed in both LNPs and V-SiO_2-P/LB treated groups. Histopathological examination showed no obvious damage or abnormalities in the liver and kidney in all three groups (Figure 5A). In addition, the serum biochemical indices (AST, ALT, CREA and UREA) in the LNP and V-SiO_2-P/LB groups did not change significantly compared with the PBS blank group, indicating that both the LNPs and V-SiO_2-P/LB nanoparticles are highly biocompatible (Figures 5B–D). Notably, we did not find any fluctuations in the levels of cytokines or chemokines in the blood between the groups (Figure 6), indicating that the V-SiO_2-P/LB nanoparticles had a satisfying biosafety profile. To date, we have only demonstrated the ability of this delivery system to load GFP mRNA and target the liver in normal hepatocytes and in mice. Therefore, we further explore the functional mRNA loading ability, mRNA integrity, targeting ability and therapeutic effect of this antiviral nano-delivery system by constructing different liver disease models.

4 Conclusion

In this work, we have successfully developed V-SiO_2-P/LB nanocarrier for the first time and it can efficiently deliver mRNA to the liver tissue. In this novel nanoplatform, PEI was uniformly modified on the surface of virus-like mesoporous silica nanoparticles, and LB was completely coated on this surface. V-SiO_2-P/LB nanoparticles had excellent biocompatibility compared with LNPs, especially the more excellent mRNA delivering capability both *in vitro* and *in vivo*. The rough bionic inspired surface and PEI modification of the silica nanoparticles can sustainably increase loading and binding capacity of GFP mRNA (71.52 ng/μg), and the unique physical morphology enhanced hepatocyte endocytosis efficiency. Meanwhile, LB effectively prevented mRNA degradation and enhanced the blood circulation period of mRNA. Thus, the present study demonstrates that V-SiO_2-P/LB nanoparticles with satisfied biosafety have great potential to effectively deliver mRNA.

Data availability statement

The raw data supporting the conclusions of this article will be made available by the authors, without undue reservation.

Ethics statement

The animal study was reviewed and approved by all animal experiments were performed in accordance with the Guide for the Care and Use of Laboratory Animals and approved by the Experimental Animal Ethics Committee in Renji Hospital, School of Medicine, Shanghai Jiao Tong University.

Author contributions

TY, LX, and GL proposed and designed the experiments. JZ (4th author), JL, JG, and QY carried out the experiments. TY, LX, and GL drafted the article and interpreted the data. JZ (8th author), KH, and QX revised the article. All the authors approved the final version of the article.

Funding

This work was supported by grants from the China Postdoctoral Science Foundation (No. 2021M702180), the National Natural Science Foundation of China (82102618), the Shanghai Municipal Health Commission Health Industry Clinical Research Project (20204Y0351), the Shanghai Science and Technology Development Funds (No. 22YF1423900), the Nucleic Acid Drug Project of the National Biopharmaceutical Technology Innovation Center (No. NCTIB2022HS02004), the National and provincial multidisciplinary cooperative diagnosis and treatment capacity building project for major diseases (82241221), and the National key project, special project of medical innovation research of Shanghai "Science and Technology Innovation Action Plan" (22Y21900400).

Conflict of interest

The authors declare that the research was conducted in the absence of any commercial or financial relationships that could be construed as a potential conflict of interest.

The handling editor XL declared a shared parent affiliation with the author(s) TY, LX, GL, JZ, JL, JG, JZ, KH, and QX at the time of review.

Publisher's note

Supplementary material

The Supplementary Material for this article can be found online at: https://www.frontiersin.org/articles/10.3389/fbioe.2023.1160509/full#supplementary-material

References

Akinc, A., and Battaglia, G. (2013). Exploiting endocytosis for nanomedicines. *Cold Spring Harb. Perspect. Biol.* 5 (11), a016980. doi:10.1101/cshperspect.a016980

Anderson, E. J., Rouphael, N. G., Widge, A. T., Jackson, L. A., Roberts, P. C., Makhene, M., et al. (2020). Safety and immunogenicity of SARS-CoV-2 mRNA-1273 vaccine in older adults. *N. Engl. J. Med.* 383 (25), 2427–2438. doi:10.1056/NEJMoa2028436

Baden, L. R., El Sahly, H. M., Essink, B., Kotloff, K., Frey, S., Novak, R., et al. (2021). Efficacy and safety of the mRNA-1273 SARS-CoV-2 vaccine. *N. Engl. J. Med.* 384 (5), 403–416. doi:10.1056/NEJMoa2035389

Dirisala, A., Uchida, S., Li, J., Van Guyse, J. F. R., Hayashi, K., Vummaleti, S. V. C., et al. (2022). Effective mRNA protection by poly(l-ornithine) synergizes with endosomal escape functionality of a charge-conversion polymer toward maximizing mRNA introduction efficiency. *Macromol. Rapid Commun.* 43 (12), e2100754. doi:10.1002/marc.202100754

Dirisala, A., Uchida, S., Tockary, T. A., Yoshinaga, N., Li, J., Osawa, S., et al. (2019). Precise tuning of disulphide crosslinking in mRNA polyplex micelles for optimising extracellular and intracellular nuclease tolerability. *J. Drug Target* 27 (5-6), 670–680. doi:10.1080/1061186X.2018.1550646

Fenton, O. S., Kauffman, K. J., McClellan, R. L., Appel, E. A., Dorkin, J. R., Tibbitt, M. W., et al. (2016). Bioinspired alkenyl amino alcohol ionizable lipid materials for highly potent *in vivo* mRNA delivery. *Adv. Mater* 28 (15), 2939–2943. doi:10.1002/adma.201505822

Gao, Y., Men, K., Pan, C., Li, J., Wu, J., Chen, X., et al. (2021). Functionalized DMP-039 hybrid nanoparticle as a novel mRNA vector for efficient cancer suicide gene therapy. *Int. J. Nanomedicine* 16, 5211–5232. doi:10.2147/IJN.S319092

Granot-Matok, Y., Kon, E., Dammes, N., Mechtinger, G., and Peer, D. (2019). Therapeutic mRNA delivery to leukocytes. *J. Control Release* 305, 165–175. doi:10.1016/j.jconrel.2019.05.032

Guan, S., and Rosenecker, J. (2017). Nanotechnologies in delivery of mRNA therapeutics using nonviral vector-based delivery systems. *Gene Ther.* 24 (3), 133–143. doi:10.1038/gt.2017.5

Hou, X., Zaks, T., Langer, R., and Dong, Y. (2021). Lipid nanoparticles for mRNA delivery. *Nat. Rev. Mater* 6 (12), 1078–1094. doi:10.1038/s41578-021-00358-0

Hu, X., Hu, J., Tian, J., Ge, Z., Zhang, G., Luo, K., et al. (2013). Polyprodrug amphiphiles: Hierarchical assemblies for shape-regulated cellular internalization, trafficking, and drug delivery. *J. Am. Chem. Soc.* 135 (46), 17617–17629. doi:10.1021/ja409686x

Kowalski, P. S., Rudra, A., Miao, L., and Anderson, D. G. (2019). Delivering the messenger: Advances in technologies for therapeutic mRNA delivery. *Mol. Ther.* 27 (4), 710–728. doi:10.1016/j.ymthe.2019.02.012

Li, Z., Zhang, X. Q., Ho, W., Bai, X., Jaijyan, D. K., Li, F., et al. (2022). Lipid-polymer hybrid "Particle-in-Particle" nanostructure gene delivery platform explored for lyophilizable DNA and mRNA COVID-19 vaccines. *Adv. Funct. Mater* 32 (40), 2204462. doi:10.1002/adfm.202204462

Lin, Y., Wagner, E., and Lachelt, U. (2022). Non-viral delivery of the CRISPR/cas system: DNA versus RNA versus RNP. *Biomater. Sci.* 10 (5), 1166–1192. doi:10.1039/d1bm01658j

Meng, H., Wang, M., Liu, H., Liu, X., Situ, A., Wu, B., et al. (2015). Use of a lipid-coated mesoporous silica nanoparticle platform for synergistic gemcitabine and paclitaxel delivery to human pancreatic cancer in mice. *ACS Nano* 9 (4), 3540–3557. doi:10.1021/acsnano.5b00510

Niu, Y., Yu, M., Hartono, S. B., Yang, J., Xu, H., Zhang, H., et al. (2013). Nanoparticles mimicking viral surface topography for enhanced cellular delivery. *Adv. Mater. Deerf. Beach, Fla)* 25 (43), 6233–6237. doi:10.1002/adma.201302737

Noureddine, A., Maestas-Olguin, A., Saada, E. A., LaBauve, A. E., Agola, J. O., Baty, K. E., et al. (2020). Engineering of monosized lipid-coated mesoporous silica nanoparticles for CRISPR delivery. *Acta Biomater.* 114, 358–368. doi:10.1016/j.actbio.2020.07.027

Packer, M., Gyawali, D., Yerabolu, R., Schariter, J., and White, P. (2021). A novel mechanism for the loss of mRNA activity in lipid nanoparticle delivery systems. *Nat. Commun.* 12 (1), 6777. doi:10.1038/s41467-021-26926-0

Polack, F. P., Thomas, S. J., Kitchin, N., Absalon, J., Gurtman, A., Lockhart, S., et al. (2020). Safety and efficacy of the BNT162b2 mRNA covid-19 vaccine. *N. Engl. J. Med.* 383 (27), 2603–2615. doi:10.1056/NEJMoa2034577

Riley, R. S., Kashyap, M. V., Billingsley, M. M., White, B., Alameh, M. G., Bose, S. K., et al. (2021). Ionizable lipid nanoparticles for *in utero* mRNA delivery. *Sci. Adv.* 7 (3), eaba1028. doi:10.1126/sciadv.aba1028

Robinson, E., MacDonald, K. D., Slaughter, K., McKinney, M., Patel, S., Sun, C., et al. (2018). Lipid nanoparticle-delivered chemically modified mRNA restores chloride secretion in cystic fibrosis. *Mol. Ther.* 26 (8), 2034–2046. doi:10.1016/j.ymthe.2018.05.014

Shuai, Q., Zhu, F., Zhao, M., and Yan, Y. (2021). mRNA delivery via non-viral carriers for biomedical applications. *Int. J. Pharm.* 607, 121020. doi:10.1016/j.ijpharm.2021.121020

Song, H., Yu, M., Lu, Y., Gu, Z., Yang, Y., Zhang, M., et al. (2017). Plasmid DNA delivery: Nanotopography matters. *J. Am. Chem. Soc.* 139 (50), 18247–18254. doi:10.1021/jacs.7b08974

Turnbull, I. C., Eltoukhy, A. A., Fish, K. M., Nonnenmacher, M., Ishikawa, K., Chen, J., et al. (2016). Myocardial delivery of lipidoid nanoparticle carrying modRNA induces rapid and transient expression. *Mol. Ther. J. Am. Soc. Gene Ther.* 24 (1), 66–75. doi:10.1038/mt.2015.193

Wang, Y., Song, H., Yu, M., Xu, C., Liu, Y., Tang, J., et al. (2018). Room temperature synthesis of dendritic mesoporous silica nanoparticles with small sizes and enhanced mRNA delivery performance. *J. Mater Chem. B* 6 (24), 4089–4095. doi:10.1039/c8tb00544c

Wang, H. X., Li, M., Lee, C. M., Chakraborty, S., Kim, H. W., Bao, G., et al. (2017). CRISPR/Cas9-Based genome editing for disease modeling and therapy: Challenges and opportunities for nonviral delivery. *Chem. Rev.* 117 (15), 9874–9906. doi:10.1021/acs.chemrev.6b00799

Wang, W., Wang, P., Tang, X., Elzatahry, A. A., Wang, S., Al-Dahyan, D., et al. (2017). Facile synthesis of uniform virus-like mesoporous silica nanoparticles for enhanced cellular internalization. *ACS central Sci.* 3 (8), 839–846. doi:10.1021/acscentsci.7b00257

Wang, Y., and Yu, C. (2020). Emerging concepts of nanobiotechnology in mRNA delivery. *Angew. Chem. Int. Ed. Engl.* 59 (52), 23374–23385. doi:10.1002/anie.202003545

Xia, T., Kovochich, M., Liong, M., Meng, H., Kabehie, S., George, S., et al. (2009). Polyethyleneimine coating enhances the cellular uptake of mesoporous silica nanoparticles and allows safe delivery of siRNA and DNA constructs. *ACS Nano* 3 (10), 3273–3286. doi:10.1021/nn900918w

Xiao, Y., Tang, Z., Huang, X., Chen, W., Zhou, J., Liu, H., et al. (2022). Emerging mRNA technologies: Delivery strategies and biomedical applications. *Chem. Soc. Rev.* 51 (10), 3828–3845. doi:10.1039/d1cs00617g

Yang, T., Poenisch, M., Khanal, R., Hu, Q., Dai, Z., Li, R., et al. (2022). Corrigendum to 'Therapeutic HNF4A mRNA attenuates liver fibrosis in a preclinical model' [J Hepatol (2021) 1420-1433]. *J. Hepatol.* 77 (1), 270. doi:10.1016/j.jhep.2022.03.023

Yang, T., Poenisch, M., Khanal, R., Hu, Q., Dai, Z., Li, R., et al. (2021). Therapeutic HNF4A mRNA attenuates liver fibrosis in a preclinical model. *J. Hepatol.* 75 (6), 1420–1433. doi:10.1016/j.jhep.2021.08.011

Yen, A., Cheng, Y., Sylvestre, M., Gustafson, H. H., Puri, S., and Pun, S. H. (2018). Serum nuclease susceptibility of mRNA cargo in condensed polyplexes. *Mol. Pharm.* 15 (6), 2268–2276. doi:10.1021/acs.molpharmaceut.8b00134

frontiers | Frontiers in Bioengineering and Biotechnology

TYPE Original Research
PUBLISHED 16 May 2023
DOI 10.3389/fbioe.2023.1136406

OPEN ACCESS

EDITED BY
Si Chen,
Alexander Dubcek University in Trencin, Slovakia

REVIEWED BY
Guoli Hu,
University of Texas Southwestern Medical Center, United States
Xin Liu,
Shanghai Jiao Tong University School of Medicine, China

*CORRESPONDENCE
Fuming He,
hfm@zju.edu.cn
Antian Xu,
xuantian@zju.edu.cn

†These authors have contributed equally to this work and share first authorship

RECEIVED 03 January 2023
ACCEPTED 25 April 2023
PUBLISHED 16 May 2023

CITATION
Li J, Zhao J, Xu Y, Xu A and He F (2023), Titanium surface interacting with blood clot enhanced migration and osteogenic differentiation of bone marrow mesenchymal stem cells.
Front. Bioeng. Biotechnol. 11:1136406.
doi: 10.3389/fbioe.2023.1136406

Titanium surface interacting with blood clot enhanced migration and osteogenic differentiation of bone marrow mesenchymal stem cells

Jia Li†, Juan Zhao†, Yangbo Xu, Antian Xu* and Fuming He*

Department of Prosthodontics, Stomatology Hospital, School of Stomatology, Zhejiang University School of Medicine, Zhejiang Provincial Clinical Research Center for Oral Diseases, Key Laboratory of Oral Biomedical Research of Zhejiang Province, Cancer Center of Zhejiang University, Hangzhou, China

Introduction: Blood clot formation is the initial phase upon implantation, and the feature of blood clot orchestrates the following complement system activation, coagulation cascade, and bone marrow mesenchymal stromal cells (BMSCs) recruitment. This study aimed to investigate the effect of implant surface on blood-material interactions and subsequent BMSC cellular behaviors.

Methods: This study was established to imitate the physiological process of implantation *in vivo* and *in vitro*. Whole blood was incubated with polished titanium (PT) surfaces and sandblasted and double acid-etching (SLA) surfaces for 10 min or 2 h, then seeded with BMSCs. The adhesion, proliferation, migration, and differentiation of cells were studied at specific time points. Titanium implants were implanted into the tibia in vivo and were screwed out after implantation. The activation of the coagulation cascade, platelets, complement system, and clot networks were assessed and further quantitatively analyzed.

Results: Compared with the PT surface, the SLA surface induced the earlier and stronger blood coagulation cascade and formed a more stratified clots network with fibrinogen, platelets, and CD14 positive cell. The adhesion, proliferation, and migration of BMSCs were enhanced by pre-incubated surfaces. The higher levels of the osteogenic-related genes, ALP activity, and calcium nodule formation were showed on SLA surfaces with blood incubation.

Conclusion: SLA titanium surfaces play a role in influencing the formation of blood clots and coordinating surface-blood interactions and cell biological processes. These findings provide the idea of modifying the blood clots formed on the implant surface by biomaterials modification and thus has implications for the development of better osteogenic biomaterials.

KEYWORDS

dental implants, blood clot, blood incubation, bone marrow mesenchymal stromal cells, osteogenesis

1 Introduction

Biomaterials are commonly used to repair damaged or missing tissue, and implants are the gold standard for dental replacement. Implant integration is a multi-temporal process mediated by numerous molecular, cellular, and immune cascades (Trindade et al., 2016). It is well known that the surface properties of materials can influence the clinical outcome of implants, and materials can even regulate cell behavior by directly altering the initial blood clot structure and protein adsorption (Yang and Xiao, 2020).

As blood clot formation is the initial and foremost phase upon implantation, and the feature of blood clot orchestrates the following provisional matrix around the biomaterial surface, causing further activation and aggregation of platelets and the division of fibrinogen into fibrin via thrombin (Gorbet and Sefton, 2004; Wei et al., 2018). Meanwhile, complement proteins, activated upon contact with biomaterials, immediately facilitate platelets adhesion and activation that further propagate the coagulation cascade, the complement system activation, and immune cell recruitment. The provisional matrix releases a myriad of pluripotent factors, chemokines, and growth factors, and provides an interlaced scaffold for inflammatory, mesenchymal cells, and osteogenic cells (Wang et al., 2016; Huang et al., 2019).

The thickness and density of the clot network are affected by the miscellaneous surface physicochemical modifications (Fan et al., 2017; Bai et al., 2021). To date, nanostructured titanium surfaces perform better osseointegration due to continuous protein adsorption and dense blood clot (Lukaszewska-Kuska et al., 2018). The clot features are modulated by arrays of titanium dioxide nanotubes with distinct nano-diameters, which induce macrophages to polarize to the M2 phenotype and lead to a favorable immune response (Kopf et al., 2015a). Also, blood-derived products and blood pre-fabricated scaffolds have been trialed as potential bioactive materials to enhance bone regeneration (Melville et al., 2019). Accordingly, a clot network with appropriate structure is gradually considered an alternative nature healing scaffold to accelerate bone repair and integration. The previous studies usually conducted experiments *in vitro*, and the complexity of the *in vivo* environment makes the formation and features of clots on the material surface with distinct characteristics, which have not been well-understood. Besides, most of these studies have focused on the role of single blood components, other than the complex composition of whole blood.

In addition, moderate roughness and hydrophilic surfaces have better osteogenic properties, dues to the enhancement of the adhesion, proliferation, and osteogenic differentiation of cells (Faia-Torres et al., 2014; Huang et al., 2019; Xing et al., 2020). However, current studies mainly focused on the direct interactions between biomaterials and cells and neglected the physiological involvement of the blood and interstitial fluids. The role of the clot network formed immediately between surface properties and bone marrow stromal cells (BMSCs) biological behaviors is still unclear.

Our study utilized the fresh whole blood pre-incubated titanium surfaces *in vitro* to investigate the synergic effect of the clot network on the adhesion, migration, and osteogenic differentiation of BMSCs. Further, the physiological processes of implantation placement were simulated *in vivo* to assess platelet activation, coagulation cascade, complement systems, and cellular responses, and to analyze the adsorbed proteins and clot features. This study is to explore the effect of surface properties on early bone healing and osteogenesis: 1) whether titanium surface roughness and hydrophilicity affect the platelet activation and the clot features; 2) if the clot features steer the recruitment and osteogenic differentiation of BMSCs.

2 Materials and methods

2.1 Sample preparation and characterization

The commercially pure titanium slices (10 mm in length, 1 mm in thickness for *in vitro* experiments) and screw-shaped titanium implants (Ø 2 mm × 4 mm for *in vivo* studies) were prepared by Zhejiang Guangci Medical Appliance Co., Ltd., Ningbo, China. Then, the samples were divided into two groups: 1) the experimental group with sandblasted and double-acid etched titanium (SLA) surface was prepared as previously described (He et al., 2009). 2) the control group with polished titanium (PT) surface was sequentially polished with 280-, 600-, and 1200-grid silicon carbide papers (CarbiMet, Buehler). Before the following procedures, all samples were sterilized by UV irradiation.

The surface microstructure of the samples was observed using a field-emission scanning electron microscope (FE-SEM, SU8010, Hitachi, Japan). The static contact angle was measured as the assessment of hydrophobicity via Contact Angle Meter (JC 2000C, POWEREACH, China). A liquid drop of deionized water was deposited on the flat surface under the same environmental condition. The contact angle with water was measured from photographs using ImageJ software. The roughness of samples was evaluated by the arithmetic average of the absolute values of the irregularity (Ra), the root means square of the roughness of the profile (Rq), and the maximum height of the profile (Rz) via surface rough-meter (NAHOSCPEIVA, Veeco, United States). Each measurement was repeated three times.

2.2 Isolation and culture of BMSCs

BMSCs were obtained from the femur of 4-week-old male Sprague-Dawley (SD) rats. The bone marrow of the femoral midshaft was flushed out and suspended in alpha-modified eagle medium (α-MEM, Hyclone) supplemented with 10% fetal bovine serum (FBS, Hyclone) and 100 U/mL of penicillin and streptomycin. The cells were incubated at 37°C in a 95% humidified atmosphere with 5% CO_2. Passages three to five of cells were used in the following *in vitro* experiments.

2.3 Blood incubation of titanium surface

To mimic the initial contact between implant surfaces and fresh blood during surgery, pre-incubated titanium slices were prepared. The whole blood of healthy male SD rats was collected with the blood collection tube with 10 IU heparin (Solarbio). Each slice was

transferred into a 24-well plate using sterile forceps and incubated in 500 μL fresh rat blood for 10 min or 2 h at 37°C. The plates were placed on the table concentrator with steady shaking at 10 rpm to avoid blood sedimentation. After gently washing and removing non-adsorbed components, some titanium slices were collected as samples for the following assays. The other titanium slices were immersed in normal mediums for 6 h, then the supernatants were collected as conditioned mediums for subsequent experiments.

2.4 Cell adhesion and proliferation assays

To evaluate the effect of the formation of clot network and the release of blood components on initial cell adhesion and proliferation, the BMSCs were seeded at an initial density of 2×10^4 cells/mL on the control or pre-incubated titanium slices which were placed in the bottom of 24-well plates and cultured with Dulbecco's modified eagle medium (DMEM, Hyclone) + 10% FBS. After 4 and 24 h culture, adherent cells were fixed with 4% paraformaldehyde (PFA, Solarbio) and stained with rhodamine-phalloidin (Cytoskeleton, Inc.) and 4′,6-diamidino-2-phenylindole dihydrochloride (DAPI). The cell morphology was observed and imaged by a laser confocal scanning microscope (LCSM, Nikon A1, Japan).

The proliferation of cells was detected by AlamarBlue assay (Invitrogen, Grand Island, NY) at 1, 3, and 7 days. Briefly, the cells were incubated on control or pre-incubated surfaces for 3 h in a medium complemented with 10% (v/v) AlamarBlue reagent. The optical density was valued (λex = 540 nm, λem = 590 nm) by a SpectraMax M5 (Molecular Devices, China). The results were analyzed by plotting optical density against cell concentration.

2.5 Scratch wound assays

A scratch wound assay was performed to study the influence of the pre-incubated titanium on BMSCs migration. BMSCs were seeded on SLA and PT slices in 24-well plates for 24 h to obtain monolayers and then a vertical scratch was made to generate an acellular region on each sample. After washing and removing the detached cells, each well was added 1 mL DMEM containing 5% FBS for 12 or 24 h. The F-actin and nuclei were labeled with rhodamine-phalloidin and DAPI. The movement of the cell to the acellular area of each sample was photographed under LCSM.

To further investigate the effects of the release of blood components on BMSCs mobility, the BMSCs were seeded in 6-well plates directly and grown to 75%–85% confluence in a normal medium. After vertically scratched to create a "wound" score, each well was covered with 2 mL conditioned medium as previously described for 12 and 24 h. Then the wounds were recorded by an inverted microscope (CKX41, Olympus, Japan). The wound healing rate was calculated by the percentage of the wound closure area at different time points using the ImageJ software.

2.6 Transwell assays

Transwell assay was conducted in the 24-well transwell chambers of 8 μm nitrocellulose pore filters (Corning-Costar, Kennebunk, United States). BMSCs with a density of about 3×10^5 cells/mL were inoculated into the upper chamber (200 μL DMEM + 1% FBS), and 1 mL of conditioned mediums was added into the lower chamber. After incubation for 6 h, the cells penetrating the upper chamber membranes were fixed with 4% PFA and stained with 1% crystal violet dye solution (Saichuang Technology, Wuhan, China), and photographed by a microscope (CKX41, Olympus, Japan). The migration rate was quantified by counting the staining regions of five randomly selected fields on each transwell membrane.

2.7 Real-time quantitative PCR (RT-qPCR)

The RT-qPCR assay was performed to study the effect of different pre-incubated surfaces on the osteogenic and angiogenic potential of BMSCs at the gene level. After being cultured for 3 or 7 days, the total RNA of BMSCs was isolated and purified by an RNAeasy Mini kit (No.74106, Qiagen). The relative mRNA expression level of osteogenic genes [runt-related transcription factor 2 (*Runx2*), alkaline phosphatase (*Alp*), osteoprotegerin (*Opg*), and *osterix*] and angiogenic genes [vascular endothelial growth factor (*Vegf*) and platelet derived growth factor (*Pdgf*)] were determined by using an SYBR Green I kit (Takara, Osaka, Japan) on AppliedBiosystems ViiA 7 (Thermo Fisher Scientific, United States). Each sample was analyzed in triplicate, and the expression levels of target genes are shown relative to the housekeeping gene GAPDH as a control using the comparative Ct ($2^{-\Delta\Delta CT}$) method. All primer sequences are listed in Supplementary Table S1.

2.8 Osteogenic differentiation assays

To further assess the osteogenic differentiation of BMSCs, cells were seeded on Ti slices with or without pre-incubation. The osteogenic medium (OM: growth medium supplemented with 10 nM dexamethasone, 100 μM ascorbic acid, and 10 mM β-glycerophosphate) was changed twice per week. These cultures were used for alkaline phosphatase activity and alizarin red staining.

2.8.1 Alkaline phosphatase activity

After 4 and 7 days, cells were lysed with 100 μL RIPA lysis buffer. The supernatant was collected after centrifugation of 12,000 rpm/min at 4°C for 15 min. The level of ALP activity was measured using an ALP Assay Kit (Wako, Osaka, Japan) according to the manufacturer's instruction.

2.8.2 Alizarin red staining and quantification

After 21 days, cell layers were washed with phosphate-buffered saline (PBS) and then fixed with 4% PFA for 15 min. Cells were stained with 0.2% alizarin red solution (Solaibio, Technology) for 20 min. Staining cells and calcium nodules were washed with double-dilution water and were photographed under a light microscope. For quantitative analysis of alizarin red of cell layers, 1 mL of 10% cetylpyridinium chloride (C129534, Aladdin, China) was added into each well. After the dissolution of calcium nodules,

the optical density of solution was detected by a microplate reader at the wavelength of 590 nm.

2.9 Animals and surgical procedures

Animal experiments were approved by the Institutional Animal Care and Use Committee of Zhejiang University, Hangzhou, China (ZJU20190084). A total of 36 male SD rats weighing around 300 g were used. These rats were kept at a constant temperature and sterile operating table for implantation. In brief, SD rats were fixed on the bench and maintained under anesthesia by intraperitoneal injection of 10% chloral hydrate (0.33 mL/100 g, C104202, Aladdin). After shaving and disinfection of the operation areas, the skin was cut longitudinally and the periosteum was removed with a blunt instrument to expose the proximal surface of the tibia. Under the irrigation of 0.9% NaCl, the implant hole was drilled with a slow rotation. SLA implants and PT implants were in random order placed into the left and right tibias, respectively. The periosteum and skin were sutured postoperatively. Penicillin (400,000 U/d) was intramuscularly injected into the rats instantly.

After implantation of 10 min or 2 h, a total of 36 rats were sacrificed with a lethal dose of the anesthetic. All implants were screwed out in an anticlockwise direction and gently rinsed with 1 mL PBS 3 times. Then rinsing solution of four implants was collected and centrifuged at 1,000 *g* for 15 min at 4°C. The supernatant was stored at −80°C for further experiments. Implants were fixed with 2.5% glutaraldehyde or 4% PFA for further observation.

2.10 SEM of clot network structure

Scanning electron microscopy (SEM, Zeiss Gemini SEM 300, Germany) was used to observe the structure of the blood clot network. Implants retrieved at each time point were fixed in 2.5% glutaraldehyde for 30 min, followed fixed by 2% osmium tetroxide for 20 min, both at room temperature (RT). After dehydration using an ascending series of ethanol from 30% to 100% and critical point drying, the surface of samples was gold-palladium sputter-coated and then observed by SEM. Experiments were performed three times and five images per sample were used for observation.

2.11 Immunofluorescence staining of deposited blood components

LCSM was performed to visualize the deposited blood components. After fixation with 4% PFA, a rinse with PBS, permeabilization with 0.5% Triton X-100 for 5 min at RT. SLA and PT implants were blocked in bovine serum albumin (BSA) for 15 min, and then separately incubated with anti-human fibrin antibody (GeneTex, GTX19079, United States) for fibrin, monoclonal anti-integrin α2β-CD41 (Santa, sc-365938, United States) for platelets, monoclonal antiCD62p-P-selectin (Santa, sc-8419, United States) for activated platelets and monoclonal antiCD14 (Santa, sc-515785, United States) for monocytes/macrophages at 4°C overnight. Alexa Fluor 488-conjugated goat anti-mouse secondary antibodies (Abcam, ab150113, Britain) were used for the detection. The F-actin and nuclei were labeled with rhodamine-phalloidin and DAPI. Stained and mounted titanium implants were imaged and analyzed with an LCSM. A confocal z-stack was used to quantify the conformation and components of clots.

2.12 ELISA of the coagulation cascade, complement system, and platelets activation

The collected supernatant stored at −80°C was subsequently analyzed by using enzyme-linked immunosorbent assay (ELISA) kits Rat thrombin-antithrombin Complexes (TAT, CUSABIO, CSB-E08432r), Complement Fragment 5a (C5a, CUSABIO, CSB-E08513r), soluble P-selectin (P-selectin or CD62p, CUSABIO, CSB-E07339r) to detect TAT complexes, complement factor, and activated platelets, respectively. ELISAs were performed according to the manufacturer's protocols.

2.13 Specimen harvest for RNA-sequencing

Tibia implantation model was established in C57BL/6 male mice aged 6–8 weeks. The operation was the same as that of SD rats. After 3 days of implantation, tibiae (the proximal metaphysis, cylinder) with implants inside were harvested by cutting off the skin and removing soft tissues. Total RNA was extracted from dissociated cells using a Trizol reagent kit. RNA quality was assessed on an Agilent 2100 Bioanalyzer (Agilent Technologies, United States) and checked using RNase-free agarose gel electrophoresis. After total RNA was extracted, the enriched mRNA was fragmented into short fragments and reverse transcribed into cDNA with random primers. Then the cDNA fragments were purified with a QiaQuick PCR extraction kit (Qiagen, Netherlands), end-repaired, poly(A) added, and ligated to Illumina sequencing adapters. The ligation products were size selected by agarose gel electrophoresis, PCR amplified and sequenced using Illumina HiSeq2500. Differentially expressed genes (DEGs) RNAs differential expression analysis was performed by DESeq2 (Love et al., 2014) software between two different groups. The genes with the parameter of false discovery rate (FDR) below 0.05 and absolute fold change ≥ 2 were considered DEGs.

2.14 Statistical analysis

Quantified data were presented as mean ± standard deviation (SD) of at least three independent experiments. All data were analyzed by GraphPad Prism 9 (GraphPad Software Inc., United States), and the statistical significance between different groups was determined by two-way ANOVA. Asterisks denoted statistical significance as follows: $*p < 0.05$, $**p < 0.01$, $***p < 0.001$, $****p < 0.0001$.

10.3389/fbioe.2023.1136406

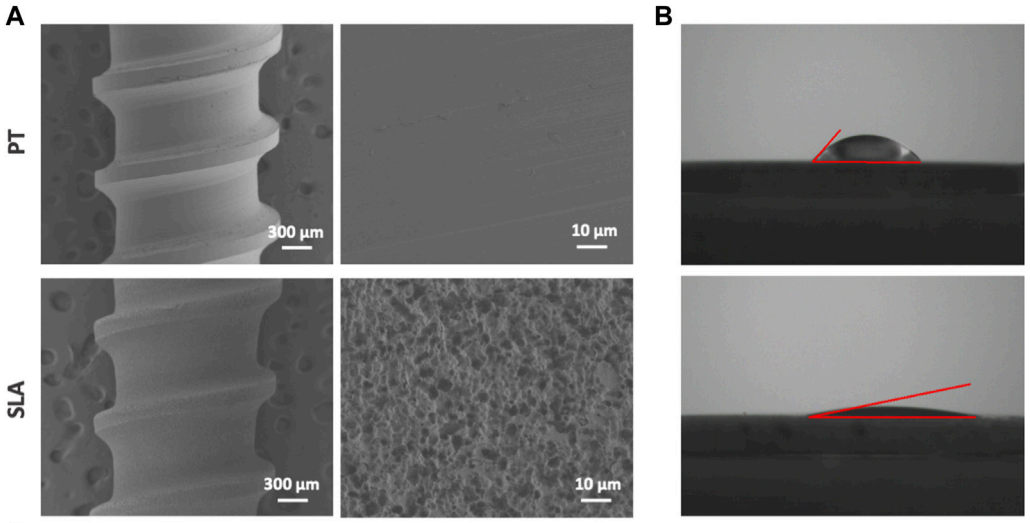

C

Results of Roughness and Wettability Measurement

Surface Type	Ra (μm)	Rq (μm)	Rz (μm)	Contact Angle (°)
PT	0.186±0.009	0.243±0.007	1.419±0.018	51.760±2.450
SLA	3.716±0.294	4.672±0.392	24.583±1.188	8.335±3.085

FIGURE 1
Representative SEM and water CA photographs of PT and SLA surfaces. **(A)** Surface topography was observed by SEM under different magnifications of PT and SLA titanium surface. **(B)** The hydrophilicity of PT and SLA surfaces was assessed by the measure of water contact angle. **(C)** The analysis for the characteristic parameter of surface roughness and hydrophily. Each experiment was repeated three times.

3 Results

3.1 Surface characterization

Scanning electron micrographs of titanium surfaces are shown in Figure 1A. The PT surface did not show any microtextures. After sandblasting and acid etching, the micro rough surface is characterized by numerous heterogeneous ridges and concavities with equally distributed honeycomb-like texture with 1–2 micron scale pits. At higher magnification, the disorganized micropore arranged 5–15 μm large holes outside and 100–200 nm small holes inside. Further to assess the hydrophobicity, we measured contact angles to explore the adsorption capacity of titanium surfaces to blood components. The water contact angles were 49.31° for PT surface and 11.42° for SLA surface in static condition displayed in Figure 1B The mean surface roughness (Ra) was 0.186 and 3.716 μm for the titanium surfaces of the PT and SLA groups, respectively (Figure 1C). It was indicated that SLA implants have a rougher surface with micro-size particles and higher hydrophilicity than PT implants.

3.2 Cell adhesion and proliferation on pre-incubated surfaces

In vitro, the initial cell adhesion and morphology of cells on PT and SLA surfaces with or without blood incubation were observed by staining the nuclei and F-actin 4 or 12 h after cell culture. As shown in Figures 2A, B, the number of adherent cells increased over blood-incubated time on both titanium surfaces, especially in 2 h-pre-incubated surfaces (Figure 2C). BMSCs cultured on the PT and SLA surfaces showed no significant difference in the number of the initially attached cells but showed a difference in morphology. There are a large number of slender BMSCs on the surface of SLA. In contrast, BMSCs adhered to the PT surfaces were rounder with shorter parapodia. After blood incubation, the morphology of cells was significantly extended compared with that of the un-incubated group, especially after 2 h pre-incubation (Figure 2D). This phenomenon indicates that the BMSCs adhered to the SLA surfaces are more active and have the potential for further differentiation.

Besides, cell proliferation on the pre-incubated surfaces significantly increased after being cultured for 3 or 7 days (Figure 2E). The data showed that the proliferation rate of BMSCs on the pre-incubated SLA was significantly higher than that on the control surfaces, especially after 2 h pre-incubation. These results revealed that SLA surfaces with clot networks and blood components might conduce to BMSCs proliferation.

3.3 Effects of titanium surface with clot networks and blood-derived conditioned medium on cell migration and recruitment

To further determine whether various titanium surfaces with whole blood incubation could affect cell migration and recruitment,

10.3389/fbioe.2023.1136406

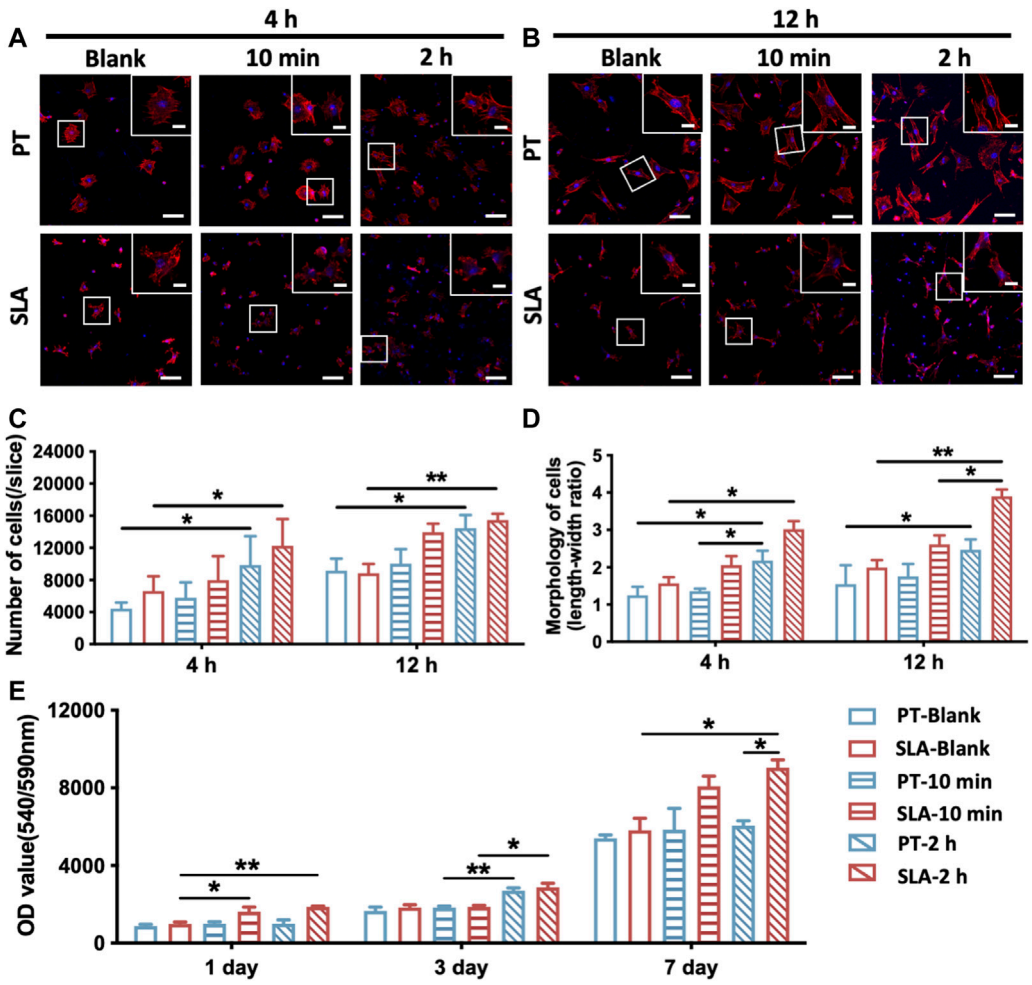

FIGURE 2
Adhesion and proliferation of BMSCs on PT and SLA surfaces. **(A,B)** LCSM images of BMSCs stained with F-actin (red) and nuclei (blue), cultured after 4 and 24 h on PT and SLA surfaces with or without blood incubation (Scale bars: 200 μm; Inserts: 25 μm). **(C)** Semi-quantitative analysis of the number of adhered cells on surfaces after 4 and 12 h culture. Data represent means ± S.D. **(D)** Quantitative analysis of the ratio of the longest and shortest diameters of the adherent cells on surfaces after 4 and 12 h culture. **(E)** AlamarBlue assay to assess the proliferation of BMSCs grown on different surfaces with or without blood incubation. *$p < 0.05$, **$p < 0.01$, ****$p < 0.0001$.

the scratch wound-healing assay and the transwell assay were performed (Figure 3). The migratory capacity of BMSCs was gradually enhanced after being cultured on pre-incubated titanium surfaces via the scratch wound-healing assay. After 24 h, the wound closure rate of BMSCs seeded on with 2 h-pre-incubated SLA surface was 72.3% ± 2.3%, which led to an approximately 0.83-fold increment than PT counterparts (39.6% ± 4.2%, Figures 3A, D). To further exclude the influence of surface topography, the conditioned medium derived from the pre-incubated surfaces was used to culture BMSCs seeded on culture plates in the wound healing assay. No statistically significant difference in the migration area proportion was observed between the 10 min-pre-incubated and the control group at 12 h. Nevertheless, the cell mobility displayed an increased tendency at 24 h when treated with the conditioned medium from the pre-incubated SLA surfaces in contrast to the PT counterparts (Figures 3B, E).

Transwell assay was conducted to further verify the effect of the paracrine effect of blood components on the recruitment of BMSCs. As shown in Figures 3C, F, the conditioned medium from 2 h-pre-incubated SLA and PT surfaces respectively led to 0.55-flod and 0.57-fold increment than control group in cell mobility. Consistent with the scratch wound experiments, the proportion of recruited BMSCs rose sharply with extended blood-incubation time, from 33.08% to 51.33% in the SLA group.

The above results supported that different titanium with fresh clots could facilitate the mobility of BMSCs. Moreover, blood components release factors that stimulate cell migration and enhance the recruitment of BMSCs, which might contribute to wound healing.

3.4 The osteogenic differentiation of BMSCs cultured on the pre-incubated surfaces

To verify the effect of blood clots on the osteogenic differentiation of BMSCs, the expression level of osteogenesis-

10.3389/fbioe.2023.1136406

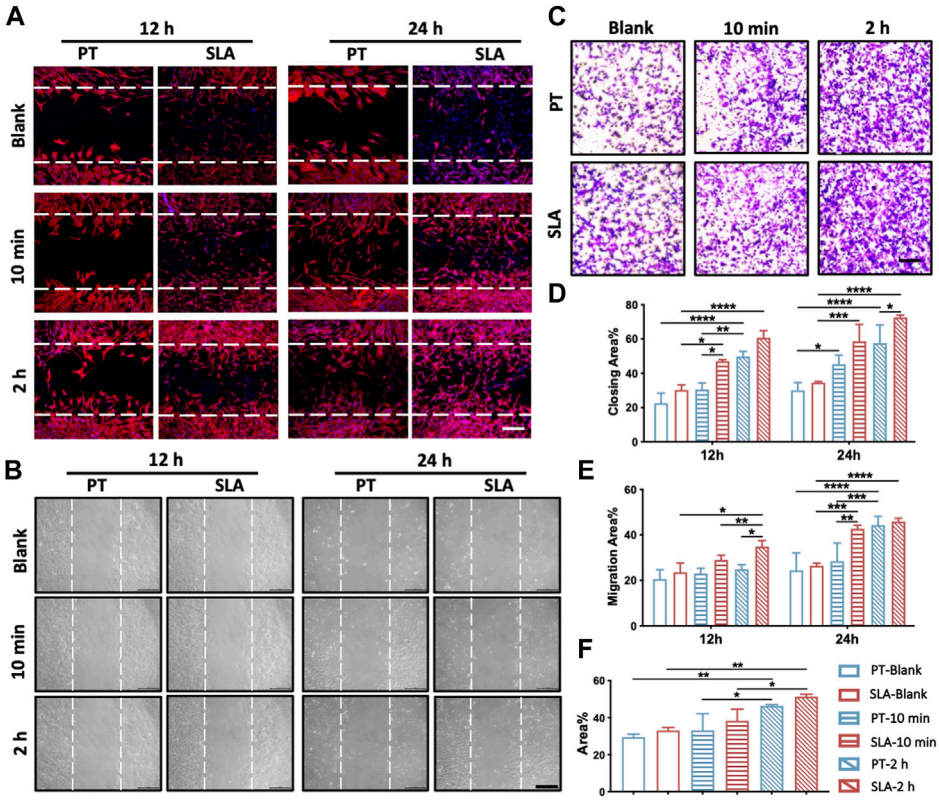

FIGURE 3
Migration and recruitment of BMSCs on various surfaces. **(A)** Representative images of the scratch wound assay. BMSCs were cultured on the control, 10 min- or 2 h-pre-incubated titanium surfaces in normal media. Scale bars: 250 μm. **(B)** Representative images of the wound healing assay with conditioned media. BMSCs were treated with the extract of control, 10 min- or 2 h-pre-incubated surfaces, respectively. Scale bars: 200 μm. **(C)** Representative images of the transwell assay with conditioned media. Scale bars: 200 μm. **(D)** Quantitative comparison of migratory cells among different groups. **(E)** The proportion of cell migration into the wound under conditioned media was quantified as the level of wound healing. **(F)** Quantitative comparison of recruiting cells with conditioned media among different groups. These experiments were repeated three times with similar results. *$p < 0.05$, **$p < 0.01$, ***$p < 0.001$, ****$p < 0.0001$.

related and angiogenesis-related genes were evaluated by RT-qPCR after 3 or 7 days of culture (Figures 4A, B). The expression of *Osterix* and *Opg* in the SLA group was higher than that in the PT group without blood incubation on the seventh day. On the pre-incubated surfaces, the transcriptional levels of *Runx2*, *Alp*, *Osterix*, and *Opg* showed an upward trend and were highest on the 2 h-pre-incubated SLA surface. A marked elevation of genes expression in cells cultured on pre-incubated disks than those of un-incubated surfaces. Especially on day 7, the mRNA levels of the *Vegf* and *Pdgf* on 10 min- and 2 h-pre-incubated SLA surface were significantly increased compared with the ctrl group.

Given that osteogenic differentiation in gene level was upregulated by blood clots, we further evaluated the ALP activity and bone calcium nodule formation of BMSCs. BMSCs cultures on the pre-incubated surfaces displayed higher ALP activity than the blank group, especially on 2 h-pre-incubated surfaces (Figures 4C, D). In addition, the ALP activity of BMSCs cultured on the pre-incubated SLA surfaces was significantly higher than that on the PT counterparts at both time points. The calcium nodule formation on titanium surfaces was stained and quantified by cetylpyridinium chloride solution (Figures 4E, F). 10 min- and 2 h-pre-incubated SLA surfaces showed 1.67 times and 2.27 times alizarin red than the control group, respectively. Meanwhile, the pre-incubated PT surface showed the same trend. It hinted at the promotive role of blood clots on the osteogenic differentiation of BMSCs.

3.5 Characterization of blood clot features on titanium surfaces

Representative SEM images of blood clot characteristics on different implant surfaces *in vivo* were presented in Figure 5. With the prolongation of time after implantation into tibia, a stronger blood coagulation response was observed, showing a tightly-packed and hierarchical structure with filamentous fibers, more entrapped platelets, and blood cells. Moreover, distinct morphological differences between the clots formed on the different titanium surfaces. The scattered blood components stick to the PT surface, with only a cluster of platelets and a few fibers loosely interwoven. While on the SLA surface, more platelets and fibers adhered within 10 min. After 2 h, holes and path-like structures within a thick layer of blood clot were formed.

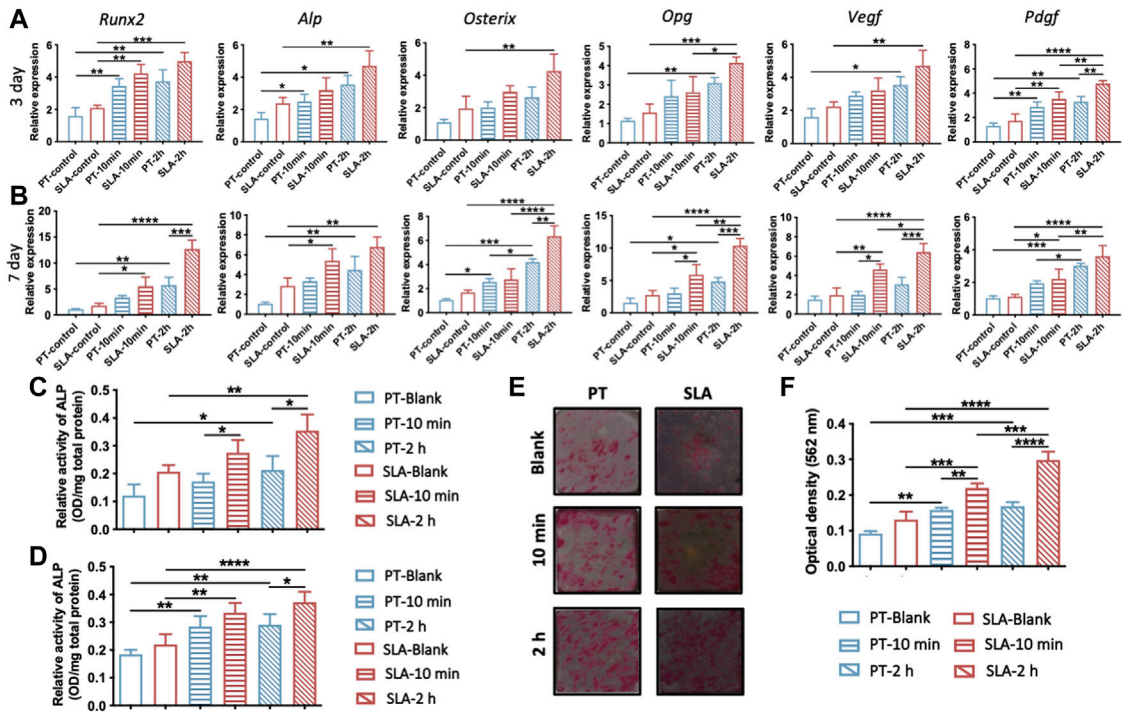

FIGURE 4
Osteogenic and angiogenic differentiation of BMSCs on various titanium surfaces. **(A,B)** Expression levels of osteogenic genes (ALP/Runx2/Osterix/Opg) and angiogenic genes (Vegf/Pdgf) in BMSCs cultured on titanium surfaces with or without blood incubation were evaluated on day 3 **(A)** and day 7 **(B)**. **(C,D)** Quantitative analysis of ALP activity of BMSCs after 4 days **(C)** and 7 days **(D)** culture, respectively. **(E)** Representative photos of Alizarin Red S staining of calcium nodules on PT and SLA surfaces on the 21st days. **(F)** Quantitative analysis of calcium nodules by cetylpyridinium chloride solution. Error bars represent the SD of three independent experiments. *: $p < 0.05$, **: $p < 0.01$, ***$p < 0.001$, ***$p < 0.0001$.

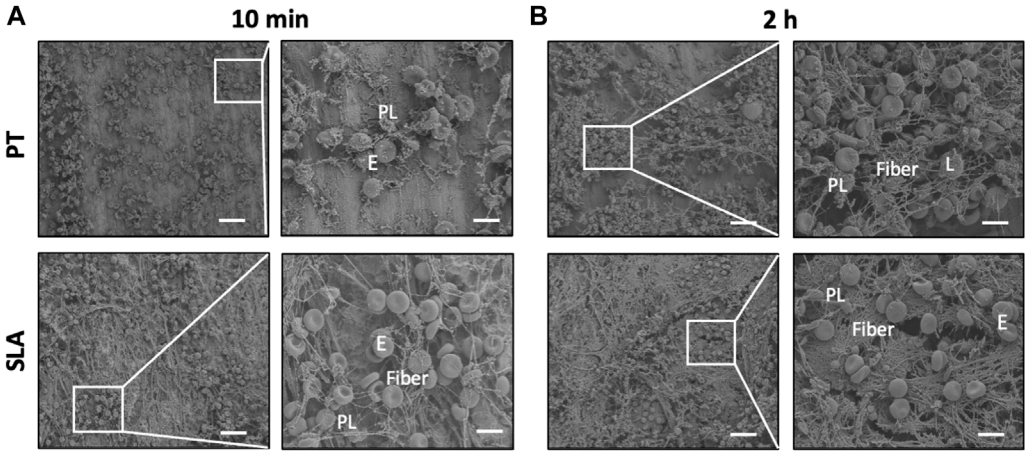

FIGURE 5
Characterization of blood clot features on titanium surfaces. **(A,B)** Scanning electron micrographs of adhering blood clots and entrapped blood components. Representative SEM images showed the adhering blood clots with entrapped platelets and cells on the surface of PT and SLA implants after 10 min **(A)** and 2 h **(B)** implantation. Scale bars: 80 μm; Inserts: 20 μm. E, erythrocytes, PL, platelets, and L, leukocytes.

3.6 Interaction of blood components with titanium surfaces after implantation

To clarify the features of blood clots formed on the titanium implant surfaces *in vivo*, LCSM was used to characterize fibrinogen, activated platelets, and monocytes/macrophages after staining with specific antibodies. Immunofluorescence micrographs and projection of z-stacks of images rebuilt the structure of implants, and semi-quantitatively analyzed (Figure 6). The SLA surfaces induced the formation of thicker blood clots with a higher density of a fibrous structure and trapped blood components.

10.3389/fbioe.2023.1136406

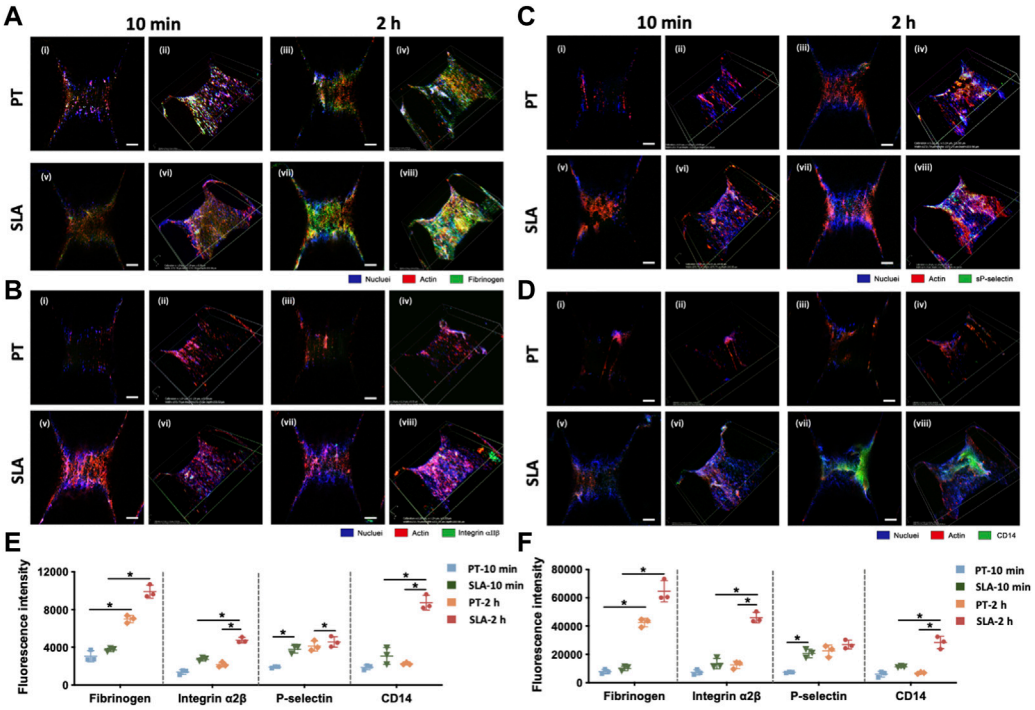

FIGURE 6
Laser confocal scanning micrographs of blood clot composition and features on PT and SLA implant surfaces. **(A–D)** The two-dimensional (i, ii, v, vi) and z-stack projective (iii, iv, vii, viii) fluorescence images were shown. Surfaces stained with DAPI for nuclei (blue), with rhodamine-phalloidin for F-actin (red) and with **(A)** Anti-fibrinogen for fibrin; **(B)** Integrin α2β for clotting response; **(C)** P-selectin for activated platelets; **(D)** CD14 for monocyte-macrophage cell linage (Scale bars: 200 μm). **(E,F)** The fluorescence intensity analysis for 2D **(E)** and 3D **(F)** z-stack images. Images represent 3 biological replicates. *$p < 0.05$, **$p < 0.01$.

The conformation of cross-linked fibrinogen was different from the macroscopic images, which was the central building block of the blood clots (Figure 6A). Immunofluorescence density of fibrinogen in confocal micrographs substantially increased after 2 h than 10 min. Furthermore, fibrinogen adsorbed more to the SLA surface than to the PT surface. Macroscopic projection of confocal z-stacks also showed a well-proportioned fibrin network attaching to SLA surfaces while only sparse fibrin fibers formed on PT surfaces.

Platelet was immune-stained with platelet membrane glycoprotein integrin α2β (CD41) and platelet activation-dependent granular membrane protein (P-selectin). Figures 6B, C shows that the mean fluorescence area coverage with CD41-positive and P-selectin-positive platelets was higher on the SLA surfaces than on the PT surfaces, and the intensity value steadily rose over time. In addition, flow cytometry was supplemented to evaluate the activated platelets surrounding the implant surfaces (Supplementary Figure S1A). Results showed that the percentage of activated platelets increased with the extension of implantation time (Supplementary Figure S1B). There was no significant difference between PT surface and SLA surface at 10 min, but SLA surface significantly activated platelets compared with PT surface after 2 h. Overall, current data suggested that the activation degree of platelets had a positive correlation with time and was influenced by biomaterial properties.

Due to the abundance of monocytes in the whole blood and the pivotal role of the monocyte-derived macrophages in inflammation and osteointegration, CD14 was used as a marker for monocytes and macrophages to count the cell number (Figure 6D). Little monocytes were adsorbed on the implant surface within 10 min after implantation. After 2 h implantation, numerous CD14-positive cells within blood clots attached to the SLA surface, in contrast to a dramatically lower fluorescence intensity on the PT surfaces.

3.7 Activation of the blood coagulation cascade, the complement system, platelets, and cellular responses *in vivo*

The activation of titanium surfaces on biological processes *in vivo* including blood coagulation, complement system, and activated platelets was monitored by ELISA against TAT complexes, the anaphylatoxin C5a, the P-selectin, and PDGF (Figures 7A–D). Compared with the PT surface, the SLA surfaces induced a significant increase in TAT and C5a concentrations at both time points. The concentration of TAT slightly decreased over time throughout the implantation period. It was indicated that both types of surfaces increased C5a concentration over time. Besides, an increasing trend was observed in P-selectin and PDGF concentrations after 2 h in contrast to the 10 min group, but the difference in P-selectin between the two surfaces was not statistically significant. After 2 h, the concentration of PDGF on the SLA surface was significantly higher than that on the PT surface. Statistically, P-selectin concentration showed surface properties with little

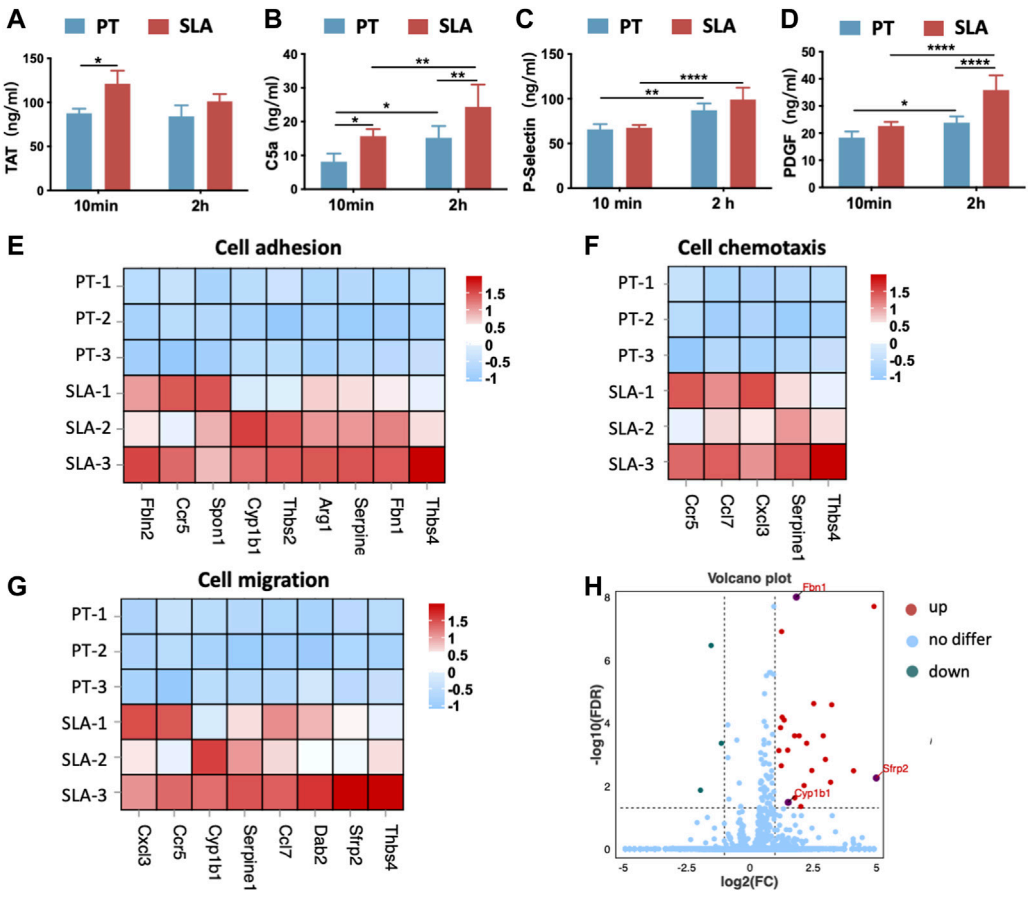

FIGURE 7
The activation of cellular response after implantation *in vivo*. **(A–D)** The concentration of TAT complexes **(A)**, C5a **(B)**, P-selectin **(C)**, and PDGF **(D)** was detected by ELISA. Error bars represent the SD of three independent experiments. *: $p < 0.05$, **: $p < 0.01$, ****: $p < 0.0001$. **(E–G)** Heatmap of genes expression in cell adhesion (GO:0007155), cell chemotaxis (GO:0060326), and cell migration (GO: 0016477). **(H)** Volcano plot showing the DEGs between two implant materials. SLA implants upregulated the expression of extracellular matrix organization-related genes (*Sfrp2*, *Cyp1ba*, *Fbn1*) when compared with the PT implants.

influence, but implantation time showed a significant effect. However, PDGF was affected by both time and surface properties.

Further, bone tissue RNA-sequencing (RNA-seq) analysis for samples harvested 3 days (n = 3) after implantation. DEGs analysis showed that the implantation of SLA implants induced a higher expression level of related genes in cell adhesion, cell chemotaxis, and cell migration when compared with PT implants (Figures 7E–G). This trend was consistent with *in vitro* results. In addition, SLA implant upregulated the differentially expressed genes associated with extracellular structure organization including *Sfrp2*, *Cyp1ba*, *and Fbn1* (Figure 7H). Thus, SLA implants initiated stronger platelet activation and more antithrombin formation, as well as promoting cell adhesion and migration than PT surfaces.

4 Discussion

Blood clots that form immediately following bone implantation play a vital role in the subsequent healing process (Wang et al., 2017). The modulation of blood clot structure within the implant surface could lead to the development of multifunctional scaffolds that mimic the natural structure to accelerate bone regeneration (Liang et al., 2021). How blood clots as mediators between the biomaterial surface and the osteogenic differentiation of BMSCs are worth further exploring. The current study demonstrated that titanium surface characteristics directly affect platelet activation and clot formation immediately after implantation, and clot features steer the recruitment and osteogenic potential of BMSCs.

The blood components and adsorption proteins act as bridging scaffolds between the implant surfaces and cells. Plasma-derived proteins, platelet-rich fibrin, or blood-prefabricated materials were used as an effective strategy to enhance bone repair and regeneration (Kopf et al., 2015b; Liang et al., 2021; Ren et al., 2022; Wu et al., 2022). The number of cells adhering and recruitment increased on the blood-pretreated surfaces (Yang et al., 2016). Interestingly, compared with the control group, BMSCs tended to extend branched projections from the cell body while showing a spindle-shaped spread after blood incubation. Ordinarily, osteogenic cells protrude more filopodia and possess stronger migratory and osteogenic potential (Kopf et al., 2015a; Schar et al., 2015). This finding supports that the surface has a blood clot and interacts with blood components are crucial in tailoring the cellular response.

The surface with clot networks is crucial for withstanding detachment forces, thus providing a migration pathway for the osteogenic cells to reach the implant surface (Arvidsson et al., 2007). The blood-prefabricated implant materials exhibit superior performance in early cell recruitment via releasing potent migration factors such as CINC-2a, IL-2, L-selectin, MCP-1, PDGF-AA, and VEGF (Lam et al., 2015; Bruekers et al., 2016; Eriksson et al., 2019). Consistent with previous studies, current results showed that migration and recruitment are improved not only on pre-incubated surfaces but also in the use of conditioned mediums. The clot networks can release cytokines and chemokines to modulate the interaction of BMSCs with the titanium surfaces and the cytokines released by the clots on the SLA surface showed stronger chemotaxis at two-time points *in vitro*. The osteogenic differentiation potential of BMSCs is enhanced after cultured on the pre-incubated surfaces over time. Thus, after interacting with blood clots on the surface, BMSCs exerted better recruitment, mobility, and osteogenic differentiation at the early stage of the bone healing process.

The blood clot acts as a "natural scaffold" that forms when the extrinsic coagulation pathway is activated. This pathway relies on a complex interaction between three major components, coagulation factors, activated platelets, and blood cells. The composition and structure of clots such as fibers thickness, porosity, number of branching points, and the strength of the adhesion of the fibrin clots depend on the surface properties (Chen et al., 2014; Chen et al., 2015). SLA surfaces due to the more intense contact activation and thrombotic characteristics, resulting in clots with thicker fibrin fibers, more platelets, and a stable porous fibrin scaffold. The initial adhesion of platelets binds to implant-surface-adsorbed fibrinogen by integrin α2β (Broberg et al., 2002). Rough surface microtopography would exhibit an increased surface area and a resultant augment in fibrinogen absorption, which explains the increase in platelet adhesion, activation, and aggregation (Collignon et al., 2017). Evidence showed that fibrinogen provided a temporary microenvironment conductive to regeneration, which led to bone repair after 8 weeks of implantation (Vasconcelos et al., 2016). Fibrinogen also modulates the activity of monocytes and macrophages through knock-on stimulatory events (Zuchtriegel et al., 2016; Kaur et al., 2017). Besides, the platelet-directed guidance of leukocyte's extravasation to implant surfaces is an essential step in the recruitment process of immune cells (Lam et al., 2015). Platelet exposure to P-selectin leads to ERK 1/2 MAPK-dependent conformational change in leukocyte integrins and promotes the continuing extravasation of neutrophils and monocytes to the implant site (Zuchtriegel et al., 2016). Afterward, the increasing number of monocytes/macrophages (CD14 positive cells) entrapped on the SLA surface shows beneficial phagocytic activity and bioactive molecules release, which are necessary for cleaning a wound site (Holmes et al., 2018). The SLA surface enhances the adhesion thickness of fibrin clots and the complexity of the three-dimensional network structure. Successful tissue healing has been shown to depend on the initial fibrin-clot formation within the defect site. Evidence suggests that the removal of a clot causes delayed fracture healing and subcutaneous implantation of a hematoma results in ectopic bone formation (Kolar et al., 2011; Wei et al., 2018).

Our study further revealed that roughness and hydrophilicity could effectively affect the structure of blood clots and the adsorption of proteins *in vivo* which is in line with the other *in vitro* studies (Fan et al., 2017; Sangkert et al., 2022). Park and colleagues demonstrated that the complexity of the surface significantly increased platelet attachment. The hydrophilic surface shows a higher platelet binding and more intense contact coagulation cascade. Rougher and hydrophilic surfaces induce greater and earlier platelet release in subsequent macrophage inflammatory cytokine responses, thereby immunomodulating the ability to bone regeneration (Zivkovic et al., 2021).

Native titanium stimulates the generation of thrombin in the blood due to contact activation *in vivo* (Zabczyk et al., 2019). Thrombin cleaves fibrinogen into fibrin monomers, which then polymerize into the initial fibrin clot, which occurs in response to the dynamic changes in thrombin concentration (Hulshof et al., 2021). Based on TAT concentration implied that the SLA surface had strong thrombosis characteristics. Thrombin inhibitor participates in BMSCs behaviors and promotes osteogenesis via canonical Wnt signaling pathway (Song et al., 2021). Furthermore, an increasing trend indicated that the activation of the complement system and platelets are time-dependent. With incubation time extended from 10 min to 2 h, more blood clots with complement factors and activated platelets on the surfaces. Both complement proteins and platelets communicate with each other and facilitate progression into the inflammatory stage of bone healing (Schraufstatter et al., 2009). The anaphylatoxins C5a present in injured tissues induce an inflammatory response and act as a chemokine for MSCs and regulate their behavior (Holmes et al., 2018).

In this study, an *in vitro* blood incubation model was adopted to simulate the immediate contact of implants *in vivo*. But heparin sodium is not present in the body, which is a limitation of the experimental design. The experimental results excluding the effect of heparin sodium at the same concentration on BMSCs are shown in Supplementary Figure S2. In addition, *in vivo* studies lack direct observation of BMSCs, which is the direction of our further research. A lot of work is still worth studying in the future.

In summary, this study reveals the interactions between clot features and the behaviors of BMSCs on titanium surfaces, providing a novel research idea for biomaterial design. SLA surfaces induced stronger platelet activation and more antithrombin formation, as well as more complex stereoscopic clot features than PT surfaces. In turn, the surface with blood clots promotes the recruitment and osteogenic differentiation of BMSCs. Given the physiological role and tailoring potential of the blood clots, it is crucial to understand the properties of blood clots formed on the implant surface in order to develop improved biomaterials for better osteogenesis.

Data availability statement

The original contributions presented in the study are publicly available. This data can be found here: https://www.ncbi.nlm.nih.gov/bioproject/PRJNA924055/.

Ethics statement

The animal study was reviewed and approved by the Institutional Animal Care and Use Committee of Zhejiang University (ZJU20190084).

Author contributions

JL and JZ contributed equally to this work and share first authorship. JZ and JL conceived the ideas; JL, YX, and AX did the experiment and collected the data; JZ and AX analyzed the data; JL and JZ wrote the manuscript; FH and AX led the writing.

Funding

The study was supported by the grants from the National Natural Science Foundation of China (No. 82271026), the Key Research and Development Program of Science and Technology Department of Zhejiang Province (No. 2019C03081), and the Research and Development Project of Stomatology Hospital Zhejiang University School of Medicine (RD2022JCEL29).

Conflict of interest

The authors declare that the research was conducted in the absence of any commercial or financial relationships that could be construed as a potential conflict of interest.

Publisher's note

All claims expressed in this article are solely those of the authors and do not necessarily represent those of their affiliated organizations, or those of the publisher, the editors and the reviewers. Any product that may be evaluated in this article, or claim that may be made by its manufacturer, is not guaranteed or endorsed by the publisher.

Supplementary material

The Supplementary Material for this article can be found online at: https://www.frontiersin.org/articles/10.3389/fbioe.2023.1136406/full#supplementary-material

References

Arvidsson, S., Askendal, A., and Tengvall, P. (2007). Blood plasma contact activation on silicon, titanium and aluminium. *Biomaterials* 28 (7), 1346–1354. doi:10.1016/j.biomaterials.2006.11.005

Bai, L., Zhao, Y., Chen, P., Zhang, X., Huang, X., Du, Z., et al. (2021). Targeting early healing phase with titania nanotube arrays on tunable diameters to accelerate bone regeneration and osseointegration. *Small* 17 (4), e2006287. doi:10.1002/smll.202006287

Broberg, M., Eriksson, C., and Nygren, H. (2002). GpIIb/IIIa is the main receptor for initial platelet adhesion to glass and titanium surfaces in contact with whole blood. *J. Lab. Clin. Med.* 139 (3), 163–172. doi:10.1067/mlc.2002.121604

Bruekers, S. M., Jaspers, M., Hendriks, J. M., Kurniawan, N. A., Koenderink, G. H., Kouwer, P. H., et al. (2016). Fibrin-fiber architecture influences cell spreading and differentiation. *Cell. Adh Migr.* 10 (5), 495–504. doi:10.1080/19336918.2016.1151607

Chen, J., Yang, P., Liao, Y., Wang, J., Chen, H., Sun, H., et al. (2015). Effect of the duration of UV irradiation on the anticoagulant properties of titanium dioxide films. *ACS Appl. Mater Interfaces* 7 (7), 4423–4432. doi:10.1021/am509006y

Chen, J., Zhao, A., Chen, H., Liao, Y., Yang, P., Sun, H., et al. (2014). The effect of full/partial UV-irradiation of TiO2 films on altering the behavior of fibrinogen and platelets. *Colloids Surf. B Biointerfaces* 122, 709–718. doi:10.1016/j.colsurfb.2014.08.004

Collignon, A. M., Lesieur, J., Vacher, C., Chaussain, C., and Rochefort, G. Y. (2017). Strategies developed to induce, direct, and potentiate bone healing. *Front. Physiol.* 8, 927. doi:10.3389/fphys.2017.00927

Eriksson, O., Mohlin, C., Nilsson, B., and Ekdahl, K. N. (2019). The human platelet as an innate immune cell: Interactions between activated platelets and the complement system. *Front. Immunol.* 10, 1590. doi:10.3389/fimmu.2019.01590

Faia-Torres, A. B., Guimond-Lischer, S., Rottmar, M., Charnley, M., Goren, T., Maniura-Weber, K., et al. (2014). Differential regulation of osteogenic differentiation of stem cells on surface roughness gradients. *Biomaterials* 35 (33), 9023–9032. doi:10.1016/j.biomaterials.2014.07.015

Fan, Y., Luo, R., Han, H., Weng, Y., Wang, H., Li, J., et al. (2017). Platelet adhesion and activation on chiral surfaces: The influence of protein adsorption. *Langmuir* 33 (39), 10402–10410. doi:10.1021/acs.langmuir.7b02283

Gorbet, M. B., and Sefton, M. V. (2004). Biomaterial-associated thrombosis: Roles of coagulation factors, complement, platelets and leukocytes. *Biomaterials* 25 (26), 5681–5703. doi:10.1016/j.biomaterials.2004.01.023

He, F. M., Yang, G. L., Li, Y. N., Wang, X. X., and Zhao, S. F. (2009). Early bone response to sandblasted, dual acid-etched and H2O2/HCl treated titanium implants: An experimental study in the rabbit. *Int. J. Oral Maxillofac. Surg.* 38 (6), 677–681. doi:10.1016/j.ijom.2009.03.716

Holmes, H. L., Wilson, B., Goerger, J. P., Silverberg, J. L., Cohen, I., Zipfel, W. R., et al. (2018). Facilitated recruitment of mesenchymal stromal cells by bone marrow concentrate and platelet rich plasma. *PLoS One* 13 (3), e0194567. doi:10.1371/journal.pone.0194567

Huang, Y. Z., He, S. K., Guo, Z. J., Pi, J. K., Deng, L., Dong, L., et al. (2019). Nanostructured titanium surfaces fabricated by hydrothermal method: Influence of alkali conditions on the osteogenic performance of implants. *Mater Sci. Eng. C Mater Biol. Appl.* 94, 1–10. doi:10.1016/j.msec.2018.08.069

Hulshof, A. M., Hemker, H. C., Spronk, H. M. H., Henskens, Y. M. C., and Ten Cate, H. (2021). Thrombin-Fibrin(ogen) interactions, host defense and risk of thrombosis. *Int. J. Mol. Sci.* 22 (5), 2590. doi:10.3390/ijms22052590

Kaur, S., Raggatt, L. J., Batoon, L., Hume, D. A., Levesque, J. P., and Pettit, A. R. (2017). Role of bone marrow macrophages in controlling homeostasis and repair in bone and bone marrow niches. *Semin. Cell. Dev. Biol.* 61, 12–21. doi:10.1016/j.semcdb.2016.08.009

Kolar, P., Gaber, T., Perka, C., Duda, G. N., and Buttgereit, F. (2011). Human early fracture hematoma is characterized by inflammation and hypoxia. *Clin. Orthop. Relat. Res.* 469 (11), 3118–3126. doi:10.1007/s11999-011-1865-3

Kopf, B. S., Ruch, S., Berner, S., Spencer, N. D., and Maniura-Weber, K. (2015a). The role of nanostructures and hydrophilicity in osseointegration: *In-vitro* protein-adsorption and blood-interaction studies. *J. Biomed. Mater Res. A* 103 (8), 2661–2672. doi:10.1002/jbm.a.35401

Kopf, B. S., Schipanski, A., Rottmar, M., Berner, S., and Maniura-Weber, K. (2015b). Enhanced differentiation of human osteoblasts on Ti surfaces pre-treated with human whole blood. *Acta Biomater.* 19, 180–190. doi:10.1016/j.actbio.2015.03.022

Lam, F. W., Vijayan, K. V., and Rumbaut, R. E. (2015). Platelets and their interactions with other immune cells. *Compr. Physiol.* 5 (3), 1265–1280. doi:10.1002/cphy.c140074

Liang, Y., He, J., and Guo, B. (2021). Functional hydrogels as wound dressing to enhance wound healing. *ACS Nano* 15 (8), 12687–12722. doi:10.1021/acsnano.1c04206

Love, M. I., Huber, W., and Anders, S. (2014). Moderated estimation of fold change and dispersion for RNA-seq data with DESeq2. *Genome Biol.* 15 (12), 550. doi:10.1186/s13059-014-0550-8

Lukaszewska-Kuska, M., Wirstlein, P., Majchrowski, R., and Dorocka-Bobkowska, B. (2018). Osteoblastic cell behaviour on modified titanium surfaces. *Micron* 105, 55–63. doi:10.1016/j.micron.2017.11.010

Melville, J. C., Manon, V. A., Blackburn, C., and Young, S. (2019). Current methods of maxillofacial tissue engineering. *Oral Maxillofac. Surg. Clin. North Am.* 31 (4), 579–591. doi:10.1016/j.coms.2019.07.003

Ren, S., Tang, X., Liu, L., Meng, F., Yang, X., Li, N., et al. (2022). Reinforced blood-derived protein hydrogels enable dual-level regulation of bio-physiochemical microenvironments for personalized bone regeneration with remarkable enhanced efficacy. *Nano Lett.* 22 (10), 3904–3913. doi:10.1021/acs.nanolett.2c00057

Sangkert, S., Juncheed, K., and Meesane, J. (2022). Osteoconductive silk fibroin binders for bone repair in alveolar cleft palate: Fabrication, structure, properties, and *in vitro* testing. *J. Funct. Biomater.* 13 (2), 80. doi:10.3390/jfb13020080

Schar, M. O., Diaz-Romero, J., Kohl, S., Zumstein, M. A., and Nesic, D. (2015). Platelet-rich concentrates differentially release growth factors and induce cell migration *in vitro*. *Clin. Orthop. Relat. Res.* 473 (5), 1635–1643. doi:10.1007/s11999-015-4192-2

Schraufstatter, I. U., Discipio, R. G., Zhao, M., and Khaldoyanidi, S. K. (2009). C3a and C5a are chemotactic factors for human mesenchymal stem cells, which cause prolonged ERK1/2 phosphorylation. *J. Immunol.* 182 (6), 3827–3836. doi:10.4049/jimmunol.0803055

Song, J., Jiang, N., Gan, X., Zhi, W., and Zhu, Z. (2021). Thrombin inhibitor argatroban modulates bone marrow stromal cells behaviors and promotes osteogenesis through canonical Wnt signaling. *Life Sci.* 269, 119073. doi:10.1016/j.lfs.2021.119073

Trindade, R., Albrektsson, T., Tengvall, P., and Wennerberg, A. (2016). Foreign body reaction to biomaterials: On mechanisms for buildup and breakdown of osseointegration. *Clin. Implant Dent. Relat. Res.* 18 (1), 192–203. doi:10.1111/cid.12274

Vasconcelos, D. M., Goncalves, R. M., Almeida, C. R., Pereira, I. O., Oliveira, M. I., Neves, N., et al. (2016). Fibrinogen scaffolds with immunomodulatory properties promote *in vivo* bone regeneration. *Biomaterials* 111, 163–178. doi:10.1016/j.biomaterials.2016.10.004

Wang, X., Friis, T. E., Masci, P. P., Crawford, R. W., Liao, W., and Xiao, Y. (2016). Alteration of blood clot structures by interleukin-1 beta in association with bone defects healing. *Sci. Rep.* 6, 35645. doi:10.1038/srep35645

Wang, X., Friis, T., Glatt, V., Crawford, R., and Xiao, Y. (2017). Structural properties of fracture haematoma: Current status and future clinical implications. *J. Tissue Eng. Regen. Med.* 11 (10), 2864–2875. doi:10.1002/term.2190

Wei, F., Liu, G., Guo, Y., Crawford, R., Chen, Z., and Xiao, Y. (2018). Blood prefabricated hydroxyapatite/tricalcium phosphate induces ectopic vascularized bone formation via modulating the osteoimmune environment. *Biomater. Sci.* 6 (8), 2156–2171. doi:10.1039/c8bm00287h

Wu, S., Guo, W., Li, R., Zhang, X., and Qu, W. (2022). Progress of platelet derivatives for cartilage tissue engineering. *Front. Bioeng. Biotechnol.* 10, 907356. doi:10.3389/fbioe.2022.907356

Xing, Z., Cai, J., Sun, Y., Cao, M., Li, Y., Xue, Y., et al. (2020). Altered surface hydrophilicity on copolymer scaffolds stimulate the osteogenic differentiation of human mesenchymal stem cells. *Polym. (Basel)* 12 (7), 1453. doi:10.3390/polym12071453

Yang, J., Zhou, Y., Wei, F., and Xiao, Y. (2016). Blood clot formed on rough titanium surface induces early cell recruitment. *Clin. Oral Implants Res.* 27 (8), 1031–1038. doi:10.1111/clr.12672

Yang, Y., and Xiao, Y. (2020). Biomaterials regulating bone hematoma for osteogenesis. *Adv. Healthc. Mater* 9, e2000726. doi:10.1002/adhm.202000726

Zabczyk, M., Stachowicz, A., Natorska, J., Olszanecki, R., Wisniewski, J. R., and Undas, A. (2019). Plasma fibrin clot proteomics in healthy subjects: Relation to clot permeability and lysis time. *J. Proteomics* 208, 103487. doi:10.1016/j.jprot.2019.103487

Zivkovic, J. M., Stojanovic, S. T., Vukelic-Nikolic, M. D., Radenkovic, M. B., Najdanovic, J. G., Ciric, M., et al. (2021). Macrophages' contribution to ectopic osteogenesis in combination with blood clot and bone substitute: Possibility for application in bone regeneration strategies. *Int. Orthop.* 45 (4), 1087–1095. doi:10.1007/s00264-020-04826-0

Zuchtriegel, G., Uhl, B., Puhr-Westerheide, D., Pornbacher, M., Lauber, K., Krombach, F., et al. (2016). Platelets guide leukocytes to their sites of extravasation. *PLoS Biol.* 14 (5), e1002459. doi:10.1371/journal.pbio.1002459

frontiers | Frontiers in Bioengineering and Biotechnology

TYPE Original Research
PUBLISHED 02 June 2023
DOI 10.3389/fbioe.2023.1162202

OPEN ACCESS

EDITED BY
Si Chen,
Alexander Dubcek University in Trencin, Slovakia

REVIEWED BY
Luzhong Zhang,
Nantong University, China
Ahmed El-Fiqi,
Dankook University, Republic of Korea

*CORRESPONDENCE
Song Zhu,
zhusong1965@163.com
Quan Lin,
Linquan@jlu.edu.cn

†These authors have contributed equally to this work and share first authorship

RECEIVED 09 February 2023
ACCEPTED 18 May 2023
PUBLISHED 02 June 2023

CITATION
Pang Y, Guan L, Zhu Y, Niu R, Zhu S and Lin Q (2023), Gallic acid-grafted chitosan antibacterial hydrogel incorporated with polydopamine-modified hydroxyapatite for enhancing bone healing.
Front. Bioeng. Biotechnol. 11:1162202.
doi: 10.3389/fbioe.2023.1162202

Gallic acid-grafted chitosan antibacterial hydrogel incorporated with polydopamine-modified hydroxyapatite for enhancing bone healing

Yuxuan Pang[1†], Lin Guan[2†], Yanlin Zhu[3], Ruijuan Niu[4], Song Zhu[1*] and Quan Lin[2*]

[1]Department of Prosthodontics, School and Hospital of Stomatology, Jilin University, Changchun, China, [2]State Key Laboratory of Supramolecular Structure and Materials, College of Chemistry, Jilin University, Changchun, China, [3]Department of Oral Implantology, School and Hospital of Stomatology, Jilin University, Changchun, China, [4]Meilong Community Health Service Center, Shanghai, China

An open critical-size bone defect is a major medical problem because of the difficulty in self-healing, leading to an increased risk of bacterial infection owing to wound exposure, resulting in treatment failure. Herein, a composite hydrogel was synthesized by chitosan, gallic acid, and hyaluronic acid, termed "CGH." Hydroxyapatite was modified with polydopamine (PDA@HAP) and introduced to CGH to obtain a mussel-inspired mineralized hydrogel (CGH/PDA@HAP). The CGH/PDA@HAP hydrogel exhibited excellent mechanical performances, including self-healing and injectable properties. Owing to its three-dimensional porous structure and polydopamine modifications, the cellular affinity of the hydrogel was enhanced. When adding PDA@HAP into CGH, Ca^{2+} and PO_4^{3-} could release and then promoted differentiation of BMSCs into osteoblasts. Without any osteogenic agent or stem cells, the area of new bone at the site of defect was enhanced and the newly formed bone had a dense trabecular structure after implanting of the CGH/PDA@HAP hydrogel for 4 and 8 weeks. Moreover, the growth of *Staphylococcus aureus* and *Escherichia coli* was effectively inhibited through the grafting of gallic acid onto chitosan. Above, this study provides a reasonable alternative strategy to manage open bone defects.

KEYWORDS

hydrogel, polydopamine, gallic acid, antibacterial, bone regeneration

1 Introduction

Large bone defects caused by trauma seriously affect the physical and psychological health of patients (Xie et al., 2020). Although autologous grafts and allografts are widely used as the gold-standard bone repair materials for clinical treatment, they are associated with numerous disadvantages, including immune rejection, surgical trauma, and limited biological activity (Wang et al., 2022). Use of a scaffold exhibiting desirable biomechanical properties, degradability, and osteogenic activity is considered a reasonable method to promote bone regeneration in the field of tissue engineering.

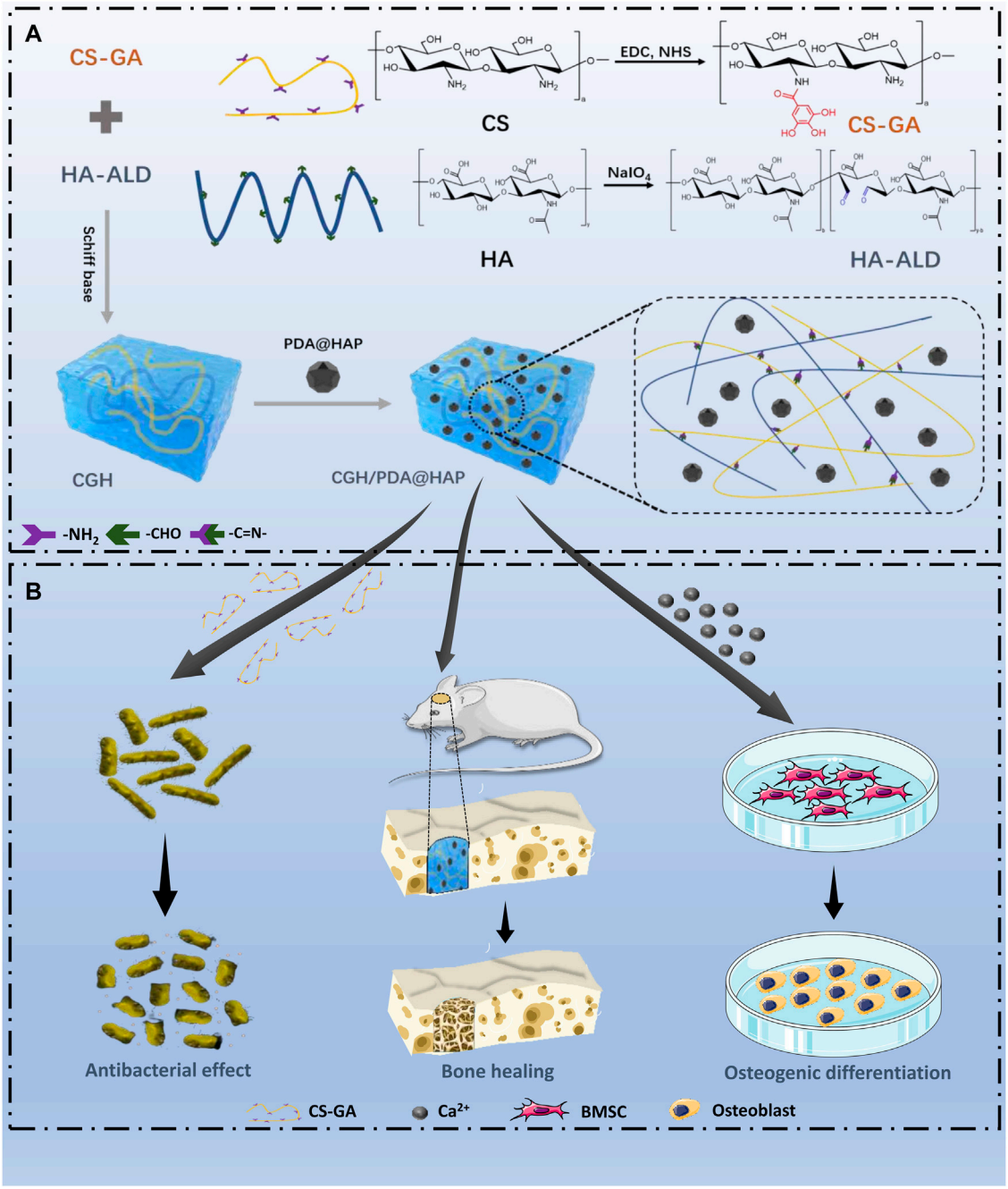

SCHEME 1
Preparation and biological effects of the CGH/PDA@HAP hydrogel. **(A)** Synthetic process **(B)** Biological effects.

Hydrogels have been developed with these advantageous properties, which have been shown to effectively accelerate the bone healing process, thus offering great application value (Sahiner et al., 2016; Guan et al., 2019; Liu et al., 2022). In particular, the extracellular matrix-like structure and properties of hydrogels conferred by loading osteogenically active substances can effectively regulate the adhesion, diffusion, and osteogenic differentiation of bone marrow-derived mesenchymal stem cells (BMSCs), thus laying a solid foundation for the subsequent formation of bone tissue (Sun et al., 2016; Liu et al., 2018).

Hydroxyapatite (HAP) is mainly responsible for the support, protection, and carrying capacity of natural bone tissue, and organic components such as type I collagen, type III collagen, and fibrin mainly control the proliferation, migration, and differentiation of BMSCs (Gao et al., 2018; Leng et al., 2020). Accordingly, biomineralized hydrogels with HAP as the main active ingredient have been manufactured that exhibit desirable hydrophilicity, degradability, and mechanical strength (Zhao et al., 2020; Ren et al., 2022; Wan et al., 2022). Such HAP-based hydrogels not only positively regulate the biological behavior of BMSCs but

also provide a suitable biochemical environment for the osteogenic differentiation of BMSCs via the continuous release of Ca^{2+} and PO_4^{3-} from HAP (Lee et al., 2014; Chen et al., 2016; Gao et al., 2022). However, HAP is prone to aggregation in hydrogels, leading to high concentrations during degradation, which interfere with the adhesion, proliferation and osteogenic differentiation of BMSCs (Jiang et al., 2017; Pan et al., 2020; Xu et al., 2020). Thus, improving the biocompatibility of HAP-based hydrogels is an important clinical need.

Inspired by the proteins responsible for the strong adhesion property of mussels, polydopamine (PDA) has been applied in the functionalization of biomaterials to bind with Ca^{2+} owing to its catechol structure (Zhou et al., 2012; Peng et al., 2014). Through PDA coating, HAP is evenly distributed on materials, which can avoid its aggregation and excessive ion concentration (Gao et al., 2022). Furthermore, the catechol group of PDA has strong surface activity for nucleophilic functional groups, which can promote cell growth onto the materials (Cui et al., 2012; Park et al., 2014; Wang et al., 2021a). This effect can be attributed to the ability of PDA to increase the overall positive charge and thus improve the hydrophilicity of the material (Zhang et al., 2022b; Li et al., 2022).

Post-traumatic bone infection is one of the common complications of an open bone defect because an open wound provides the opportunity for *Staphylococcus aureus* and other Gram-negative pathogenic bacteria to invade the defect area, leading to bone destruction and non-union (Lüthje et al., 2020). Although surgical debridement and postoperative application of antibiotics reduce the probability of infection to some extent, the disadvantages of a longer treatment cycle and generation of drug-resistant strains cannot be ignored, and bacteria colonizing deep areas of the wound are often difficult to detect (Wang et al., 2021b). Therefore, introducing an active substance with inherent antibacterial properties into scaffolds is a reasonable modification strategy (Han et al., 2019; Chen et al., 2021; Yang et al., 2021). Gallic acid (GA) has been widely applied for antibacterial modification of biomaterials given its ability to destroy the integrity of the bacterial cell wall and interfere with the activity of the respiratory electron transport chain (Shi et al., 2021). Moreover, catechol groups on the surface of GA react actively with various functional groups to promote cell adhesion, providing multiple possibilities for its application in hydrogel grafting (Asha et al., 2022).

In this study, we developed a mussel-inspired mineralized hydrogel based on GA-grafted chitosan (CS) by introducing PDA-modified HAP (PDA@HAP), which exhibited excellent osteogenic and antibacterial properties (Scheme 1). Specifically, this hybrid hydrogel (CGH/PDA@HAP) was fabricated from the assembly of CS-grafted GA (CG), hyaluronic acid (HA), and PDA@HAP. The three-dimensional porous structure of the CGH/PDA@HAP hydrogel allows BMSCs to adhere to and proliferate on its surface, showing good biocompatibility. The HAP is evenly distributed along the hydrogel owing to the grafted PDA, thereby avoiding aggregation and stabilizing the ion concentration in the local environment. As a result, PDA@HAP effectively promoted the differentiation of BMSCs into osteoblasts and upregulated the expression of osteoblast-related genes *in vitro*. Further, imaging with micro-computed tomography (micro-CT) and histological observations with hematoxylin-eosin (HE) and Masson staining revealed the desirable therapeutic effect of the CGH/PDA@HAP hydrogel on rat calvarium defects. Finally, GA grafting clearly improved the antibacterial properties of the hydrogel, preventing bacterial infection during bone regeneration *in vivo*.

2 Materials and methods

2.1 Preparation and characterization of the CGH/PDA@HAP hydrogel

2.1.1 Preparation of PDA@HAP

For PDA functionalization of HAP, 90 mL of Tris-hydrochloride buffer (pH 8.5; Aladdin, China) was mixed with 10 mL of ethanol. Subsequently, 2 g of HAP (Aladdin, China) was dispersed over the solution by ultrasound. Dopamine hydrochloride (1 mg/mL; Aladdin, China) was then added to the above solution and stirred in the dark for 24 h. The unreacted dopamine hydrochloride was removed by washing with water and centrifugation, and the product was ultrasonically dispersed. Finally, PDA@HAP was obtained by freeze-drying.

2.1.2 Preparation of oxidized HA (HA-ALD)

One Gram of HA (Yuanye, China) was uniformly dissolved in 100 mL of H_2O, followed by the addition of 1 g of sodium periodate ($NaIO_4$; Sigma, America), which was left to react for 3 h in the dark. Subsequently, 3 mL ethylene glycol (Beijing Chemical Works, China) was added to the solution and stirred for 1 h to terminate the reaction. The obtained solution was dialyzed in deionized water for 3 days and the water was changed at least three times a day. Finally, the solution was freeze-dried to obtain HA-ALD.

2.1.3 Preparation of GA-modified CS (CS-GA)

CS (Aladdin, China) was dissolved in water and adjusted to form a 1 wt% solution with 5 M HCl. The solution was heated in a water bath and deoxidized with N_2 for 15 min. GA (Aladdin, China) was then dissolved in the CS solution. The N-(3-Dimethylaminopropyl)-N′-ethylcarbodiimide hydrochloride (EDC; Aladdin, China) and N-Hydroxysuccinimide (NHS; Aladdin, China) dissolved in 50 mL H_2O were dropped into the GA and CS mixture, and left to react for 10 h in the N_2 environment while maintaining the pH at 5. The obtained solution was dialyzed with acidified deionized water for 3 days to inhibit oxidation of the catechol group. Finally, the CS-GA powder was obtained by freeze-drying.

2.1.4 Preparation of the CGH/PDA@HAP hydrogel

The 1 wt% HA-ALD solution was dissolved in a 2 wt% CS-GA solution, and then 1 wt% PDA@HAP was dissolved in a 5 wt% HA-ALD solution and uniformly distributed under ultrasonic stirring. The two solutions were then mixed and shaken to obtain a uniform GGH/PDA@HAP hydrogel. CS hydrogels without the GA modification were prepared under the same process for comparison.

2.1.5 Characterization of the CGH/PDA@HAP hydrogel

The synthesized hydrogel was characterized by Fourier-transform infrared (FTIR) spectra obtained on a BLUCK spectrophotometer over a wavenumber range from 4000 to 500 cm^{-1}, ultraviolet (UV)-visible absorption spectra measured

TABLE 1 Primer sequences for RT-qPCR.

Primer	Forward sequence (5′–3′)	Reverse sequence (5′–3′)
Runx2	CTTCGTCAGCGTCCTATCAGTTCC	TCCATCAGCGTCAACACCATCATTC
Alp	GGCGTCCATGAGCAGAACTACATC	CAGGCACAGTGGTCAAGGTTGG
Ocn	GGACCCTCTCTCTGCTCACTCTG	ACCTTACTGCCCTCCTGCTTGG
β-actin	TGTCACCAACTGGGACGATA	GGGGTGTTGAAGGTCTCAAA

with a Lambad 800 spectrophotometer, and H-nuclear magnetic resonance (NMR) spectroscopy on a BLUCK AVANCEIII600 device. The dynamic mechanical properties of the hydrogel were determined with a rheometer (TA Instruments-waters LLC). The morphology of the hydrogels was observed by cryo-scanning electron microscopy (Cryo-SEM; Zeiss Sigma-300, Germany) at −140°C. X-ray diffraction (XRD; Rigaku, Japan) was used to analyze the phase compositions of the CGH and CGH/PDA@HAP hydrogels. The swelling ratio of the hydrogels was measured in PBS at 37°C. For enzymatic degradation assay, the CGH and CGH/PDA@HAP hydrogels were incubated in the PBS solution containing hyaluronidase (900U/mL; Solarbio, China) at 37°C for 21 days. The CGH/PDA@HAP hydrogel was immersed in sterile deionized water for 5 days and inductively coupled plasma emission spectrometer (ICAP-7400; ThermoFisher, America) was used to an investigate the calcium (Ca^{2+}) and phosphorus (PO_4^{3-}) release.

2.2 Cytotoxicity and cell proliferation assay

2.2.1 Cell culture

The BMSCs were isolated from three-week-old male Sprague-Dawley (SD) rats (Changsheng Biotechnology, China) and cultured in low-glucose Dulbecco's modified Eagle medium (LG-DMEM; Solarbio, China) supplemented with 10% fetal bovine serum (FBS; Genemini, United States) and 1% penicillin-streptomycin (P-S; Hyclone, United States) at 37°C in a 5% CO_2 atmosphere. BMSCs were used at passage 3 for further *in vitro* experiments.

To assess the effects of the hydrogel on BMSCs, the culture medium was supplemented with CGH and CGH/PDA@HAP. Briefly, the hydrogels were immersed in LG-DMEM and cultured for 48 h (Xu et al., 2020). The extracts were filtered for sterilization and the cells were subsequently cultured in osteogenic medium (85% LG-DMEM, 10% FBS, 1% P-S, 50 μM ascorbate, 100 mM β-sodium glycerophosphate, 100 nM dexamethasone).

2.2.2 Cell live/dead staining

The Calcein AM/propidium iodide (PI) cell live and dead staining kit (Yeasen, China) was used to observe the survival of BMSCs for evaluating the cytotoxicity of CGH and CGH/PDA@HAP hydrogels. In brief, the bottom of a 6-well plate was covered with the prepared hydrogel, sterilized by UV light, cleaned in deionized water, and pre-soaked in DMEM before the experiment. The hydrogel was then inoculated with 5×10^4 BMSCs. After culturing for 24 h, the fluorescence staining solution (2 μM Calcein AM and 4.5 μM PI) was added, incubated for 15 min, and imaged by a live cell imager.

2.2.3 Proliferation assay

To further assess the effect of the hydrogels on the proliferation of BMSCs, the Cell Counting Kit-8 (CCK-8; Yeasen, China) assay was used to evaluate the number of live BMSCs in the hydrogels. The hydrogel was pre-treated as described above. Subsequently, 5×10^3 BMSCs were seeded onto the surfaces of the hydrogels in a 96-well plate and the complete medium was replaced every 3 days. The cell proliferation was assessed at 1, 4, and 7 days. At each time point, the medium was replaced with fresh basic medium and CCK-8 reacting solutions were added. After incubation for 2 h, the optical density (OD) value was measured at 450 nm with a microplate reader. BMSCs cultured only in complete medium were used as the control group.

2.3 Osteogenic differentiation assay *in vitro*

2.3.1 Alkaline phosphatase (ALP) staining

ALP is a marker of early osteogenesis that is often used to evaluate the degree of the early osteogenic differentiation of BMSCs (Wang et al., 2021a). ALP staining and corresponding quantitative analysis were performed to evaluate the effect of the hydrogel on the osteogenic differentiation ability of BMSCs in the early stage. Briefly, BMSCs were cultured in the extract-modified osteogenic medium for 14 days, washed twice by phosphate-buffered saline (PBS), and then fixed with 4% paraformaldehyde for 30 min. The staining procedure was performed according to the protocol described in the kit instructions (Beyotime, China). After staining, BMSCs were washed with PBS and observed under a light microscope, and images were captured. A quantification kit (Jiancheng, China) was also used to quantify the ALP activity in the BMSCs. Briefly, BMSCs were fully lysed and the protein supernatant was obtained to measure the ALP activity. A bicinchoninic acid (BCA) kit (Beyotime, China) was used to normalize the total protein concentration. BMSCs incubated in osteogenic medium alone were set as the control group.

2.3.2 Alizarin Red staining (ARS)

ARS was used to observe the mineralization in the extracellular matrix of BMSCs. Briefly, after culture for 21 days, BMSCs were washed with PBS, fixed with 4% paraformaldehyde for 30 min, and then ARS reaction solution (Solarbio, China) was added to the 6-well plate. After incubating in the dark for 30 min, the solution was aspirated and the 6-well plate was washed with deionized water three times, followed by image capture and analysis. Quantification of mineralization in the extracellular matrix was performed using 10% cetylpyridinium chloride (Aladdin, China) to dissolve the cells

stained by Alizarin Red. The OD value was measured at 562 nm using a microplate reader. BMSCs incubated in osteogenic medium alone were set as the control group.

2.3.3 Reverse transcription-quantitative polymerase chain reaction (RT-qPCR)

RT-qPCR was used to evaluate the osteogenic differentiation of BMSCs according to the mRNA expression of the osteogenic markers Runt-related transcription factor-2 (*Runx2*), alkaline phosphatase (*Alp*), and osteocalcin (*Ocn*). Briefly, after culture for 7 and 14 days, BMSCs were washed with PBS and total RNA was isolated by Trizol Reagent (Yeasen, China) according to the manufacturer instructions. The concentration and purity of RNA were measured by a NanoDrop 2000c spectrophotometer (ThermoFisher Scientific, United States). RNA with a concentration of 100–1000 ng/μL and an absorbance ratio at 260/280 nm of approximately 1.8–2.2 was considered to be of suitable quality for further analysis. The total RNA was reverse-transcribed into cDNA using Strand cDNA Synthesis SuperMix kit (Yeasen, China). The cDNA was then used as the template for qPCR with SYBR Green Master Mix (Yeasen, China) and primers for the target gene, and the results were analyzed on a Lightcycler 960 system. The primers were synthesized by Sangon Biotech and their sequences are shown in Table 1; β-actin served as housekeeping gene for normalization. The $2^{-\triangle\triangle Ct}$ method was used to compare relative mRNA expression levels between experimental and control groups. BMSCs incubated in osteogenic medium alone were set as the control group.

2.4 Bone regeneration assay *in vivo*

2.4.1 Rat calvarium defect model establishment and hydrogel implantation

All animal studies were approved by the Institutional Animal Care and Use Committee of Jilin University (IACUC No. SY202203100). A critical-sized rat calvarium defect was made to evaluate the osteogenesis effects of the CGH/PDA@HAP hydrogel *in vivo*. Eighteen male SD rats with a weight of 220–250 g were weighed and anesthetized by intraperitoneal injection of pentobarbital sodium (45 mg/kg). After successful anesthesia, the rats were fixed in prone position. After routine preparation of the cranial skin, 1% iodophor and 75% alcohol were used for disinfection and sterile towels were spread. A 1.5-cm incision was made along the sagittal line of the skull. The skin and periosteum were dissected, and the periosteum was separated with an exfoliator to fully expose the skull. An annular bone drill was connected to the implant base, and a bone defect of 5 × 5 mm was prepared by drilling a hole (drilling rate <1500 rpm) in the outer lower quadrant of the skull where the median suture and the herringbone suture crossed. During the operation, normal saline was used to avoid overheating that could cause local tissue necrosis and to avoid the damage of brain tissue due to drilling too deep. After confirming successful model establishment, the hydrogels were injected at the same time, and the periosteum, subcutaneous tissue, and epidermis were sutured in sequential layers. The rats were placed in a warm and ventilated cage until they regained consciousness and crawled on their own. After the operation, aspirin (100 mg/kg) was dissolved in the drinking water for free ingestion of analgesia for no less than 3 days. The rats were divided into three groups: CGH, CGH/PDA@HAP, and control group (without any hydrogel).

2.4.2 Micro-CT analysis

To detect the new bone regenerated at defect sites, micro-CT (SCANCO, Switzerland) was employed for observation and quantitative analysis. Briefly, three-dimensional reconstruction of samples of each group was performed, and the bone volume/tissue volume (BV/TV) and trabecular separation (Tb.Sp) were automatically determined according to manufacturer's operational protocol for further evaluating the healing effect on bone defects of each group.

2.4.3 Histological evaluation

All samples were decalcified with 15% ethylenediaminetetraacetic acid (pH 7.2) for 4 weeks. The dehydrated specimens were embedded in paraffin and cut into 5-μm continuous sections for staining. The pathological sections of each group were evaluated by HE and Masson's trichrome staining, and the films were taken under a light microscope. Additionally, the major organs, including the heart, liver, spleen, lung, and kidney, were harvested for HE staining to evaluate the biosafety of the hydrogels.

2.5 Antibacterial assay

2.5.1 Bacterial strains and culture

Staphylococcus aureus (ATCC29213; Fenghui, China) and *Escherichia coli* (ATCC25922; Fenghui, China) were selected in this study. Briefly, each species was incubated with Luria-Bertani (LB) medium at 37°C under relative humidity above 90%. Based on the OD value measured at 600 nm in a UV spectrophotometer, the bacterial suspension was adjusted to 1×10^6 colony-forming units (CFU)/mL for subsequent experiments.

2.5.2 Planktonic bacteria inhibition assay

Time-kill curves construction and bacterial colony counting were applied to evaluate the bacterial inhibitory ability of the CGH/PDA@HAP and CGH hydrogels. Briefly, hydrogels (200 μL) were co-cultured with the bacterial suspension (500 μL) in 24-well plates for 12 h. The OD value was measured at 600 nm every 2 h for 12 h and time-kill curves were constructed. Subsequently, the suspension treated with the hydrogel materials was diluted to a certain ratio, and a 30 μL solution was evenly spread onto agar LB plates. The colonies were observed and the CFU was calculated after culturing for 48 h. *Staphylococcus aureus* and *E. coli* simply cultured in LB medium were set as the control groups.

2.5.3 Bacteria live/dead staining assay

The SYTO 9/PI (live/dead) staining kit (ThermoFisher, America) was used to determine the survival status of *S. aureus* and *E. coli* cultured on CGH/PDA@HAP and CGH hydrogels. Briefly, the bacteria were cultured as described above. SYTO 9 (2.5 mM) and PI (2.5 mM) were mixed to form a reacting solution, added onto the surface of the hydrogel, and then left to react in the dark for 15 min. Images were observed and captured with an inverted fluorescence microscope.

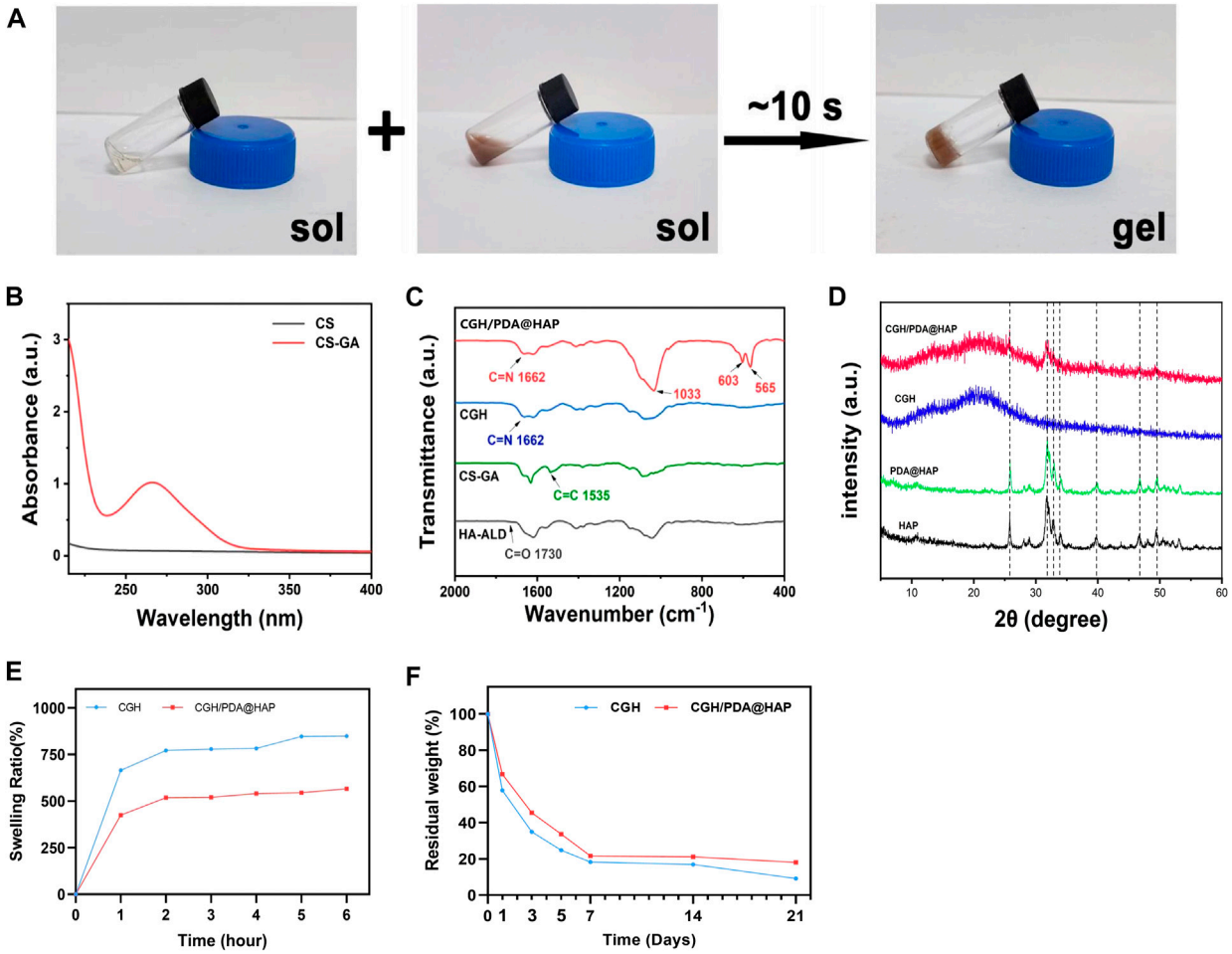

FIGURE 1
Preparation of the CGH/PDA@HAP hydrogel. **(A)** Optical image of the gelation process. **(B)** UV absorbance spectrum of CS-GA. **(C)** FTIR spectra. **(D)** XRD analysis. **(E)** Swelling ratio. **(F)** Enzymatic degradation.

2.5.4 Metabolic activity

The 3-(4,5-dimethylthiazol-2-yl)-2,5-diphenyltetrazolium bromide (MTT; Beyotime, China) assay was used to evaluate the biofilm activity of *S. aureus* and *E. coli* when co-cultured with the CGH and CGH/PDA@HAP hydrogels. Briefly, 0.4 mL MTT solution (0.5 mg/mL) (Beyotime, China) was added onto the hydrogel in a 24-well plate and incubated for 2 h at 37°C. Equal amounts of dimethyl sulfoxide was added to each well to dissolve the formaldehyde crystals after reacting in the dark. The MTT dye was transferred onto a new 96-well plate and the OD value was measured at 540 nm in a standard enzyme assay instrument.

2.6 Statistical analysis

Quantitative values are presented as mean ± standard deviation from at least three independent experiments and differences among groups were analyzed using one-way analysis of variance (GraphPad Prism 8.0.1 software) to assess statistical significance. $p < 0.05$ was considered statistically significant.

3 Results and discussion

3.1 Preparation of the CGH/PDA@HAP hydrogel

To overcome the problem of poor HAP dispersion, we modified the surface of HAP with PDA (PDA@HAP) to effectively improve its hydrophilicity, which is mainly achieved due to the large number of hydrophilic groups on the surface of PDA (Wu et al., 2019; Gao et al., 2022). The successful preparation of the PDA@HAP material was confirmed by the FTIR spectra (Supplementary Figure S1). Moreover, we synthesized CS-GA by the amidation reaction of CS and GA, which significantly improved the solubility of CS. The UV absorbance spectrum exhibited an obvious characteristic peak, demonstrating the successful preparation of CS-GA (Figure 1B). Aldehyde-modified HA (HA-ALD) was synthesized by oxidizing HA with periodate. H-NMR data further confirmed the successful synthesis of the CS-GA and HA-ALD, as shown in Supplementary Figures S2 and S3. We then added the PDA@HAP into the HA-ALD with ultrasonic stirring. We successfully synthesized the injective hydrogel by a Schiff-base reaction between the aldehyde-modified

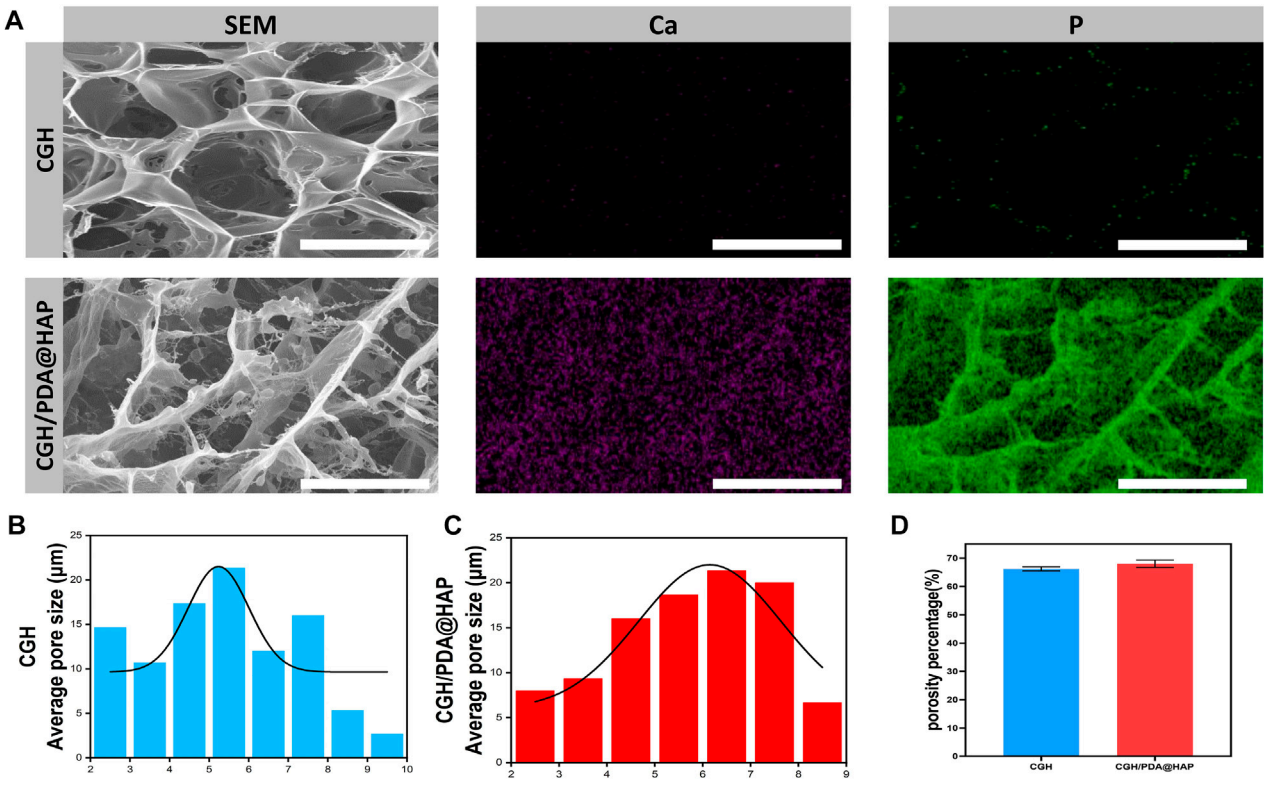

FIGURE 2
Cyro-SEM observation of the CGH and CGH/PDA@HAP hydrogels. **(A)** SEM images and elemental mapping. **(B)** Average pore size of the CGH hydrogel. **(C)** Average pore size of the CGH/PDA@HAP hydrogel. **(D)** Porosity percentage of the CGH and CGH/PDA@HAP hydrogels. Scale bar: 2.5 μm.

HA-ALD and the amino group of CS-GA. It provides a smart strategy to fill irregular defects and promote tissue healing (Pan et al., 2020; Zhang et al., 2022a). The sol-to-gel transformation process is shown in Figure 1A The successful synthesis of hydrogels occurred after the two solutions were homogeneously mixed at a volume ratio of 1:1 for 10 s. The FTIR spectra were measured to characterize the chemical structure of the composite hydrogel. As shown in Figure 1C new carbonyl peak of the acyl hydrazone bond appeared at 1662 cm^{-1}, indicating the Schiff binding between CS-GA and HA-ALD. The FTIR spectra of the CGH/PDA@HAP hydrogel also showed characteristic peaks of PDA@HAP at 565, 603, and 1033 cm^{-1}, demonstrating the successful introduction of PDA@HAP. Further, XRD was performed to analyze the composition of hydrogels. As shown in Figure 1D, the diffraction peak intensities of PDA@HAP were weaker than those of HAP, which indicate that the PDA was coated on the surface of HAP. The main peak of the CGH/PDA@HAP hydrogel is matched to that of HAP, which proves that HAP was present in the hydrogel.

Since the swelling ratio of materials is closely related to the behavior of cells and the effect of tissue healing, the swelling profiles of the CGH and CGH/PDA@HAP hydrogels were evaluated. As shown in Figure 1E, the freeze-dried hydrogels were quickly swelled at the first 1 h, then reached an equilibrium state. Both of the hydrogels exhibited a favorable ability of water uptake. In particular, the swelling ratio decreased through PDA@HAP introducing, proving that PDA grafting is an effective method to make hydrogel stable (Huang et al., 2022). Further, enzymatic degradation assay was performed to evaluate the degradability and stability of the CGH and CGH/PDA@HAP hydrogels in a simulated *in vivo* environment. As show in Figure 1F, the CGH and CGH/PDA@HAP hydrogels could degrade in the hyaluronidase solution, indicating the degradability of them. The long-term application of HA remains challenge due to the enzymatic degradation mediated by tissue (Ito et al., 2007). Previous study has been proved that HA was completely degraded in a hyaluronidase solution with a concentration of 10U/mL for 5 days (Lin et al., 2015). The results in this study indicated that the CGH and CGH/PDA@HAP hydrogels remains more than 25% of residual weight on 5 days even in a relative high concentration of hyaluronidase solution (900U/mL). It can be attributed to that the Schiff-base triggers the crosslinking reaction, thus prolonging the degradation time (Yuan et al., 2017). This is consistent with previous study (Ma et al., 2021).

The microstructure of the CGH/PDA@HAP hydrogel was also observed by Cyro-SEM. As shown in Figure 2A, the CGH and CGH/PDA@HAP hydrogel had uniform porous microstructures, indicating the three-dimensional mesh structure of these hydrogels. As shown in Figures 2B–D, the addition of PDA@HAP has no obvious effect on the pore size and porosity percentage of the hydrogel. In particular, the interconnected porous structures could mimic the histological morphology of the native bone, thus increasing the osteo-conductivity (Zhao et al., 2020). This is essential to promote proliferation and differentiation of BMSC (Yi et al., 2016). Moreover, elemental mapping (Figure 2A)

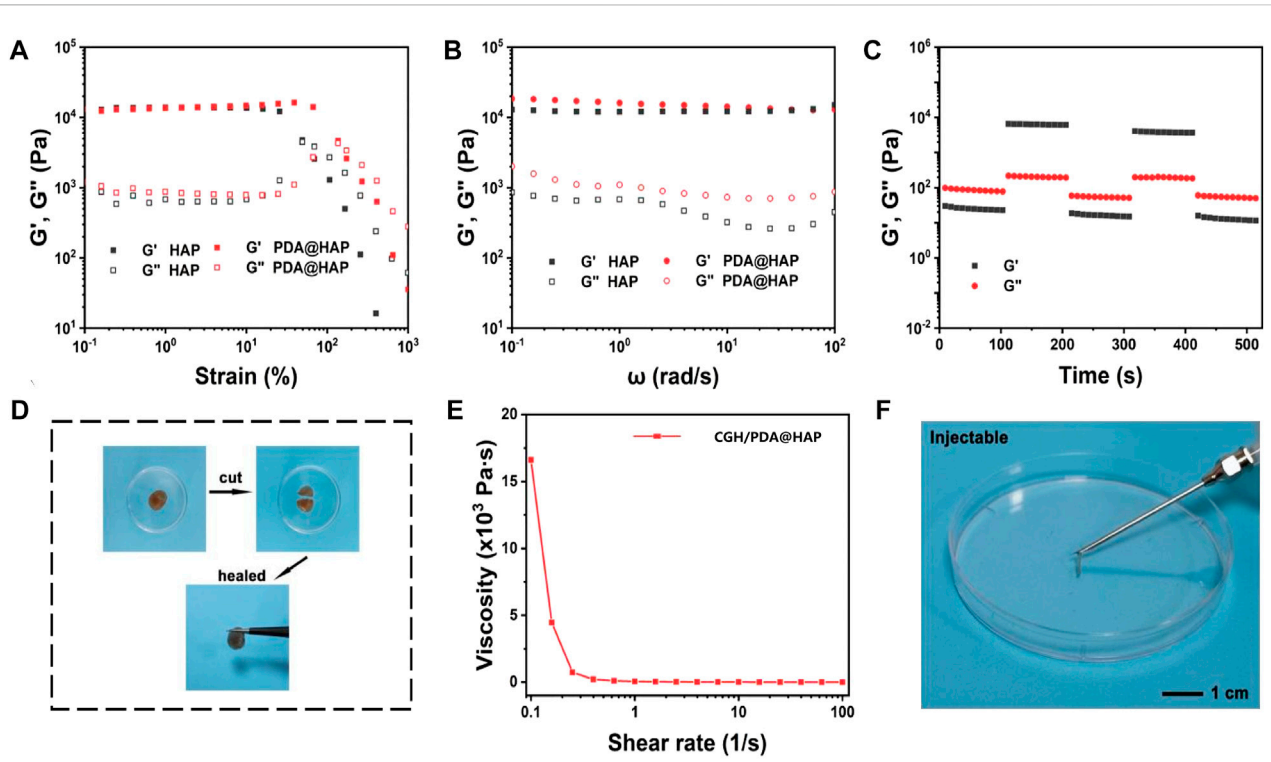

FIGURE 3
Characterization of the CGH/PDA@HAP hydrogel. **(A)** Rheological strain sweeps. **(B)** Rheological frequency sweeps. **(C)** Step strain sweeps. **(D)** Optical images of the self-healing phenomenon. **(E)** Viscosity as a function of shear rate. **(F)** Optical images of the injectable property of the hydrogel.

demonstrated that the distribution of HAP was evenly on the CGH/PDA@HAP hydrogel through PDA modification, thus overcoming the disadvantage of aggregation (Gao et al., 2022).

3.2 Characterization of the CGH/PDA@HAP hydrogel

The oscillatory rheology of the CGH/PDA@HAP hydrogel was characterized to further investigate the stability and mechanical behaviors. First, we prepared the nano-HAP–loaded CGH (CGH/HAP) hydrogel as a control. As shown in Figure 3A, The CGH/HAP and CGH/PDA@HAP hydrogels exhibited a similar elastic modulus, suggesting that the introduction of PDA had little effect on the mechanical strength. As shown in Figure 3B, the storage modulus (G') was consistently larger than the loss modulus (G'') when the angular frequency ranged from 0.1 to 100 rad/s, confirming the elastic behavior of the CGH/HAP and CGH/PDA@HAP hydrogels. Moreover, rheological recovery and macroscopic self-healing behavior tests were conducted to estimate the self-healing properties of the CGH/PDA@HAP hydrogel. Based on the strain amplitude sweep measurement, no obvious change of the modulus was observed even after five cycles, demonstrating the outstanding self-healing ability of the CGH/PDA@HAP hydrogel (Figure 3C). We also cut the CGH/PDA@HAP hydrogel into two parts, which healed within a short time (Figure 3D), further indicating the self-healing of the CGH/PDA@HAP hydrogel from a macro perspective.

The dependence of viscosity on shear rate was explored to investigate the injectability of CGH/PDA@HAP hydrogel. As shown in Figure 3E, the viscosity of the hydrogel decreased with the shear rate increased, confirming the CGH/PDA@HAP had the ability to shear thinning. Therefore, the CGH/PDA@HAP hydrogel can be extruded through a syringe and maintain a stable gel state after removing the shear stress, further demonstrating the injectability of the CGH/PDA@HAP hydrogel.

3.3 Biocompatibility evaluation

To determine whether the concentration of the PDA@HAP in hydrogel could affect the viability of BMSC, three hydrogels containing different mass fractions (0.5% wt, 1% wt and 2% wt) were prepared. As shown in Figure 4A, most of the BMSCs survived and were capable of migration and adhesion in each group, suggesting that the hydrogel scaffolds have minimal cytotoxicity. Notably, BMSCs cultured with the hydrogel containing 1% wt PDA@HAP exhibited higher metabolic rates than the other groups (Figure 4B). Thus, the CGH/PDA@HAP-1%wt was selected for the subsequent studies.

It is generally acknowledged that the advantage of the three-dimensional porous structure of a hydrogel is to guide the orderly migration and proliferation of cells (Zhang et al., 2021c; Zhou et al., 2022). Compared with traditional two-dimensional culture, this three-dimensional culture structure can establish favorable conditions for the growth of cells in a given space, which lays a good foundation for osteogenic differentiation (Shanbhag et al., 2021; Xu et al., 2021; Zhu et al., 2022). As reported in previous studies, a PDA-modified material has an increased surface positive

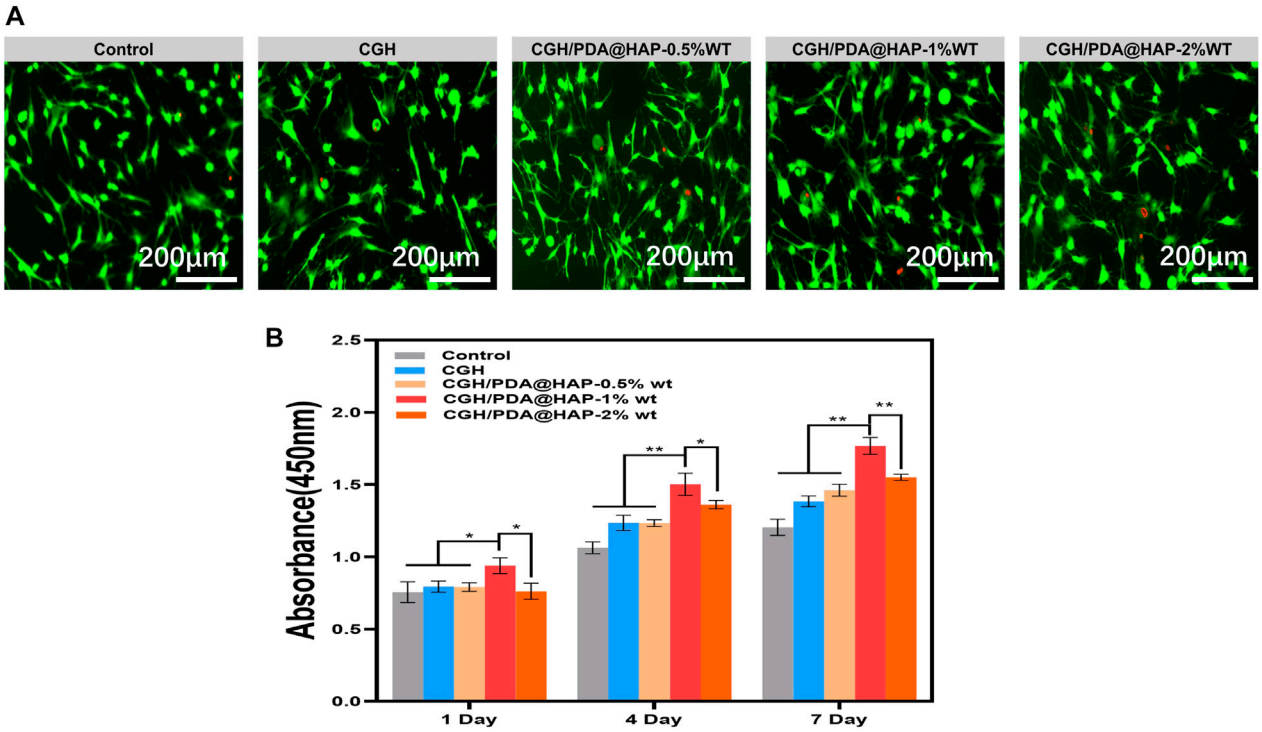

FIGURE 4
Biocompatibility of CGH and CGH/PDA@HAP hydrogel. **(A)** Live/Dead cell staining. **(B)** CCK-8 assay. (*indicates significant differences; $*p < 0.05$, $**p < 0.01$).

charge, which makes it easier to bind to integrin receptors on the surface of cell membranes and attract cells for attachment on the material (Yu et al., 2021; Im et al., 2022). Moreover, the hydrophilicity of the material itself increases after PDA grafting, which offers another advantage to promote cell attachment (Wu et al., 2019; Zhang et al., 2020). Given these properties, the CGH/PDA@HAP hydrogel was verified to be able to support BMSC adhesion and proliferation, which are key factors contributing to osteogenesis.

3.4 Osteogenic differentiation effect of the CGH/PDA@HAP hydrogel *in vitro*

To explore the osteogenic differentiation effect of the CGH/PDA@HAP hydrogel on BMSCs, ALP activity assessment and ARS were performed. As shown in Figures 5A, B, ALP activity was significantly increased in the CGH/PDA@HAP group compared with that of the control and CGH groups when BMSCs were treated for 14 days. After 21 days of treatment, orange-red calcium nodules formed in the extracellular matrix of BMSCs in all groups. However, the number and area of orange-red nodules in the CGH/PDA@HAP group were significantly higher than those in the control and CGH groups (Figure 5C). Corresponding quantitative analysis of ARS demonstrated the same trend and was consistent with the staining results (Figure 5D). It is generally acknowledged that the hydrogel scaffolds are with the remarkable drug loading characteristics and capable to form a slow-release effect in the injured site, ensuring a long-term and effective treatment to promote tissue healing (Zhang et al., 2021b; Wang et al., 2023). In this study, Ca^{2+}, as well as PO_4^{3-}, were confirmed to be released from the CGH/PDA@HAP hydrogel (Supplementary Figure S4). These results may reflect the fact that the PDA@HAP in the hydrogel can continuously release Ca^{2+}, which can provide a favorable chemical environment for the differentiation of BMSCs into osteoblasts (Ciobanu et al., 2018).

To further evaluate the osteogenic differentiation effect of CGH/PDA@HAP, RT-qPCR was employed to detect the expression of several osteogenesis-related genes, including *Runx2, Alp*, and *Ocn*. As shown in Figures 5E–J, the expression of these genes in the CGH/PDA@HAP group was notably upregulated compared with that in the control and CGH groups, which was consistent with the staining results summarized above. Although HAP can improve the osteogenic conduction and induction of a hydrogel scaffold, its aggregation may cause a high ion concentration in the microenvironment, thereby impairing the proliferation and osteogenic differentiation of BMSCs (Pan et al., 2020; Xu et al., 2020). Therefore, we adopted the strategy of modifying HAP with PDA to evenly distribute the HAP in the hydrogel, preventing the production of excessively high concentrations of ions to provide a favorable condition for osteoblast differentiation (Gao et al., 2022). Moreover, Ca^{2+} can further promote the osteogenic differentiation of BMSCs through the activation of calcium channels on the surface of BMSCs by endogenous electrical signals, thus increasing the intracellular Ca^{2+} concentration (Ciobanu et al., 2018). These results demonstrated that the effect of inducing osteogenic differentiation of BMSC was

10.3389/fbioe.2023.1162202

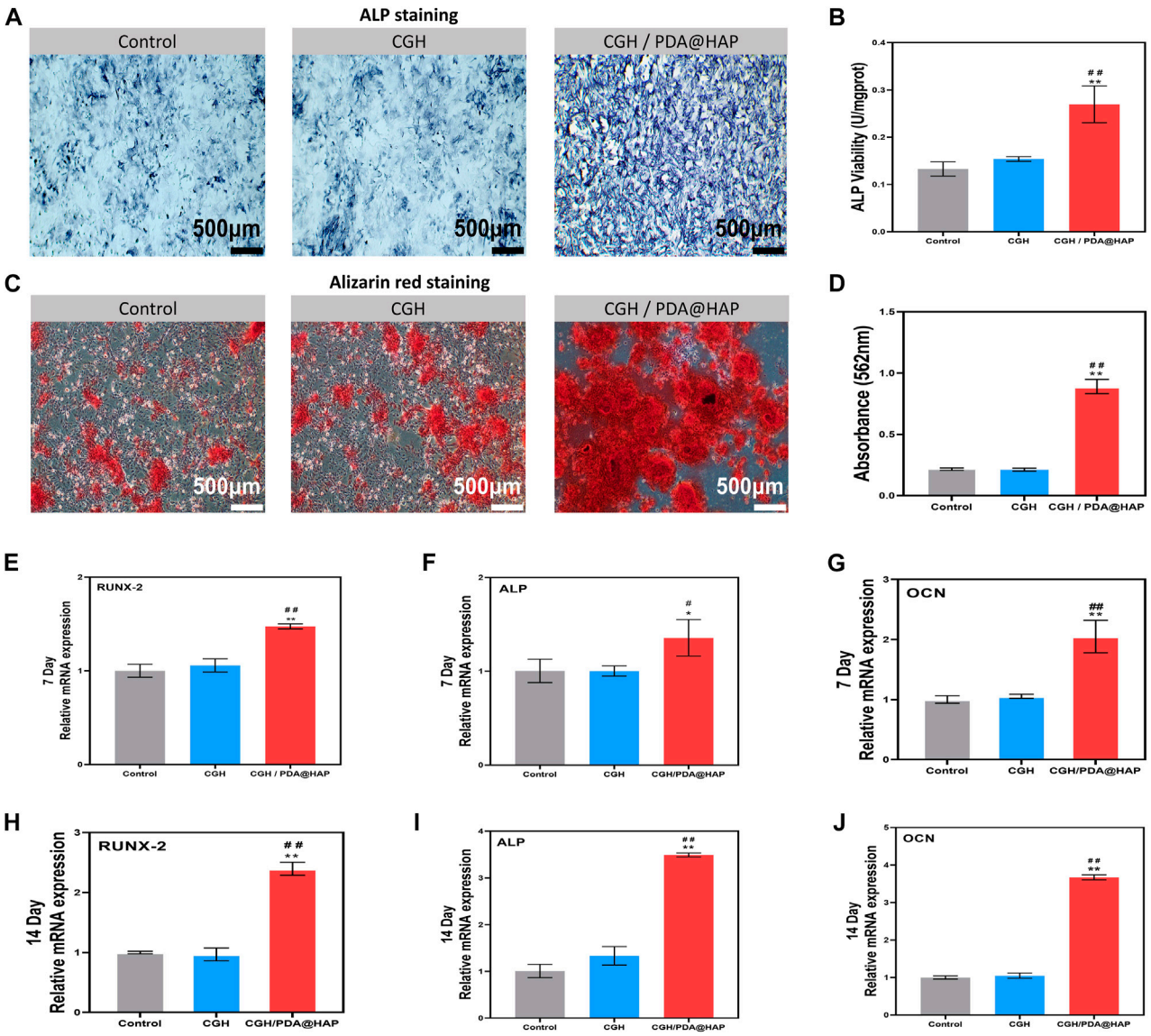

FIGURE 5
Osteogenic differentiation of BMSCs. **(A)** ALP staining of BMSCs cultured in osteogenic medium supplemented with extracts of various materials for 14 days. **(B)** Quantification of ALP activity of BMSCs cultured in osteogenic medium supplemented with extracts of various materials. **(C)** ARS assay of BMSCs cultured with osteogenic medium supplemented with extracts of various materials for 21 days. **(D)** Quantitative analysis of **(C)**. **(E,F and G)** Expression of osteoblastic genes of BMSCs after culture for 7 days. **(H,I and J)** Expression of osteoblastic genes of BMSCs cultured for 14 days. (*indicates significant differences compared with the control group and # indicates significant differences compared with the CGH group; *$p < 0.05$, **$p < 0.01$, #$p < 0.05$, ##$p < 0.01$).

enhanced when introducing PDA@HAP into the hydrogel, and the expression of osteogenic-related genes was upregulated, especially at 14 days. Moreover, there was no inhibition of cell proliferation and differentiation due to HAP aggregation.

3.5 Effect of the CGH/PDA@HAP hydrogel on bone healing *in vivo*

To evaluate the bone healing effect of the CGH/PDA@HAP hydrogel *in vivo*, a 5-mm-diameter critical cranial defect was created in SD rats to study the osteogenic effect. At 4 weeks and 8 weeks post-surgery, micro-CT was employed to assess the healing of the cranium defect. As shown in Figure 6A, bone healing in the CGH/PDA@HAP group was more obvious compared to that observed in the control and CGH groups at both 4 and 8 weeks post-surgery. At 8 weeks after implantation, the CGH/PDA@HAP hydrogel induced significant new bone formation both in the periphery and in the center of the defect. Moreover, the BV/TV was remarkably increased in the CGH/PDA@HAP group compared with that of the control and CGH groups, whereas the opposite result was found for the Tb. Sp measurement (Figures

10.3389/fbioe.2023.1162202

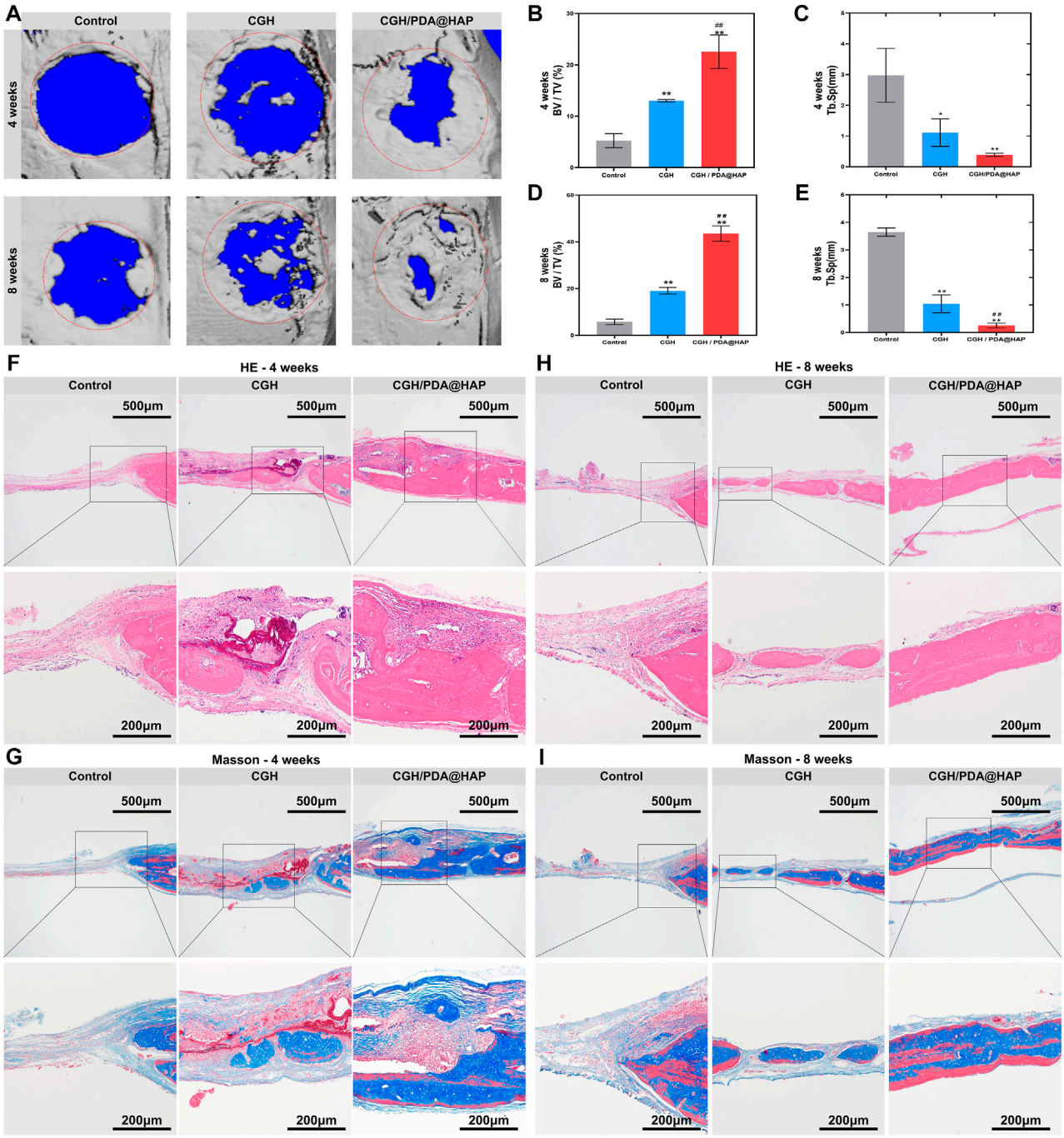

FIGURE 6
The CGH/PDA@HAP hydrogel promotes bone regeneration *in vivo*. **(A)** Three-dimensional reconstructed micro-CT images of rat cranial bone defects at 4 and 8 weeks after injecting hydrogel materials. Red circles illustrate the original defect area and blue parts in the images represent the background. Gray areas in red circles indicate new bone formation. **(B)** BV/TV of the defect area of each group at 4 weeks post-surgery. **(C)** Tb. Sp of the newly formed bone of each group at 4 weeks post-surgery. **(D)** BV/TV of the defect area of each group at 8 weeks post-surgery. **(E)** Tb. Sp of the newly formed bone of each group at 8 weeks post-surgery. **(F)** HE staining images of each group at 4 weeks post-surgery. **(G)** Masson's trichrome staining images of each group at 4 weeks post-surgery. **(H)** HE staining images of each group at 8 weeks post-surgery. **(I)** Masson's trichrome staining images of each group at 8 weeks post-surgery. (*indicates significant differences compared with the control group and # indicates significant differences compared with the CGH group; $*p < 0.05$, $**p < 0.01$, $\#\#p < 0.01$).

6B–E). These findings suggested that the CGH/PDA@HAP hydrogel has improved osteogenic effects *in vivo*, consistent with the results found *in vitro*.

This effect can be attributed to the fact that the differentiation of BMSCs into osteoblasts is closely related to the structure of scaffold materials (Zhang et al., 2021c). The

10.3389/fbioe.2023.1162202

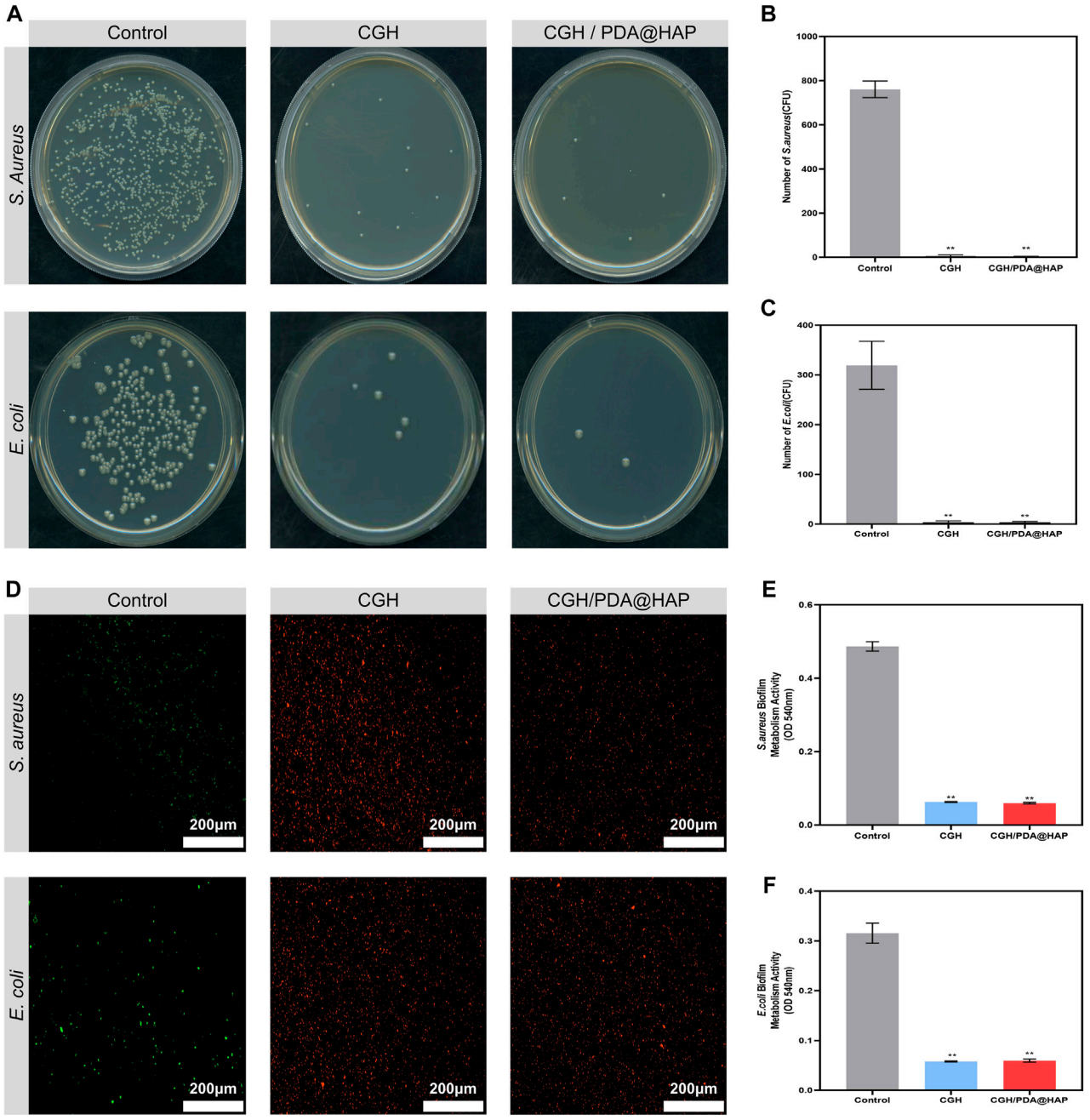

FIGURE 7
Antibacterial properties of the CGH/PDA@HAP and CGH hydrogels against *Staphylococcus aureus* and *Escherichia coli*. **(A)** Typical images of *Staphylococcus aureus* and *Escherichia coli* bacterial colonies after culture with CGH/PDA@HAP and CGH hydrogels. **(B,C)** Quantitative analysis of **(A)**. **(D)** Live/dead bacteria staining to evaluate the capability of CGH/PDA@HAP and CGH hydrogels to prevent adhesion of *Staphylococcus aureus* and *Escherichia coli*. **(E,F)** MTT assay to assess the effects of CGH/PDA@HAP and CGH hydrogels on the metabolic activity of *Staphylococcus aureus* and *Escherichia coli* biofilms. (*indicates significant differences compared with the control group; **$p < 0.01$).

three-dimensional porous structure of the hydrogel can not only recruit more cells to the defect area, but its morphological regulatory function also plays an essential role in the osteogenic differentiation of BMSCs (Xu et al., 2021; Zhu et al., 2022). The *in vivo* three-dimensional culture conditions created by the hydrogel not only facilitate the migration and proliferation of BMSCs through the paracrine secretion of exosomes via activation of the HMGB1/AKT pathway, but also synergize with osteogenically active substances in the system to accelerate osteogenic differentiation (Matsumoto

et al., 2011; Oliveros et al., 2021; Ren et al., 2021; Tavakol et al., 2021). More importantly, the catechol group on the surface of PDA-modified scaffolds can effectively anchor calcium ions in HAP, which stabilizes the local calcium concentration and induces the osteogenic differentiation of BMSCs (Gao et al., 2022). On this basis, the formation of hydroxyapatite on the scaffold surface can be promoted to accelerate the process of osseointegration (Matsumoto et al., 2011; Wu et al., 2011; Wu et al., 2019; Zhang et al., 2021a).

Furthermore, HE staining and Masson's trichrome staining were used to verify the effect of the CGH/PDA@HAP hydrogel on bone defect healing at the histology level. As shown in Figures 6F,H large amount of newly regenerated bone was induced from the margin to the central area of the defect in the CGH/PDA@HAP group, whereas new bone formation was hardly detected in the control group. Masson's trichrome staining images showed the same tendency as found for the HE staining results (Figures 6G,I). In addition, no obvious pathological changes were observed in the HE-staining images of the major organs, including the heart, liver, spleen, lung, and kidney, suggesting that the CGH/PDA@HAP hydrogel has good biological safety *in vivo* (Supplementary Figure S5). The Cyro-SEM images further proved that the CGH/PDA@HAP hydrogel has a three-dimensional porous structure, which is a key feature to endow the hydrogel with excellent osteogenic conduction for directing BMSC migration toward the center of the bone defect. Moreover, PDA enhanced the bioactivity of the hydrogel surface and made it easier to recruit cells, laying a solid foundation for bone regeneration (Gao et al., 2022). Significantly, the HAP in the hydrogel can effectively induce the osteogenic differentiation of BMSCs, promoting mineralization of the extracellular matrix to form mature new bone (Zhao et al., 2020). These findings are thus consistent with the results of the *in vitro* experiments. In summary, the CGH/PDA@HAP hydrogel recruited cells to the center of the defect and regulated the behavior of cells in a programmed manner at both the internal morphology and the active substance, thus achieving a satisfactory therapeutic effect of bone healing.

3.6 Antibacterial effect *in vitro*

S. aureus and *E. coli* were used to study the antibacterial effect of the CGH and CGH/PDA@HAP hydrogels on Gram-negative and Gram-positive bacteria, respectively. To evaluate the inhibiting effect of the CGH and CGH/PDA@HAP hydrogels on planktonic bacteria, time-kill curves were constructed. As shown in Supplementary Figure S7, the growth curves of *S. aureus* and *E. coli* exhibited an increasing trend within 12 h in the control group, whereas growth was maintained at a stable level in the CGH and CGH/PDA@HAP groups. To further investigate these effects, the CFU count was quantified. Accordingly, colony formation was significantly inhibited when the bacteria were cultured with CGH and CGH/PDA@HAP hydrogels (Figure 7A). Quantitative analysis demonstrated that the inhibitory rate of the CGH hydrogel against *S. aureus* and *E. coli* was above 90% (Figures 7B, C). To further investigate the inhibition of *S. aureus* and *E. coli* biofilm formation, bacteria live and dead staining was used, in which live bacteria are stained with green fluorescence while dead bacteria are stained red. As shown in Figure 7D, *S. aureus* and *E. coli* in the CGH and CGH/PDA@HAP groups emitted a strong red signal, indicating that most of the bacteria had been killed on the hydrogels. Moreover, the MTT assay showed that the metabolic activity of *S. aureus* and *E. coli* biofilms significantly decreased in both the CGH and CGH/PDA@HAP groups compared with that of the control group (Figures 7E, F).

Staphylococcus aureus is considered the main pathogen of postoperative infection in open bone defect cases, which is attributed to the fact that it can induce the differentiation of osteoclasts via the secretion of proinflammatory factors and proteins, either directly or indirectly (Tong et al., 2022). Moreover, intense inflammatory reactions initiated by infection lead to the release of inflammatory factors, which inevitably increases apoptosis and inhibits the osteogenic differentiation of BMSCs (Xu et al., 2016). Our results demonstrated that the CGH/PDA@HAP hydrogel represents a scaffold with broad-spectrum antibacterial activity that could inhibit *S. aureus*, thereby showing potential to prevent infection and effectively avoiding the negative effects of inflammation on bone regeneration.

Notably, GA can penetrate the bacterial cell wall to change osmotic pressure and inhibit the bacterial respiratory chain, thus reducing the drug resistance (Shi et al., 2021; Wei et al., 2023). A previous study demonstrated that GA can effectively decrease metabolic activity and destroy the biofilms of *S. aureus* and *E. coli* (Sun et al., 2022). In this study, the CGH and CGH/PDA@HAP hydrogels successfully inhibited *S. aureus* and *E. coli,* preventing bacterial colonization and biofilm formation, and reducing metabolic activity. Therefore, the inherent antibacterial properties of hydrogel scaffolds can be improved through GA grafting even without loading antibacterial substances, which overcomes the lack of antibacterial properties of traditional bone scaffolds.

4 Conclusion

We developed a mussel-inspired mineral CGH/PDA@HAP hydrogel through the assembly of PDA@HAP, CS, GA, and HA, which exhibited desirable properties, including a porous structure, tunable mechanical property, injectability, as well as self-healing ability. It is expected that PDA enhances the bioactivity of the hydrogel and plays a positive role in bone formation in collaboration with HAP. Moreover, GA modification was used to improve the antibacterial properties of the hydrogel so as to promote bone regeneration while preventing infection. Based on this concept, we have proven that the CGH/PDA@HAP hydrogel has superior performance for promoting the adhesion, proliferation, and osteogenic differentiation of BMSCs *in vitro*. Notably, animal experiments further proved that the CGH/PDA@HAP hydrogel could meet the demand of promoting bone tissue regeneration and reconstruction when the defect reaches a certain critical size that prevents regeneration. In addition, GA grafting greatly

improved the antibacterial performance of the hydrogel system, which inhibited the growth, adhesion, colonization, and biofilm formation of *S. aureus* and *E. coli in vitro*. In conclusion, our study provides a new strategy for treating open bone defects and preventing the occurrence of infection during bone healing.

Data availability statement

The original contributions presented in the study are included in the article/Supplementary Material, further inquiries can be directed to the corresponding authors.

Ethics statement

The animal study was reviewed and approved by Institutional Animal Care and Use Committee, Jilin University.

Author contributions

Methodology and experimentation, YP and LG; writing and original draft preparation, YP; review and editing, YZ and RN; project administration, SZ and QL. All authors contributed to the article and approved the submitted version.

Funding

This work was supported by the National Key R&D Program of China (2021YFC2400405).

Conflict of interest

The authors declare that the research was conducted in the absence of any commercial or financial relationships that could be construed as a potential conflict of interest.

Publisher's note

All claims expressed in this article are solely those of the authors and do not necessarily represent those of their affiliated organizations, or those of the publisher, the editors and the reviewers. Any product that may be evaluated in this article, or claim that may be made by its manufacturer, is not guaranteed or endorsed by the publisher.

Supplementary material

The Supplementary Material for this article can be found online at: https://www.frontiersin.org/articles/10.3389/fbioe.2023.1162202/full#supplementary-material

References

Asha, A. B., Chen, Y., and Narain, R. (2022). Bioinspired dopamine and zwitterionic polymers for non-fouling surface engineering. *Chem. Soc. Rev.* 50, 11668–11683. doi:10.1039/d1cs00658d

Chen, C., Zhou, P., Huang, C., Zeng, R., Yang, L., Han, Z., et al. (2021). Photothermal-promoted multi-functional dual network polysaccharide hydrogel adhesive for infected and susceptible wound healing. *Carbohydr. Polym.* 273, 118557. doi:10.1016/j.carbpol.2021.118557

Chen, Y., Zhang, F., Fu, Q., Liu, Y., Wang, Z., and Qi, N. (2016). *In vitro* proliferation and osteogenic differentiation of human dental pulp stem cells in injectable thermosensitive chitosan/β-glycerophosphate/hydroxyapatite hydrogel. *J. Biomater. Appl.* 31, 317–327. doi:10.1177/0885328216661566

Ciobanu, F., Golzio, M., Kovacs, E., and Teissié, J. (2018). Control by low levels of calcium of mammalian cell membrane electropermeabilization. *J. Membr. Biol.* 251, 221–228. doi:10.1007/s00232-017-9981-y

Cui, J., Yan, Y., Such, G. K., Liang, K., Ochs, C. J., Postma, A., et al. (2012). Immobilization and intracellular delivery of an anticancer drug using mussel-inspired polydopamine capsules. *Biomacromolecules* 13, 2225–2228. doi:10.1021/bm300835r

Gao, F., Xu, Z., Liang, Q., Liu, B., Li, H., Wu, Y., et al. (2018). Direct 3D printing of high strength biohybrid gradient hydrogel scaffolds for efficient repair of osteochondral defect. *Adv. Funct. Mat.* 28, 1706644. doi:10.1002/adfm.201706644

Gao, F., Zeng, D., Liu, H., Qin, R., Zhang, J., Chen, Y., et al. (2022). Porous cellulose microspheres coated in one step with a polydopamine suspension of hydroxyapatite for bone tissue engineering. *Cellulose* 29, 1955–1967. doi:10.1007/s10570-021-04395-4

Guan, L., Yan, S., Liu, X., Li, X., and Gao, G. (2019). Wearable strain sensors based on casein-driven tough, adhesive and anti-freezing hydrogels for monitoring human-motion. *J. Mat. Chem. B* 7, 5230–5236. doi:10.1039/c9tb01340g

Han, L., Li, P., Tang, P., Wang, X., Zhou, T., Wang, K., et al. (2019). Mussel-inspired cryogels for promoting wound regeneration through photobiostimulation, modulating inflammatory responses and suppressing bacterial invasion. *Nanoscale* 29, 15846–15861. doi:10.1039/c9nr03095f

Huang, B., Chen, M., Tian, J., Zhang, Y., Dai, Z., Li, J., et al. (2022). Oxygen-carrying and antibacterial fluorinated nano-hydroxyapatite incorporated hydrogels for enhanced bone regeneration. *Adv. Healthc. Mat.* 11, 2102540. doi:10.1002/adhm.202102540

Im, S., Choe, G., Seok, J. M., Yeo, S. J., Lee, J. H., Kim, W. D., et al. (2022). An osteogenic bioink composed of alginate, cellulose nanofibrils, and polydopamine nanoparticles for 3D bioprinting and bone tissue engineering. *Int. J. Biol. Macromol.* 30, 520–529. doi:10.1016/j.ijbiomac.2022.02.012

Ito, T., Yeo, Y., Highley, C. B., Bellas, E., Benitez, C. A., and Kohane, D. S. (2007). The prevention of peritoneal adhesions by *in situ* cross-linking hydrogels of hyaluronic acid and cellulose derivatives. *Biomaterials* 28, 975–983. doi:10.1016/j.biomaterials.2006.10.021

Jiang, L., Li, Y., Xiong, C., Su, S., and Ding, H. (2017). Preparation and properties of bamboo fiber/nano-hydroxyapatite/poly(lactic-co-glycolic) composite scaffold for bone tissue engineering. *Acs. Appl. Mat.* 9, 4890–4897. doi:10.1021/acsami.6b15032

Lee, J. S., Baek, S. D., Venkatesan, J., Bhatnagar, I., Chang, H. K., Kim, H. T., et al. (2014). *In vivo* study of chitosan-natural nano hydroxyapatite scaffolds for bone tissue regeneration. *Int. J. Biol. Macromol.* 67, 360–366. doi:10.1016/j.ijbiomac.2014.03.053

Leng, Q., Chen, L., and Lv, Y. (2020). RNA-Based scaffolds for bone regeneration: Application and mechanisms of mRNA, miRNA and siRNA. *Theranostics* 10, 3190–3205. doi:10.7150/thno.42640

Li, Y., Yang, L., Hou, Y., Zhang, Z., Chen, M., Wang, M., et al. (2022). Polydopamine-mediated graphene oxide and nanohydroxyapatite-incorporated conductive scaffold with an immunomodulatory ability accelerates periodontal bone regeneration in diabetes. *Bioact. Mat.* 18, 213–227. doi:10.1016/j.bioactmat.2022.03.021

Lin, C., Peng, H., Chen, M., Sun, J., Liu, T., and Chen, M. (2015). *In situ* forming hydrogel composed of hyaluronate and polygalacturonic acid for prevention of peridural fibrosis. *J. Mat. Sci. Mat. Med.* 26, 168. doi:10.1007/s10856-015-5478-3

Liu, L., Shi, J., Sun, X., Zhang, Y., Qin, J., Peng, S., et al. (2022). Thermo-responsive hydrogel-supported antibacterial material with persistent photocatalytic activity for continuous sterilization and wound healing. *Compos. Part. B-Eng.* 229, 109459. doi:10.1016/j.compositesb.2021.109459

Liu, Z., Tang, M., Zhao, J., Chai, R., and Kang, J. (2018). Looking into the future: Toward advanced 3D biomaterials for stem-cell-based regenerative medicine. *Adv. Mat.* 30, e1705388. doi:10.1002/adma.201705388

Lüthje, F. L., Jensen, L. K., Jensen, H. E., and Skovgaard, K. (2020). The inflammatory response to bone infection-a review based on animal models and human patients. *APMIS* 128, 275–286. doi:10.1111/apm.13027

Ma, X., Yang, R., Kanaparedu, P. C., and Chi, B. (2021). Injectable hyaluronic acid/poly(γ-glutamic acid) hydrogel with step-by-step tunable properties for soft tissue engineering. *Chin. J. Polym. Sci.* 39, 957–965. doi:10.1007/s10118-021-2558-3

Matsumoto, T., Mizuno, A., Kashiwagi, M., Yoshida, S. S., Sasaki, J. I., and Nakano, T. (2011). Cell-based fabrication of organic/inorganic composite gel material. *Materials* 4, 327–338. doi:10.3390/ma4010327

Oliveros, A. L., Kingham, P. J., Lammi, M. J., Wiberg, M., and Kelk, P. (2021). Three-dimensional osteogenic differentiation of bone marrow mesenchymal stem cells promotes matrix metallopeptidase 13 (MMP13) expression in type I collagen hydrogels. *Int. J. Mol. Sci.* 22, 13594. doi:10.3390/ijms222413594

Pan, Y., Zhao, Y., Kuang, R., Liu, H., Sun, D., Mao, T., et al. (2020). Injectable hydrogel-loaded nano-hydroxyapatite that improves bone regeneration and alveolar ridge promotion. *Mat. Sci. Eng. C* 116, 111158. doi:10.1016/j.msec.2020.111158

Park, J., Brust, T. F., Lee, H. J., Lee, S. C., Watts, V. J., and Yeo, Y. (2014). Polydopamine-based simple and versatile surface modification of polymeric nano drug carriers. *Acs. Nano.* 8, 3347–3356. doi:10.1021/nn405809c

Peng, S., Meng, H., Ouyang, Y., and Chang, J. (2014). Nanoporous magnetic cellulose-chitosan composite microspheres: Preparation, characterization, and application for Cu(II) adsorption. *Ind. Eng. Chem. Res.* 53, 2106–2113. doi:10.1021/ie402855t

Ren, S., Tang, X., Liu, L., Meng, F., Yang, X., Li, N., et al. (2022). Reinforced blood-derived protein hydrogels enable dual-level regulation of bio-physiochemical microenvironments for personalized bone regeneration with remarkable enhanced efficacy. *Nano. Lett.* 22, 3904–3913. doi:10.1021/acs.nanolett.2c00057

Ren, Y., Zhang, H., Wang, Y., Du, B., Yang, J., Liu, L., et al. (2021). Hyaluronic acid hydrogel with adjustable stiffness for mesenchymal stem cell 3D culture via related molecular mechanisms to maintain stemness and induce cartilage differentiation. *Acs. Appl. Bio. Mat.* 4, 2601–2613. doi:10.1021/acsabm.0c01591

Sahiner, N., Sagbas, S., Sahiner, M., Silan, C., Aktas, N., and Turk, M. (2016). Biocompatible and biodegradable poly(tannic acid) hydrogel with antimicrobial and antioxidant properties. *Int. J. Biol. Macromol.* 82, 150–159. doi:10.1016/j.ijbiomac.2015.10.057

Shanbhag, S., Suliman, S., Mohamed-Ahmed, S., Kampleitner, C., Hassan, M. N., Heimel, P., et al. (2021). Bone regeneration in rat calvarial defects using dissociated or spheroid mesenchymal stromal cells in scaffold-hydrogel constructs. *Stem. Cell. Res. Ther.* 12, 575. doi:10.1186/s13287-021-02642-w

Shi, Y. G., Zhang, R. R., Zhu, C. M., Xu, M. F., Gu, Q., Ettelaie, R., et al. (2021). Antimicrobial mechanism of alkyl gallates against *Escherichia coli* and *Staphylococcus aureus* and its combined effect with electrospun nanofibers on Chinese Taihu icefish preservation. *Food. Chem.* 346, 128949. doi:10.1016/j.foodchem.2020.128949

Sun, C., Zeng, X., Zheng, S., Wang, Y., Li, Z., Zhang, H., et al. (2022). Bio-adhesive catechol-modified chitosan wound healing hydrogel dressings through glow discharge plasma technique. *Chem. Eng. J.* 427, 130843. doi:10.1016/j.cej.2021.130843

Sun, S., Mao, L. B., Lei, Z., Yu, S. H., and Cölfen, H. (2016). Hydrogels from amorphous calcium carbonate and polyacrylic acid: Bio-inspired materials for "mineral plastics". *Angew. Chem. Int. Ed. Engl.* 55, 11765–11769. doi:10.1002/anie.201602849

Tavakol, D. N., Bonini, F., Tratwal, J., Genta, M., Brefie-Guth, J., Braschler, T., et al. (2021). Cryogel-based injectable 3D microcarrier co-culture for support of hematopoietic progenitor niches. *Curr. Protoc.* 1, e275. doi:10.1002/cpz1.275

Tong, Z., Chen, Z., Li, Z., Xie, Z., and Zhang, H. (2022). Mechanisms of promoting the differentiation and bone resorption function of osteoclasts by *Staphylococcus aureus* infection. *Int. J. Med. Microbiol.* 312, 151568. doi:10.1016/j.ijmm.2022.151568

Wan, Z., Dong, Q. Y., Liu, Y. S., Zhang, X., Zhang, P., Lv, L. W., et al. (2022). Programmed biomolecule delivery orchestrate programmed biomolecule delivery orchestrate bone tissue regeneration via MSC recruitment and epigenetic modulation. *Chem. Eng. J.* 438, 135518. doi:10.1016/j.cej.2022.135518

Wang, F., Liu, S., Ren, C., Xiang, S., Li, D., Hao, X., et al. (2021b). Construction of hollow polydopamine nanoparticle based drug sustainable release system and its application in bone regeneration. *Int. J. Oral. Sci.* 13, 27. doi:10.1038/s41368-021-00132-6

Wang, F., Liu, Y., Qiu, X., Fei, H., Liu, W., and Yuan, K. (2021a). Effect of anti-infective reconstituted bone xenograft combined with external fixator on serum CRP and PCT levels and prognosis of patients with bone infection after lower extremity long bone trauma. *Evid. Based. Complement. Altern. Med.* 30, 5979514. doi:10.1155/2021/5979514

Wang, N., Qi, D., Liu, L., Zhu, Y., Liu, H., and Zhu, S. (2022). Fabrication of *in situ* grown hydroxyapatite nanoparticles modified porous polyetheretherketone matrix composites to promote osteointegration and enhance bone repair. *Front. Bioeng. Biotechnol.* 10, 831288. doi:10.3389/fbioe.2022.831288

Wang, Y., Zhu, L., Wei, L., Zhou, Y., Yang, Y., and Zhang, L. (2023). A bio-orthogonally functionalized chitosan scaffold with esterase-activatable release for nerve regeneration. *Int. J. Biol. Macromol.* 229, 146–157. doi:10.1016/j.ijbiomac.2022.12.113

Wei, J., Zhu, L., Lu, Q., Li, G., Zhou, Y., Yang, Y., et al. (2023). Recent progress and applications of poly(beta amino esters)-based biomaterials. *J. Control. Release.* 354, 337–353. doi:10.1016/j.jconrel.2023.01.002

Wu, C., Fan, W., Chang, J., and Xiao, Y. (2011). Mussel-inspired porous SiO_2 scaffolds with improved mineralization and cytocompatibility for drug delivery and bone tissue engineering. *J. Mat. Chem.* 21, 18300–18307. doi:10.1039/c1jm12770e

Wu, J., Cao, L., Liu, Y., Zheng, A., Jiao, D., Zeng, D., et al. (2019). Functionalization of silk fibroin electrospun scaffolds via BMSC affinity peptide grafting through oxidative self-polymerization of dopamine for bone regeneration. *Acs. Appl. Mat. Interfaces.* 11, 8878–8895. doi:10.1021/acsami.8b22123

Xie, L., Liu, N., Xiao, Y., Liu, Y., Yan, C., Wang, G., et al. (2020). *In vitro* and *in vivo* osteogenesis induced by icariin and bone morphogenetic protein-2: A dynamic observation. *Front. Pharmacol.* 11, 1058. doi:10.3389/fphar.2020.01058

Xu, H., Wang, C., Liu, C., Li, J., Peng, Z., Guo, J., et al. (2021). Stem cell-seeded 3D-printed scaffolds combined with self-assembling peptides for bone defect repair. *Tissue. Eng. Part. a.* 28, 111–124. doi:10.1089/ten.TEA.2021.0055

Xu, J., Wang, Y., Li, J., Zhang, X., Geng, Y., Huang, Y., et al. (2016). IL-12p40 impairs mesenchymal stem cell-mediated bone regeneration via CD4+ T cells. *Cell. death. Differ.* 23, 1941–1951. doi:10.1038/cdd.2016.72

Xu, L., Bai, X., Yang, J., Li, J., Xing, J., Yuan, H., et al. (2020). Preparation and characterisation of a gellan gum-based hydrogel enabling osteogenesis and inhibiting *Enterococcus faecalis*. *Int. J. Biol. Macromol.* 165, 2964–2973. doi:10.1016/j.ijbiomac.2020.10.083

Yang, X., Wang, B., Sha, D., Liu, Y., Liu, Z., Shi, K., et al. (2021). PVA/poly(hexamethylene guanidine)/gallic acid composite hydrogel films and their antibacterial performance. *Acs. Appl. Polym. Mat.* 3, 3867–3877. doi:10.1021/acsapm.1c00447

Yi, H., Rehman, F. U., Zhao, C., Liu, B., and He, N. (2016). Recent advances in nano scaffolds for bone repair. *Bone Res.* 4, 16050. doi:10.1038/boneres.2016.50

Yu, Q., Zheng, Z., Dong, X., Cao, R., Zhang, S., Wu, X., et al. (2021). Mussel-inspired hydrogels as tough, self-adhesive and conductive bioelectronics: A review. *Soft. Matter.* 17, 8786–8804. doi:10.1039/d1sm00997d

Yuan, L., Wu, Y., Gu, Q., El-Hamshary, H., El-Newehy, M., and Mo, X. (2017). Injectable photo crosslinked enhanced double-network hydrogels from modified sodium alginate and gelatin. *Int. J. Biol. Macromol.* 96, 569–577. doi:10.1016/j.ijbiomac.2016.12.058

Zhang, C., Wu, B., Zhou, Y., Zhou, F., Liu, W., and Wang, Z. (2020). Mussel-inspired hydrogels: From design principles to promising applications. *Chem. Soc. Rev.* 49, 3605–3637. doi:10.1039/c9cs00849g

Zhang, J., He, X., Yu, S., Zhu, J., Wang, H., Tian, Z., et al. (2021a). A novel dental adhesive containing Ag/polydopamine-modified HA fillers with both antibacterial and mineralization properties. *J. Dent.* 111, 103710. doi:10.1016/j.jdent.2021.103710

Zhang, J., Liu, M., and Pei, R. (2021c). An *in situ* gelling BMSC-laden collagen/silk fibroin double network hydrogel for cartilage regeneration. *Mat. Advan.* 2, 4733–4742. doi:10.1039/d1ma00285f

Zhang, J., Yao, K., Wang, Y., Zhou, Y., Fu, Z., Li, G., et al. (2021b). Brain-targeted dual site-selective functionalized poly(β-Amino Esters) delivery platform for nerve regeneration. *Nano. Lett.* 21, 3007–3015. doi:10.1021/acs.nanolett.1c00175

Zhang, L., Li, J., Chen, J., Peng, Z. X., Chen, J. N., Liu, X., et al. (2022b). Enhanced bone regeneration via PHA scaffolds coated with polydopamine-captured BMP2. *J. Mat. Chem. B* 10, 6214–6227. doi:10.1039/d2tb01122k

Zhang, L., Yao, K., Wei, J., Li, G., Lin, Y., Zhou, Y., et al. (2022a). Convenient *in situ* synthesis of injectable lysine-contained peptide functionalized hydrogels for spinal cord regeneration. *Appl. Mat. Today* 27, 101506. doi:10.1016/j.apmt.2022.101506

Zhao, Y., Li, Z., Jiang, Y., Liu, H., Feng, Y., Wang, Z., et al. (2020). Bioinspired mineral hydrogels as nanocomposite scaffolds for the promotion of osteogenic marker expression and the induction of bone regeneration in osteoporosis. *Acta. Biomater.* 113, 614–626. doi:10.1016/j.actbio.2020.06.024

Zhou, S., Bei, Z., Wei, J., Yan, X., Wen, H., Cao, Y., et al. (2022). Mussel-inspired injectable chitosan hydrogel modified with catechol for cell adhesion and cartilage defect repair. *J. Mat. Chem. B* 10, 1019–1030. doi:10.1039/d1tb02241e

Zhou, Y. Z., Cao, Y., Liu, W., Chu, C. H., and Li, Q. L. (2012). Polydopamine-induced tooth remineralization. *Acs. Appl. Mat. Interfaces.* 4, 6901–6910. doi:10.1021/am302041b

Zhu, Y., Ye, L., Cai, X., Li, Z., Fan, Y., and Yang, F. (2022). Icariin-loaded hydrogel regulates bone marrow mesenchymal stem cell chondrogenic differentiation and promotes cartilage repair in osteoarthritis. *Front. Bioeng. Biotechnol.* 10, 755260. doi:10.3389/fbioe.2022.755260

frontiers | Frontiers in Bioengineering and Biotechnology

TYPE Original Research
PUBLISHED 01 August 2023
DOI 10.3389/fbioe.2023.1156525

OPEN ACCESS

EDITED BY
Juncen Zhou,
Stony Brook University, United States

REVIEWED BY
Sheng Lu,
Jiangsu University of Science and Technology, China
Rong-Chang Zeng,
Shandong University of Science and Technology, China

*CORRESPONDENCE
Ying-Sui Sun,
yingsuisun@tmu.edu.tw

RECEIVED 01 February 2023
ACCEPTED 02 May 2023
PUBLISHED 01 August 2023

CITATION
Wang C-C, Hung J-Y, Uan J-Y, Fang C-Y, Kuo Y-L, Chang W-J, Ohiro Y and Sun Y-S (2023), Facile bioactive transformation of magnesium alloy surfaces for surgical implant applications.
Front. Bioeng. Biotechnol. 11:1156525.
doi: 10.3389/fbioe.2023.1156525

Facile bioactive transformation of magnesium alloy surfaces for surgical implant applications

Cheng-Chieh Wang[1], Jing-Ya Hung[2], Jun-Yen Uan[3], Chih-Yuan Fang[4], Yu-Lin Kuo[5], Wei-Jen Chang[6,7], Yoichi Ohiro[8] and Ying-Sui Sun[2]*

[1]Division of Endodontics, Department of Dentistry, Taipei Medical University Hospital, Taipei, Taiwan, [2]School of Dental Technology, College of Oral Medicine, Taipei Medical University, Taipei, Taiwan, [3]Department of Materials Science and Engineering, National Chung Hsing University, Taichung, Taiwan, [4]Division of Oral and Maxillofacial Surgery, Department of Dentistry, Wan Fang Hospital, Taipei, Taiwan, [5]Department of Mechanical Engineering, National Taiwan University of Science and Technology, Taipei, Taiwan, [6]School of Dentistry, College of Oral Medicine, Taipei Medical University, Taipei, Taiwan, [7]Dental Department, Shuang-Ho Hospital, Taipei Medical University, Taipei, Taiwan, [8]Oral and Maxillofacial Surgery, Division of Oral Pathobiological Science, Faculty of Dental Medicine and Graduate School of Dental Medicine, Hokkaido University, Sapporo, Japan

The market for orthopedic implant alloys has seen significant growth in recent years, and efforts to reduce the carbon footprint of medical treatment (i.e., green medicine) have prompted extensive research on biodegradable magnesium-based alloys. Magnesium alloys provide the mechanical strength and biocompatibility required of medical implants; however, they are highly prone to corrosion. In this study, Mg-9Li alloy was immersed in cell culture medium to simulate degradation in the human body, while monitoring the corresponding effects of the reaction products on cells. Variations in pH revealed the generation of hydroxyl groups, which led to cell death. At day-5 of the reaction, a coating of $MgCO_3$ $(H_2O)_3$, HA, and α -TCP appeared on sample surfaces. The coating presented three-dimensional surface structures (at nanometer to submicron scales), anti-corrosion effects, and an altered surface micro-environment conducive to the adhesion of osteoblasts. This analysis based on bio-simulation immersion has important implications for the clinical use of Mg alloys to secure regenerated periodontal tissue.

KEYWORDS

magnesium alloy, biodegradable, corrosion resistance, bone screw, osteoblasts responses

1 Introduction

It is expected that for the next several years, low-carbon medical care will be a major target in the transition toward sustainable net-zero development. One approach to reducing the carbon emissions associated with medical care involves reducing the burden of additional treatment. To this end, researchers have been developing biodegradable metal alloys for the fabrication of so-called green medical devices. One recent development is referred to as temporary implants, which are commonly fabricated using alloys of magnesium, due to their excellent biocompatibility and Young's modulus close to that of bone. Note however that magnesium alloy degrades too rapidly for most clinical applications other than as bone screws for fixation and suturing (Lu et al., 2021). In recent years, scholars have invested considerable time and cost seeking to extend the clinical applicability of these materials.

Mg is essential to the functioning of many human tissue types, and Mg ions are abundant in biological fluids and stored in large quantities in bone tissue. Mg is a cofactor for enzymes in human metabolism. Mg plays important roles in maintaining wall tension in blood vessels, promoting tissue healing, and regulating muscle contraction. It also participates in the formation of antibodies, tissue calcification, and other processes. Mg is easily corroded in the human body; however, Mg ions are not cytotoxic in a physiological environment and can be excreted in urine (Wolf and Cittadini, 2003). Mg is highly biocompatible, and the other elements used in most Mg alloys do not present a toxic hazard. Magnesium concentrations in serum/plasma generally remain within a healthy range; however, bone and soft tissue are prone to gradual depletion (Elin, 1987). Unlike other ions, magnesium ions maintain a transmembrane concentration gradient in cells. Normal intracellular and extracellular concentrations of free Mg^{2+} generally range from 10 to 30 mM (Rahman et al., 2020). In a previous study on the *in vivo* degradation of magnesium alloys (3% Al + 1% Zn, 9% Al + 1% Zn, 4% Y + 3% Nd, and 4% Li + 4% Al + 2% Ce), it was found that Mg corroded more slowly when alloyed with Li and Al. In that study, alloy elements were observed in the corrosion layer adjacent to the amorphous calcium phosphate layer but not in adjacent bone tissue (Witte, 2015).

Alloying with lithium (Li) can alter the hexagonal close packed (hcp) structure of Mg to form a body centered cubic (bcc) structure. Li is the metal with the lowest density, such that combining metallic Mg with Li results in an ultra-light alloy with outstanding properties. Binary alloys of Mg and Li are die-cast in the form of implants using the vacuum stirring casting method. Mg-Li alloys can be extruded to improve stretchability or to increase the content of secondary phases and thereby enhance hardness (Ebel et al., 1980). The biocompatibility of Li is reflected in its wide clinical use as a psychotropic drug. Several studies have also confirmed that Li promotes the osteogenic differentiation of bone marrow mesenchymal stem cells by activating the Wnt/GSK-3 signaling pathway, thereby promoting bone regeneration and ameliorating osteoporosis (Staiger et al., 2006). The fact that Li promotes osteogenesis has attracted considerable attention in the field of bone tissue engineering (Rahulan et al., 2019). However, the low corrosion resistance of Mg-Li alloy, due largely to the chemical reactivity of Li, limits its clinical applicability (Li et al., 2021; Chen et al., 2022). The primary disadvantage of all Mg alloys is rapid corrosion, which can lead to uncontrolled degradation, structural failure, hydrogen formation, and elevated pH levels. Note that the release of high concentrations of corrosion products can have detrimental effects on biocompatibility (Song et al., 2009). Nonetheless, the susceptibility of Mg-Li-based alloys to corrosion can be suppressed by subjecting implants to surface treatment prior to insertion.

Mg alloy implants have several advantages over other materials, including 1) biocompatibility and the promotion of osteogenesis, 2) biodegradability to eliminate the need for secondary surgery, 3) good mechanical properties, 4) processability and dimensional stability, and 5) high compression resistance (Elin, 1987). The Young's modulus of human bone (3–20 GPa) is closer to that of Mg alloy (41–45 GPa) than to other implant materials, such as stainless steel (190–205 GPa), Ti (110–117 GPa), and Co-Cr alloys (230 GPa) (Rahman et al., 2020). Researchers have also developed numerous methods by which to tune the degradability of magnesium and its alloys.

Previous research has focused largely on magnesium-lithium-based alloys (Mg-9Li-1Zn) with mechanical strength comparable to that of natural bone. Researchers have developed several surface treatment methods to enhance the corrosion resistance of Mg alloys; however, most of those methods are complex or require expensive machinery (Toorani et al., 2019). Our primary objective in this research was to develop a simple surface treatment method involving the repeated immersion of alloy implants in solutions that simulate human physiological conditions (i.e., cell culture medium). We then assessed the suitability of the devices for implantation within the human body. Experiments were conducted to analyze the corrosion resistance of the material as well as the growth of bone cells on the surface of the material. Note that this testing did not involve analyzing the composition of surface deposits or the physical properties of the material after impregnation. Our analysis of biomimetic responses has important implications for the clinical application of Mg-Li-based alloys in the form of bone screws to promote the regeneration of periodontal ligaments without the need for subsequent surgical resection. We found that by controlling the rate of magnesium alloy degradation, it should be possible to create dental implants that meet clinical requirements. The proposed immersion method was shown to improve the corrosion resistance and bio-responsiveness of the material surface. The proposed approach to surface modification is simple to implement and consumes very little energy, compared to alloy recasting (Cao et al., 2008). Nonetheless, further studies will be required to elucidate the long-term cellular responses and implications for tissue regeneration.

2 Materials and methods

Mg-Li and LZ alloy samples were fabricated via melting and casting. As-cast samples underwent homogenization treatment at 330°C, followed by air cooling to room temperature. The samples were then hot rolled at 240°C to fabricate the Mg-Li and LZ alloy plates with a thickness of 0.8 mm. A water-jet cutter was used to cut the plates into discs for subsequent analysis.

2.1 Surface treatment of magnesium-lithium alloy

The mechanical properties of Mg can be greatly enhanced by alloying it with Li and/or Zn to form binary Mg-Li alloys or ternary Mg-Li-X (X = Al, Zn, Ca, Y, Ce) alloys (Peng et al., 2019). This study focused on a Li-containing Mg alloy (Mg-9Li-1Zn; hereafter referred to as LZ). Disc-shaped samples of this material measuring 2 cm in diameter with a thickness of 2 mm were fabricated.

The surface oxide layer of the LZ was removed using #1200 silicon carbide water sandpaper, after which the samples were dried and stored in a moisture-proof box until use. The LZ samples were then immersed in osteoblast culture medium to simulate degradation under *in vitro* environmental conditions (Panasonic MCO-18AC-PT). The surface properties of the material (physical, chemical, and corrosion resistance) and cell attachment were examined at various time points (0, 24, 48, 72, and 96 h) throughout the immersion process, as indicated by the

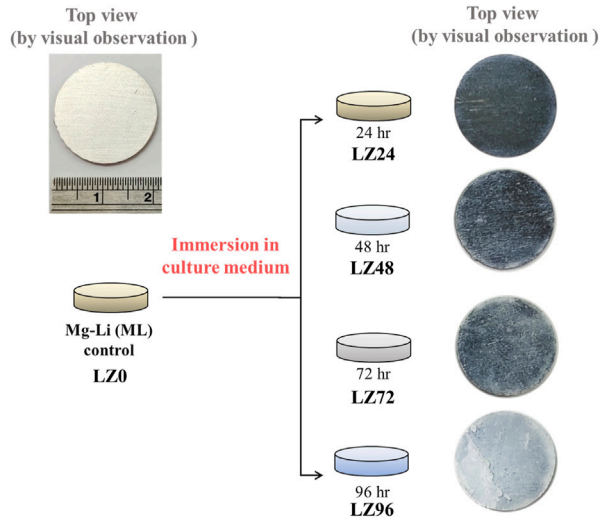

FIGURE 1
Schematic illustration showing sample preparation and a top-view of all samples.

naming of the samples (i.e., LZ0, LZ24, LZ48, LZ72, and LZ96). Samples of osteoblast culture medium were collected to test for ion release (see Figure 1).

2.2 Material surface properties

Top-view visual observation and field emission scanning electron microscopy (FE-SEM, JEOL JSM-6500F, Japan) were used to observe the surface morphology and cell adhesion morphology of the LZ samples. Energy-dispersive X-ray spectrometry (EDS, JEOL JSM-6500F, Japan) and X-ray diffraction (XRD, D8 DISCOVER - Bruker) were respectively used to identify surface element composition and chemical composition. Surface roughness was measured using a white-light interferometer (Filmetrics® Profilm3D® Optical Profilometer, KLA, United States).

2.3 Ion release

Inductively coupled plasma optical emission spectrometry (ICP-OES, Thermo Fisher Scientific iCAP TQ) was used to analyze the concentration of ions released into the culture medium as an indication of corrosion rate. We also measured the pH of the culture medium at 3 h to quantify the release of hydroxy groups associated with the corrosion process. Note that any change in the pH of cell culture medium could affect cell growth.

2.4 Potentiodynamic polarization curve analysis

In the electrochemical experiments, the test piece was placed in an electrolyte of phosphate-buffered solution (PBS). An electrochemical workstation (Jiehan 5000, Taiwan) was used to obtain potentiodynamic polarization curves indicating the corrosion resistance (i.e., corrosion potential and corrosion current) of the material surface, while immersed in PBS. Polarization curves were measured with an onset potential of −3.0 V and a stop potential of +2.5 V at a scanning rate of 0.001 V/s. The counter electrode (CE) was a platinum plate. The reference electrode (RE) was a saturated calomel electrode (SCE). The working electrode (WE) was the sample being tested.

2.5 Cellular responses

The osteoblasts (MG63) used in this experiment were purchased from the Bioresource Collection and Research Center (BCRC 60279). The MG63 were cultured in Minimum Essential Medium (MEM, Gibico-Thermo Fisher Scientific) supplemented with 10% fetal bovine serum, 1.5 g/L sodium bicarbonate, and 1% penicillin/streptomycin and grown in an incubator (at 37°C and in 5% CO_2). All cell experiments were performed at the School of Dentistry, Taipei Medical University. The front and back of the test pieces were sterilized using ultraviolet light on a sterile operating table. MG63 cells were then cultured on the surfaces of the test pieces at a concentration of 1.6×10^5 for 3 h. Note that the area of the test piece was 1 cm^2. After fixing the cells on the surface, the samples were subjected to alcohol gradient dehydration and critical point drying (CPD, LEICA EM CPD 030) to facilitate the observation of cell extension morphology, cell attachment, and cell-to-cell interactions. MG63 cell were cultured in DMEM containing 10% fetal bovine serum at 37°C.

2.6 Statistical analysis

Experiment data are expressed as the mean ± standard deviation (SD). All measurements were performed in triplicate. Three samples from each test group were measured at each time point. The Student's *t*-test was used to analyze the effects of surface treatment on surface properties and cellular responses, with significant effects indicated by a p-value of < 0.05.

3 Results

3.1 Material surface properties

3.1.1 Surface morphology and element analysis of materials following immersion in culture medium

In this study, binary Mg-9wt.%Li alloy (LZ) was selected as a substrate. Note that the number following the LZ designation indicates the time spent immersed in culture medium at the time of testing (in hours). Optical microscopy and FE-SEM revealed that after immersion in culture solution for 0, 24, 48, 72 or 96 h, the LZ alloy exhibited deposits of corrosion products and a rough surface morphology (see Figure 2A). EDS analysis revealed that the initial corrosion deposits contained calcium from the cell culture solution; however, no calcium was observed in the deposits after 96 h of immersion, indicating that the Ca ions had been deposited with Mg (Figure 2B).

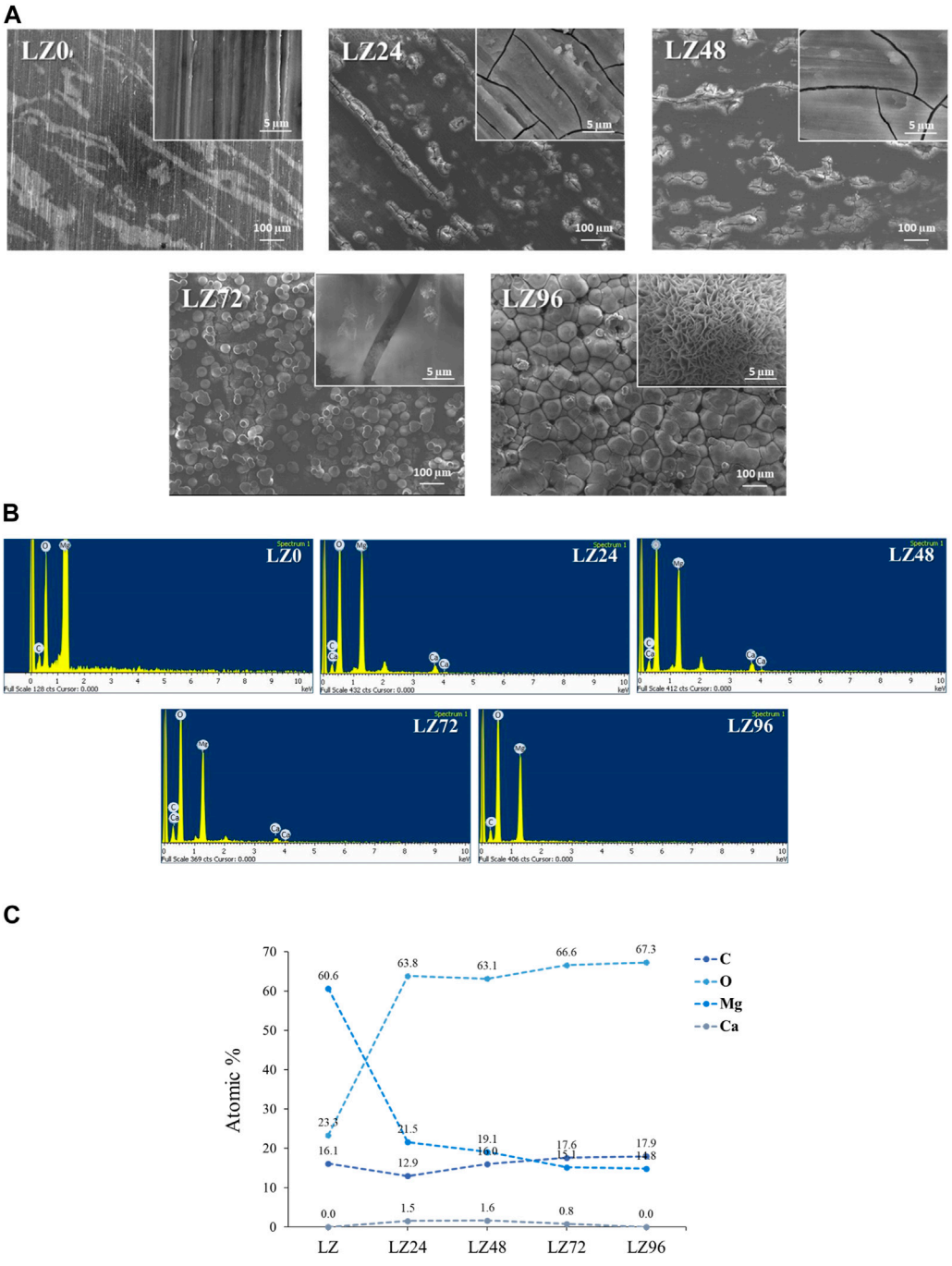

FIGURE 2
(A) FE-SEM results showing surface morphology of alloy samples; **(B)** EDX results showing the chemical composition of alloy samples; and **(C)** exact values of elements.

3.1.2 Surface crystal composition following immersion in culture medium

As shown in Figure 3A, the Primary phase (main peak) is Mg and Li and the secondary phase is Li_2O_2. The surface of the untreated sample (LZ0) at room temperature presented two crystal phase structures composed of Mg or Li alloy products (β-Li and α-Mg). α-Mg was also detected on the surfaces of LZ24 and LZ48 samples. HA, and α-TCP crystal phases were detected on the surfaces of LZ72 and LZ96 samples. Li_2O_2 was detected in all samples. Li_2O_2, MgO_2, hydroxides ($Mg(OH)_2$) and carbonates ($MgCO_3$ $(H_2O)_3$) were also detected on the surface of LZ72 and LZ96. The peak of LZ96 was more obvious than that of LZ72.

The three phases of β-L, α-Mg and Li_2O_2 tend to decrease with the increase of immersion treatment time, and even after 72 h of immersion, β-Li and α-Mg have not been detected at all. By analyzing the integrated peak area of each phase on the XRD

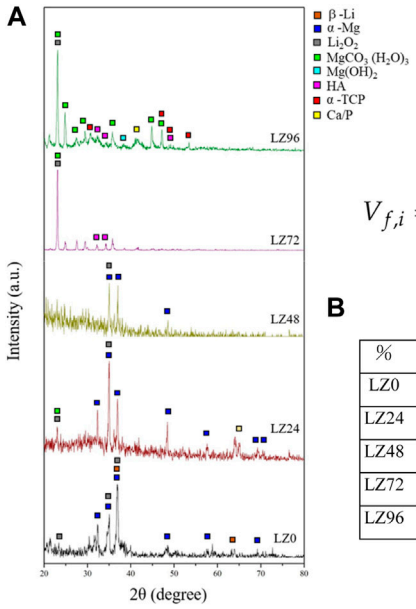

$$V_{f,i} = \frac{A_i}{\sum A_i} \quad \text{.....(1)}$$

B

%	β-Li	α-Mg	Li_2O_2	$MgCO_3(H_2O)_3$	$Mg(OH)_2$	HA	α-TCP	Ca/P
LZ0	28.92%	33.79%	36.59%					
LZ24		48.39%	26.25%	10.44%				14.93%
LZ48		50.07%	49.93%					
LZ72			20.14%	36.16%		43.70%		
LZ96			7.45%	44.47%	1.26%	8.32%	25.57%	12.93%

FIGURE 3
XRD results show the element composition on sample surfaces as a function of immersion time in the culture medium. **(A)** qualitative spectrum; **(B)** quantitative volume percent data.

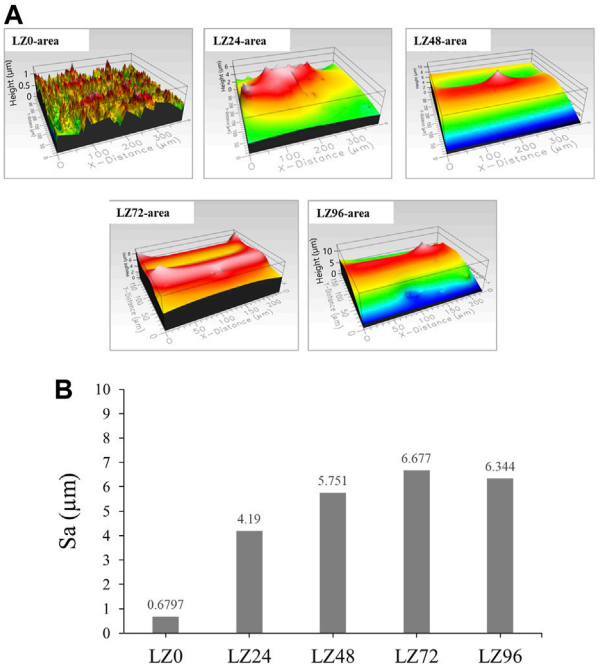

FIGURE 4
Roughness (Sa) of LZ0, LZ24, LZ48, LZ72, and LZ96 samples: **(A)** Surface morphology of all test samples; **(B)** Quantitative roughness results of all samples.

pattern, the volume fraction of each phase in the coating can be calculated using the Pearson VII function in software such as Origin. Using this calculation, it is possible to determine the relative amounts of the different phases present in the coating and assess its overall composition (Amukarimi and Mozafari, 2021). The equation used is shown in Formula 1.

It is particularly worth noting that the Li oxide (Li_2O_2) tends to increase from 0, 24, and 48 h the longer the soaking time. It was further found that Li_2O_2 decreased as the immersion time increased to 72 h. And there are other products. For example, $MgCO_3$ $(H_2O)_3$ and HA.

3.1.3 Surface roughness following immersion in culture medium

Surface roughness was shown to increase with immersion time. Immersion for 72 h resulted in a relatively flat surface profile. The surface roughness of samples LZ72 and LZ96 groups was very similar (Sa = 0.6, 4.2, 5.7, 6.7, and 6.3 μm) (Figures 4A, B). The surface roughness of L24 samples was 7-fold higher than that of the untreated group, resulting from flaky surface deposits of reaction products.

3.2 Corrosion resistance

3.2.1 Analysis of corrosion resistance

Potentiodynamic polarization (PD) curves were obtained by recording changes in potential, current values, and resistance using a potentiostat. This study used these values to assess the corrosion resistance of alloys immersed in PBS. PD tests were performed between a potential of −3.0 V (vs. OCP) and 2 V at a scanning rate of 0.1 mV s^{-1}. Figure 5 presents the potentiodynamic polarization, polarization resistance (Rp), corrosion current values (Icorr), and corrosion potential (Ecorr) of the samples as a function of immersion duration. The fitting results of Ecorr, Icorr, and Rp were calculated by Faraday's law using Eq. (15).

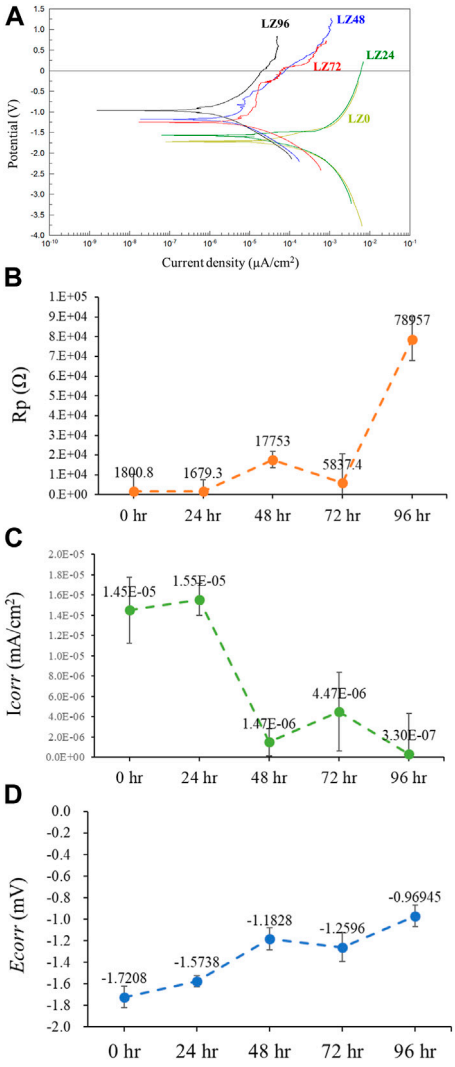

FIGURE 5
Electrochemical analysis of samples LZ0, LZ24, LZ48, LZ72, and LZ96 following immersion in PBS: **(A)** Potentiodynamic polarization curves; **(B)** Rp; **(C)** Icorr; and **(D)** Ecorr.

The Ecorr and Rp values of LZ96 samples exceeded those in the other groups, while the Icorr value of LZ96 was the lowest (at least 10-fold lower than that of the untreated control). Ecorr and Rp values increased and Icorr decreased with immersion duration. We also determined that the surface corrosion resistance improved with an increase in immersion duration. We speculate that the reaction with the cell culture medium resulted in the formation of a corrosion-resistant layer on the surface of the alloy.

3.2.2 Ion release into the culture medium

Samples of cell culture fluid collected at various time points throughout the immersion period were analyzed using ICP-OES to quantify the release of ions by the alloy into the culture medium. As shown in Figure 6, the concentration of lithium ions increased linearly with immersion time, as indicated by the Li^{2+} concentrations: LZ24 (220 ppm), LZ48 (411 ppm), LZ72 (413 ppm) LZ96 (497 ppm). Note however that after an initial sharp increase in Li-ion concentrations, the levels gradually slowed down at around 72 h before increasing again during the last 24 h. The Mg^{2+} concentrations were as follows: LZ24 (134 ppm), LZ72 (179 ppm), and LZ96 (167 ppm). The release of Mg ions increased until 48 h, at which point it leveled off and increased only gradually thereafter. Calcium ion concentrations were as follows: medium only (37 ppm), LZ24 (12 ppm), LZ48 (10 ppm), LZ72 (11 ppm), and LZ96 (11 ppm).

3.2.3 pH values

When immersed in an aqueous solution, the corrosion of magnesium alloy generates corrosion products and free species that can affect the pH of the solution. This experiment involved collecting cell culture medium to test the pH before immersion at various time points throughout the immersion period. The results were as follows: LZ0 (7.4), LZ24 (8.7), LZ48 (8.5), LZ72 (8.9), and LZ96 (8.7). Note that the pH of the magnesium alloy-impregnated solution increased rapidly in the first 24 h; however, pH levels leveled off thereafter (see Figure 7).

3.3 Cell attachment and initial cell morphology

Cell adhesion is crucial to the survival of anchorage-dependent cells on biological matrices. In this study, cell adhesion was assessed by incubating MG63 cells on the surface of alloy samples for 3 h (Figure 8). FE-SEM was then used to observe cell adhesion, growth, and morphology. Almost no cells adhered to the surface of LZ0 control samples. A few cells adhered to sample LZ24; however, they were inactive. Cells readily adhered to samples LZ72 and LZ96 and appeared to be in a healthy state with a robust morphology. It appears that the long sheets of corrosion products on the surface of the samples presented good attachment points for pseudopodia. The yellow arrows in Figure 7 indicate cells attached to the alloy surface and the pink arrows indicate filopodia extensions. Note that the morphology of cells on LZ72 and LZ96 did not differ significantly.

4 Discussion

In pilot experiments, we observed no significant difference in the pH of the cell culture medium following immersion for 96, 120, 136, or 144 h (data not shown). We, therefore, selected 96 h as the longest immersion time in the current study. Corrosion resistance analysis and cell response tests were performed after immersion for 24, 48, 72, or 96 h.

4.1 Surface morphology and element analysis of alloys following immersion in culture medium

This study examined simple binary Mg-9wt.%Li alloys. Visual observation and FE-SEM analysis of the proposed LZ alloy revealed corrosion products and rough surface morphology. EDX analysis also revealed the presence of Ca on the surface of samples after immersion for 72 h. We speculate that the cell culture medium was the source of

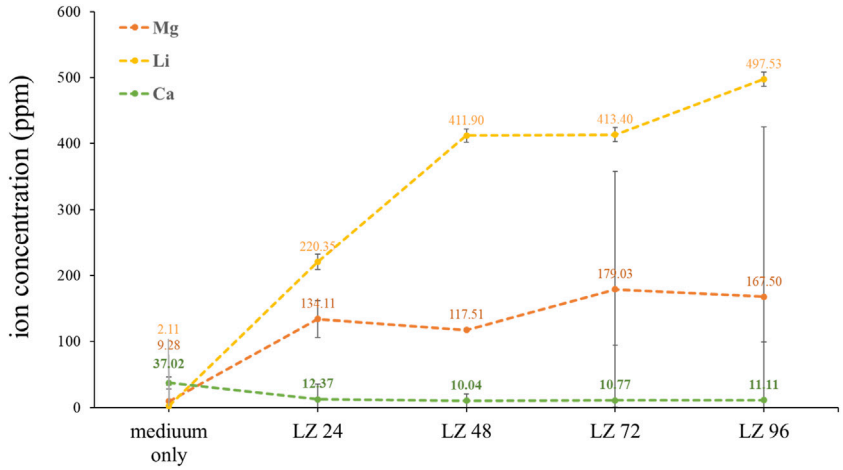

FIGURE 6
Li, Mg, and Ca ion concentrations in culture media following alloy immersion for 0, 24, 48, 72, or 96 h.

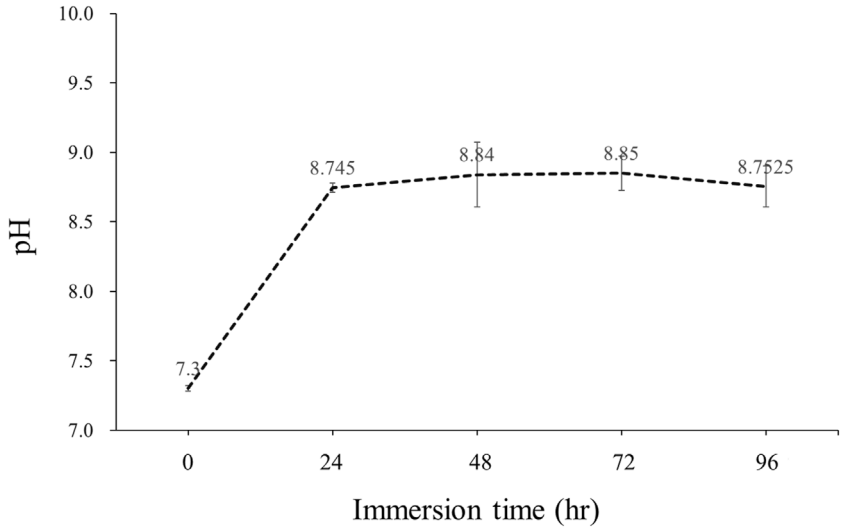

FIGURE 7
pH values as a function of Mg-Li alloy immersion time.

the Ca. Note that no Ca was observed on the surfaces of samples that were not immersed in the culture medium (LZ0) or on the surfaces of LZ96. It appears that corrosion progressed for roughly 72 h, at which point the corrosion products underwent redeposition on the samples. Sample LZ72 presented a few flake-like deposits of hydroxyapatite (HA), Ca-deficient HA, and β-TCP (Figure 2), whereas sample LZ96 was uniformly coated. The above-mentioned flakey deposits may account for the high roughness values obtained on the surface samples LZ72 and LZ96. Roughness increased linearly with immersion time until 72 h and then changed very little in the subsequent 24-h period (see Figure 2). Our results identified 96 h as the optimal soaking duration. The material is soaked in the culture solution for 96 h, which is the optimal soaking time for the experimental design confirmed by the data of this study. Electrochemical surface treatment is a relatively common surface treatment method, such as: micro-arc fluorination (Chen et al., 2021).

After grinding and polishing (i.e., before immersion), the Mg-Li alloy at room temperature exhibited a two-phase structure consisting of a Li-rich BCC structure β phase and a Mg-rich HCP structure α phase (Liu et al., 2109; Chang et al., 2006) (Figure 2). XRD results revealed that the surface compositions of LZ72 and LZ96 were identical. We selected samples covering a range of roughness values (Sa = 0.6, 4.2, 5.7, 6.7, and 6.3 μm) to analyze *in vitro* degradation as a function of immersion duration (Figure 3). The degree to which roughness changed (qualitatively) was also derived from data related to surface topography (see Figure 2).

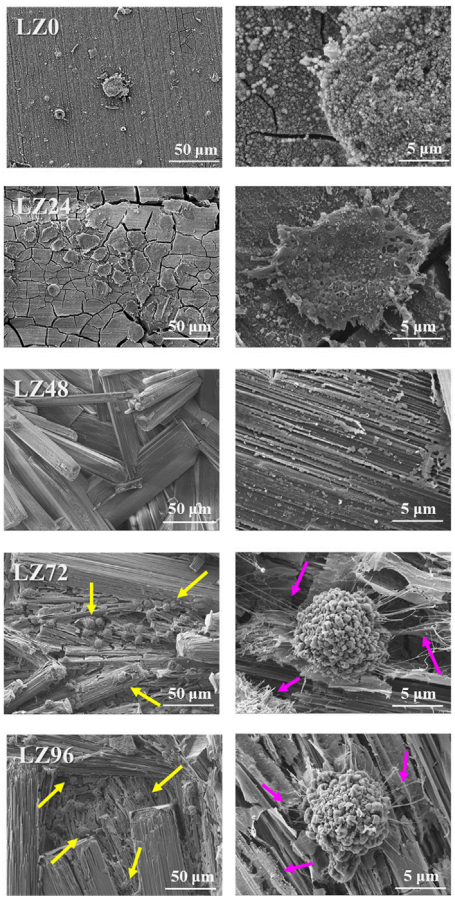

FIGURE 8
Adhesion morphology of MG63 cells on the surface of samples LZ0, LZ24, LZ48, LZ72, and LZ96. The yellow arrows indicate cells and the pink arrows indicate filopodia.

4.2 Corrosion resistance

EDX analysis revealed a decrease in Mg ion concentrations at 96 h, due presumably to the redeposition of Mg ions released in the first 48 h (see Figure 3). Mg^{2+} plays a key role in bone development by promoting the attachment and differentiation of osteoblasts and accelerating mineralization to promote bone healing. During osseointegration, Mg^{2+} concentration also plays a key role in regulating bone regeneration (Cain and Labukas, 2020). Wang et al. demonstrated that Mg^{2+} (at a concentration of 10 mM) promoted the adhesion and proliferation of osteoblasts. Note however that at higher concentrations (>18 mM), Mg^{2+} significantly inhibited these effects (Cain and Labukas, 2020). The concentration of Mg ions in the culture medium (Figure 5) gradually increased with immersion time, with the ion concentration plateauing at 72 h and then gradually decreasing. Note that the ion concentrations were derived as follows: ppm = mM × MW, where MW indicates molecular weight. Mg^{2+} concentrations in the culture solution varied over time as follows: LZ24 (5.6 mM), LZ72 (7.3 mM), and LZ96 (7.0 mM).

This study was based on the hypothesis that the deposits that formed on the surface of LZ96 samples would protect against further corrosion. As for the underlying mechanism, we posit that the reaction of the Mg alloy with the cell culture medium led to the formation of a thick ceramic surface layer (possessing a crystalline structure), which blocked further corrosion (see Figure 7). This assertion is supported by the fact that the LZ sample surfaces were more stable than oxidized surfaces in cell culture media (Li_2O_2 layer) but less stable in water (Wang et al., 2014).

When Mg alloy implants were first assessed nearly a hundred years ago, it was found that the rapid degradation of the alloys led to the accumulation of large quantities of hydrogen gas in the form of subcutaneous bubbles, which essentially precluded the use of magnesium as a medical material (Wang et al., 2014). The primary chemical reaction involves the Mg and water (abundant in body fluids), wherein the formation of hydroxide ions and hydrogen gas involves the following chemical reaction:

$$Mg + 2H_2O \rightarrow Mg(OH)_2 + H_2 \quad (1)$$

The corrosion of magnesium alloys generates corrosion products that can affect biocompatibility (e.g., hydrogen and hydroxide ions) (Tsakiris et al., 2021). For example, bubbles of hydrogen gas accumulating in the tissue surrounding implants can cause the separation of tissue layers, whereas hydroxide ions can cause surface alkalization sufficient to damage cells. Numerous researchers have sought to alloy Mg with nontoxic elements or coat the surfaces of Mg-based implants to counter these effects; however, our results indicate that this is not necessary as the rapid increase in alkalinity ceases within 24 h (Figure 5).

Limitations on sample preparation capacity made it impossible to fabricate the sample quantities required for conventional statistical analysis. Three samples were fabricated in each experiment run, and each run was repeated three times. Thus, the reported statistical values were derived from a total of nine samples, which should be sufficient to ensure data reliability (on par with previous papers). In future research, we will seek to develop techniques for the mass fabrication of samples.

4.3 Initial cell attachment and morphology

Cytotoxicity can be assessed in terms of cell response via direct or indirect testing (Yuan et al., 2019). In the current study, cell cultures were placed in direct contact with Mg alloy samples and then immersed in a cell culture medium. Following immersion in culture solution for 72 or 96 h, the Mg-Li alloy presented micron-scale spherical corrosion products. Culturing MG63 cells on samples LZ72 and LZ96 for 3 h was shown to cover pores at the micron to submicron scale. More importantly, cell culturing changed the structure of the corrosion products from a staggered lamellar structure into a long lamellar structure, corresponding to the three-dimensional porous fiber morphology of the extracellular matrix. Numerous studies have demonstrated that surfaces with a structure similar to that of the extracellular matrix are highly conducive to cell adhesion (Wang et al., 2017).

Surface deposits on Mg alloys can have a profound effect on cell-implant interactions and implant degradation (Johnson et al., 2012). The surface deposits that formed on Mg alloy implants after immersion for extended durations (72 or 96 h) were shown to facilitate cell adhesion and promote cell survival. Figure 8 presents a graphical abstract of this study. The immersion method used in this

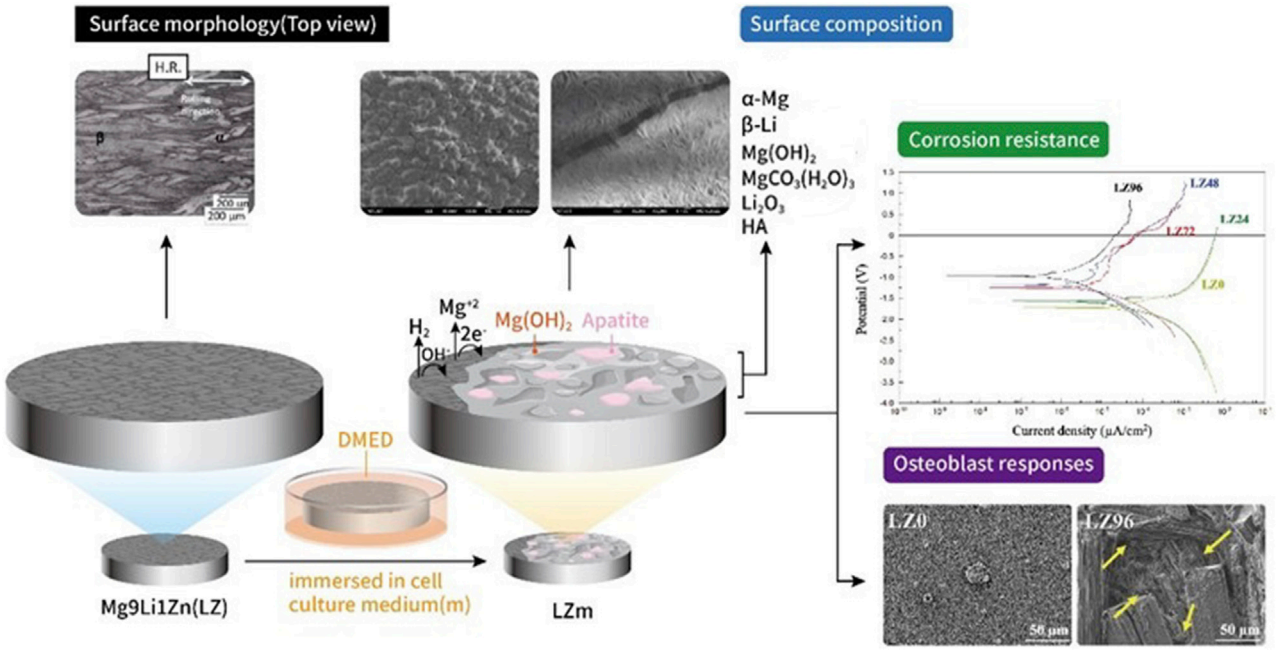

FIGURE 9
Schematic illustration showing that immersing Mg alloy in cell culture medium prompted surface degradation as well as the deposition of corrosion products, which slowed or halted further corrosion. The surface deposits included bioactive calcium and phosphorus compounds with a porous surface morphology (micron to nanometer scale), which was shown to promote cell adhesion and survival.

study was a simple inexpensive surface treatment process aimed at stimulating the natural physiological environment, leading to the formation of an anti-corrosion layer on the surface of the Mg alloy. The immersion solution used in this study was a cell culture with ion types and pH values very close to the physiological environment. As a result, the ions contained in the resulting sedimentary layer do not induce bio repulsion in the human body. This approach could likely be adopted for a wide range of applications.

One common disadvantage of magnesium alloys is their rapid degradation, which can compromise the implant support function before bone tissue healing is complete (Harrison et al., 2014). The degradation of magnesium alloys can lead to the generation of hydrogen ions (potentially causing emphysema) as well as hydroxide ions (generating a high pH microenvironment with negative effects on osteoblast growth and bone regeneration) (Kannan and Wallipa, 2013; Chen et al., 2014). Magnesium alloys also lack bioactivity and osteoconductivity (Hornberger et al., 2012; Razavi et al., 2014).

In the current study, magnesium alloys released ions at concentrations of 650–700 ppm (mg/L) (Figure 6), which is roughly 25 times the concentration required for normal physiology. Note that these concentrations were measured locally in the physiological environment with a reaction area of only 3 cm^2. When compared with the size of the human body, it is reasonable to surmise that the release of magnesium ions at this concentration would not affect the normal physiological function of the overall organism.

The surface treatment method proposed in this study was shown to slow the release of Mg ions to enable the gradual degradation of the material (Figure 9). Moreover, the degradation process fostered a microenvironment well-suited to the growth of osteocytes.

5 Conclusion

In this study, we sought to overcome the rapid degradation typical of Mg alloys when used as an implant material. This was achieved by preparing an Mg-Li alloy with a corrosion-resistant surface layer through the immersion of Mg alloy samples in a cell culture medium. The proposed surface treatment was shown to promote the formation of a surface coating, which enhanced the corrosion resistance of the Mg alloy and provided a microenvironment favorable for osteoblast attachment. The proposed surface modification scheme applies to the preparation of Mg alloy bone screws. The gradual degradation of the Mg alloy should delay the absorption of Mg ions by the human body, preserve the implant for a duration sufficient to ensure healing and eliminate the need for surgical resection, thereby avoiding the pain of secondary surgery. Note however that the effect of this surface treatment regimen on osseointegration will require further analysis. The proposed process is simple and easy to implement without the need for costly equipment.

Data availability statement

The original contributions presented in the study are included in the article/Supplementary Material, further inquiries can be directed to the corresponding author.

Author contributions

Conceptualization, J-YU and Y-SS; methodology, J-YU and Y-SS; software, C-CW and Y-SS; validation, J-YH and C-YF; formal analysis, YO; investigation, C-CW and J-YH; resources, C-CW; data curation, J-YH, J-YU, and Y-SS; writing—original draft preparation, Y-SS; writing—review and editing, Y-SS, C-YF, and YO; visualization, C-YF, Y-LK, and YO; supervision, Y-SS and W-JC; project administration, Y-SS and W-JC; funding acquisition, C-CW and Y-SS. All authors have read and agreed to the published version of the manuscript. All authors listed have made a substantial, direct, and intellectual contribution to the work and approved it for publication.

Funding

This research was funded by Ministry of Science and Technology, Taiwan (Grant No. 110-2314-B-038-029) and Taipei Medical University Hospital, Taiwan (Grant Nos. 110-TMUH-NE-11, TMU108-AE1-B44).

Acknowledgments

We would like to thank the Ministry of Science and Technology, Taiwan (110-2314-B-038-029) and Taipei Medical University Hospital (110-TMUH-NE-11) and Taipei Medical University (TMU108-AE1-B44) for their support in funding this project. We would also like to thank Professor Jyh-Wei Lee of Ming Chi University of Technology, Professor Her-Huang Huang of National Yang Ming Chiao Tung University, Professor Ren-Jei Chung of National Taipei University of Technology, and National Taiwan University of Science and Technology/National Chung Hsing University Precious Instrument Center for their assistance in the experiments. We would also like to thank Amli Materials Technology Co., Ltd. for providing the materials used in these experiments.

Conflict of interest

The authors declare that the research was conducted in the absence of any commercial or financial relationships that could be construed as a potential conflict of interest.

Publisher's note

References

Amukarimi, S., and Mozafari, M. (2021). Biodegradable magnesium-based biomaterials: An overview of challenges and opportunities. *MedComm* 2 (2), 123–144. doi:10.1002/mco2.59

Bang, L. T., Ramesh, S., Purbolaksono, J., Long, B. D., Chandran, H., Othman, R., et al. (2015). Development of a bone substitute material based on alpha-tricalcium phosphate scaffold coated with carbonate apatite/poly-epsilon-caprolactone. *Biomed. Mater. Eng.* 10 (4), 045011. doi:10.1088/1748-6041/10/4/045011

Cain, T. W., and Labukas, J. P. (2020). The development of β phase Mg–Li alloys for ultralight corrosion resistant applications. *npj Mater. Degrad.* 4 (17), 17–10. doi:10.1038/s41529-020-0121-2

Cao, D., Wu, L., Sun, Y., Wang, G., and Lv, Y. (2008). Electrochemical behavior of Mg–Li, Mg–Li–Al and Mg–Li–Al–Ce in sodium chloride solution. *J. Power Sources* 177 (2), 624–630. doi:10.1016/j.jpowsour.2007.11.037

Chang, C. T., Wang, J. Y., Chu, C. L., and Lee, S. (2006). Mechanical properties and microstructures of various Mg–Li alloys. *Mater. Lett.* 60 (27), 3272–3276. doi:10.1016/j.matlet.2006.03.052

Chen, L. Y., Zhang, H. Y., Zheng, C., Yang, H. Y., Qin, P., Zhao, C., et al. (2021). Corrosion behavior and characteristics of passive films of laser powder bed fusion produced Ti–6Al–4V in dynamic Hank's solution. *Mater. Des.* 208, 109907. doi:10.1016/j.matdes.2021.109907

Chen, Y., Chen, L., Wang, Y., Lin, K., and Liu, J. (2022). Lithium-containing bioactive glasses enhanced 3D-printed PLGA scaffolds for bone regeneration in diabetes. *Compos. B. Eng.* 230 (1), 109550–109562. doi:10.1016/j.compositesb.2021.109550

Chen, Y., Xu, Z., Smith, C., and Sankar, J. (2014). Recent advances on the development of magnesium alloys for biodegradable implants. *Acta Biomater.* 10 (11), 4561–4573. doi:10.1016/j.actbio.2014.07.005

Ebel, H., Günther, T., and Günther, H. E. T. (1980). Magnesium Metabolism: A review. *Clin. Chem. Lab. Med.* 18, 257–270. doi:10.1515/cclm.1980.18.5.257

Elin, R. J. (1987). Assessment of magnesium status. *Clin. Chem.* 33 (11), 1965–1970. doi:10.1093/clinchem/33.11.1965

Harrison, R., Maradze, D., Lyons, S., Zheng, Y., and Liu, Y. (2014). Corrosion of magnesium and magnesium–calcium alloy in biologically-simulated environment. *Prog. Nat. Sci. Mater. Int.* 24 (5), 539–546. doi:10.1016/j.pnsc.2014.08.010

Hornberger, H., Virtanen, S., and Boccaccini, A. (2012). Biomedical coatings on magnesium alloys–a review. *Acta Biomater.* 8 (7), 2442–2455. doi:10.1016/j.actbio.2012.04.012

Johnson, I., Perchy, D., and Liu, H. (2012). *In vitro* evaluation of the surface effects on magnesium-yttrium alloy degradation and mesenchymal stem cell adhesion. *J. Biomed. Mater. Res. A* 100 (2), 477–485. doi:10.1002/jbm.a.33290

Kannan, M. B., and Wallipa, O. (2013). Potentiostatic pulse-deposition of calcium phosphate on magnesium alloy for temporary implant applications—An *in vitro* corrosion study. *Mater. Sci. Eng. C* 33 (2), 675–679. doi:10.1016/j.msec.2012.10.017

Li, J., Wang, W., Li, M., and Liu, L. (2021). Repair of segmental bone defect using tissue engineered heterogeneous deproteinized bone doped with lithium. *Sci. Rep.* 11 (1), 4819. doi:10.1038/s41598-021-84526-w

Liu, J., Lin, Y., Bian, D., Wang, M., Lin, Z., Chu, X., et al. (2109). *In vitro* and *in vivo* studies of Mg-30Sc alloys with different phase structure for potential usage within bone. *Acta Biomater.* 98 (1), 50–66. doi:10.1016/j.actbio.2019.03.009

Lu, Y., Deshmukh, S., Jones, I., and Chiu, Y. (2021). Biodegradable magnesium alloys for orthopedicorthopedic applications. *Biomater. Transl.* 2, 00. doi:10.12336/biomatertransl.2021.01.000

Peng, S., Chen, L.-Y., Zhao, C., Wang, Z.-X., Wang, H., Lu, S., et al. (2019). Particle size-dependent Microstructure, hardness and electrochemical corrosion behavior of Atmospheric plasma Sprayed NiCrBSi coatings. *Metals - Open Access Metallurgy J.* 9, 1342. doi:10.3390/met9121342

Rahman, M., Dutta, N. K., and Roy Choudhury, N. (2020). Magnesium alloys with tunable interfaces as bone implant materials. *Front. Bioeng. Biotechnol.* 10 (8), 564–585. doi:10.3389/fbioe.2020.00564

Rahulan, N., Gopalan, S., and Kumaran, S. (2019). Effect of lithium on the mechanical behavior of magnesium. *Mater. Today Proc.* 18 (1), 2573–2580. doi:10.1016/j.matpr.2019.07.115

Razavi, M., Fathi, M., Savabi, O., Vashaee, D., and Tayebi, L. (2014). Improvement of biodegradability, bioactivity, mechanical integrity and cytocompatibility behavior of biodegradable mg based orthopedic implants using nanostructured bredigite (Ca7MgSi4O16) bioceramic coated via ASD/EPD technique. *Ann. Biomed. Eng.* 42 (12), 2537–2550. doi:10.1007/s10439-014-1084-7

Song, Y., Shan, D., Chen, R., and Han, E. H. (2009). Corrosion characterization of Mg–8Li alloy in NaCl solution. *Corros. Sci.* 51 (5), 1087–1094. doi:10.1016/j.corsci.2009.03.011

Staiger, M. P., Pietak, A. M., Huadmai, J., and Dias, G. (2006). Magnesium and its alloys as orthopedic biomaterials: A review. *Biomaterials* 27 (9), 1728–1734. doi:10.1016/j.biomaterials.2005.10.003

Sun, L., Zhao, B. C., Wang, T., Cui, J. Y., Zhang, S., Li, F., et al. (2020). Surface characterization and corrosion resistance of biomedical AZ31 Mg alloy treated by micro-arc fluorination. *Scanning* 2020, 5936789. doi:10.1155/2020/5936789

Toorani, M., Aliofkhazraei, M., and Naderi, R. (2019). Ceria-embedded MAO process as pretreatment for corrosion protection of epoxy films applied on AZ31-magnesium alloy. *J. Alloys Compd.* 785, 669–683. doi:10.1016/j.jallcom.2018.12.257

Tsakiris, V., Tardei, C., and Clicinschi, F. M. (2021). Biodegradable Mg alloys for orthopedic implants–A review. *J. Magnesium Alloys* 9 (6), 1884–1905. doi:10.1016/j.jma.2021.06.024

Wang, H., Zhu, S., Wang, L., Feng, Y., Ma, X., and Guan, S. (2014). Formation mechanism of Ca-deficient hydroxyapatite coating on Mg–Zn–Ca alloy for orthopaedic implant. *Appl. Surf. Sci.* 307 (1), 92–100. doi:10.1016/j.apsusc.2014.03.172

Wang, J., Ma, X. Y., Feng, Y. F., Ma, Z. S., Ma, C. T., Zhang, Y., et al. (2017). Magnesium ions promote the biological Behaviour of Rat Calvarial osteoblasts by activating the PI3K/Akt Signalling pathway. *Biol. Trace Elem. Res.* 179 (2), 284–293. doi:10.1007/s12011-017-0948-8

Witte, F. (2015). Reprint of: The history of biodegradable magnesium implants: A review. *Acta biomater.* 23, S28–S40. doi:10.1016/j.actbio.2015.07.017

Wolf, F. I., and Cittadini, A. (2003). Chemistry and biochemistry of magnesium. *Mol. Asp. Med.* 24 (1-3), 3–9. doi:10.1016/s0098-2997(02)00087-0

Yuan, Z., Wei, P., Huang, Y., Zhang, W., Chen, F., Zhang, X., et al. (2019). Injectable PLGA microspheres with tunable magnesium ion release for promoting bone regeneration. *Acta Biomater.* 85 (1), 294–309. doi:10.1016/j.actbio.2018.12.017

frontiers | Frontiers in Bioengineering and Biotechnology

TYPE Original Research
PUBLISHED 13 October 2023
DOI 10.3389/fbioe.2023.1269246

OPEN ACCESS

EDITED BY
Juncen Zhou,
Stony Brook University, United States

REVIEWED BY
Vadanasundari Vedarethinam,
Cornell University, United States
Yuyun Yang,
Harbin Engineering University, China

*CORRESPONDENCE
Xiao-Ying Lü,
luxy@seu.edu.cn

†These authors have contributed equally to this work and share first authorship

RECEIVED 29 July 2023
ACCEPTED 03 October 2023
PUBLISHED 13 October 2023

CITATION
Chen Y-Z, Huang Y and Lü X-Y (2023), Molecular mechanism of a novel root-end filling material containing zirconium oxide on the osteogenic/odontogenic differentiation of human osteosarcoma MG-63 cells.
Front. Bioeng. Biotechnol. 11:1269246.
doi: 10.3389/fbioe.2023.1269246

Molecular mechanism of a novel root-end filling material containing zirconium oxide on the osteogenic/odontogenic differentiation of human osteosarcoma MG-63 cells

Yao-Zhong Chen[1,2†], Yan Huang[2†] and Xiao-Ying Lü[2*]

[1]Department of Operative Dentistry and Endodontics, Zhongda Hospital, Medical College, Southeast University, Nanjing, China, [2]State Key Laboratory of Digital Medical Engineering, School of Biological Science and Medical Engineering, Southeast University, Nanjing, China

Although the novel root-end filling material containing zirconium oxide (NRFM-Zr) which is hydroxyapatite-based may promote osteoblast differentiation, the molecular mechanism remains unclear. The aim of this study is to investigate it underlying the osteogenic/odontogenic differentiation of human osteosarcoma MG-63 cells induced by NRFM-Zr, compared with calcium silicate-based mineral trioxide aggregate (MTA), and glass ionomer cement (GIC). Firstly, three different types of root filling materials were co-cultured with MG-63 cells, and their cell toxicity, alkaline phosphatase (ALP) activity, and calcium ion concentration were evaluated. Next, gene expression profiling microarray was employed to analyze the impact of the materials on the gene expression profile of MG-63 cells. The results of cell viability revealed that NRFM-Zr group had no significant difference compared to the negative control group. After 5 and 7 days of cultivation, both the NRFM-Zr and MTA groups exhibited significantly higher ALP activity compared to the negative control ($p < 0.05$). Moreover, the NRFM-Zr group had the highest calcium ion concentration, while the GIC group was the lowest ($p < 0.05$). Gene expression profiling microarray analysis identified 2915 (NRFM-Zr), 2254 (MTA) and 392 (GIC) differentially expressed genes, respectively. GO functional and KEGG pathway analysis revealed that differentially expressed genes of NRFM-Zr, MTA and GIC participated in 8, 6 and 0 differentiation-related pathways, respectively. Comparing the molecular mechanisms of osteogenic/odontogenic differentiation induced by hydroxyapatite-based NRFM-Zr and calcium silicate-based MTA, it was found that they shared similarities in their molecular mechanisms of promoting osteogenic differentiation. NRFM-Zr primarily promotes differentiation and inhibits cell apoptosis, thereby enhancing osteogenic/odontogenic differentiation of MG-63 cells. Furthermore, the inducing efficacy of NRFM-Zr was found to be superior to MTA.

KEYWORDS

root-end filling material, hydroxyapatite, gene expression profiling microarray, bioinformatics, osteogenic/odontogenic differentiation molecular mechanism

1 Introduction

When non-surgical retreatment of the root canal fails or cannot be undertaken, apical surgery is generally considered as the preferred treatment option. The main objective of apical surgery is to prevent microorganisms or their by-products from entering the surrounding periapical tissues by filling it with a tight root-end filling material (RFM) following root-end resection (von Arx, 2011). Therefore, the performance of the RFM is one of the key factors that influence the success rate of apical surgery.

Ideal RFM should not only present good biocompatibility, antimicrobial activity, non-toxicity, and radiopacity, but also exhibit osteogenic or odontogenic properties. This is because the RFM should have the capability to form hydroxyapatite, enabling creating a bond between with dentin, thus promoting a physiological seal. Currently, there are numerous root-end filling materials available in clinical practice; however, few of them present osteogenicity and odontogenicity (Koh et al., 1998).

As one of traditional non-bioactive RFMs, glass ionomer cement (GIC) has been widely used in the field of dentistry due to its excellent adhesive properties to dental tissues and the ability to release fluoride ions. However, it lacks bioactivity. Sangsuwan et al. (2015) showed that GIC inhibited alkaline phosphatase (ALP) activity and downregulated the expression of bone morphogenetic protein-2 (BMP-2) and osteopontin (OPN) genes in normal human osteoblasts. Additionally, GIC had been found to inhibit the formation of apatite in simulated body fluid (Kamitakahara et al., 2001).

Unlike traditional non-bioactive RFMs such as GIC and silver amalgam, mineral trioxide aggregate (MTA) is recognized as a bioactive material with properties of hard tissue conductivity and induction (Gandolfi et al., 2010). Torabinejad et al. (1995) showed that out of six root ends filled with MTA, five had complete cementum formation over the filling material, whereas cementum formation was absent on the surface of silver amalgam. Gandolfi et al. (2010) confirmed the formation of a layer of apatite on the surface of ProRoot MTA in a simulated body fluid containing phosphates. As a hydrated calcium-silicate cement material, MTA appears to have become the gold standard for root-end filling materials (von Arx, 2011; Sanz et al., 2021). However, MTA still has challenges such as long setting time, poor handling properties, and so on (Gandolfi et al., 2010; von Arx, 2011).

In recent years, our research group has developed a novel root-end filling material containing zirconium oxide (NRFM-Zr), whose main components are hydroxyapatite, calcium carboxylate, and zirconium dioxide, etc., therefore, it belongs to the hydroxyapatite-based materials (Chen Y. Z. et al., 2013; Chen et al., 2018). NRFM-Zr exhibits favorable physicochemical properties such as good washout resistance, radiopacity, and hydrophilicity, as well as excellent biocompatibility, making it a promising RFM. Moreover, NRFM-Zr is a bioactive material that can enhance ALP activity and mineral deposition in Saos-2 cells, indicating its potential to promote osteoblast differentiation (Chen et al., 2018). However, the molecular mechanism underlying its osteogenic/odontogenic differentiation effect remains unclear.

Gene expression profiling microarray technology enables the efficient and rapid detection and analysis of a large number of genes. When combined with bioinformatics analysis, it allows for a comprehensive study of gene-gene relationships, making it possible to elucidate the molecular mechanisms underlying the different effects of biomaterials on tissues and cells. For instance, gene expression profiling microarray technology has been applied to investigate the molecular mechanisms of osteogenic differentiation in calcium silicate-based materials such as MTA and iRoot BP (Kim et al., 2010; Torun et al., 2016). However, to date, there have been no comparative studies on the osteogenic/odontogenic differentiation mechanisms between calcium silicate-based materials (such as MTA) and hydroxyapatite-based materials (such as NRFM-Zr).

The aim of this study is to first compare the biocompatibility of NRFM-Zr, MTA, and GIC at the cellular level. Subsequently, gene expression profiling microarray technology combined with bioinformatics analysis will be used to investigate the molecular mechanisms underlying the osteogenic/odontogenic differentiation induction of human osteosarcoma MG-63 cells by NRFM-Zr at the molecular level.

2 Materials and methods

2.1 Materials preparation

The NRFM-Zr powder was composed of 34.4% hydroxyapatite, 34.4% tetracalcium phosphate, 7.2% solid polyacrylic acid, 2.4% solid citric acid, 1.6% sodium citrate, and 20.0% zirconium dioxide (by mass percentage) which was used to improve its radio-opacity (Chen et al., 2018; Mahgoub et al., 2019). NRFM-Zr circular disk samples in two sizes (diameter 5 mm × thickness 2 mm, diameter 20 mm × thickness 1 mm) was prepared as follows: the material powder was mixed with distilled water in a 5:1 mass ratio and then placed in a circular plastic plate which was stored at 37°C and 100% humidity for 1 day (Chen et al., 2018). Subsequently, the samples were sterilized for 12 h in an ethylene oxide sterilizer (Anprolene AN 74ix; Andersen, Haw River, NC, United States). Before conducting biological experiments, the samples were degassed for 7 days to remove residual ethylene oxide and rinsed with sterile phosphate-buffered saline (PBS) (Chen Y. Z. et al., 2013). Additionally, ProRoot MTA (Dentsply Tulsa Dental Specialties, Johnson City, TN, United States of America) and GIC (FX-II, Shofu, Inc., Kyoto, Japan) were used as control materials, which were fabricated according to the manufacturer's instructions, with powder/liquid mass ratios of 3.3:1 and 2.6:1, respectively (Chen et al., 2018).

2.2 Cell viability assay

The MG-63 cells (Institute of Cell Biology, Chinese Academy of Sciences, Shanghai, PRC) were cultured in calcium-containing MEM medium (Gibco Laboratories, Grand Island, United States) containing 10% fetal bovine serum, 0.15% sodium bicarbonate, penicillin (100 U/mL), and streptomycin (100 mg/mL) in a humidified atmosphere containing 5% CO_2 at 37°C. Logarithmic growth phase MG-63 cells were seeded at a density of 3×10^4 cells per well in a 24-well plate and incubated overnight (Ceci et al., 2015; Margunato, et al., 2015). The culture medium was then removed, and transwells (diameter 6.5 mm, Corning Gilbert Inc., Glendale, AZ, United States) containing test material samples (diameter 5 mm × thickness 2 mm) were placed in the wells. An empty

transwell without samples was served as the negative control group. The culture medium was changed every 3 days. After culturing for 3, 5, and 7 days respectively, the cell viability of each group was assessed using MTT assay (Chen Y. Z. et al., 2013). The optical density (OD) was measured at a wavelength of 492 nm using a microplate reader (Multiskan MK3, Thermo Labsystems Co., Shanghai, PRC). According to ISO 10993–5 (International Standards Organization, 2009), cell viability was calculated as a percentage using the following formula:

$$\text{Cell Viability\%} = \left(\text{OD}_{\text{test material}} / \text{OD}_{\text{negative control}}\right) \times 100\%$$

The cell toxicity grades were defined as follows: 0 (cell viability ≥100%), 1 (75%–99%), 2 (50%–74%), 3 (25%–49%), 4 (1%–24%), and 5 (0%) (Lü et al., 2009; Chen et al., 2018).

2.3 Alkaline phosphatase activity assay

MG-63 cells were seeded at a density of 3×10^4 cells per well in a 24-well plate and incubated overnight. The MEM medium was then replaced with osteogenic induction medium (100 nM dexamethasone, 10 mM β-glycerophosphate, and 50 μg/mL L-ascorbic acid (Sigma-Aldrich, St. Louis, MO, United States)). Transwells containing the test samples (diameter 5 mm × thickness 2 mm) were placed in the 24-well plate, and co-cultured with MG-63 cells for 3, 5, and 7 days respectively. After removing the samples, transwells and culture medium, the cells were washed twice with PBS. Then, 500 μL of 10 mM Tris-HCl buffer (pH 7.6) containing 0.1% Triton X-100 was added to each well. The ALP activity and total protein concentration of the cells were measured according to the instructions of the ALP assay kit (Nanjing Jiancheng Chemical Industrial Co., Ltd., Nanjing, China) (Chen et al., 2018). ALP activity was reported as nanomoles of p-nitrophenol produced per microgram of total protein, and the percentage of the sample group was calculated relative to the negative control group. An empty transwell was served as the negative control group.

2.4 Calcium ion concentration measurement

Samples of the three materials (diameter 5 mm × thickness 2 mm) were placed in a 24-well plate with one sample per well. Blank wells without the test materials were used as the negative control group. Each well was filled with 1 mL of MEM medium, which was changed every 3 days. After culturing for 3, 5, and 7 days respectively in a humidified atmosphere containing 5% CO_2 at 37°C, 100 μL of the culture medium was collected and the calcium ion concentration was measured using an AU5800 fully automated biochemical analyzer (Beckman Coulter Inc., Brea CA, United States) (Liu H. et al., 2020).

2.5 Gene expression profiling microarray experiment

MG-63 cells were seeded at a density of 7×10^4 cells/mL in a 6-well plate with 3 mL per well. After 24 h, the MEM medium was replaced with osteogenic induction medium. Three types of test samples (diameter 20 mm × thickness 1 mm) in transwells were co-cultured with MG-63 cells for 5 days, with an empty transwell without samples serving as the negative control group. Cells were rinsed with PBS (pH 7.2) twice, and total RNA from each group was extracted using Trizol reagent (Invitrogen Corporation, Grand Island, NY, United States). The quantity and quality of RNA were measured using a NanoDrop ND-1000 spectrophotometer (Thermo Fisher Scientific, Waltham, MA, United States), and the RNA integrity was assessed by standard denaturing agarose gel electrophoresis. The gene expression profiles of the cells in each sample were analyzed using a whole-genome oligo microarray (4 × 44K; Agilent Technologies, Inc., Santa Clara, CA, United States) (performed by Shanghai Kangcheng Biotechnology Company). Genes with a fold change ≥2 or ≤0.5 and a p-value <0.05, compared to the negative control group, were defined as upregulated or downregulated, respectively (Lü et al., 2009; Lü et al., 2010; Lü et al., 2014).

2.6 Bioinformatics analysis

First, the differential expression genes were analyzed using the DAVID online database (https://david.ncifcrf.gov/, 6 April 2023 version) to perform Gene Ontology (GO) analysis. Then, genes related to bone and tooth development were selected from the functional categories, and further analysis was conducted on the Kyoto Encyclopedia of Genes and Genomes (KEGG) pathways in which these genes are involved. And pathways at least two differentially expressed genes involved were selected.

2.7 Real-time fluorescent quantitative PCR analysis (qRT-PCR)

Four differentially expressed genes (*ENPP1*, *NPY*, *NOG* and *P2RX7*) associated with osteogenic/odontogenic differentiation of MG-63 cells were select for qRT-PCR analysis. *GAPDH* was served as the internal reference, and the primer sequences were listed in Table 1. The experiment was conducted in Shanghai Kangcheng Biotechnology Company.

2.8 Statistical analysis

All data were presented as mean ± standard deviation (mean ± SD). Statistical analysis of the data was performed using one-way analysis of variance (ANOVA), followed by Fisher's least significant difference (LSD) test or Dunnett's test for multiple comparisons using SPSS software (version 11.50; SPSS Inc., Chicago, IL, United States). Differences with $p < 0.05$ were considered statistically significant.

3 Results

3.1 Cell viability

The cell viability at different time points following the treatment with the three materials is shown in Table 2. Except for day 5 and

TABLE 1 Sequences of the used primers for the RT-PCR experiment.

Gene	Forward primer	Reverse primer
ENPP1	5′-CCCTTTGGACATCCTATACCGT-3′	5′-CTTTCTTCAGCATACTTTCGCAG-3′
NPY	5′-CGACACTACATCAACCTCATCA-3′	5′-GGTCTTCAAGCCGAGTTCTG-3′
NOG	5′-ACCGCCTCCAACCAGTT-3′	5′-GCAACAACCAGAATAAGTCTCT-3′
P2RX7	5′-GCCCTGTGTGGTCAACGAAT-3′	5′-AGGAATCGGGGGTGTGTCA-3′
GAPDH	5′-GGGAAACTGTGGCGTGAT-3′	5′-GAGTGGGTGTCGCTGTTGA-3′

TABLE 2 Cell viability and cytotoxicity grade for test materials in MTT assay (n = 4).

Test groups	3 days		5 days		7 days	
	Cell viability (%)	Toxicity grade	Cell viability (%)	Toxicity grade	Cell viability (%)	Toxicity grade
Negative control	100.00 ± 3.39	0	100.00 ± 6.70	0	100.00 ± 6.28	0
NRFM-Zr	98.40 ± 11.77	1	93.26 ± 9.25	1	95.80 ± 12.18	1
MTA	93.40 ± 9.42	1	80.91 ± 10.27[a]	1	84.94 ± 3.75[a]	1
GIC	86.48 ± 8.84	1	81.86 ± 8.30[a]	1	91.99 ± 3.99	1

The superscript letters indicate statistical significifance levels compared with the negative control at the same time (one-way ANOVA, followed by Dunnett's test. [a]$p < 0.05$; [b]$p < 0.01$).

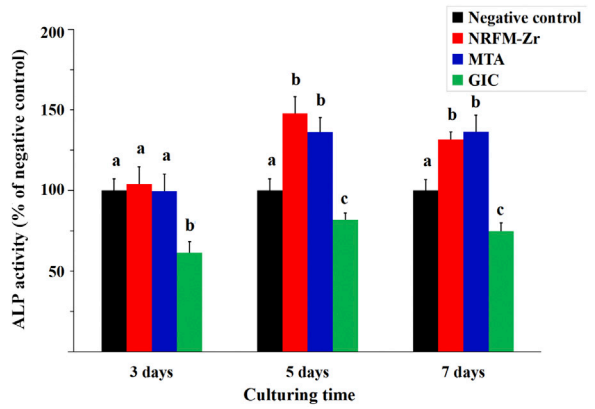

FIGURE 1
ALP activity of NRFM-Zr, MTA, GIC and negative control at various time intervals. Different letters above the bars indicate significant differences between the materials at the same time (one-way ANOVA followed by Fisher's LSD test, $p < 0.05$).

day 7 for MTA, and day 5 for GIC ($p < 0.05$), there were no statistically significant differences in cell viability between the test groups and the negative control group ($p > 0.05$). The toxicity level of the experimental materials was classified as grade 1.

3.2 Alkaline phosphatase activity

Figure 1 shows that the ALP activity in the NRFM-Zr and MTA groups was significantly higher than the negative control on day 5 and day 7 ($p < 0.05$), while there was no significant difference on day 3 ($p > 0.05$). The ALP activity in the GIC group was significantly lower than the other three groups at all intervals ($p < 0.05$).

3.3 Calcium ion concentration

The calcium ion concentration of the test materials is shown in Table 3. Among them, the calcium ion concentration NRFM-Zr was significantly higher than the other three groups at all intervals ($p < 0.05$), while that of GIC was lower than the other groups ($p < 0.05$). Compared to the negative control group, MTA showed a higher calcium ion concentration on day 3 ($p < 0.05$), while there were no significant differences on day 5 and day 7 ($p > 0.05$).

3.4 Gene expression profiling microarray experiment

Table 4 shows the number of differentially expressed genes (fold change ≥2 or ≤0.5, $p < 0.05$) in the NRFM-Zr and MTA groups, which were 2915 and 2254, respectively, higher than the number in the GIC group (392). Additionally, in each group, the number of downregulated genes was greater than the number of upregulated genes. Detailed gene information can be found in Supplementary Tables S1–S3.

3.5 Bioinformatics analysis

3.5.1 Gene ontology functional analysis

The total number of GO functional categories involved in the differentially expressed genes in the NRFM-Zr, MTA, and GIC

TABLE 3 Calcium ion concentration of test materials (n = 4).

Test groups	3 days (mmol/L)	5 days (mmol/L)	7 days (mmol/L)
Negative control	1.19 ± 0.03[a]	1.17 ± 0.03[a]	1.18 ± 0.02[a]
NRFM-Zr	4.85 ± 0.23[b]	1.60 ± 0.29[b]	1.45 ± 0.15[b]
MTA	1.45 ± 0.04[c]	1.20 ± 0.03[a]	1.19 ± 0.12[a]
GIC	0.65 ± 0.16[d]	0.90 ± 0.09[c]	1.01 ± 0.03[c]

Different letters indicate significant differences between the materials at the same time (one-way ANOVA, followed by Fisher's LSD test, $p < 0.05$).

TABLE 4 The numbers of differentially expressed genes and their involved GO terms.

Test groups	Differentially expressed genes			GO terms		
	Upregulated	Downregulated	Total	Biological process	Cellular component	Molecular function
NRFM-Zr	1096	1819	2915	1715	189	192
MTA	955	1299	2254	1396	197	154
GIC	193	199	392	405	75	45

TABLE 5 Osteogenesis-related and odontogenesis-related GO terms in NRFM-Zr and MTA treated groups.

GO BP terms		NRFM-Zr		MTA	
		Count	*p*-Value	Count	*p*-Value
Osteogenesis-related	GO:0030278~Regulation of ossification	48	2.21E-05	35	2.19E-03
	GO:0001503~Ossification	74	9.17E-05	57	1.92E-03
	GO:0030279~Negative regulation of ossification	20	4.45E-03	17	5.98E-03
	GO:0045667~Regulation of osteoblast differentiation	28	5.44E-03	21	3.57E-02
	GO:0045668~Negative regulation of osteoblast differentiation	15	5.76E-03	13	6.61E-03
	GO:0045778~Positive regulation of ossification	21	1.19E-02	17	2.52E-02
	GO:0001649~Osteoblast differentiation	39	1.41E-02		
	GO:0002076~Osteoblast development	6	4.47E-02		
Odontogenesis-related	GO:0042476~Odontogenesis	30	2.30E-04	21	1.29E-02
	GO:0042475~Odontogenesis of dentin-containing tooth	16	4.48E-02		

groups were listed in Table 4. In order to analyze the effects of these three materials on osteogenesis and odontogenesis, the functional categories related to osteogenic/odontogenic differentiation were further screened from the biological process (BP) categories. The results were presented in Table 5.

In the NRFM-Zr group, 8 GO functional categories related to osteogenesis and 2 categories related to odontogenesis were identified, involving 92 differentially expressed genes (43 upregulated and 49 downregulated; detailed information could be found in Supplementary Table S4). In the MTA group, 6 GO functional categories related to osteogenesis and 1 category related to odontogenesis were found, involving 71 differentially expressed genes (37 upregulated and 34 downregulated; detailed information can be found in Supplementary Table S5). There were 52 common genes between the two groups. However, the GIC group did not show any GO functional categories related to osteogenesis or odontogenesis.

3.5.2 Kyoto encyclopedia of genes and genomes pathway analysis

The 92 genes identified from the NRFM-Zr group and the 71 genes from the MTA group, which were related to osteogenesis and odontogenesis as selected in Section 3.5.1, were subjected to KEGG pathway analysis. It was found that the differentially expressed genes in the NRFM-Zr group were involved in 89 pathways, while those in the MTA group were involved in 46 pathways. Among them, there were 8 pathways related to osteogenic/odontogenic differentiation in the NRFM-Zr group and 6 pathways in the MTA group. The detailed information could be found in Table 6. The pathway maps and the genes involved were shown in Figures 2, 3.

TABLE 6 Pathways and genes associated with osteogenic/odontogenic differentiation in the NRFM-Zr and MTA Groups.

No.	Pathway	NRFM-Zr	MTA
1	PI3K-Akt signaling pathway	12 (*AREG*, *BCL2L11*, *FGF4*, *FGF8*, *FGFR3*, *LAMB1*, *BCL2*, *CREB3L1*, *EGFR*, *FGF2*, *FGFR2*, *SPP1*)	8 (*AREG*, *BCL2L11*, *FGF4*, *FGF8*, *FGFR3*, *LAMB1*, *COMP*, *LAMA5*)
2	MAPK signaling pathway	7 (*AREG*, *FGF4*, *FGF8*, *FGFR3*, *EGFR*, *FGF2*, *FGFR2*)	4 (*AREG*, *FGF4*, *FGF8*, *FGFR3*)
3	TGF-β signaling pathway	6 (*BMP5*, *BMP6*, *BMP8B*, *INHBA*, *NOG*, *CHRD*)	5 (*BMP5*, *BMP6*, *BMP8B*, *INHBA*, *NOG*)
4	EGFR tyrosine kinase inhibitor resistance	6 (*BCL2L11*, *FGFR3*, *BCL2*, *FGF2*, *EGFR*, *FGFR2*)	2 (*BCL2L11*, *FGFR3*)
5	Wnt signaling pathway	4 (*AXIN2*, *WNT3A*, *WNT7B*, *SFRP2*)	4 (*AXIN2*, *WNT3A*, *WNT7B*, *FZD9*)
6	JAK-STAT signaling pathway	3 (*IL6ST*, *BCL2*, *EGFR*)	2 (*IL6ST*, *LEP*)
7	ErbB signaling pathway	2 (*AREG*, *EGFR*)	
8	cGMP-PKG signaling pathway	2 (*CREB3L1*, *SLC8A1*)	

Red letters indicate upregulated genes and green letters indicate downregulated genes.

3.6 qRT-PCR results

Figure 4 shows the fold changes of the 4 genes (*ENPP1*, *NPY*, *NOG* and *P2RX7*) associated with osteogenesis and odontogenesis from qRT-PCR and gene expression profiling microarray. The expression trends of the two methods were largely consistent, demonstrating the reliability of the gene expression profiling microarray experiment results.

4 Discussion

4.1 Cell viability

Given that RFMs come into direct contact with periapical tissues, ideal RFMs should present desirable cytocompatibility. The results of this study (Table 2) showed that the cell viability of NRFM-Zr co-cultured with MG-63 cells ranged from 93.26% to 98.40% at three time points. Our previous research demonstrated that the extract of freshly prepared or set NRFM-Zr exhibited good cell compatibility with L929 mouse fibroblasts (Chen et al., 2018). These results indicate that NRFM-Zr has favorable cell compatibility. Additionally, this study also showed that the cell viability of MTA (at 5 and 7 days) and GIC (at 5 days) was significantly lower than the negative control group ($p < 0.05$), although their cell toxicity levels were also classified as grade 1. These findings are consistent with other studies (Keiser et al., 2000; Chen Y. Z. et al., 2013; Chen et al., 2018), such as the study by Keiser et al. (2000) which demonstrated that high concentrations of MTA extract had an inhibitory effect on human periodontal ligament cell proliferation. However, other studies have shown that MTA does not exhibit cytotoxicity towards human periodontal ligament cells (Gorduysus et al., 2007).

4.2 Alkaline phosphatase activity

Apart from desirable cytocompatibility, osteogenic/odontogenic performance is another important property of RFMs. ALP activity is a marker of early differentiation of osteoblasts (Fan et al., 2015), therefore, in this study, ALP activity was used to investigate the osteogenic/odontogenic differentiation potential of NRFM-Zr. The results showed that the NRFM-Zr group at day 5 and day 7 exhibited significantly higher ALP activity compared to the negative control group ($p < 0.05$). Our previous research also demonstrated that the extract of NRFM-Zr significantly increased the ALP activity of Saos-2 cells (Chen et al., 2018). Similar to NRFM-Zr, MTA at day 5 and day 7 significantly increased the ALP activity of MG-63 cells ($p < 0.05$), which is consistent with previous studies (Chang et al., 2014). For example, Chang et al. (2014) showed that MTA increased ALP activity and promoted mineralized nodule formation in human dental pulp cells. In contrast, the ALP activity of GIC was significantly lower than the negative control at all time points. Chen et al. (2002) found that GIC and resin-modified light-cured GIC inhibited the ALP activity of human dental pulp fibroblasts. Therefore, NRFM-Zr and MTA can promote the osteogenic/odontogenic differentiation of MG-63 cells, while GIC inhibits the osteogenic/odontogenic differentiation of MG-63 cells.

4.3 Calcium ion concentration

Calcium ions may play an important role in the formation and mineralization of hard tissues, therefore, the calcium ion concentration of the materials was also tested in this study. The results showed that the calcium ion concentration of NRFM-Zr ranged from 1.45 to 4.85 mmol/L, which was significantly higher than the negative control group. The increase of extracellular calcium ion concentration could cause a dramatic increase of intracellular calcium ion concentration through calcium channels (Zayzafoon, 2006). Jung et al. (2010) further showed that HA-released Ca^{2+} improved the MC3T3-E1 cell differentiation by increasing bone sialoprotein and osteopontin expression through L-type calcium channel which triggered calcium/calmodulin mediated calcium/calmodulin-dependent protein kinase 2 (CaM–CaMK2) pathway. Moreover, Maeno et al. (2005) demonstrated that slightly higher concentrations of calcium ions are beneficial for osteoblast differentiation and matrix mineralization. Therefore, the calcium ions released from the main components of NRFM-Zr, hydroxyapatite and carboxylate

10.3389/fbioe.2023.1269246

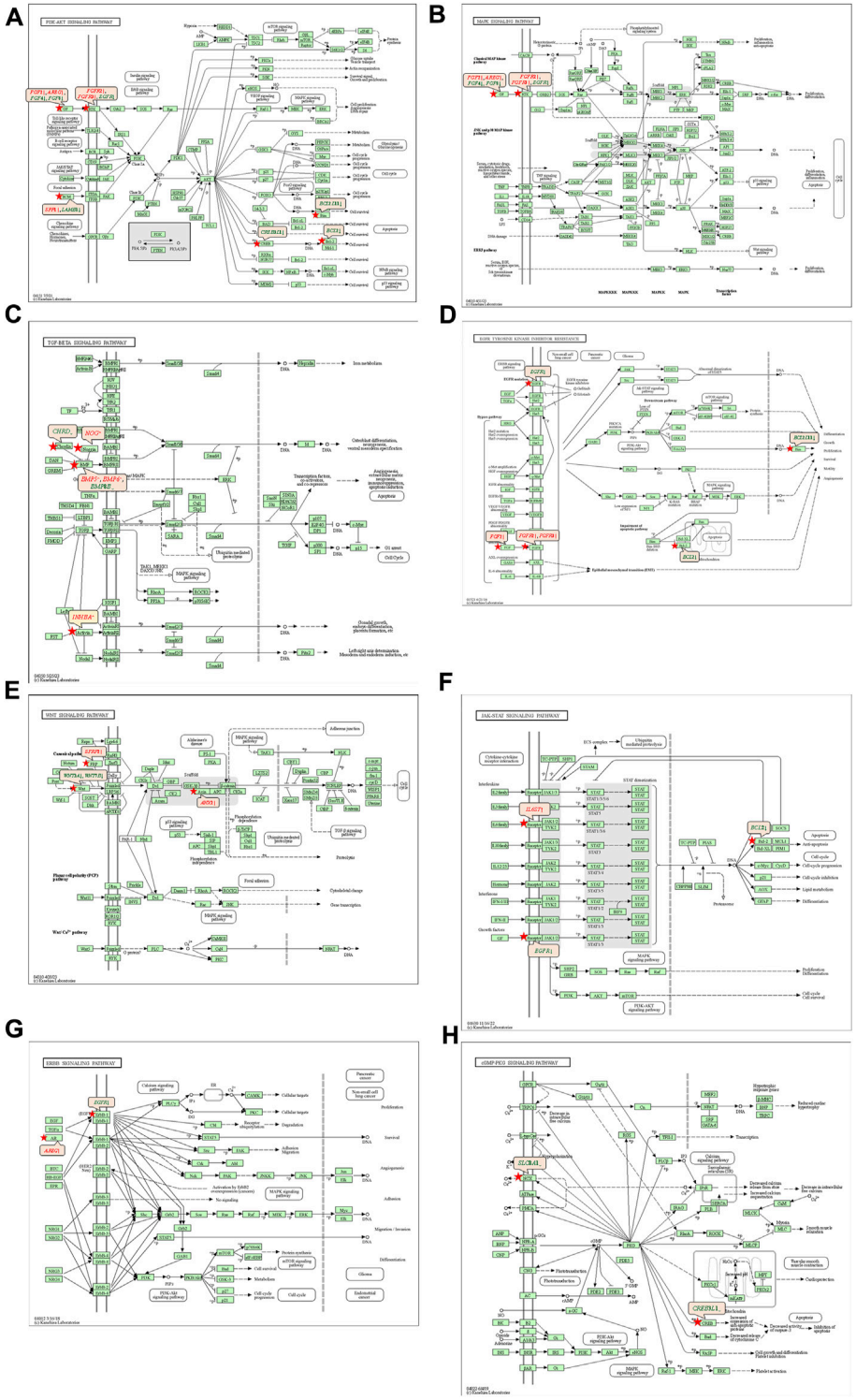

FIGURE 2
Pathways associated with osteogenic/odontogenic differentiation and the differentially epressed genes in the NRFM-Zr Group. **(A)** PI3K-Akt signaling pathway. **(B)** MAPK signaling pathway. **(C)** TGF-β signaling pathway. **(D)** EGFR tyrosine kinase inhibitor resistance. **(E)** Wnt signaling pathway. **(F)** JAK-STAT signaling pathway. **(G)** ErbB signaling pathway. **(H)** cGMP-PKG signaling pathway. Red letters indicate upregulated genes and green letters indicate downregulated genes.

calcium salts, are believed to promote the osteogenic/odontogenic differentiation of MG-63 cells. Similar to NRFM-Zr, MTA exhibited a higher calcium ion concentration (1.45 mmol/L) at day 3 ($p <$ 0.05). Many studies have indicated that MTA's promotion of osteoblast differentiation is not only associated with higher calcium ion concentration but also with alkaline pH values

FIGURE 3
Pathways associated with osteogenic/odontogenic differentiation and the differentially expressed genes in the MTA Group. **(A)** PI3K-Akt signaling pathway. **(B)** MAPK signaling pathway. **(C)** TGF-β signaling pathway. **(D)** EGFR tyrosine kinase inhibitor resistance. **(E)** Wnt signaling pathway. **(F)** ErbB signaling pathway. Red letters indicate upregulated genes and green letters indicate downregulated genes.

(Bonson et al., 2004; Matsumoto et al., 2013; Gandolfi et al., 2014). In contrast to NRFM-Zr and MTA, GIC exhibited an acidic pH and lower calcium ion concentration (0.65–1.01 mmol/L), thereby exerting an inhibitory effect on the osteogenic/odontogenic differentiation of MG-63 cells.

4.4 Gene expression profiling microarray experiment and bioinformatics analysis

To further investigate the molecular mechanisms underlying NRFM-Zr's promotion of osteogenic/odontogenic differentiation in MG-63 cells, this study conducted comprehensive analysis using gene expression profiling microarray and bioinformatics analysis. The results of the gene expression profiling microarray showed that the number of differentially expressed genes in the NRFM-Zr (2915) and MTA (2254) groups was much higher than in the GIC group (392), indicating that the former two had a greater impact on the gene expression profile of MG-63 cells than the latter. The results of GO functional analysis on the differentially expressed genes revealed that the 8 osteogenesis and 2 odontogenesis related categories involved in the NRFM-Zr group fully encompassed the 6 osteogenesis and 1 odontogenesis related categories in the MTA group ($p < 0.05$). Moreover, the two groups shared 52 consistently differentially expressed genes. These results suggested that NRFM-Zr and MTA might have some similar molecular mechanisms, with NRFM-Zr exerting a broader impact. In contrast, unlike the two aforementioned materials, the

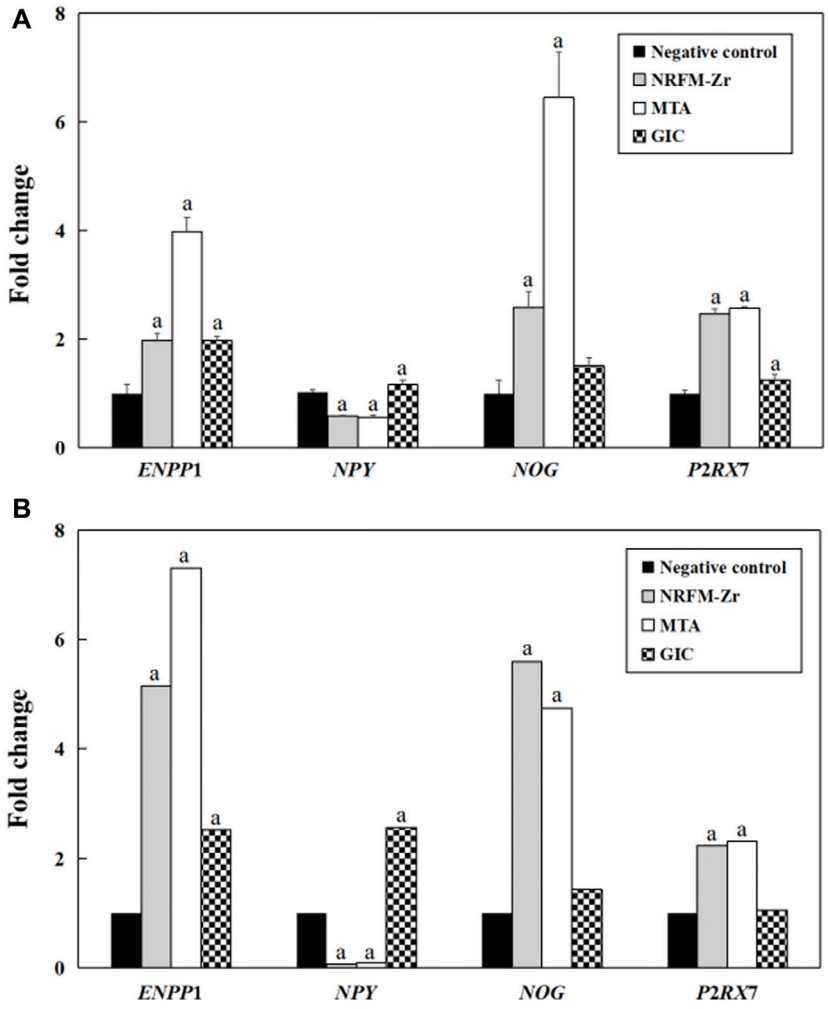

FIGURE 4
Validation of gene expression profiling microarray results by analyzing the expression levels of four genes with qRT-PCR. **(A)** qRT-PCR. **(B)** Gene expression profiling microarray. "a" represents $p < 0.05$ comparing with negative control.

GIC group did not show any osteogenesis and odontogenesis related functional categories, which supported its lack of significant promotion on osteogenic/odontogenic differentiation in MG-63 cells at the molecular level. Therefore, further discussion on GIC was not conducted in the subsequent sections.

The KEGG pathway analysis revealed that the NRFM-Zr group had more pathways (8) and a greater number of genes (24) associated with osteogenic/odontogenic differentiation compared to the MTA group (6 pathways, 19 genes). Among these pathways, 6 were common to both groups, while the NRFM-Zr group had 2 unique pathways (Table 6). This indicated that NRFM-Zr had a greater impact on the osteogenic/odontogenic differentiation of MG-63 cells compared to MTA.

4.4.1 PI3K-AKT signaling pathway and MAPK signaling pathway

From Table 6 and Figure 2, and Figure 3, it could be observed that genes involved in the PI3K-AKT signaling pathway in the NRFM-Zr/MTA group included all genes involved in the MAPK signaling pathway, EGFR tyrosine kinase inhibitor resistance pathway, and ErbB signaling pathway. Therefore, these four pathways would be discussed together.

The PI3K-Akt signaling pathway consists of PI3K and its downstream molecule Akt, which has been shown to be crucial for osteogenic differentiation, growth, and survival (Liu Y. et al., 2020). NRFM-Zr activates the PI3K-Akt signaling pathway in MG-63 cells, resulting in the downregulation of downstream genes *CREB3L1*, *BCL2*, and *BCL2L11*. *BCL2* is located downstream of *CREB3L1*, and studies by Moriishi et al. (2011, 2014) had shown that low expression of *BCL2* promoted osteogenic differentiation, while overexpression of *BCL2* inhibited osteogenic differentiation, reduced the progression of osteoblasts, and led to osteoblast apoptosis. Therefore, the downregulation of *BCL2* in this study might promote osteogenic differentiation of MG-63 cells. In addition, a study by Chen Y. T. et al. (2013) demonstrated that inhibition of Bim protein (BCL2L11) expression protected osteoblasts from apoptosis. Liang et al. (2008) also showed that partial protection against cell apoptosis could be achieved by specifically knocking out *Bim* in osteoblasts. In this study, the downregulation of the *BCL2L11* gene might protect MG-63 cells

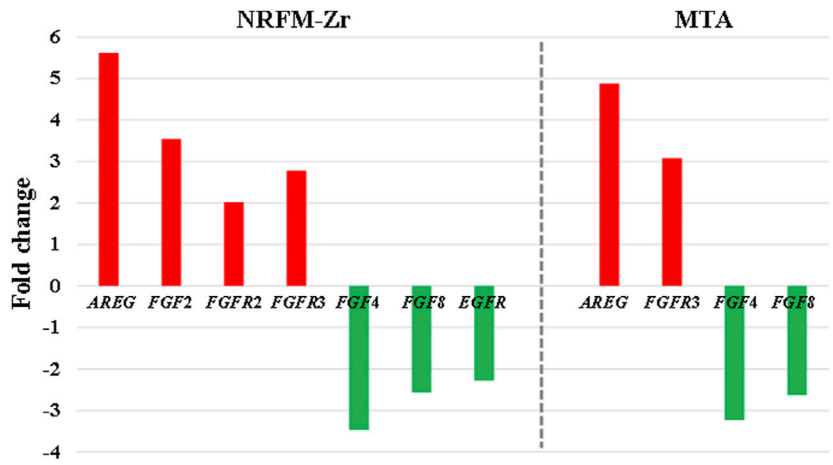

FIGURE 5
The fold changes of differentially expressed genes involved in the MAPK signaling pathway in the NRFM-Zr and MTA groups. To facilitate comparison, the fold changes of downregulated genes were represented as the negative reciprocal of their expression values.

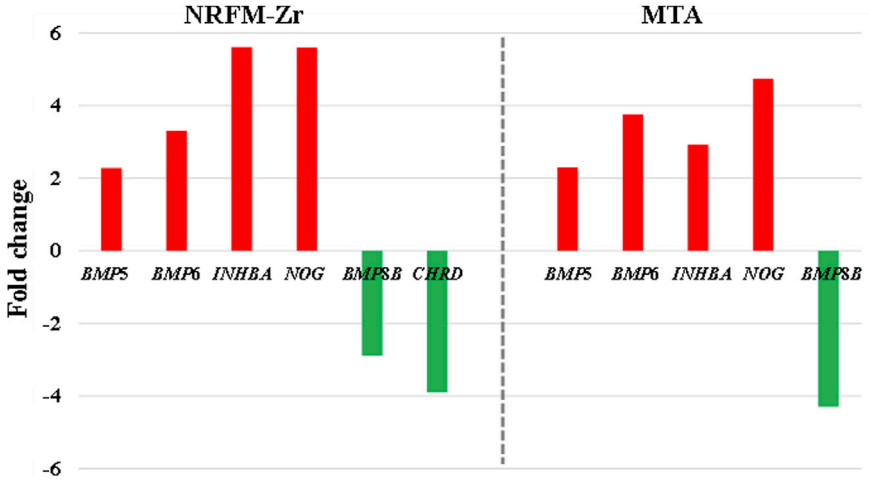

FIGURE 6
The fold changes of differentially expressed genes involved in the TGF-β signaling pathway between the NRFM-Zr and MTA groups. To facilitate comparison, the fold changes of downregulated genes were represented by the negative reciprocal of their expression values.

from apoptosis. Although MTA also activated the PI3K-Akt signaling pathway in MG-63 cells, it only exhibited downregulation of the *BCL2L11* gene downstream, suggesting that it might only play a role in inhibiting apoptosis, and its osteogenic differentiation potential might be lower than that of NRFM-Zr.

The MAPK signaling pathway mediates various physiological processes, including cell growth, development, proliferation, differentiation, aging, and death. Studies have shown that the MAPK signaling pathway promotes osteoblast proliferation, differentiation, and delayed apoptosis through various pathways (Luo et al., 2005; Greenblatt et al., 2022). In the NRFM-Zr group, there were 7 genes involved in this pathway, while the MTA group had 4 genes (Table 6). *AREG* is associated with bone physiology and intermittent parathyroid hormone treatment-mediated bone anabolic metabolism, and overexpression of *AREG* in osteoblasts could induce a high bone mass phenotype (Vaidya et al., 2015). *FGF2*, *FGF4*, and *FGF8* belong to the fibroblast growth factor family. *FGF2* not only directly participated in the regulation of osteogenic differentiation but also synergized with Wnt/beta-catenin, bone morphogenetic protein, and MAPK signaling pathways to regulate bone metabolism (Ahn et al., 2009). *FGF4* could affect osteogenic differentiation through the activation of MAPK-mediated signaling pathways (Kook et al., 2013). *FGF8* was an effective stimulator of Wnt/β-catenin protein activity and an important factor in tooth development (Kimura et al., 2022). Enhanced functionality of *FGFR2* could enhance Erk1/2 phosphorylation in bone marrow mesenchymal stem cells (BMSCs), thereby promoting osteogenic differentiation (Zhang et al., 2022). Downregulation of FGFR3 inhibited osteogenic

TABLE 7 Comparison of NRFM-Zr, MTA and GIC.

Contents	NRFM-Zr	MTA	GIC
Cell viability (%)	93.26–98.40	80.91–93.40	81.86–91.99
ALP activity	Significantly increased on day 5 and day 7	Significantly increased on day 5 and day 7	Lower than ALP activity in NRFM-Zr and MTA group
Ca^{2+} concentration (mmol/L)	1.45–4.85	1.19–1.45	0.65–1.01
GO functional categories related to osteogenesis and odontogenesis	10	7	0
Genes related to osteogenesis and odontogenesis	92	71	0
Pathways related to osteogenesis and odontogenesis	8	6	0
(1)PI3K-Akt signaling pathway	Downregulation of *BCL2* promoted differentiation	Downregulation of *BCL2L11* inhibited apoptosis	
	Downregulation of *BCL2L11* inhibited apoptosis		
(2)MAPK signaling pathway	4 genes favored osteogenic differentiation, while 3 genes hindered osteogenic differentiation	2 genes promoted osteogenic differentiation and 2 genes hindered osteogenic differentiation	
	The sum of fold change was +5.64 (greater than 0, indicating a favorable effect on differentiation)	The sum of fold change was +2.09	
(3)EGFR tyrosine kinase inhibitor resistance	4 genes promoted osteogenic differentiation and only 1 gene hindered osteogenic differentiation	1 gene promoted osteogenic differentiation	
(4)ErbB signaling pathway	The expression levels of *AREG* was greater than *EGFR*.		
(5)TGF-β signaling pathway	4 genes promoted osteogenic differentiation and 2 genes inhibited osteogenic differentiation	4 genes promoted osteogenic differentiation and 1 gene inhibited osteogenic differentiation	
	The sum of fold change was +10.02	The sum of fold change was +9.42	
(6) Wnt signaling pathway	The fold change of *AXIN2* was 2.21	The fold change of *AXIN2* was 2.02	
(7)JAK-STAT signaling pathway	The downregulation of *BCL2* promoted differentiation		
(8)cGMP-PKG signaling pathway	The downregulation of *CREB3L1* inhibited apoptosis		

differentiation of BMSCs in *TBXT* gene mutant mice (Su et al., 2023). EGFR is a tyrosine kinase involved in regulating cell homeostasis. EGFR and its ligands regulate key biological processes in cells, such as proliferation, survival, differentiation, and migration. Downregulation of *EGFR* had an inhibitory effect on osteogenesis (Ge et al., 2021). Among the 7 differentially expressed genes in the NRFM-Zr group, 4 genes (upregulated *AREG*, *FGF2*, *FGFR2*, *FGFR3*) promoted osteogenic differentiation, while 3 genes (downregulated *FGF4*, *FGF8*, *EGFR*) hindered osteogenic differentiation. In the MTA group, there were 2 genes each that promoted (upregulated *AREG*, *FGFR3*) or hindered (downregulated *FGF4*, *FGF8*) osteogenic differentiation. Overall, NRFM-Zr (the sum of fold change of was +5.64) exhibited a greater osteoinductive effect than MTA (the sum of fold change was + 2.09) (Figure 5). The EGFR signaling pathway (EGFR tyrosine kinase inhibitor resistance pathway in this study), is an important regulatory pathway in bone regulation and plays a crucial anabolic role in bone metabolism (Zhu et al., 2011). Among the 6 differentially expressed genes involved in this pathway induced by NRFM-Zr, 4 genes (upregulated *FGF2*, *FGFR2*, *FGFR3*, and downregulated *BCL2*) were favorable for osteoblastic differentiation, while only 1 gene (downregulated *EGFR*) was unfavorable. In contrast, the MTA group had only 1 gene (upregulated *FGFR3*) that was favorable for osteoblastic differentiation. This suggested that NRFM-Zr might have a greater potential for osteoinduction compared to MTA in terms of its effect on the EGFR signaling pathway.

The ErbB family couples extracellular growth factor ligands to intracellular signaling pathways that regulate various biological responses, including proliferation, differentiation, cell motility, and survival. This pathway was specific to the NRFM-Zr group and involved the upregulation of *AREG* and downregulation of *EGFR*. The fold change of *AREG* was greater than that of *EGFR* (as shown in Figure 5), indicating an overall promotion of osteoinductive effects.

4.4.2 TGF-β signaling pathway

The TGF-β signaling pathway plays a crucial role in various cellular functions, including proliferation, apoptosis, differentiation, and migration. During osteogenic differentiation, the TGF-β signaling pathway transmits signals through type I and type II serine/threonine kinase receptors (Almuraikhi, 2023).

In the NRFM-Zr group, there were 6 differentially expressed genes involved in this pathway. Among them, 4 genes (*BMP*5, *BMP*6, *INHBA*, and *NOG*) were beneficial for osteogenic differentiation (Hopwood et al., 2007; Zou et al., 2013), while 2 genes (*BMP*8*B* and *CHRD*) were unfavorable for osteogenic differentiation (Macsai et al., 2012; Wang et al., 2022). The MTA group also contained the same 4 beneficial genes and 1 unfavorable gene (*BMP*8*B*) for osteogenic differentiation. However, overall, NRFM-Zr (the sum of fold change was +10.02) might have a greater osteoinductive effect than MTA (the sum of fold change was + 9.42) (Figure 6).

4.4.3 Wnt signaling pathway

Wnt proteins are essential for the fundamental developmental processes in various species and organs, including cell fate specification, progenitor cell proliferation, and control of asymmetric cell division. Upon activation of the Wnt signaling pathway, β-catenin translocates to the nucleus and becomes stabilized, where it then binds to DNA-binding proteins of the TCF/LEF family and regulates osteogenesis through target genes mediated by Wnt (Sharma et al., 2022).

Both NRFM-Zr and MTA upregulate the downstream gene *AXIN*2 in the Wnt signaling pathway. *AXIN*2 facilitates the binding activity of I-SMAD and ubiquitin protein ligase, and it is involved in the regulation of centromere sister chromatid cohesion. It plays a role in multiple processes, including negative regulation of osteoblast differentiation and regulation of chondrocyte development. Previous study found that IL-35 enhanced the expression of key components, such as p-catenin and *Axin*2, in the Wnt/β-catenin pathway during the differentiation of mesenchymal stem cells into osteoblasts. This indicated that the upregulation of *Axin*2 suggested the occurrence of osteogenic differentiation (Li et al., 2023). The fold change of *AXIN*2 in the NRFM-Zr group (2.21) was slightly higher than that in the MTA group (2.02), suggesting that NRFM-Zr might have a slightly superior effect on osteogenic differentiation compared to MTA.

4.4.4 JAK-STAT signaling pathway

In mammals, the JAK/STAT pathway is a major signaling conduction mechanism for various cytokines and growth factors. The JAK/STAT pathway is involved in bone homeostasis and plays an important role in the proliferation and differentiation of certain cell types, including osteoblasts and osteoclasts (Sanpaolo et al., 2020). Compared to MTA, NRFM-Zr inhibited the expression of the downstream gene *BCL*2 in this pathway. The downregulation of BCL2 promoted osteoblast differentiation.

4.4.5 cGMP-PKG signaling pathway

cGMP is an intracellular second messenger that mediates the actions of nitric oxide and natriuretic peptides, regulating a wide range of physiological processes. Elevated intracellular cGMP levels exert their physiological effects through cGMP-dependent protein kinase (PKG), cGMP-regulated phosphodiesterases, and cGMP-gated cation channels, with PKG being a major mediator. PKG can also open mitochondrial ATP-sensitive K^+ channels, leading to the release of ROS for protective effects. This pathway is specific to the NRFM-Zr group and involved the downstream gene *CREB3L*1, and the downregulation of CREB3L1 was unfavorable for osteoblast differentiation (Hansamuit et al., 2020).

4.5 qRT-PCR

The comparison between the validation experiments by qRT-PCR and the gene expression profiling microarray results showed that although there were certain differences in the expression levels of genes such as *ENPP*1, the majority of the results were consistent. This indicated that the results obtained from the gene expression profiling microarray were reliable and reproducible.

5 Conclusion

In this study, gene expression profiling microarray and bioinformatics techniques were employed to comparatively investigate the impact molecular mechanisms underlying osteogenic/odontogenic differentiation of three different types of root-end filling materials (hydroxyapatite-based NRFM-Zr, calcium silicate-based MTA, and GIC) on MG-63 cells. The results revealed the following findings: 1) Hydroxyapatite-based and calcium silicate-based root-end filling materials shared similar molecular mechanisms in influencing osteogenic/odontogenic differentiation. 2) NRFM-Zr may promote the osteogenic/odontogenic differentiation of MG-63 cells through eight signaling pathways including PI3K-Akt and MAPK, as well as affecting the expression of related genes in these pathways which promote differentiation and inhibit cell apoptosis. 3)The inducing efficacy of NRFM-Zr was found to be superior to MTA due to desirable cell viability, ALP activity and calcium ion concentration (Table 7).

Based on the results of this study, not only have we found that NRFM-Zr appears as a suitable root-end filling material, but we have also basically elucidated its molecular mechanism in promoting osteogenic/odontogenic differentiation. However, further investigations are still needed to validate the key gene or pathway function obtained in this paper, and *in vivo* animal experiments need to be carried out to further verify its osteogenic/odontogenic properties and lay a foundation for future clinical applications.

Data availability statement

The original contributions presented in the study are included in the article/Supplementary Material, further inquiries can be directed to the corresponding author.

Author contributions

Y-ZC: Conceptualization, Data curation, Funding acquisition, Investigation, Writing–original draft. YH: Data curation, Writing–original draft. X-YL: Conceptualization, Funding acquisition, Project administration, Supervision, Writing–review and editing.

Funding

The author(s) declare financial support was received for the research, authorship, and/or publication of this article. This work was supported by the Research Fund of Oral Health Incubation Project for the Elderly of Health and Family Planning Commission of Jiangsu Province (Y-ZC).

Conflict of interest

The authors declare that the research was conducted in the absence of any commercial or financial relationships that could be construed as a potential conflict of interest.

Publisher's note

All claims expressed in this article are solely those of the authors and do not necessarily represent those of their affiliated organizations, or those of the publisher, the editors and the reviewers. Any product that may be evaluated in this article, or claim that may be made by its manufacturer, is not guaranteed or endorsed by the publisher.

Supplementary material

The Supplementary Material for this article can be found online at: https://www.frontiersin.org/articles/10.3389/fbioe.2023.1269246/full#supplementary-material

SUPPLEMENTARY TABLE S1
Differentially expressed genes of NRFM-Zr.

SUPPLEMENTARY TABLE S2
Differentially expressed genes of MTA.

SUPPLEMENTARY TABLE S3
Differentially expressed genes of GIC.

SUPPLEMENTARY TABLE S4
Osteogenesis-related and odontogenesis-related differentially expressed genes of NRFM-Zr.

SUPPLEMENTARY TABLE S5
Osteogenesis-related and odontogenesis-related differentially expressed genes of MTA.

References

Ahn, H. J., Lee, W. J., Kwack, K., and Kwon, Y. D. (2009). FGF2 stimulates the proliferation of human mesenchymal stem cells through the transient activation of JNK signaling. *FEBS Lett.* 583 (17), 2922–2926. doi:10.1016/j.febslet.2009.07.056

Almuraikhi, N. (2023). Inhibition of TGF-β type I receptor by SB505124 down-regulates osteoblast differentiation and mineralization of human mesenchymal stem cells. *Cell Biochem. Funct.* 41 (5), 564–572. doi:10.1002/cbf.3812

Bonson, S., Jeansonne, B. G., and Lallier, T. E. (2004). Root-end filling materials alter fibroblast differentiation. *J. Dent. Res.* 83 (5), 408–413. doi:10.1177/154405910408300511

Ceci, M., Beltrami, R., Chiesa, M., Colombo, M., and Poggio, C. (2015). Biological and chemical-physical properties of root-end filling materials: a comparative study. *J. Conserv. Dent.* 18 (2), 94–99. doi:10.4103/0972-0707.153058

Chang, S. W., Lee, S. Y., Kum, K. Y., and Kim, E. C. (2014). Effects of ProRoot MTA, Bioaggregate, and Micromega MTA on odontoblastic differentiation in human dental pulp cells. *J. Endod.* 40 (1), 113–118. doi:10.1016/j.joen.2013.09.036

Chen, C. C., Chen, R. C., and Huang, S. T. (2002). Enzymatic responses of human deciduous pulpal fibroblasts to dental restorative materials. *J. Biomed. Mater Res.* 60 (3), 452–457. doi:10.1002/jbm.1291

Chen, Y. T., Song, X. C., Zhang, F. P., and Liang, M. (2013). Expression of Bim, Bax and Bak in the process of gingipain-induced osteoblast apoptosis. *Zhonghua kou qiang yi xue za zhi* 48 (5), 272–277. doi:10.3760/cma.j.issn.1002-0098.2013.05.005

Chen, Y. Z., Lü, X. Y., and Liu, G. D. (2013). A novel root-end filling material based on hydroxyapatite, tetracalcium phosphate and polyacrylic acid. *Int. Endod. J.* 46 (6), 556–564. doi:10.1111/iej.12028

Chen, Y. Z., Lü, X. Y., and Liu, G. D. (2018). Effects of different radio-opacifying agents on physicochemical and biological properties of a novel root-end filling material. *PloS one* 13 (2), e0191123. doi:10.1371/journal.pone.0191123

Fan, J. Z., Yang, X., and Bi, Z. G. (2015). The effects of 6-gingerol on proliferation, differentiation, and maturation of osteoblast-like MG-63 cells. *Braz J. Med. Biol. Res.* 48 (7), 637–643. doi:10.1590/1414-431X20154494

Gandolfi, M. G., Siboni, F., Primus, C. M., and Prati, C. (2014). Ion release, porosity, solubility, and bioactivity of MTA Plus tricalcium silicate. *J. Endod.* 40 (10), 1632–1637. doi:10.1016/j.joen.2014.03.025

Gandolfi, M. G., Taddei, P., Tinti, A., and Prati, C. (2010). Apatite-forming ability (bioactivity) of ProRoot MTA. *Int. Endod. J.* 43 (10), 917–929. doi:10.1111/j.1365-2591.2010.01768.x

Ge, Y., Chen, Z., Fu, Y., Xiao, X., Xu, H., Shan, L., et al. (2021). Identification and validation of hub genes of synovial tissue for patients with osteoarthritis and rheumatoid arthritis. *Hereditas* 158 (1), 37. doi:10.1186/s41065-021-00201-0

Gorduysus, M., Avcu, N., Gorduysus, O., Pekel, A., Baran, Y., Avcu, F., et al. (2007). Cytotoxic effects of four different endodontic materials in human periodontal ligament fibroblasts. *J. Endod.* 33 (12), 1450–1454. doi:10.1016/j.joen.2007.08.017

Greenblatt, M. B., Shim, J. H., Bok, S., and Kim, J. M. (2022). The extracellular signal-regulated kinase mitogen-activated protein kinase pathway in osteoblasts. *J. Bone Metab.* 29 (1), 1–15. doi:10.11005/jbm.2022.29.1.1

Hansamuit, K., Osathanon, T., and Suwanwela, J. (2020). Effect of Jagged1 on the expression of genes in regulation of osteoblast differentiation and bone mineralization ontology in human dental pulp and periodontal ligament cells. *J. Oral Biol. Craniofac Res.* 10 (2), 233–237. doi:10.1016/j.jobcr.2019.12.003

Hopwood, B., Tsykin, A., Findlay, D. M., and Fazzalari, N. L. (2007). Microarray gene expression profiling of osteoarthritic bone suggests altered bone remodelling, WNT and transforming growth factor-beta/bone morphogenic protein signalling. *Arthritis Res. Ther.* 9 (5), R100. doi:10.1186/ar2301

International Standards Organization (2009). *Biological evaluation of medical devices. ISO 10993-5: Tests for in vitro cytotoxicity.*

Jung, G. Y., Park, Y. J., and Han, J. S. (2010). Effects of HA released calcium ion on osteoblast differentiation. *J. Mater Sci. Mater Med.* 21 (5), 1649–1654. doi:10.1007/s10856-010-4011-y

Kamitakahara, M., Kawashita, M., Kokubo, T., and Nakamura, T. (2001). Effect of polyacrylic acid on the apatite formation of a bioactive ceramic in a simulated body fluid: fundamental examination of the possibility of obtaining bioactive glass-ionomer cements for orthopaedic use. *Biomaterials* 22 (23), 3191–3196. doi:10.1016/s0142-9612(01)00071-0

Keiser, K., Johnson, C. C., and Tipton, D. A. (2000). Cytotoxicity of mineral trioxide aggregate using human periodontal ligament fibroblasts. *J. Endod.* 26 (5), 288–291. doi:10.1097/00004770-200005000-00010

Kim, Y. B., Shon, W. J., Lee, W., Kum, K. Y., Baek, S. H., and Bae, K. S. (2010). Gene expression profiling concerning mineralization in human dental pulp cells treated with mineral trioxide aggregate. *J. Endod.* 36 (11), 1831–1838. doi:10.1016/j.joen.2010.08.028

Kimura, M., Saito, A., Onodera, S., Nakamura, T., Suematsu, M., Shintani, S., et al. (2022). The concurrent stimulation of Wnt and FGF8 signaling induce differentiation of dental mesenchymal cells into odontoblast-like cells. *Med. Mol. Morphol.* 55 (1), 8–19. doi:10.1007/s00795-021-00297-3

Koh, E. T., McDonald, F., Pitt Ford, T. R., and Torabinejad, M. (1998). Cellular response to mineral trioxide aggregate. *J. Endod.* 24 (8), 543–547. doi:10.1016/S0099-2399(98)80074-5

Kook, S. H., Jeon, Y. M., Lim, S. S., Jang, M. J., Cho, E. S., Lee, S. Y., et al. (2013). Fibroblast growth factor-4 enhances proliferation of mouse embryonic stem cells via activation of c-Jun signaling. *PloS one* 8 (8), e71641. doi:10.1371/journal.pone.0071641

Li, Y., Wang, X., and Lu, J. (2023). Interleukin-35 promote osteogenesis and inhibit adipogenesis: role of wnt/β-catenin and PPARγ signaling pathways. *Inflammation* 46 (2), 522–533. doi:10.1007/s10753-022-01749-3

Liang, M., Russell, G., and Hulley, P. A. (2008). Bim, Bak, and Bax regulate osteoblast survival. *J. Bone Min. Res.* 23 (5), 610–620. doi:10.1359/jbmr.080106

Liu, H., Ma, Q., Han, X., and Huang, W. (2020a). Bone mineral density and its correlation with serum 25-hydroxyvitamin D levels in patients with hyperthyroidism. *J. Int. Med. Res.* 48 (2), 030006052090366. doi:10.1177/0300060520903666

Liu, Y., Wang, H., Zhou, X. Z., Li, N., Guo, Y. C., and Chen, T. P. (2020b). Pentraxin 3 promotes the osteoblastic differentiation of MC3T3-E1 cells through the PI3K/Akt signaling pathway. *Biosci. Rep.* 40 (6), BSR20201165. doi:10.1042/BSR20201165

Lü, X., Bao, X., Huang, Y., Qu, Y., Lu, H., and Lu, Z. (2009). Mechanisms of cytotoxicity of nickel ions based on gene expression profiles. *Biomaterials* 30 (2), 141–148. doi:10.1016/j.biomaterials.2008.09.011

Lü, X., Lu, H., Zhao, L., Yang, Y., and Lu, Z. (2010). Genome-wide pathways analysis of nickel ion-induced differential genes expression in fibroblasts. *Biomaterials* 31 (8), 1965–1973. doi:10.1016/j.biomaterials.2009.12.044

Lü, X., Wang, J., Li, B., Zhang, Z., and Zhao, L. (2014). Gene expression profile study on osteoinductive effect of natural hydroxyapatite. *J. Biomed. Mater Res. Part A* 102 (8), 2833–2841. doi:10.1002/jbm.a.34951

Luo, X. H., Guo, L. J., Yuan, L. Q., Xie, H., Zhou, H. D., Wu, X. P., et al. (2005). Adiponectin stimulates human osteoblasts proliferation and differentiation via the MAPK signaling pathway. *Exp. Cell Res.* 309 (1), 99–109. doi:10.1016/j.yexcr.2005.05.021

Macsai, C. E., Georgiou, K. R., Foster, B. K., Zannettino, A. C., and Xian, C. J. (2012). Microarray expression analysis of genes and pathways involved in growth plate cartilage injury responses and bony repair. *Bone* 50 (5), 1081–1091. doi:10.1016/j.bone.2012.02.013

Maeno, S., Niki, Y., Matsumoto, H., Morioka, H., Yatabe, T., Funayama, A., et al. (2005). The effect of calcium ion concentration on osteoblast viability, proliferation and differentiation in monolayer and 3D culture. *Biomaterials* 26 (23), 4847–4855. doi:10.1016/j.biomaterials.2005.01.006

Mahgoub, N., Alqadasi, B., Aldhorae, K., Assiry, A., Altawili, Z. M., and Tao, H. (2019). Comparison between iRoot BP plus (EndoSequence root repair material) and mineral trioxide aggregate as pulp-capping agents: a systematic review. *J. Int. Soc. Prev. Community Dent.* 9 (6), 542–552. doi:10.4103/jispcd.JISPCD_249_19

Margunato, S., Taşlı, P. N., Aydın, S., Karapınar Kazandağ, M., and Şahin, F. (2015). *In vitro* evaluation of ProRoot MTA, biodentine, and MM-MTA on human alveolar bone marrow stem cells in terms of biocompatibility and mineralization. *J. Endod.* 41 (10), 1646–1652. doi:10.1016/j.joen.2015.05.012

Matsumoto, S., Hayashi, M., Suzuki, Y., Suzuki, N., Maeno, M., and Ogiso, B. (2013). Calcium ions released from mineral trioxide aggregate convert the differentiation pathway of C2C12 cells into osteoblast lineage. *J. Endod.* 39 (1), 68–75. doi:10.1016/j.joen.2012.10.006

Moriishi, T., Kawai, Y., Komori, H., Rokutanda, S., Eguchi, Y., Tsujimoto, Y., et al. (2014). Bcl2 deficiency activates FoxO through Akt inactivation and accelerates osteoblast differentiation. *PloS one* 9 (1), e86629. doi:10.1371/journal.pone.0086629

Moriishi, T., Maruyama, Z., Fukuyama, R., Ito, M., Miyazaki, T., Kitaura, H., et al. (2011). Overexpression of Bcl2 in osteoblasts inhibits osteoblast differentiation and induces osteocyte apoptosis. *PloS one* 6 (11), e27487. doi:10.1371/journal.pone.0027487

Sangsuwan, J., Wanichpakorn, S., and Kedjarune-Leggat, U. (2015). Translationally controlled tumor protein supplemented chitosan modified glass ionomer cement promotes osteoblast proliferation and function. *Mater Sci. Eng. C Mater Biol. Appl.* 54, 61–68. doi:10.1016/j.msec.2015.04.036

Sanpaolo, E. R., Rotondo, C., Cici, D., Corrado, A., and Cantatore, F. P. (2020). JAK/STAT pathway and molecular mechanism in bone remodeling. *Mol. Biol. Rep.* 47 (11), 9087–9096. doi:10.1007/s11033-020-05910-9

Sanz, J. L., Rodríguez-Lozano, F. J., Lopez-Gines, C., Monleon, D., Llena, C., and Forner, L. (2021). Dental stem cell signaling pathway activation in response to hydraulic calcium silicate-based endodontic cements: a systematic review of *in vitro* studies. *Dent. Mater* 37 (4), e256–e268. doi:10.1016/j.dental.2021.01.025

Sharma, A. R., Sharma, G., Lee, Y. H., Chakraborty, C., Lee, S. S., and Seo, E. M. (2022). Sodium selenite promotes osteoblast differentiation via the WNT/ß-Catenin signaling pathway. *Cell J.* 24 (6), 309–315. doi:10.22074/cellj.2022.8314

Su, H., Yang, G., Yang, H. X., Liu, M. N., Li, X. D., Chen, L., et al. (2023). Downregulated FGFR3 expression inhibits *in vitro* osteogenic differentiation of bone marrow mesenchymal stem cells of mice with TBXT gene mutation. *Bull. Exp. Biol. Med.* 174 (4), 578–584. doi:10.1007/s10517-023-05750-0

Torabinejad, M., Hong, C. U., Lee, S. J., Monsef, M., and Pitt Ford, T. R. (1995). Investigation of mineral trioxide aggregate for root-end filling in dogs. *J. Endod.* 21 (12), 603–608. doi:10.1016/S0099-2399(06)81112-X

Torun, D., Torun, Z. Ö., Demirkaya, K., Sarper, M., Elçi, M. P., and Avcu, F. (2016). Gene expression changes in bioceramic paste-treated human dental pulp cells. *J. Oral Sci.* 58 (3), 307–315. doi:10.2334/josnusd.15-0600

Vaidya, M., Lehner, D., Handschuh, S., Jay, F. F., Erben, R. G., and Schneider, M. R. (2015). Osteoblast-specific overexpression of amphiregulin leads to transient increase in femoral cancellous bone mass in mice. *Bone* 81, 36–46. doi:10.1016/j.bone.2015.06.012

von Arx, T. (2011). Apical surgery: a review of current techniques and outcome. *Saudi Dent. J.* 23 (1), 9–15. doi:10.1016/j.sdentj.2010.10.004

Wang, Y. W., Lin, W. Y., Wu, F. J., and Luo, C. W. (2022). Unveiling the transcriptomic landscape and the potential antagonist feedback mechanisms of TGF-β superfamily signaling module in bone and osteoporosis. *Cell Commun Signal. Cell Commun. Signal. CCS* 20 (1), 190. doi:10.1186/s12964-022-01002-2

Zayzafoon, M. (2006). Calcium/calmodulin signaling controls osteoblast growth and differentiation. *J. Cell Biochem.* 97 (1), 56–70. doi:10.1002/jcb.20675

Zhang, Y., Ling, L., Ajay D/O Ajayakumar, A., Eio, Y. M., van Wijnen, A. J., Nurcombe, V., et al. (2022). FGFR2 accommodates osteogenic cell fate determination in human mesenchymal stem cells. *Gene* 818, 146199. doi:10.1016/j.gene.2022.146199

Zhu, J., Shimizu, E., Zhang, X., Partridge, N. C., and Qin, L. (2011). EGFR signaling suppresses osteoblast differentiation and inhibits expression of master osteoblastic transcription factors Runx2 and Osterix. *J. Cell Biochem.* 112 (7), 1749–1760. doi:10.1002/jcb.23094

Zou, S., Zhang, S., Long, Q., Cao, Y., and Zhang, W. (2013). Marker gene screening for human mesenchymal stem cells in early osteogenic response to bone morphogenetic protein 6 with DNA microarray. *Genet. Test. Mol. Biomarkers* 17 (8), 641–645. doi:10.1089/gtmb.2012.0449

frontiers | Frontiers in Bioengineering and Biotechnology

TYPE Original Research
PUBLISHED 06 November 2023
DOI 10.3389/fbioe.2023.1284359

OPEN ACCESS

EDITED BY
Xin Liu,
Shanghai Jiao Tong University School of Medicine, China

REVIEWED BY
Randall Scott Williamson,
University of Mississippi Medical Center, United States
Carlos Roberto Grandini,
São Paulo State University, Brazil

*CORRESPONDENCE
Penglai Wang,
penglai_w@163.com
Xiaoping Luo,
l_xiaoping@yahoo.com

RECEIVED 28 August 2023
ACCEPTED 23 October 2023
PUBLISHED 06 November 2023

CITATION
Wang L, Wang F, Ayisen S, Ren T, Luo X and Wang P (2023), Enhancing the mechanical properties and surface morphology of individualized Ti-mesh fabricated through additive manufacturing for the treatment of alveolar bone defects.
Front. Bioeng. Biotechnol. 11:1284359.
doi: 10.3389/fbioe.2023.1284359

Enhancing the mechanical properties and surface morphology of individualized Ti-mesh fabricated through additive manufacturing for the treatment of alveolar bone defects

Lingxu Wang[1], Fangfang Wang[2], Saimi Ayisen[2], Tianshui Ren[1], Xiaoping Luo[2]* and Penglai Wang[1]*

[1]School of Stomatology, Xuzhou Medical University, Xuzhou, China, [2]School of Stomatology, Nanjing University, Nanjing, China

Titanium meshes are widely utilized in alveolar bone augmentation, and this study aims to enhance the properties of titanium meshes through heat treatment (HT) and the synergistic finishing technology of electric field and flow field (EFSF). Our findings illustrate that the titanium mesh exhibits improved mechanical properties following HT treatment. The innovative EFSF technique, in combination with HT, has a substantial impact on improving the surface properties of titanium meshes. HT initiates grain fusion and reduces surface pores, resulting in enhanced tensile and elongation properties. EFSF further enhances these improvements by significantly reducing surface roughness and eliminating adhered titanium powder, a byproduct of selective laser melting printing. Increased hydrophilicity and surface-free energy are achieved after EFSF treatment. Notably, the EFSF-treated titanium mesh exhibits reduced bacterial adhesion and is non-toxic to osteoblast proliferation. These advancements increase its suitability for clinical alveolar bone augmentation.

KEYWORDS

additive manufacturing, titanium meshes, heat treatment, mechanical properties, synergistic finishing technology of electric field and flow field (EFSF), surface characteristics, bacterial adhesion

1 Introduction

Titanium meshes are widely used for repairing complex bone defects and have shown good bone augmentation effects (Merli et al., 2015 Boyne et al., 1985). When using commercial meshes, adapting to each patient's complicated atrophic bone structure takes considerable time and efforts, increasing the operation time and the risk of infection (Sumida et al., 2015). Compared with to prefabricated titanium meshes, additive manufacturing enables the production of customized three-dimensional titanium meshes. These meshes meet the individual needs of patients through preoperative design and digital virtual reconstruction. This approach facilitates precise bone grafting procedures, streamlines surgical processes, and shortens operation time, presenting promising clinical applications (Sumida et al., 2015).

Currently, titanium alloys such as Ti-6Al-4V (TC4) are commonly used for titanium mesh fabrication. However, the leakage of aluminum and vanadium from TC4 into the complex oral environment raises concerns about their potential harm to human bodies (Gomes et al., 2011; Rao et al., 1996). On the other hand, pure titanium offers several advantages. It is a single-element material that is lightweight with high specific strength, low thermal conductivity, minimal magnetism, x-ray translucency, excellent corrosion resistance, and favorable biological properties (Dong et al., 2020). However, pure titanium exhibits lower mechanical strength compared with titanium alloys.

In surgery, titanium meshes need to be sufficiently rigid to withstand pressure from the overlying flap, muscle movements, and chewing loads (Rakhmatia et al., 2013). Studies have suggested that an adult male individual can generate biting forces ranging from 45 to 68 kg (441.3–666.8 MPa), indicating that the bending fracture of the titanium mesh should be tested within this range (De Angelis et al., 2021). However, in the case of titanium mesh implantation, the surgical area typically does not directly bear the full force of occlusal pressures. A study suggests that stress from intraoral soft tissues can be the primary cause of displacement in bone grafting materials, leading to inadequate bone regeneration (Buser et al., 1996). Therefore, a testing pressure of 21N, which was intended to simulate the maximum force that healthy intraoral soft tissues could exert (Ulrich Sommer et al., 2014), was used to assess the mechanical performance of the titanium mesh (Lee et al., 2017) This approach provided a more realistic scenario of the conditions that the mesh was likely to encounter in clinical practice.

Selective laser melting (SLM) is a prevalent method in additive manufacturing. During the rapid cooling phase of the SLM process, significant temperature gradients are formed within the metal specimens, potentially causing deformation or curling. A proposed solution to these structural defects is HT, which has been successful in mitigating residual stresses and enhancing both the mechanical and biological properties of SLM-manufactured titanium meshes (Wang et al., 2020; Scarano et al., 2018; , 2020; Li et al., 2021). Studies indicate that HT refines grains, enhances fusion, increases the elongation rate, and improves the mechanical strength of the specimens (Wang et al., 2020; Li et al., 2021). However, to date, data on the strength characteristics of pure titanium meshes are lacking.

Furthermore, the additive manufacturing of titanium meshes results in the adherence of unmelted metal powder to the surfaces, making the surfaces highly rough and difficult to polish. The rough surfaces not only stimulate gingival attachment but can also contribute to bone adhesion, making retrieval more challenging. Once the titanium meshes are exposed to oral cavities, the rough surfaces provide favorable conditions for bacterial adhesion. Researches have shown that increased surface roughness enlarges the surface area of the materials; also, features such as pits, grooves, scratches, and cracks on rough surfaces can influence bacterial adhesion and serve as favorable sites for biofilm formation (Ribeiro et al.,2012; Santhosh Kumar et al., 2019). Highly roughened materials increase the likelihood of bacterial adherence, increasing wound healing duration and postoperative infection (Dank et al., 2019).

Various methodologies are currently employed for modifying the surface of titanium mesh, including mechanical abrasion, electrolytic polishing, sandblasting, computer numerical control machining, chemical mechanical polishing, and laser polishing (Wang et al., 2016). Notably, electrolytic polishing, in particular, is commonly employed to reduce the roughness of titanium implants produced through additive manufacturing. However, using corrosive chemicals in this approach raises concerns regarding environmental impact and safety. Electrochemical plasma polishing (ECPP) (combining conventional electrolysis with atmospheric plasma processes) has been used for removing contaminants and reducing oxide layers to address these issues (Yang et al., 2016). This synergistic technique produces exceptionally smooth and glossy surfaces with enhanced corrosion resistance. ECPP is an environmentally friendly and cost-effective approach, making it a promising choice for reducing the roughness of 3D-printed titanium implants (Zeidler et al., 2016). However, researches on ECPP for titanium mesh substrates are still limited.

This study aimed to optimize the mechanical and surface properties of additively manufactured pure titanium meshes using two methods: vacuum HT and a novel synergistic finishing technology called synergistic finishing technology of electric field and flow field (EFSF). The study evaluated the bending resistance, elongation rate, tensile strength, biocompatibility, and bacterial adhesion of the additively manufactured pure titanium meshes (before/after vacuum HT and with/without EFSF), thus providing experimental data for exploring the more promising titanium meshes.

TABLE 1 Chemical composition of the TA1 alloy powder.

Element	Ratio (%)
Ti	Bal
Fe	0.0021
C	0.0011
H	0.0049
O	0.012
N	0.002

2 Materials and methods

2.1 Preparation of experimental specimens

Commercially pure titanium (cpTi), which is used in current dental implants (McCracken, 1999), can be classified into four grades based on purity and oxygen content (Liu et al., 2017). These grades exhibit variations in corrosion resistance, ductility, and strength. This study selected flow-treated TA1 titanium powder (15–53 μm; Jiangsu Vilory Advanced Materials Technology Co., Ltd., China) (Table 1) as the powder material. Modeling and slicing were performed using Magics 22.0 software (Materialise, Belgium), and the Tr150 printer (Nanjing Qianzhi Intelligent Technology Co., Ltd., China) was employed for layer-by-layer laser printing under an argon atmosphere. Tables 2, 3, respectively, list the printing and HT parameters for As-built

TABLE 2 SLM titanium printing parameters.

Printing parameter	Laser intensity (W)	Scanning speed	Hatch space (μm)	Layer thickness (μm)
	120	1,000 mm/s	80	30

TABLE 3 HT parameters.

HT	Heating rate	Temperature (°C)	Hold time (h)	Method of cooling
	8°C/min	700	1.5	Air cooling

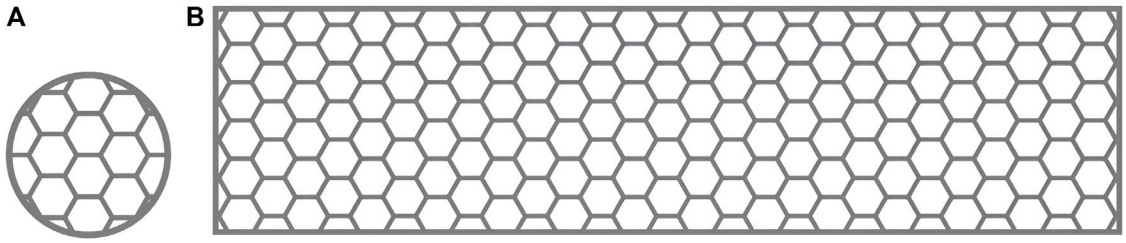

FIGURE 1
(A) Biological test specimen and **(B)** mechanical performance test specimen.

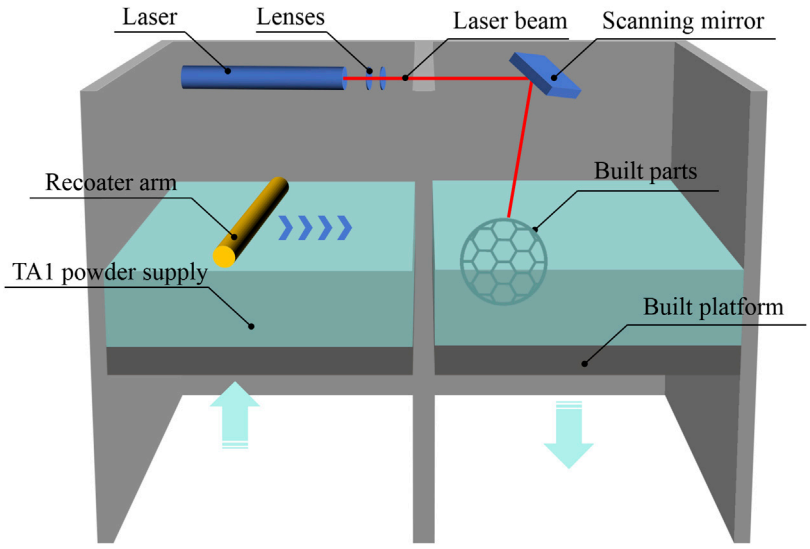

FIGURE 2
SLM printing process flowchart.

laser melting deposition parts. The printing parameters were set as follows: laser intensity of 120 W, scanning speed of 1,000 mm/s, and layer thickness of 0.030 mm. Wire cutting and support removal were conducted after printing, followed by sandblasting treatment (110-μm alumina sandblasting agent; Renfert, Germany), to refine the surface. HT was conducted in a vacuum HT furnace (RZF110014230S; Shanghai Refan High-Temperature Equipment Co., Ltd., China). Biological test specimens were prepared as circular disks with a diameter of 10 mm and a thickness of 0.3 mm (Figure 1A), as well as hexagonal mesh structures with a diameter of 2 mm (Figure 1). After ultrasonic cleaning (KQ-250DE; Kunshan Ultrasonic Instruments Co., Ltd., Suzhou, China) with deionized water, the specimens were soaked in ethanol for 3 h and then dried for further use.

According to the requirements of YB/T5349-2014 for the test specimens for evaluating mechanical performance, a rectangular

mesh thin-plate specimen with a length of 60 mm, a width of 15 mm, and a thickness of 0.3 mm was designed using 3-matic digital software. The mesh configuration was hexagonal (Figure 1B). The designed sample was saved in ". stl" format. The design file of the 0.3-mm sample was sent to a 3D printer, and the medical-grade pure titanium TA1 powder was used to print the mechanical performance test sample 2 of the titanium mesh. The relevant HT temperature and printing parameters were based on a previous study (Li et al., 2021) and the pilot experimental results. We processed the biological and mechanical performance test samples by printing and HT based on the requirements listed in Table 1. The SLM printing process flowchart for all specimens is depicted in Figure 2.

The mechanical performance test specimens were categorized into two groups: the As-built group and the heat-treated HT group. The specimens for biological testing and surface performance testing were categorized into the As-built, HT, and EFSF groups. The specimens in the EFSF group underwent surface treatment, and the samples were sequentially washed with an ultrasonic cleaner (90 kHz, 90 W output power), ethanol, and deionized water. The plasma polishing equipment (SFM20D-T; Nanjing Additive Manufacturing Research Institute Development Co., Ltd., China) was used, and an appropriate amount of electrolyte (2 wt% aqueous solution, pH = 5–7) was prepared in the working tank, with the electrolyte preheated to 55°C. The cathode tool and anode specimen were connected to the cathode and anode of the power supply system, respectively. The anode specimen was fixed in the working tank, rotating at 50 rpm centered on the workpiece axis. The micro-nano bubble generation device was activated, delivering an electrolyte containing micro-nano bubbles to the appropriate position on the surface of the anode specimen. The flow rate of this device was 0.6 m^3/h, and the gas dissolution rate was 10%. The plasma polishing process was initiated by activating the constant-voltage power supply set at 280 V, operating a frequency of 500 Hz, pulse width of 100 s, voltage of 350 V, current of 2.5 A, and a duration of 10 min. The workpiece was removed, cleaned, and dried after polish.

2.2 Experimental methods

2.2.1 Surface crystallographic observation

The As-built group and HT group samples were polished using standard metallographic procedures and etched with a corrosive solution (2 mL of HF + 4 mL of HNO3 + 94 mL of H2O). The microstructures were observed using a laser scanning confocal microscope (LSM800; Zeiss, Germany).

2.2.2 Mechanical testing

In the tensile test, the tensile strength and fracture elongation were measured for specimens in both the HT and the As-built groups. The test was conducted using a universal testing machine (Autograph DCS-10T; Shimadzu, Kyoto, Japan) at a crosshead speed of 1.0 mm/min. The tensile test was conducted using a video extensometer with a strain rate of 1×10^{3} s^{-1} at room temperature. The tensile performance of the samples was derived from the average of seven independent measurements for each group. The yield strength (σys) was calculated using the 2% offset method.

In the three-point bending test, each group contained seven samples. Three-point bending tests were performed using a computer-controlled electronic universal testing machine (MTS; MTS Systems, MN, USA) and following the requirements of ISO 7438:2020. At an ambient temperature of 28°C, a force at a rate of 1 mm/min was applied vertically on the centerline of the samples. Constant vertical pressure was applied until the specimen was fractured, and the maximum bending or breaking force was recorded. The bending strength was calculated from the linear elastic area of the stress–strain curve. The calculation formula was as follows:

$$\sigma = \frac{3FL}{2bh^2}$$

where σ represents the bending strength (MPa), F represents the maximum bending force (N), L represents the beam span (mm), b represents the sample width (mm), and h represents the sample height (mm). Seven specimens were tested for each group, and the data were presented as mean ± standard deviation.

For the As-built and HT groups, Vickers hardness (WHW Microcre Optics-Mech; Shanghai Yanrun Optomechanical Technology Co., Ltd., China) was assessed on five specimens from each group. The measurements were conducted using a 9.8-kg load and a dwell time of 10 s at five distinct locations per specimen. Vickers hardness indentations appeared as diamond-shaped marks with a central "+" symbol. The Vickers hardness was calculated by measuring the lengths of the two extended diagonals of this symbol.

2.2.3 Surface characterization

The internal scaffold and outer edge of the polished specimens were observed under a stereo microscope at a magnification of 100 times. The surface roughness of the three groups of titanium specimens was measured using a JB-4C precision surface roughness tester (Shanghai Taiming Optical Instrument Co., Ltd., Shanghai, China). Five specimens were randomly selected from each group, and three measurement points were taken on each specimen. The parameters of average roughness (Ra) and root mean square deviation (Rz) were determined. Ra corresponded to the arithmetic mean of the absolute values of the deviations of the profiles of a given sample length. Rz corresponded to the sum of the maximum peak height and the maximum valley depth within the sampling length. The water contact angle of the samples was measured at room temperature using a contact angle meter (JC 2000D2A; Shanghai Zhongchen, China) with a droplet volume of 0.013 mL, and three measurements were taken and averaged. The contact angle was measured with two different liquids, water and diiodomethane, to calculate the surface free energy (SFE). The SFE was calculated using the Owens and Wendt equation (Kasemo and Gold, 1999):

$$\gamma_L \cdot (1 + \cos\theta) = 2 \cdot \left(\left(\gamma_L^d \cdot \gamma_S^d \right)^{\frac{1}{2}} + \left(\gamma_L^p \cdot \gamma_S^p \right)^{\frac{1}{2}} \right)$$

2.2.4 Bacterial culture and adhesion

Further, 1 mL of *Staphylococcus aureus* (Sa) 8325-4 was placed in a test tube, and 5 mL of Luria–Bertani (LB) culture (containing

1% glucose) medium (without antibiotics) was added to it. The tube was then placed on a shaker overnight (37°C, 250 rpm, 12 h) and stored at 4°C for later use. The bacterial suspension density was adjusted to 1 × 109 CFU/mL using a serial dilution and plate counting method with 1 μL of the bacterial suspension. LB culture medium was added to the liquid until the final density reached 1 × 106 CFU/mL. The metal samples were divided into three groups: As-built group, HT228group, and heat-treated followed by EFSF group. Each group contained 8 specimens andwas further divided into a 2-h group and a 4-h group. They were placed in 24-well culture plates and sterilized with gamma radiation (25 kGy), and 10 mL of the 1 × 106 CFU/mL liquid was added to each well. After 2 and 4 h, scanning electron microscopy (SEM) and fluorescence laser confocal microscopy were performed to observe bacterial adhesion.

2.2.5 SEM observation of bacteria on different surfaces

After rinsing the samples with 0.01M phosphate-buffered saline (PBS) to remove surface-floating bacteria, the samples were transferred to six-well culture plates and 2.5% glutaraldehyde (AGAR, Stansted, UK) was added. They were then stored at 4°C overnight and washed with 0.01M PBS (twice, each time for 10 min). The samples were dehydrated with 50%, 70%, 90% ethanol, and absolute ethanol, followed by conversion with isoamyl acetate. Bacterial adhesion was observed under a Hitachi S-4800 (Hitachi, Tokyo, Japan) field emission SEM operated in secondary electron detection mode.

2.2.6 Bacterial adhesion and fluorescence microscopy counting

The samples were washed with PBS (0.01M) twice to remove loosely attached or unattached bacteria on the specimen surfaces. They were then stained with the fluorescence oxidation–reduction dye Syto 9 at 37°C for 30 min, avoiding exposure to light. The bacterial observation was performed using fluorescence laser confocal microscopy within a 1.5 × 1.5 mm^2 field of view. After colony formation, the number of bacteria was counted in 10 random areas of each substrate using Image-Pro software. Data were statistically analyzed using one-way analysis of variance (ANOVA) with Tukey's test, and the experiment was repeated three times.

2.2.7 Cell viability testing

MC3T3-E1 mouse osteoblast cells (National Collection of Authenticated Cell Cultures, China) were cultured in a humidified atmosphere at 37°C with 5% CO2. The medium used consisted of 10% fetal bovine serum and 1% penicillin/streptomycin for cell viability testing. The pretreated As-built, HT, and EFSF samples were placed in 48-well plates and immersed in 200 μL of fresh culture medium. Then, 500 μL of a cell suspension with a density of 1.0 × 104 cells/mL was evenly seeded onto the surface of each sample. Five parallel samples were prepared for each group (n = 5). All samples were placed at the bottom of the 48-well plate and immersed in 200 μL of fresh culture medium. Further, 500 μL of medium containing MC3T3-E1 cells was added to each well. The samples were divided into control and experimental groups. Additionally, 1 mL of PBS was added to the unused wells. After intervals of 1, 4, and 7 days, the culture medium was replaced with a mixed solution of 700 μL of the medium and CCK-8 solution in a 10:1 ratio. After incubating at 37°C for 2 h, 100 μL of the solution was transferred from each well to a 96-well plate, and the absorbance at 450 nm was measured using an enzyme-linked immunosorbent assay (ELISA; Sunrise-basic Tecan, Austria) reader. The cell viability was calculated as follows:

$$Cell\ Viability\,(\%) = OD450\,(sample)/OD450\,(control) \times 100\%$$

Toxic grade assessment was based on the six-grade toxicity rating standard (G.X. Pei et al., 2006), as listed in Table 4.

TABLE 4 Relative growth rate and toxicity grade.

Relative growth rate	Toxicity grade	Evaluation results
≥100	0	Qualified
75–99	1	Qualified
50–74	2	Re-review
25–49	3	Failed
1–24	4	Failed
0	5	Failed

2.2.8 Statistical analysis

The statistical analysis was performed using IBM SPSS Statistics version 22.0 (IBM, NY, USA). A one-way ANOVA in conjunction with Tukey's post hoc test was employed for the statistical analysis. Each experiment was conducted in triplicate and repeated three times to ensure robustness. All results were presented as mean values accompanied by their respective standard deviations. A comparative t test was carried out at a confidence level of 95% to assess the significance of differences among the various groups. Specifically, P values <0.05 indicated significant differences.

3 Results

3.1 Metallographic observation and mechanical property testing

The metallographic structure morphology of the As-built samples at 0°, 45°, and 90° is depicted in Figure 3. The emergence of *ß* columnar crystals was observed following direct printing of the alloy, with a width of 70–100 μm and height exceeding 1,000 μm. High-power laser confocal microscopy indicated the formation of a large number of α′ martensite needles, which were 0.5–2 μm wide. Additionally, black defect tissues were scattered throughout the structure, which were likely surface pores with incomplete crystal fusion.

A significant fusion of grains occurred following the HT treatment (700°C for 90 min). The higher heating temperature in HT compared with the non-heat-treated state led to an increase in the size of the grains after fusion. The observation of high-power

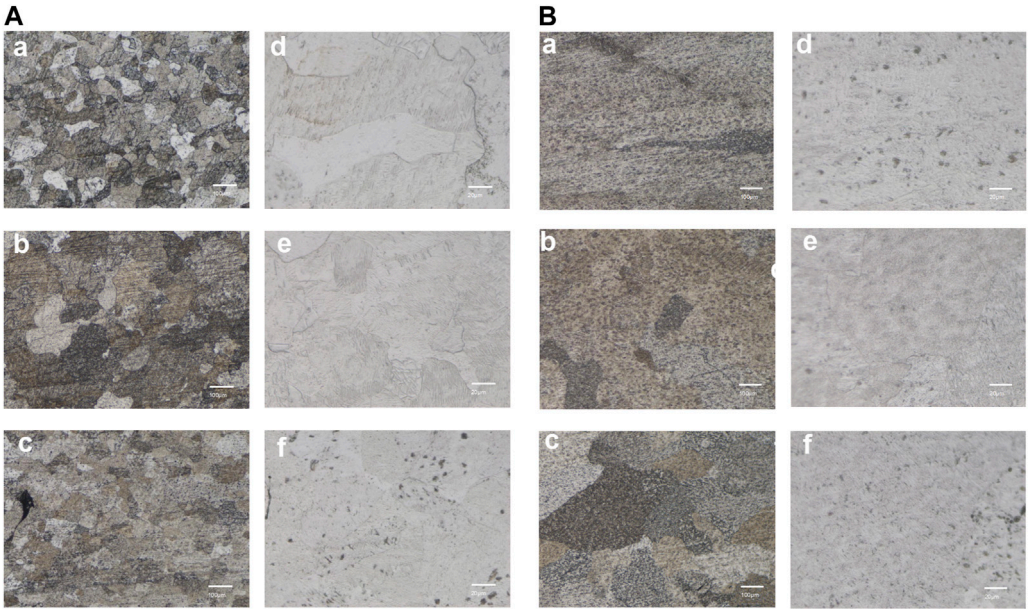

FIGURE 3
Microstructure of the SLM-printed TA1 samples (representing results of the **(A)** As-built **(B)** HT, **(a–c)** are the 100x metallographic micrographs at printing angles of 0°, 45°, and 90° respectively; **(d–f)** are the corresponding 500x laser confocal images.

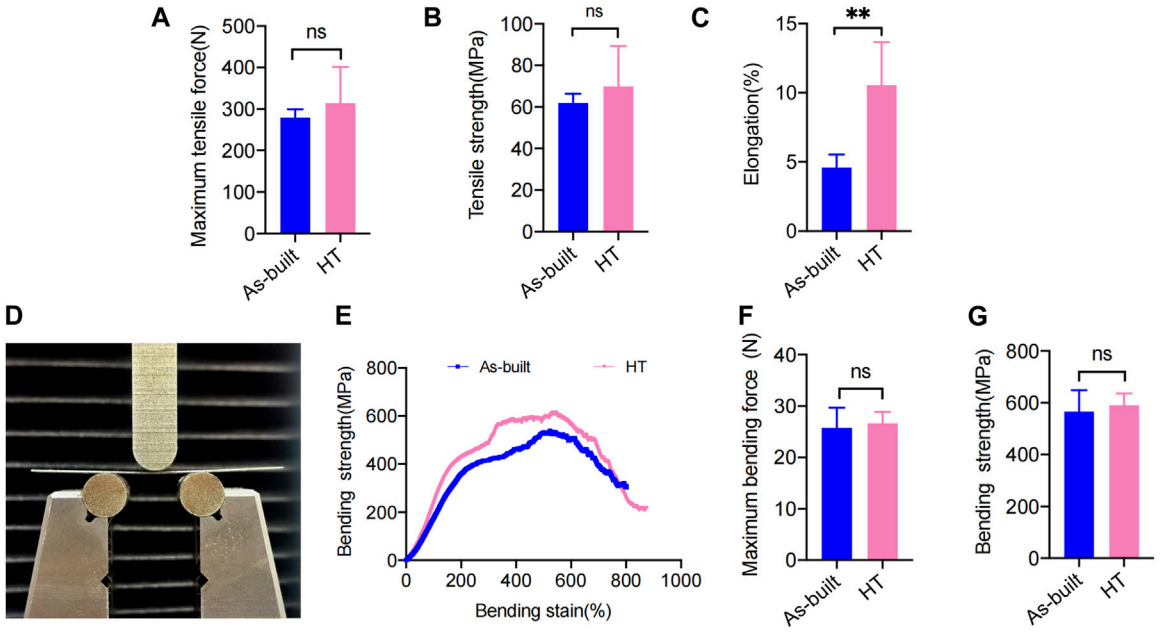

FIGURE 4
Statistical analysis of the mechanical test. **(A)** Maximum tensile force. **(B)** Tensile strength. **(C)** Elongation. **(D)** Front view of the bending test. **(E)** Stress–strain curves. **(F)** Maximum bending force. **(G)** Bending strength (*$p < 0.05$; **$p < 0.01$; ***$p < 0.001$).

backscatter images revealed the presence of some residual α′ martensite structures within the heat-treated sample. The number of surface pores significantly reduced, and the grain boundary of the HT sample was relatively clean. The number of circular pores, which are a type of printing defect, reduced in size to 20–30 μm. Further fusion of the unfused refined grains was observed over an extended time.

The mechanical property assessment involved tensile tests performed for the As-built and HT samples. The As-built titanium mesh showed an average maximum tensile force of

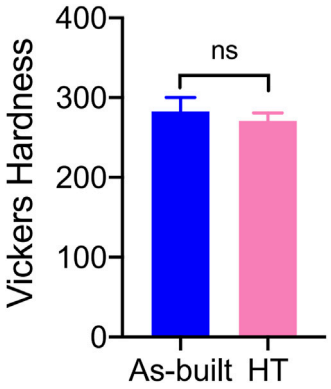

FIGURE 5
Comparison of surface Vickers hardness between As-built and HT titanium meshes.

297.3 ± 19.95 N and a tensile strength of 61.83 ± 4.53 MPa (Figures 4A, B). The HT samples demonstrated an increased maximum tensile force (314.0 ± 87.35 N) and tensile strength (69.83 ± 19.50 MPa) compared with the As-built samples, indicating a trend toward enhanced tensile strength with the HT protocol, despite the lack of statistical significance ($p > 0.05$).

In terms of elongation, the HT samples (10.56% ± 3.11%) showed a significant increase compared with the As-built samples (4.59% ± 0.93%) (Figure 4C), reaching statistical significance ($p < 0.001$). The As-built titanium mesh exhibited a maximum bending force of 21.63 ± 6.936 N and a bending strength of 566.2 ± 82.90 MPa in the three-point bending tests. A slight increase was observed in the HT samples, showing a maximum bending force (26.65 ± 2.20 N) (Figure 4F) and an increase in bending strength (590.9 ± 45.36 MPa) (Figure 4G) compared with the As-built samples, despite no statistical significance ($p > 0.05$).

3.2 Vickers hardness testing

The Vickers hardness values are shown in Figure 5. The Vickers hardness value for the HT group was 270.8 ± 10.16 HV, whereas the Vickers hardness value for the As-built group was 282.9 ± 17.11 HV. The difference between the two groups was not statistically significant ($t = 1.920$, $p = 0.0708$).

3.3 Analysis of surface morphology of EFSF-treated titanium mesh

The optical microscope and SEM images of the specimens before and after EFSF treatment are shown in Figure 6. After SLM printing, a significant amount of residual titanium powder accumulated on the surface of the printed parts, resulting in surface roughness (Figures 6A, C, E, G). The inner side of the titanium mesh scaffold exhibited the highest powder accumulation, making it challenging to remove the adhered titanium powder manually; the powder tended to aggregate along the printing direction. A relatively smooth polished surface was obtained after EFSF treatment, with most of the adhered titanium powder removed (Figures 6B, D, F, H). However, larger defects on the surface could not be polished away, and potential cracks were present.

Figures 7A, B illustrates the findings from the roughness tests. No significant difference was found in Ra and Rz values between the As-built and HT groups. However, a significant difference was found between the EFSF group and the other two groups ($p < 0.01$).

The results concerning SFE values and wettability are detailed in Figures 7C–E. The SFE and water contact angle values showed significant differences among the three groups (all $p < 0.01$ except $p < 0.05$ between the As-built and HT groups of the water contact angle). The EFSF group presented the highest SFE value and lowest water contact angle, affirming increased hydrophilicity, followed by the HT group. In contrast, the As-built group showed the lowest SFE value and highest water contact angle.

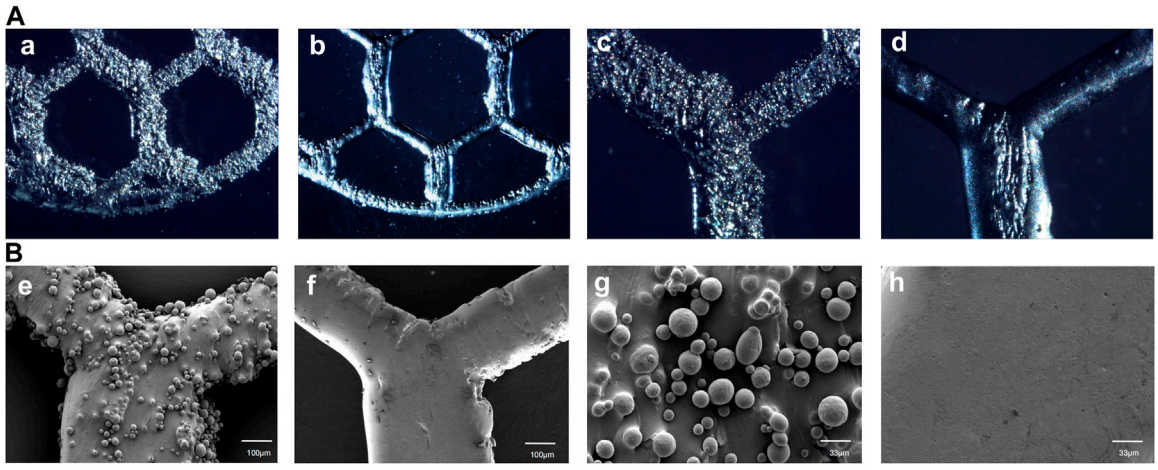

FIGURE 6
High-magnification optical microscope images of As-built characterization and EFSF-treated surfaces at ×50 magnification **(a, b)** and at ×100 magnification **(c, d)**, as well as SEM images of As-built and EFSF-treated surfaces at ×100 magnification **(e, f)** and at ×300 magnification **(g, h)**.

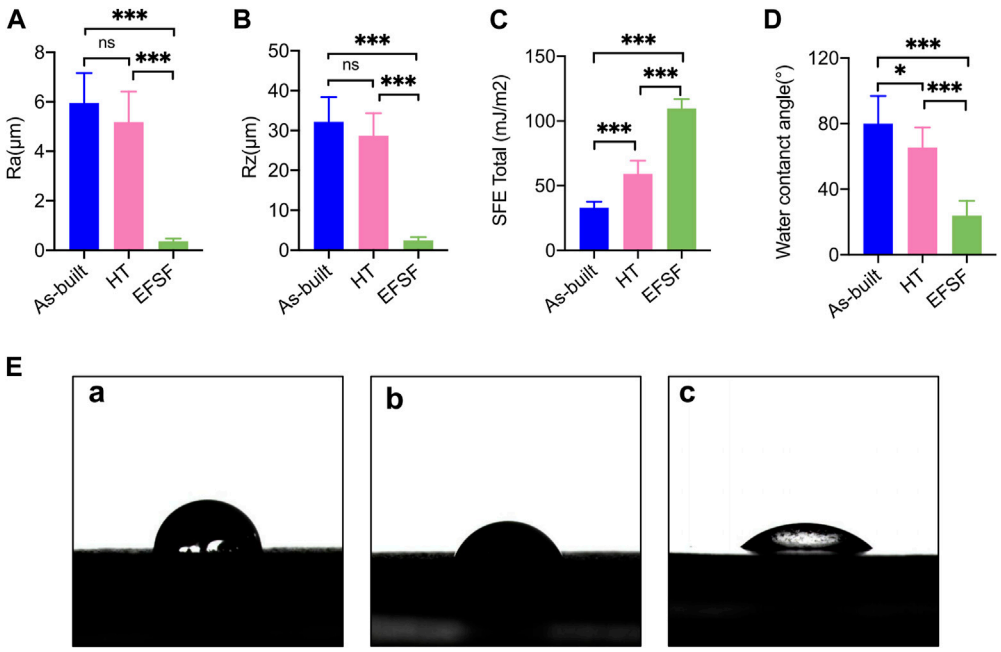

FIGURE 7
Roughness parameters **(A)** Ra and **(B)** Rz, SFE values **(C)**, and water contact angle values **(D)** of the specimens under different treatment conditions. **(E) (a)** Photograph of water droplet shape on the As-built scaffold after printing, **(b)** on the scaffold after HT, and **(c)** on the scaffold surface after EFSF (*$p < 0.05$; **$p < 0.01$; ***$p < 0.001$).

3.4 Analysis of bacterial adhesion experiments with different treatments

In the visualization of Sa on different surfaces, SEM images were obtained after culturing for 2 and 4 h on the surfaces of the specimens in the As-built, HT, and EFSF groups (Figure 8A). SEM observations revealed that bacteria were more prone to adhere to rough surfaces. The surface of the specimens in the HT group showed a significant reduction in bacterial adhesion; further reduction was observed in the EFSF group. The EFSF group exhibited scattered distribution of Sa bacteria with occasional small bacterial clusters. In contrast, the As-built group showed a large number of bacteria with mutual aggregation, forming clustered bacterial colonies. The HT group also exhibited clustered bacterial colonies attached to irregular pits on the surface of the specimens, but with a noticeable reduction compared with the As-built group.

Fluorescence confocal laser scanning microscopy images in Figure 8B depicts the bacterial colonies formed on the surfaces of specimens in the As-built, HT, and EFSF groups after 2 and 4 h of cultivation. These images showed that the surfaces in the HT and EFSF groups had fewer and smaller bacterial colonies compared with the surfaces in the As-built group. In particular, the smallest number of bacteria were observed on the surface of specimens in the EFSF group compared with the other two groups.

Figure 9 presents the bacterial colony counts obtained using Image-Pro software. One-way ANOVA with Tukey's *post hoc* test indicated a significant difference between the As-built and HT groups ($p < 0.05$), as well as between the HT and EFSF groups ($p < 0.05$).

3.5 Cell compatibility analysis of different treatments

Figure 10A presents the proliferation histograms of MC3T3-E1 cells, obtained from the CCK-8 assay after incubation for 1, 4, and 7 days in the four groups: the As-built, HT, and EFSF groups, along with a control group (cultured on blank plates without meshes). As the incubation time increased, the cells in each group exhibited different proliferation rates. Both the HT and EFSF groups notably surpassed the cell proliferation in the As-built group, with HT exhibiting the most pronounced growth. Although the cell proliferation in the EFSF group lagged behind that in the HT group, it demonstrated significant potential to show a marked increase (Figure 10B). The optical density values, measured using an ELISA reader at a wavelength of 450 nm, gradually increased over time, indicating remarkable cell proliferation on the meshes. The relative growth rates (RGRs) of the cells and the corresponding levels of cytotoxicity are listed in Figure 10. The RGRs in the As-built, HT, and EFSF titanium mesh groups on days 1, 4, and 7 were all above 80% compared with those in the control group, indicating nontoxicity and a cytotoxicity level of 0.

4 Discussion

This study investigated the mechanical properties of additively manufactured pure titanium meshes designed for oral bone augmentation. Based on prior experiments, we assessed the impact of a specific vacuum HT temperature on the mesh's

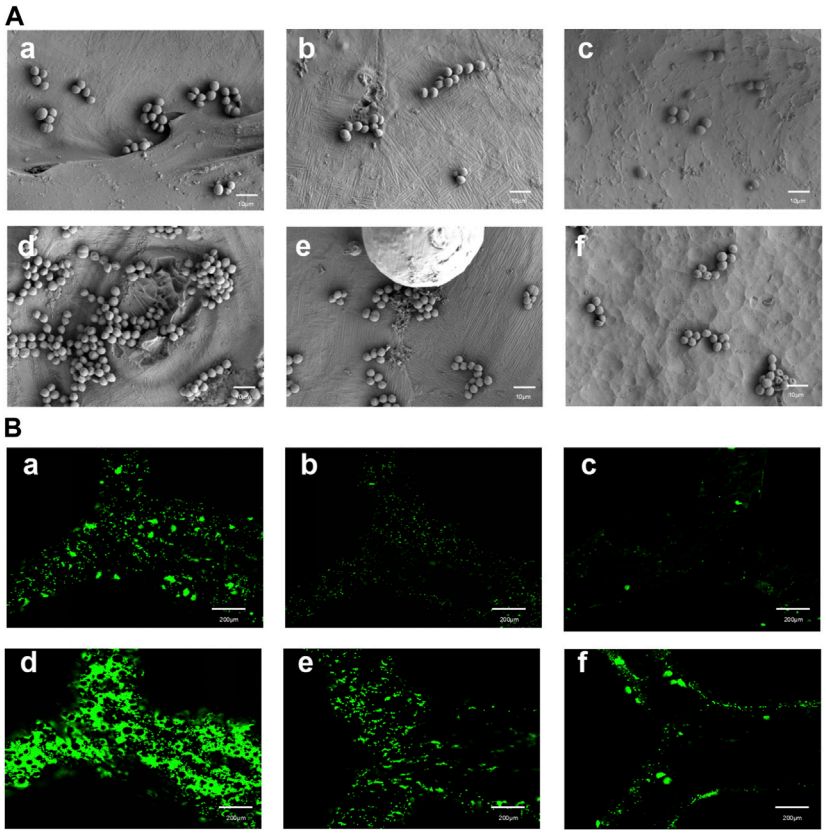

FIGURE 8
SEM and fluorescence microscopy images of TA1 specimens after specific cultivation periods and treatments. **(A) (a–f)** SEM images at a magnification of 5000× showing the surfaces of TA1 specimens after 2 h **(a–c)** and 4 h **(d–f)** of cultivation, respectively, for the printed As-built, HT, and EFSF groups. **(B) (a–f)** Fluorescence microscopy images of bacteria stained with Srty after 2 h **(a–c)** and 4 h **(d–f)** of cultivation on the surfaces of TA1 specimens, respectively, for the printed As-built, HT, and EFSF groups.

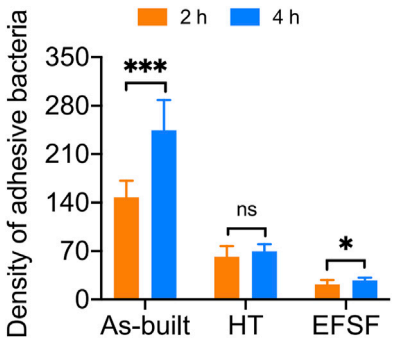

FIGURE 9
Analysis of Sa adhesion density on the surfaces of titanium scaffolds treated by three different methods.

features. This treatment significantly altered the metallographic composition of the titanium mesh, resulting in grain fusion, heightened tensile strength, enhanced fracture elongation, and reinforced bending strength. Notably, the heat-treated mesh achieved a tensile force of 314.0 N and elongation of 10.56%, compared with the measurements of 297.3 N and 4.59% in the As-built group. Remarkably, the mechanical properties of the treated meshes surpassed those of the commonly used Ti-6Al-4V (TC4) alloy (Li et al., 2022), highlighting their superior potential for clinical applications. This HT method aligned with Cheng-Lin Li's findings (Li et al., 2021), revealing that martensite structures transitioned into equiaxed grain structures at 650°C, optimizing the mesh's microstructure. This refined structure enhanced the mechanical reliability of the mesh, rendering it suitable for demanding clinical scenarios. The robust tensile and bending strengths evident in both heat-treated and As-built samples further validated the effectiveness of the manufacturing process.

The fracture elongation of the heat-treated samples significantly increased, with the HT group showing an improvement of approximately 130% compared with the As-built group without negatively affecting the strength. These findings were consistent with study research suggesting that HT could refine grains, enhance fusion, increase the elongation rate, and improve the mechanical strength of the additive manufactured metals (Hu et al., 2022; Zhang et al., 2021).

SLM manufacturing leads to a high degree of surface roughness. While this can be beneficial for porous titanium implants that aim to bond with adjacent bone (Tsukanaka et al., 2016; Trevisan et al., 2018), it is less ideal for temporary implants, such as titanium mesh. For these implants, a smoother

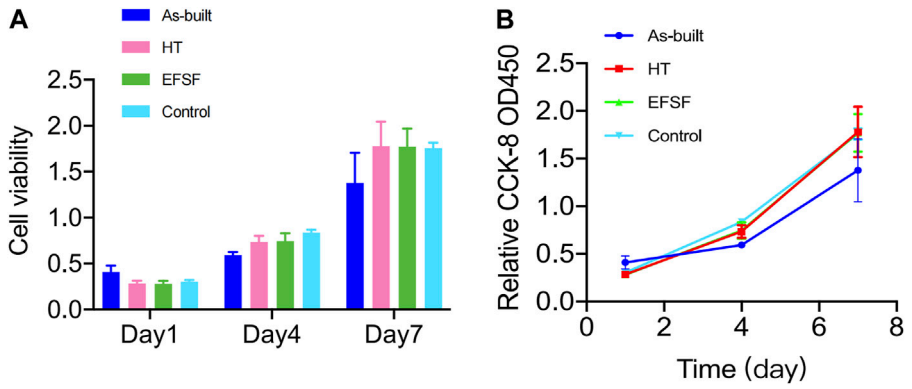

FIGURE 10
Viability of MC3T3-E1 cells measured by CCK-8 assay at different time points in each group.

surface is required to avoid tissue irritation and unwanted bone integration (Albrektsson and Wennerberg, 2004). This study harnessed the potential of an innovative technique known as EFSF to create such a smoother surface. This method ingeniously combined plasma polishing with micro-nano bubble polishing. By meticulously managing the polishing parameters and fluid dynamics, the surface roughness of the pure titanium mesh was significantly reduced by eliminating a majority of surface defects, removing the oxide layers, and eradicating residual titanium powder particles. The Ra and Rz values of the EFSF-treated surface were 0.37 ± 0.11 and 2.46 ± 0.80 μm, respectively, signifying a smooth and refined surface ideal for the application.

This study showed that the EFSF technique not only reduced the surface roughness but also increased the hydrophilicity and SFE of the titanium mesh. The smoother surfaces with higher SFE could better resist bacterial adhesion and biofilm formation compared with rougher, lower-SFE titanium surfaces (Puckett et al., 2010; Zhang et al., 2015). Bacterial adhesion is a complex process influenced by various surface features, including morphology, phase, and surface roughness. This study showed that the as-printed surfaces typically had a higher degree of roughness, which could potentially promote bacterial adhesion. This was primarily due to the fact that rough surfaces provided a more conducive environment for biofilm deposition compared with smoother surfaces (Scheuerman et al., 1998; Katsikogianni and Missirlis, 2004). Indeed, previous studies demonstrated that increased surface roughness expanded the available area for bacterial adhesion (Gharechahi et al., 2012), enabling a greater contact surface for bacteria and facilitating stronger adhesion forces and binding capabilities (Ahn et al., 2009; Almaguer-Flores et al., 2010). Moreover, in oral clinical scenarios where the titanium mesh comes into contact with the oral environment, bacteria adhering to irregular surfaces are more likely to survive for extended periods because they are shielded from natural clearance forces and oral hygiene measures. This study observed a noteworthy reduction in bacterial adhesion on the EFSF-polished titanium mesh surface. This was an encouraging finding, considering that bacterial adhesion, particularly of strains such as Sa, was a leading cause of implant-associated infections.

However, SEM observation revealed that deep scratches, defects, and uneven roughness could not be completely removed with the EFSF technique. These surface imperfections appeared to be predominantly induced by fluctuations and changes in SLM process parameters, external environment, and melt pool state (Wang, 2014; Yadollahi and Shamsaei, 2017). For titanium meshes with significant defects, it seems necessary to apply preliminary treatments, such as mechanical polishing, to the rough surface prior to EFSF processing to attain a less coarse finish. Alternatively, the EFSF may be worth considering as an intermediate polishing procedure, necessitating further exploration into its potential compatibility and combination with other polishing techniques in subsequent stages.

One potential concern associated with electrochemical plasma polishing pertains to the enrichment of cytotoxic vanadium elements on the surfaces of titanium alloy devices. However, this study demonstrated that the plasma electrolytic polishing of pure titanium, due to its single-element composition, did not adversely affect cell lifespan (Bernhardt et al., 2021). Furthermore, this study found no significant difference in cell death rates for specimens in the HT and EFSF groups, indicating their good biocompatibility (Figure 10).

Despite the promising results, further research should be conducted to refine these improvement methods. The crucial next steps are exploring different polishing parameters and conducting comprehensive biocompatibility assessments, including *in vivo* implantation and cytotoxicity testing. Additionally, long-term clinical observations and studies are necessary to ascertain the effectiveness and safety of these improvement techniques in practical oral implant surgeries.

5 Conclusion

This study illuminated the advantageous impact of both HT and EFSF polishing on titanium mesh samples, crafted using additive manufacturing with pure titanium (TA1). The application of HT at 700°C for 90 min significantly bolstered the mechanical properties of the mesh, whereas the use of EFSF processing effectively mitigated surface roughness. Importantly, both these treatments demonstrate

biocompatibility, as they show no deleterious effects on osteogenic cells. Additionally, these treatments have the potential to improve resistance against bacterial adhesion, which is a crucial parameter for successful implant surgery.

The insights gained from this study might lay the foundation for a future where the aforementioned treatments can substantially improve the properties of titanium mesh for oral implant surgeries. However, further investigations should focus on assessing the long-term clinical outcomes of these treatment methods.

Data availability statement

The original contributions presented in the study are included in the article/Supplementary material, further inquiries can be directed to the corresponding authors.

Ethics statement

The manuscript presents research on animals that do not require ethical approval for their study.

Author contributions

LW: Conceptualization, Data curation, Formal Analysis, Investigation, Methodology, Supervision, Writing–original draft, Writing–review and editing. FW: Investigation, Methodology, Supervision, Validation, Writing–review and editing. SA: Investigation, Software, Writing–review and editing. TR: Software, Writing–review and editing. XL: Funding acquisition, Project administration, Resources, Validation, Visualization, Writing–review and editing. PW: Funding acquisition, Project administration, Resources, Validation, Visualization, Writing–review and editing.

Funding

The author(s) declare financial support was received for the research, authorship, and/or publication of this article. This work was supported by the Jiangsu Province Key Research and Development Program (Social Development) Special Fund under grant number BE2021608.

Acknowledgments

Financial support from the School of Stomatology, Nanjing University and the School of Stomatology, Xuzhou Medical University is gratefully acknowledged. Appreciation is extended to Nanjing Qianzhi Intelligent Technology Co., Ltd., China, for the provision of the Ti mesh 3D printing. Acknowledgement is also given to Nanjing Additive Manufacturing Research Institute Development Co., Ltd., China, for supplying the plasma polishing equipment.

Conflict of interest

The authors declare that the research was conducted in the absence of any commercial or financial relationships that could be construed as a potential conflict of interest.

Publisher's note

References

Ahn, H. B., Ahn, S. J., Lee, S. J., Kim, T. W., and Nahm, D. S. (2009). Analysis of surface roughness and surface free energy characteristics of various orthodontic materials. *Am. J. Orthod. Dentofac. Orthop.* 136 (5), 668–674. doi:10.1016/j.ajodo.2007.11.032

Albrektsson, T., and Wennerberg, A. (2004). Oral implant surfaces: Part 1--review focusing on topographic and chemical properties of different surfaces and *in vivo* responses to them. *Int. J. Prosthodont.* 17 (5), 536–543.

Almaguer-Flores, A., Ximénez-Fyvie, L. A., and Rodil, S. E. (2010). Oral bacterial adhesion on amorphous carbon and titanium films: effect of surface roughness and culture media. *J. Biomed. Mat. Res. B Appl. Biomater.* 92 (1), 196–204. doi:10.1002/jbm.b.31506

Bernhardt, A., Schneider, J., Schroeder, A., Papadopoulous, K., Lopez, E., Brückner, F., et al. (2021). Surface conditioning of additively manufactured titanium implants and its influence on materials properties and *in vitro* biocompatibility. *Mat. Sci. Eng. C* 119, 111631. doi:10.1016/j.msec.2020.111631

Boyne, P. J., Cole, M. D., Stringer, D., and Shafqat, J. P. (1985). A technique for osseous restoration of deficient edentulous maxillary ridges. *J. Oral Maxillofac. Surg.* 43 (2), 87–91. doi:10.1016/0278-2391(85)90054-0

Buser, D., Dula, K., Hirt, H. P., and Schenk, R. K. (1996). Lateral ridge augmentation using autografts and barrier membranes: a clinical study with 40 partially edentulous patients. *J. Oral Maxillofac. Surg.* 54 (4), 420–432. doi:10.1016/s0278-2391(96)90113-5

Dank, A., Aartman, I. H. A., Wismeijer, D., and Tahmaseb, A. (2019). Effect of dental implant surface roughness in patients with a history of periodontal disease: a systematic review and meta-analysis. *Int. J. Implant Dent.* 5 (1), 12. doi:10.1186/s40729-019-0156-8

De Angelis, N., Solimei, L., Pasquale, C., Alvito, L., Lagazzo, A., and Barberis, F. (2021). Mechanical properties and corrosion resistance of tial6v4 alloy produced with SLM technique and used for customized mesh in bone augmentations. *Appl. Sci.* 11 (12), 5622. doi:10.3390/app11125622

Dong, Y. P., Tang, J. C., Wang, D. W., Wang, N., He, Z. D., Li, J., et al. (2020). Additive manufacturing of pure Ti with superior mechanical performance, low cost, and biocompatibility for potential replacement of Ti-6Al-4V. *Mat. Des.* 196, 109142. doi:10.1016/j.matdes.2020.109142

Gharechahi, M., Moosavi, H., and Forghani, M. (2012). Effect of surface roughness and materials composition. *J. Biomater. Nanobiotechnol.* 3, 541–546. doi:10.4236/jbnb.2012.324056

Gomes, C. C., Moreira, L. M., Santos, V. J., Ramos, A. S., Lyon, J. P., Soares, C. P., et al. (2011). Assessment of the genetic risks of a metallic alloy used in medical implants. *Genet. Mol. Biol.* 34 (1), 116–121. doi:10.1590/s1415-47572010005000118

Hu, Y., Chen, H., Jia, X., Liang, X., and Lei, J. (2022). Heat treatment of titanium manufactured by selective laser melting: Microstructure and tensile properties. *J. Mat. Res. Technol.* 18, 245–254. doi:10.1016/j.jmrt.2022.02.106

Kasemo, B., and Gold, J. (1999). Implant surfaces and interface processes. *Adv. Dent. Res.* 13, 8–20. doi:10.1177/08959374990130011901

Katsikogianni, M., and Missirlis, Y. F. (2004). Concise review of mechanisms of bacterial adhesion to biomaterials and of techniques used in estimating bacteria-material interactions. *Eur. Cell. Mat.* 8, 37–57. doi:10.22203/ecm.v008a05

Lee, S. H., Moon, J. H., Jeong, C. M., Bae, E. B., Park, C. E., Jeon, G. R., et al. (2017). The mechanical properties and biometrical effect of 3D preformed titanium membrane for guided bone regeneration on alveolar bone defect. *Biomed. Res. Int.* 2017, 1–12. doi:10.1155/2017/7102123

Li, C.-L., Wang, C.-S., Narayana, P. L., Hong, J.-K., Choi, S.-W., Kim, J. H., et al. (2021). Formation of equiaxed grains in selective laser melted pure titanium during annealing. *J. Mat. Res. Technol.* 11, 301–311. doi:10.1016/j.jmrt.2021.01.008

Li, L., Gao, H., Wang, C., Ji, P., Huang, Y., and Wang, C. (2022). Assessment of customized alveolar bone augmentation using titanium scaffolds vs polyetheretherketone (peek) scaffolds: a comparative study based on 3D printing technology. *ACS Biomater. Sci. Eng.* 8 (5), 2028–2039. doi:10.1021/acsbiomaterials.2c00060

Liu, X., Chen, S., Tsoi, J. K. H., and Matinlinna, J. P. (2017). Binary titanium alloys as dental implant materials-a review. *Regen. Biomater.* 4 (5), 315–323. doi:10.1093/rb/rbx027

McCracken, M. (1999). Dental implant materials: commercially pure titanium and titanium alloys. *J. Prosthodont.* 8 (1), 40–43. doi:10.1111/j.1532-849x.1999.tb00006.x

Merli, M., Mariotti, G., Moscatelli, M., Motroni, A., Mazzoni, A., Mazzoni, S., et al. (2015). Fence technique for localized three-dimensional bone augmentation: a technical description and case reports. *Int. J. Periodontics Restor. Dent.* 35 (1), 57–64. doi:10.11607/prd.2029

Pei, G. X., Wei, K. H., and Jin, D. (2006). *Experimental technology of tissue engineering*. Beijing: People's Military Medical Press.

Puckett, S. D., Taylor, E., Raimondo, T., and Webster, T. J. (2010). The relationship between the nanostructure of titanium surfaces and bacterial attachment. *Biomaterials* 31 (4), 706–713. doi:10.1016/j.biomaterials.2009.09.081

Rakhmatia, Y. D., Ayukawa, Y., Furuhashi, A., and Koyano, K. (2013). Current barrier membranes: titanium mesh and other membranes for guided bone regeneration in dental applications. *J. Prosthodont. Res.* 57 (1), 3–14. doi:10.1016/j.jpor.2012.12.001

Rao, S., Ushida, T., Tateishi, T., Okazaki, Y., and Asao, S. (1996). Effect of Ti, Al, and V ions on the relative growth rate of fibroblasts (L929) and osteoblasts (MC3T3-E1) cells. *Biomed. Mat. Eng.* 6 (2), 79–86. doi:10.3233/bme-1996-6202

Ribeiro, M., Monteiro, F. J., and Ferraz, M. P. (2012). Infection of orthopedic implants with emphasis on bacterial adhesion process and techniques used in studying bacterial-material interactions. *Biomatter* 2 (4), 176–194. doi:10.4161/biom.22905

Santhosh Kumar, S., Hiremath, S. S., Ramachandran, B., and Muthuvijayan, V. (2019). Effect of surface finish on wettability and bacterial adhesion of micromachined biomaterials. *Biotribology* 18, 100095. doi:10.1016/j.biotri.2019.100095

Scarano, A., Crocetta, E., Quaranta, A., and Lorusso, F. (2018). Influence of the thermal treatment to address a better osseointegration of Ti6Al4V dental implants: histological and histomorphometrical study in a rabbit model. *Biomed. Res. Int.* 2018, 1–7. doi:10.1155/2018/2349698

Scheuerman, T. R., Camper, A. K., and Hamilton, M. A. (1998). Effects of substratum topography on bacterial adhesion. *J. Colloid. Interface Sci.* 208 (1), 23–33. doi:10.1006/jcis.1998.5717

Sumida, T., Otawa, N., Kamata, Y. U., Kamakura, S., Mtsushita, T., Kitagaki, H., et al. (2015). Custom-made titanium devices as membranes for bone augmentation in implant treatment: clinical application and the comparison with conventional titanium mesh. *J. Craniomaxillofac. Surg.* 43 (10), 2183–2188. doi:10.1016/j.jcms.2015.10.020

Trevisan, F., Calignano, F., Aversa, A., Marchese, G., Lombardi, M., Biamino, S., et al. (2018). Additive manufacturing of titanium alloys in the biomedical field: processes, properties and applications. *J. Appl. Biomater. Funct. Mat.* 16 (2), 57–67. doi:10.5301/jabfm.5000371

Tsukanaka, M., Fujibayashi, S., Takemoto, M., Matsushita, T., Kokubo, T., Nakamura, T., et al. (2016). Bioactive treatment promotes osteoblast differentiation on titanium materials fabricated by selective laser melting technology. *Dent. Mat. J.* 35 (1), 118–125. doi:10.4012/dmj.2015-127

Ulrich Sommer, J., Birk, R., Hörmann, K., and Stuck, B. A. (2014). Evaluation of the maximum isometric tongue force of healthy volunteers. *Eur. Arch. Otorhinolaryngol.* 271 (11), 3077–3084. doi:10.1007/s00405-014-3103-6

Wang, H. (2014). Materials' fundamental issues of laser additive manufacturing for high-performance large metallic components. *Acta Aeronaut. Astronaut. Sin.* 35 (10), 2690–2698. doi:10.7527/S1000-6893.2014.0174

Wang, P., Nai, M. L. S., Tan, X., Vastola, G., Srinivasan, R., Sin, W. J., et al. (2016). "Recent progress ofAdditive manufactured Ti-6Al-4V by electron beam melting," in Proceedings of the 2016 Annual International Solid Freeform Fabrication Symposium (SFF Symp 2016) Austin, TX, USA, 691–704.

Wang, W., Xu, X., Ma, R., Xu, G., Liu, W., and Xing, F. (2020). The influence of heat treatment temperature on microstructures and mechanical properties of titanium alloy fabricated by laser melting deposition. *Mater. (Basel)* 13 (18), 4087. doi:10.3390/ma13184087

Yadollahi, A., and Shamsaei, N. (2017). Additive manufacturing of fatigue resistant materials: challenges and opportunities. *Int. J. Fatigue* 98, 14–31. doi:10.1016/j.ijfatigue.2017.01.001

Yang, G., Wang, B., Tawfiq, K., Wei, H., Zhou, S., and Chen, G. (2016). Electropolishing of surfaces: theory and applications. *Surf. Eng.* 33 (2), 149–166. doi:10.1080/02670844.2016.1198452

Zeidler, H., Boettger-Hiller, F., Edelmann, J., and Schubert, A. (2016). Surface finish machining of medical parts using plasma electrolytic polishing. *Proc. CIRP* 49, 83–87. doi:10.1016/j.procir.2015.07.038

Zhang, J., Liu, Y., Bayat, M., Tan, Q., Yin, Y., Fan, Z., et al. (2021). Achieving high ductility in a selectively laser melted commercial pure-titanium via *in-situ* grain refinement. *Scr. Mat.* 191, 155–160. doi:10.1016/j.scriptamat.2020.09.023

Zhang, X., Zhang, Q., Yan, T., Jiang, Z., Zhang, X., and Zuo, Y. Y. (2015). Quantitatively predicting bacterial adhesion using surface free energy determined with a spectrophotometric method. *Environ. Sci. Technol.* 49 (10), 6164–6171. doi:10.1021/es5050425

frontiers | Frontiers in Bioengineering and Biotechnology

TYPE Systematic Review
PUBLISHED 15 November 2023
DOI 10.3389/fbioe.2023.1269223

OPEN ACCESS

EDITED BY
Xin Liu,
Shanghai Jiao Tong University School of Medicine, China

REVIEWED BY
Baiyan Sui,
Shanghai Jiao Tong University School of Medicine, China
Zhen Geng,
Shanghai University, China

*CORRESPONDENCE
Heng Bo Jiang,
hengbojiang@vip.qq.com
Kai Liu,
liukaifancy@163.com

†These authors have contributed equally to this work

RECEIVED 29 July 2023
ACCEPTED 18 September 2023
PUBLISHED 15 November 2023

CITATION
Liang J, Lu X, Zheng X, Li YR, Geng X, Sun K, Cai H, Jia Q, Jiang HB and Liu K (2023), Modification of titanium orthopedic implants with bioactive glass: a systematic review of *in vivo* and *in vitro* studies.
Front. Bioeng. Biotechnol. 11:1269223.
doi: 10.3389/fbioe.2023.1269223

Modification of titanium orthopedic implants with bioactive glass: a systematic review of *in vivo* and *in vitro* studies

Jin Liang[1†], XinYue Lu[2†], XinRu Zheng[2†], Yu Ru Li[2], XiaoYu Geng[2], KeXin Sun[2], HongXin Cai[3], Qi Jia[3], Heng Bo Jiang[2*] and Kai Liu[4*]

[1]Department of Oral and Maxillofacial Surgery, School of Stomatology, Shandong First Medical University, Jinan, Shandong, China, [2]The CONVERSATIONALIST Club and Department of Stomatological Technology, School of Stomatology, Shandong First Medical University, Jinan, Shandong, China, [3]Department and Research Institute of Dental Biomaterials and Bioengineering, Yonsei University College of Dentistry, Seoul, Republic of Korea, [4]School of Basic Medicine, Shandong First Medical University, Jinan, Shandong, China

Bioactive glasses (BGs) are ideal biomaterials in the field of bio-restoration due to their excellent biocompatibility. Titanium alloys are widely used as a bone graft substitute material because of their excellent corrosion resistance and mechanical properties; however, their biological inertness makes them prone to clinical failure. Surface modification of titanium alloys with bioactive glass can effectively combine the superior mechanical properties of the substrate with the biological properties of the coating material. In this review, the relevant articles published from 2013 to the present were searched in four databases, namely, Web of Science, PubMed, Embase, and Scopus, and after screening, 49 studies were included. We systematically reviewed the basic information and the study types of the included studies, which comprise *in vitro* experiments, animal tests, and clinical trials. In addition, we summarized the applied coating technologies, which include pulsed laser deposition (PLD), electrophoretic deposition, dip coating, and magnetron sputtering deposition. The superior biocompatibility of the materials in terms of cytotoxicity, cell activity, hemocompatibility, anti-inflammatory properties, bioactivity, and their good bioactivity in terms of osseointegration, osteogenesis, angiogenesis, and soft tissue adhesion are discussed. We also analyzed the advantages of the existing materials and the prospects for further research. Even though the current research status is not extensive enough, it is still believed that BG-coated Ti implants have great clinical application prospects.

KEYWORDS

bone regeneration, surface modification, biomaterials, tissue engineering, bioglass, bioactive materials

1 Introduction

Bioactive glass (BG) can repair, restore, replace, and help regenerate tissue through the combination of tissues and materials. BG has uniform particle size and great adhesion with irregular sizes and shapes. Furthermore, its inherent biocompatibility and high strength make it an ideal biomaterial (Manam et al., 2017). After contact with biological fluids, some ions are released on the surface of the BG particles, which can regulate the osmotic pressure and pH value around the implant, thereby damaging the cell wall structure of bacteria and inducing antibacterial activity (Allan et al., 2002; Coraça-Huber et al., 2014; Drago et al., 2018). BGs also have appropriate biodegradability and particles are easily absorbed. In addition, this material has good bioactivity, which can promote osteoinduction and thus rapidly form bone-like structures. However, when compared to human bone tissue, BG is more brittle. Due to its poor mechanical properties, BG is not suitable for the load-bearing areas (Cannillo et al., 2009; Yanovska et al., 2011). The mentioned properties make it ideal for use in toothpaste, bone grafts, scaffolds, drug delivery systems, soft tissue engineering, and biomaterial coatings (Hench, 2006; Asif et al., 2014).

Titanium (Ti) alloys have better biocompatibility than other metal implants. Ti does not cause rejection after direct contact with bone tissue nor does it have negative effects or other bioelectronic reactions on biological organs. When compared with stainless steel and cobalt-based metals, Ti has lower modulus and better corrosion resistance while the corrosion resistance of metals and the biocompatibility of corrosion products can reflect metal's own biocompatibility (Long and Rack, 1998). Their inertness made them virtually unreactive to the surrounding tissue environment, resulting in low cytotoxicity. The hydroxyapatite (HA) layer is often coated on the Ti alloy surface, which leads to the combination with the host collagen fiber, demonstrating Ti alloy's osteointegration. The oxide layer on their surface is equipped with excellent corrosion resistance (Escalas et al., 1976). For mechanical property aspects, Young's modulus of Ti alloy is much smaller than that of other metallic biomaterials, such as stainless steel, thereby reducing the stress shielding effect (Niinomi, 1998). Due to their excellent biocompatibility, corrosion resistance, and mechanical properties, Ti alloys can be applied as orthopedic and stomatological implants for arthroplasty and implantology. However, due to their intrinsic inertness, Ti alloys cannot form a close connection at the interface between the implant and host tissue. Meanwhile, the low wear resistance causes implants to loosen (Long and Rack, 1998). The inability of Ti alloys to achieve both shear strength and ductility greatly limits their application as implant materials in joint replacement (Chen and Thouas, 2015). The physical and chemical properties of the implant surface are crucial and play an important role in the osseointegration process between the bone and the implant. Therefore, surface modification of titanium implants can greatly reduce their limitations in clinical application (Geng et al., 2021a).

The surface modification of Ti using BG can improve osteointegration and osteogenesis (Gomez-Vega et al., 2001; López et al., 2016), which combines the substrates' excellent mechanical properties with BG coatings' biological properties (Solai et al., 2011). In fact, HA is still a common material for titanium alloy coatings. Apatite has the same inorganic composition as bone tissue and has been widely used in the field of bone transplantation and studied as a coating material (Geng et al., 2021b). Both BG and HA have good biological properties and excellent osteoconductivity. However, BG has better osteogenesis properties than HA coating materials (Dhinasekaran et al., 2021). BG coatings lead to apatite layer formation on the surface and thus improve close integration with both human hard and soft tissues (Sanz-Herrera and Boccaccini, 2011) and help in bone growth (Moreira et al., 2018; Vuornos et al., 2019). Furthermore, the ions released by BGs in bodily fluids can stimulate angiogenesis and wound healing (Cohrs et al., 2019; Zhang et al., 2019). Multiple manufacturing technologies have been investigated to coat Ti alloys with BG, such as electrophoretic deposition (Estrada-Cabrera et al., 2019), electrochemical deposition (Balamurugan et al., 2009), pulsed laser deposition (PLD) (Wang et al., 2018), dip coating deposition (Safaee et al., 2021), magnetron sputtering (Berbecaru et al., 2010), thermal spraying (Herman et al., 2000), and laser cladding (Comesana et al., 2010). Doping different ions in BG can improve the specific properties of the coating, such as magnesium ions (Mg^{2+}), zinc ions (Zn^{2+}), and strontium ions (Sr^{2+}). Many recent studies have shown that Sr^{2+} can promote bone formation and inhibit osteoclast absorption; therefore, this element is often doped into implants or their coatings to improve the osteogenic performance of the implants (Geng et al., 2021a; Geng et al., 2022). Besides, BG coatings, when combined with other biomaterials, can improve biological properties. Drug-loaded chitosan BG coatings exhibit good cellular activity, antimicrobial capacity, and osteogenic activity (Patel et al., 2012).

In a previously published review relevant to BG coatings, Oliver et al. (2019) summarized the performance improvement of BG coatings on medical metallic implants. Maximov et al. (2021) listed different methods of BG preparation as well as coating technologies. Baino and Verné (2017) specifically discussed the different clinical areas of application of BG coatings on biomedical implants. In this systematic review, the authors have searched and screened relevant articles and summarized and analyzed the characteristics of the included studies, the manufacturing technologies of BG coatings on Ti implants, and the properties of BG coatings. Previous research status that included study types is also included in this review. This systematic review aims to evaluate the properties of BG-coated Ti implants *versus* bare Ti implants and systematically adds up previous coating technology and relevant parameters as the influencing factors for BG coatings on Ti implants, providing a theoretical basis for future studies.

2 Materials and methods

2.1 Inclusion and exclusion criteria

The inclusion and exclusion criteria were framed based on the PICOS model. *In vivo* studies and clinical trials, and *in vitro* studies that investigated both biocompatibility and bioactivity were included in the assessment. Studies applying Ti or its alloys coated with bioactive glasses or the composite coatings on the Ti implant containing bioactive glasses were included in this review. The outcome indicators discussed in this review contain biocompatibility, bioactivity, and antibacterial properties, which are shown in Figure 1. Biocompatibility refers to 1) cytotoxicity

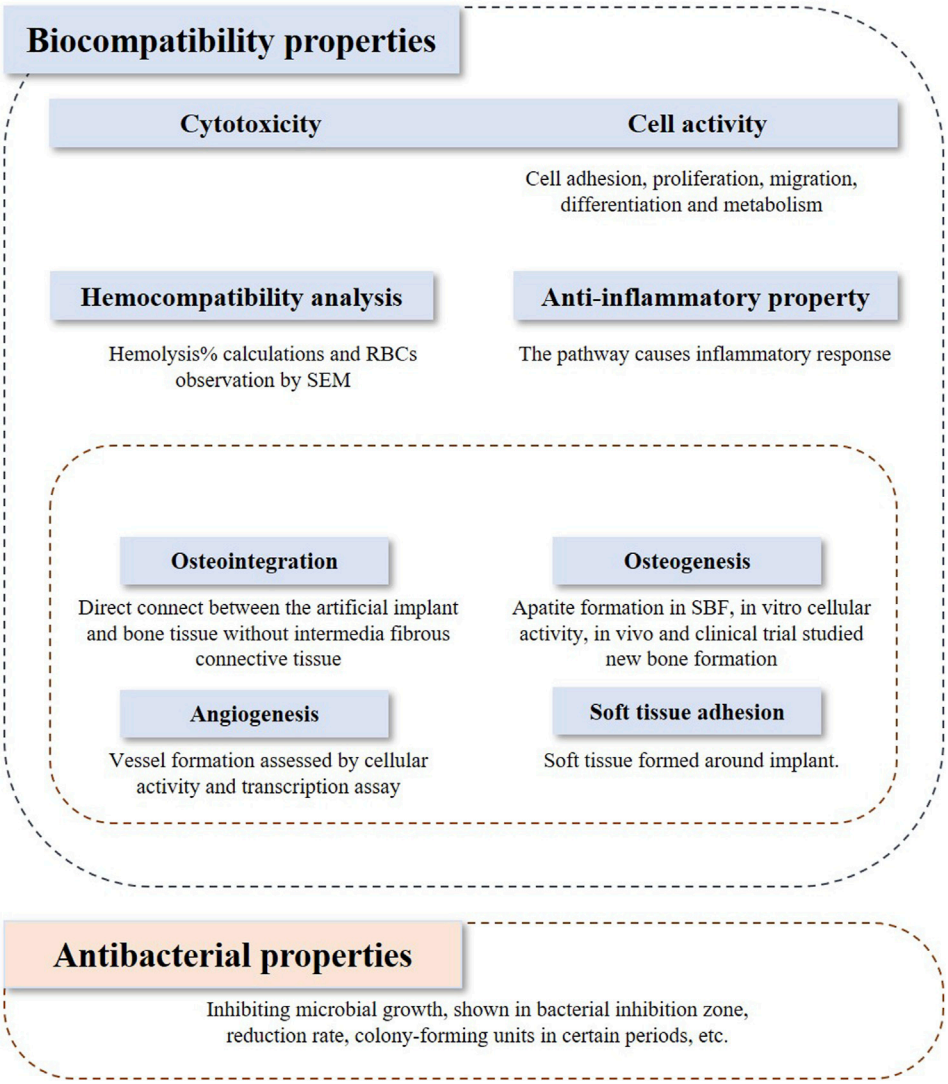

FIGURE 1
Outcome indicators for assessment.

TABLE 1 Searching strategies and results in the database.

Database	Searching strategy[a]	Result
PubMed	(((bioglass [Title/Abstract]) OR (bioactive glass [Title/Abstract]))AND ((ti [Title/Abstract]) OR (titanium [Title/Abstract])))	119
Embase	(titanium:ti,ab, kw OR ti:ti,ab,kw) AND (bioglass:ti,ab, kw OR bioactive glass:ti,ab,kw)	119
Web of Science	(TS=(titanium) OR TS=(ti)) AND (TS=(bioglass) OR TS=(bioactive glass))	566
Scopus	(TITLE-ABS-KEY (titanium) OR TITLE-ABS-KEY (ti)) AND (TITLE-ABS-KEY (bioglass) OR TITLE-ABS-KEY(Bioactive glass))	493
After Duplicates were removed		816

[a]Time filters were set from 2013 to present.
That the bold values indicates the number of studies retrieved in different databases according to the searching strategy.

and cell activity, 2) hemocompatibility, 3) anti-inflammatory properties, and 4) bioactivity. Bioactivity comprises 1) osteointegration, 2) osteogenesis, 3) angiogenesis, and 4) soft tissue adhesion.

Articles published in the last 10 years were included. There are no restrictions on the research type. Articles not published in English and whose full texts were unavailable were excluded.

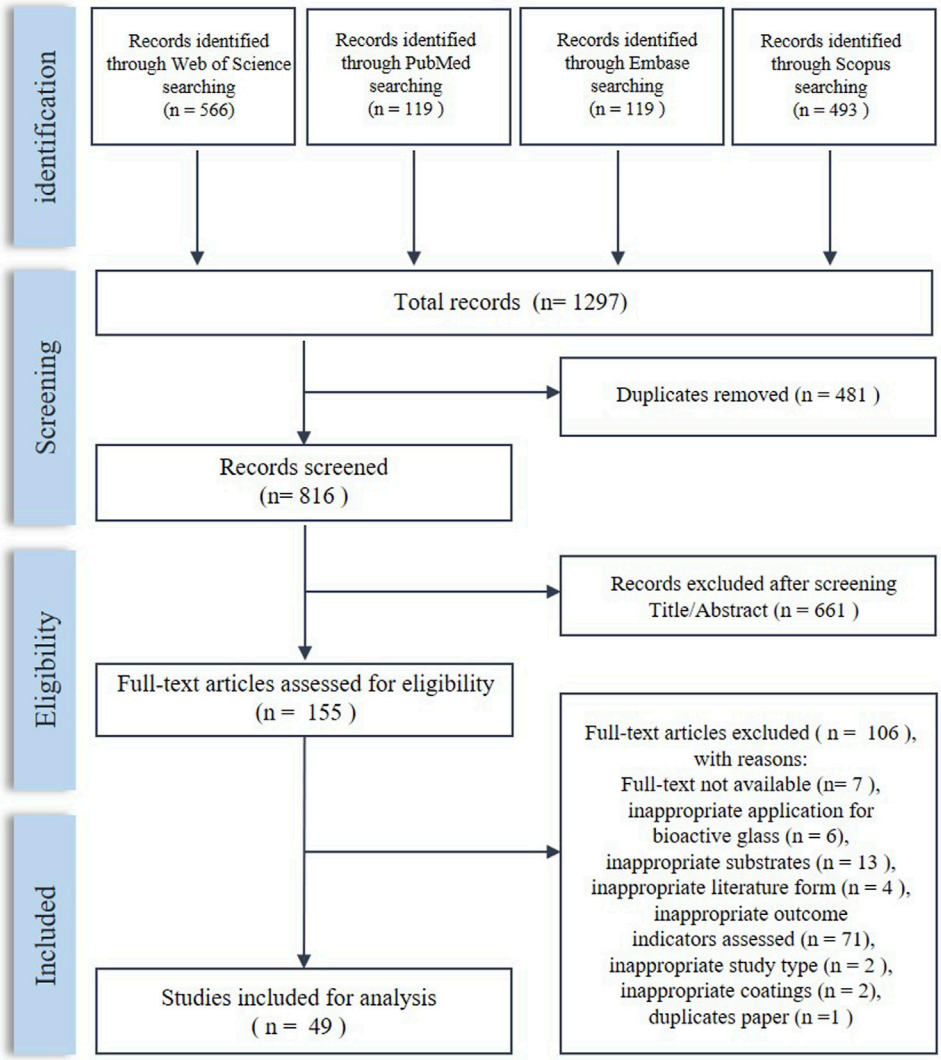

FIGURE 2
Flowchart for literature searching.

2.2 Literature search and screening

Four databases, namely, PubMed, Embase, Scopus, and Web of Science, were searched in this study. The search strategy is shown in Table 1.

Duplicates were removed using Endnote X9.3.2. The first screening was performed by filtering the title and abstract and inclusion of studies was determined after reading the full texts. The screening was done following the inclusion and exclusion criteria and was performed by two independent authors. Any conflict was resolved by a third author.

2.3 Data extraction

Data were collected using Microsoft Excel. The extracted data included substance material and samples' shapes and sizes, glass models and composites, experimental subjects, manufacturing methods, and special process parameters. Other included information can be seen in detail in the following contents.

The data were extracted independently by two researchers, and any problems were solved through discussion and a third author's help.

3 Characteristics of included studies

3.1 Basic information

The process of literature screening is shown in Figure 2. After screening, 49 articles were included in this systematic review. The characteristics of the included studies are shown in Table 2.

Ti-6Al-4V, which has been widely applied in orthopedic prostheses and dental implants, is the most widely applied alloy in the included studies. Pure Ti has also been investigated. Bioactive glasses 45S5, S35P5 (Massera et al., 2012), and 58S (Sepulveda et al., 2002) are the most commonly studied basic bioactive glass.

TABLE 2 Characteristics of included studies.

Study ID	Titanium alloy substrate	Sample shape and size	Glass model	Glass component (wt%)				Other components	Manufacturing method	Special process	Ref.
				SiO_2	Na_2O	CaO	P_2O_5				
Shaikh2019	Ti-6Al-4V	—	Bioglass 45S5	45	24.5	24.5	6	—	Melt-quenching	—	Shaikh et al. (2019)
Catauro2016	Pure Ti (commercially grade 4)	Disks; diameter: 8 mm, thickness: 2.20 mm	—	—	—	—	—	—	Sol–gel	—	Catauro et al. (2016)
Ananth2013	Ti-6Al-4V	Plate: 10 × 10 × 2 mm^3	—	54	—	24	14	MgO: 8	—	Samples pre-deposited zirconia coating and composited with zirconia in different ratios	Ananth et al. (2013)
Dhinasekaran2021	Pure Ti	Plate: 10 × 10 × 0.25 mm^3	Bioglass 45S5	44.98	24.53	24.49	6	—	Sol–gel	—	Dhinasekaran et al. (2021)
Fu2017 (a)	—	Plate: 10 × 10 × 1.2 mm^3	—	—	—	—	—	—	Sol–gel	Doped with Ag	Fu et al. (2017)
Gaweda2018	—	—	Black glasses	—	—	—	—	—	Sol–gel	—	Gaweda et al. (2018)
Patel2019	Pure Ti	Plate: 10 × 10 × 1 mm^3	—	—	—	—	—	—	—	Composited with chitosan	Patel et al. (2019)
Su2019	Ti-6Al-4V	—	—	100	—	—	—	—	Sinter–granulation	Composited with HA	Su et al. (2019)
				50	—	50	—	—			
				50	—	30	20	—			
				50	10	30	10	—			
Fu2017 (b)	Titanium (grade TA2)	Plate: 10 × 10 × 1.2 mm^3	—	—	—	—	—	—	Sol–gel	Doped with strontium	Fu et al. (2017)
Ledda2016	Pure Ti	Plate: 1 × 1 cm^2	RKKP glass-ceramic	43.68	4.53	31.3	11.1	MgO: 2.78, K_2O: 0.19, CaF_2: 4.92, La_2O_3: 0.5, and Ta_2O_5: 1	Sol–gel	—	Ledda et al. (2016)

(Continued on following page)

10.3389/fbioe.2023.1269223

TABLE 2 (*Continued*) Characteristics of included studies.

Study ID	Titanium alloy substrate	Sample shape and size	Glass model	Glass component (wt%)				Other components	Manufacturing method	Special process	Ref.
				SiO_2	Na_2O	CaO	P_2O_5				
Chen, X. C.2014	Ti-6Al-4V	Plate: 10 × 12 × 2 mm^3; cylinders; diameter: 25.4 mm, length: 25.4 mm	CaO–MgO–SiO_2-based multiphase glass-ceramic M2	49.13	—	43.19	—	MgO: 7.68	Sol–gel	—	Chen et al. (2014)
Ordikhani, F.2014	Titanium (biomedical grade)	Plate: 10 × 20 × 0.45 mm^3	—	45	24.5	24.5	6	—	Melt-drive	Composited with chitosan and vancomycin	Ordikhani and Simchi (2014)
Palangadan, R.2014	Ti-6Al-4V	Plate: 15 × 10 × 2 mm^3	Bioactive triphasic glass-ceramic composition (HASi)	34.2		44.9	16.3	MgO: 4.6, CaF_2: 0.5	Sol–gel	—	Palangadan et al. (2014)
Ordikhani2016	Titanium	Plate: 10 × 20 × 0.45 mm^3	—	45	24.5	24.5	6	—	Melt-drive	Multilayer nanocomposite coating of bioactive glass with chitosan and vancomycin	Ordikhani et al. (2016)
Popa2017	Pure Ti	Plate: 10 × 10 mm^2	—	37.8	—	33.1	13	MgO: 10, CaF_2: 0.8, and ZnO: 5.3	Melt-drive	—	Popa et al. (2017)
Rastegari2019	Ti-6Al-4V	—	SiO_2–CaO–MgO bioactive glasses	—	—	—	—	—	Coprecipitation	Composited with chitosan	Rastegari and Salahinejad (2019)
Boschetto2020	Ti-6Al-4V (grade 5)	—	Bioglass 45S5	—	—	—	—	—	—	Composited with chitosan and polyethylene oxide nanofibers	Boschetto et al. (2020)
Lung2021	Pure Ti (grade 2)	Disks; diameter: 25.4 mm; and thickness: 5.1 mm	58S	55.6	—	33.1	11.3	—	Sol–gel	Doped with silver, cobalt oxide, and titanium dioxide	Lung et al. (2021)
			Ag56S	52.8	—	32.6	11.2	Ag: 3.4			
			Co56S	53.4	—	32.9	11.3	CoO: 2.4			
			Ti56S	53.3	—	32.9	11.3	TiO_2: 2.5			
			All52S	48.5	—	32.2	11.1	TiO_2: 2.5, CoO: 2.3, Ag: 3.4			
Matter2021	Ti-6Al-4V (medical grade)	Disks; diameter: 15 mm, thickness: 1 mm	—	—	—	—	—	—	Flame-made	Composited with cerium oxide; doped with strontium oxide and Zn and then composited with cerium oxide	Matter et al. (2021)

(Continued on following page)

10.3389/fbioe.2023.1269223

TABLE 2 (*Continued*) Characteristics of included studies.

Study ID	Titanium alloy substrate	Sample shape and size	Glass model	Glass component (wt%)				Other components	Manufacturing method	Special process	Ref.
				SiO_2	Na_2O	CaO	P_2O_5				
Rau2020	Pure Ti	Plate: 1 × 1 cm^2	Silicate glasses 13–93	56.6	5.5	18.5	3.7	MgO: 4.6 and K_2O: 11.1	Melt-quenching	—	Rau et al. (2020)
			Borate glasses 13–93-B3	—	5.5	18.5	3.7	MgO: 4.6, K_2O: 11.1, and B_2O_3: 56.6			
Abushahba2020	Pure Ti (grade 5)	Plate: 10 × 10 × 1 mm^3	Bioglass 45S5	45	24.5	24.5	6	—	—	Doped with zinc oxide	Abushahba et al. (2020)
			Zn4	42.4	24.1	22.4	5.9	ZnO: 5.2			
Nesabi2021	Pure Ti (medical grade)	Disks; diameter: 12 mm, thickness: 1 mm	58S	58	—	38	4	—	Sol–gel	Samples only or samples and bioglass or both were alkali treated with sodium hydroxide	Nesabi et al. (2021)
Ye2017	Ti-6Al-4V (medical grade 23)	Cylinders; diameter: 10 mm, height: 10 mm	—	—	—	—	—	—	Sol–gel	Samples pre-deposited a silica interlayer	Ye et al. (2017)
Safaee2021	Pure Ti (commercially medical grade)	Plate: 10 × 10 × 1 mm^3	58S	58	—	33	9	—	Sol–gel	—	Safaee et al. (2021)
Zhang2016	Ti-6Al-4V	Plate: 10 × 10 × 2 mm^3	—	75.6	—	13.2	11.2	—	Sol–gel	Samples pre-deposited ZrO_2 coatings	Zhang et al. (2016)
Avcu2018	Ti-6Al-4V	Plate: 76.2 × 25.4 × 2 mm^3	Vitryxx® Bioactive Glass (bioactive glass Bioglass 45S5®)	45 ± 5	24.5 ± 3	24.5 ± 3	6 ± 2	—	—	Composited with chitosan	Avcu et al. (2018)
			Nano-bioglass (Schott NF-180 glass)	55	—	—	—	B_2O_3: 10, Al_2O_3: 10, BaO: 25			
Guimarães2020	Pure Ti (grade 4)	Plate: 4 × 2 mm^2	—	—	—	—	—	—	Sol–gel	Deposited potassium hydroxide coatings based on bioglass coatings	Guimarães et al. (2020)
Zarghami2020	Pure Ti (biomedical grade)	Plate: 5 × 5 × 0.7 mm^3	Bioactive glass nanoparticles (BGNs)	45		49	6	—	Wet synthesized	Composited with chitosan–vancomycin	Zarghami et al. (2020)
Costa2020	Pure Ti (grade 2)	Disks; diameter: 10 mm,	—	—	—	—	—	—	—	—	Costa et al. (2020)

(Continued on following page)

10.3389/fbioe.2023.1269223

TABLE 2 (*Continued*) Characteristics of included studies.

Study ID	Titanium alloy substrate	Sample shape and size	Glass model	Glass component (wt%)				Other components	Manufacturing method	Special process	Ref.
				SiO_2	Na_2O	CaO	P_2O_5				
		thickness: 2 mm									
Zarghami2021	Pure Ti (biomedical grade)	Plate: 5 × 5 × 0.7 mm^3	—	—	—	—	—	—	—	Composited with chitosan, vancomycin, and melittin	Zarghami et al. (2021)
Bargavi2022	Pure Ti (grade 2)	Plate: 20 × 10 × 1 mm^3	Bioglass 45S5	45	24.5	24.5	6	—	Sol–gel	Doped with alumina	Bargavi et al. (2022)
Bargavi2020	Pure Ti	Plate: 2 × 1 cm^2	—	—	—	—	—	—	Sol–gel	Composited with zirconia	Bargavi et al. (2020)
Wu, C. T.2014	Ti-6Al-4V	Plate: 10 × 10 × 2 mm^3	$Sr_2MgSi_2O_7$ (SMS) ceramic	—	—	—	—	—	Solid state reaction	—	Wu et al. (2014)
Catauro, M.2015	Pure Ti (grade 4)	—	Calcium silicate glass coatings containing Ag	—	—	—	—	—	Sol–gel	Doped with different percentages of silver oxide	Catauro et al. (2015)
Ledda, M.2015	Pure Ti	Plate: 1 × 1 cm^2	RKKP glass-ceramic composition	43.68	4.53	31.3	11.1	MgO: 2.78, K_2O: 0.19, CaF_2: 4.92, La_2O_3: 0.5, and Ta_2O_5: 1	Aqueous Sol–gel	—	Ledda et al. (2015)
Mistry2016	Ti-6Al-4V (clinical)	Screw; diameter: 3.5 mm, length: 11 mm and diameter: 4 mm, length: 13 mm	—	59.1	22.24	19.2	5.46	TiO_2: 1 and B_2O_3: 9.4	Melt derived	—	Mistry et al. (2016)
Soares2018	Titanium (*in vivo*)	Cylinders; diameter: 3.5 mm, length: 7 mm (*in vivo*); disks, diameter: 10 mm (*in vitro*)	BSF18	—	—	—	—	—	—	—	Soares et al. (2018)
Klyui2021	Ti-6Al-4V	Cylinders; diameter: 2 mm,	—	32	3.3	39.7	16.3	MgO: 2.7, ZnO: 5, and Al_2O_3: 1	—	Composited with HA and doped with Zn, Cu, and Ag	Klyui et al. (2021)

(Continued on following page)

10.3389/fbioe.2023.1269223

TABLE 2 (*Continued*) Characteristics of included studies.

Study ID	Titanium alloy substrate	Sample shape and size	Glass model	Glass component (wt%)				Other components	Manufacturing method	Special process	Ref.
				SiO_2	Na_2O	CaO	P_2O_5				
		length: 4 mm (*in vivo*); plate: 20 × 20 × 1 mm^3 (*in vitro*)									
vanOirschot2016 (a)	Ti-6Al-4V	Plate: 12 × 9 × 1 mm^3	S53P4	—	—	—	—	—	—	Composited with HA	van Oirschot et al. (2016)
vanOirschot2016 (b)	Ti-6Al-4V	Cylindrical screw-type; diameter: 4.0 mm, length: 12 mm	S53P4	—	—	—	—	—	—	Composited with HA	van Oirschot et al. (2016)
Wang2018	Ti-6Al-4V	Disks; diameter: 20 mm, thickness: 1 mm	Bioglass 45S5	45	24.5	24.5	6	—	Melt-quenching	Composited with HA in different ratios	Wang et al. (2018)
Mehdikhani-Nahrkhalaji, M.2015	Pure Ti (grade 2)	Piece: 20 × 10 mm^2	58S	57.72	—	35.09	7.1	—	Sol–gel	Composited with poly (lactide-co-glycolide) and hydroxyapatite; composited with poly (lactide-co-glycolide)	Mehdikhani-Nahrkhalaji et al. (2015)
Popa, A. C.2015	Ti-6Al-4V; pure Ti (grade 1)	Screws; diameter: 3.5 mm, length: 10 mm (*in vivo*); disks, area: 1 cm^2 (*in vitro*)	—	46.06	4.53	28.66	6.22	MgO: 8.83 and CaF_2: 5.7	—	—	Popa et al. (2015)
Zhang2019	Ti-6Al-4V	Cylinders; diameter: 2 mm, length: 6 mm	CaO-MgO-SiO_2–based bioactive glass-ceramic	49.13	—	43.19	—	MgO: 7.68	Sol–gel	—	Taguchi et al. (2019)
Newman, S. D.2014	Ti-6Al-4V	Cylinders; diameter: 3.5 mm,	SrBG	—	—	—	—	—	Melt-quenching	Doped with strontium	Newman et al. (2014)

(Continued on following page)

10.3389/fbioe.2023.1269223

TABLE 2 (*Continued*) Characteristics of included studies.

Study ID	Titanium alloy substrate	Sample shape and size	Glass model	Glass component (wt%)				Other components	Manufacturing method	Special process	Ref.
				SiO_2	Na_2O	CaO	P_2O_5				
		length: 6.2 mm									
Wang2020	Ti-6Al-4V	Plate: 5 × 2 × 1 mm^3	Bioglass 45S5	45	24.5	24.5	6	—	—	Composited with HA and $CaSiO_3$	Wang et al. (2020)
Zhang2021	Ti-6Al-4V (medical grade 23)	Cylinders; diameter: 5 mm, length: 10 mm	—	—	—	—	—	—	Sol–gel	Samples pre-deposited a silica interlayer	Zhang et al. (2021)
vanOirschot2014	Pure Ti	Cylindrical screw type; diameter: 3.4 mm, length: 10 mm	BG S53P4	—	—	—	—	—	—	Composited with HA	van Oirschot et al. (2014)
Orita2022	Ti6Al2Nb1Ta0.8Mo	—	AW-GC	—	—	—	—	—	—	—	Orita et al. (2022)

10.3389/fbioe.2023.1269223

TABLE 3 Characteristics of *in vitro* cell experiments.

Cell type		Test aim	Ref.
Human osteosarcoma cell line	U2OS	Impact of biomaterials on osteogenesis and cell reaction mechanism	Shaikh et al. (2019)
	MG-63		Ananth et al., 2013; Ordikhani and Simchi, 2014; Ordikhani et al., 2016; Gaweda et al., 2018; Rastegari and Salahinejad, 2019; Su et al., 2019; Dhinasekaran et al., 2021; Bargavi et al., 2020; Bargavi et al., 2022
	Saos-2		Boschetto et al. (2020)
Pre-osteoblast MC3T3-E1 cell line		Model to investigate osteoblast function	(Fu et al., 2017; Patel et al., 2019; Abushahba et al., 2020; Guimarães et al., 2020; Zarghami et al., 2020; Lung et al., 2021; Nesabi et al., 2021; Safaee et al., 2021; Zarghami et al., 2021)
Fibroblasts cells	NIH3T3 murine fibroblast cells	Possibility of cells to restore tissue injury and regulate bone regeneration	(Catauro et al., 2015; Catauro et al., 2016)
	L-929 mouse fibroblast cell line		(Mistry et al., 2016; Wang et al., 2018; Su et al., 2019)
	Normal human dermal fibroblasts (NHDFs)		Matter et al. (2021)
	Human gingival fibroblast (HGF) cells		Costa et al. (2020)
Mesenchymal stem cell (MSC)	—	Investigate possibility of cell treatment and applications in regenerative medicine	Popa et al. (2017)
	Rabbit adipose derived (rADMSC)		Palangadan et al. (2014)
	Equine adipose tissue derived (ADMSC)		Rau et al. (2020)
	Bone marrow (BMSCs)		Wu et al. (2014)
	Human amniotic mesenchymal stromal cells (hAMSCs)		Ledda et al. (2016)
	Human bone marrow stromal cells (hBMSCs)		Ye et al. (2017)
	Rabbit bone marrow stromal cells (rBMSCs)		Zhang et al. (2016)
Others	Human erythrocyte cells	Biosafety assessment for clinical application	(Bargavi et al., 2020; Dhinasekaran et al., 2021; Bargavi et al., 2022)
	Rat osteoblasts	Stimulate osteointegration	Chen et al. (2014)
	Human umbilical endothelial cell (HUV-EC-C) line	Stimulate blood treatments in early surgery period	Matter et al. (2021)
	Human bone progenitor cell (HBCs)	Stimulate osteointegration	Matter et al. (2021)
	Murine-derived macrophage cell line RAW 264.7 cells	Study mechanism of body immunity protection and regulate process of osteointegration	Wu et al. (2014)
	Osteoclasts (derived from RAW 264.7 cells)	Regulate osteointegration	Wu et al. (2014)
	Caco-2 human colon carcinoma cell line	Investigate cell therapy and strategies for regenerative medicine	Ledda et al. (2015)
	Human dental pulp stem cells (DPSCs)	Possibility of cell therapy	Popa et al. (2015)

3.2 Study type

3.2.1 *In vitro* studies

In vitro experiments were introduced in 43 studies, and the cell types tested are listed in Table 3. Among all *in vitro* studies, human osteosarcoma cells, pre-osteoblast MC3T3-E1 cells, mesenchymal matrix cells, stem cells, and fibroblasts have been widely used.

Being derived from malignant bone tumors, various types of osteosarcoma cell lines were isolated due to bone tumor categories, for example, U2OS, Saos-2, and MG-63 (Matter et al., 2021). According to their properties of having a higher capacity to help matrix mineralization, being easier to culture, having a more stable phenotype (Rau et al., 2020), and having a faster proliferation rate (Abushahba et al., 2020), they were frequently used for fabricating

TABLE 4 Characteristics of animal experiments.

Study ID	Application field (surgery type)	Basic information about animals						Number (animal numbers/site numbers)		Intervention		Ref.
		Species	Sex	Age	Weight	Surgical site	Substrate material	Control group	Experimental group	Control group	Experimental group	
Zhang2019	Femoral bone defect	New Zealand rabbit	—	—	Approximately 3.0 kg	Femur	Ti6Al4V cylinders; diameter: 2 mm, length: 6 mm	24 (48)	24 (48)	Coated with HA	Coated with CaO-MgO-SiO_2–based bioactive glass-ceramic	Taguchi et al. (2019)
Newman, S. D.2014	Skeletal reconstructive surgery	New Zealand rabbit	Male	6 months old	3.5–3.8 kg	Distal femur and proximal tibia	Ti6Al4V cylinders; diameter: 3.5 mm, length: 6.2 mm	27 (27)	27 (27)	Coated with HA	Coated with SrBG	Newman et al. (2014)
Zhang2021	Femoral bone defect	New Zealand rabbit	Male	Mature	Average weight of 2.5 kg (SD = 0.3 kg)	Distal femoral condyle	Ti6Al4V porous cylinders; diameter: 5, length: 10 mm^2, porosity: 68%	6 (12)	6 (12)	Uncoated Ti-6Al-4V	Coated with BG/MBG	Zhang et al. (2021)
Wang2020	Tibial bone defect	New Zealand rabbit	—	6 months old	3–3.5 kg	Tibia	Ti6Al4V plate; 5 mm × 2 mm × 1 mm	—	—	—	Coated with HA/BG/WS composite films	Wang et al. (2020)
Wang2018	Tibial bone defect	New Zealand rabbit	—	—	—	Tibia	Ti6Al4V plate; 5 mm × 2 mm × 1 mm	—	—	HA and BG composite films (90% HA + 10% BG film; 80% HA + 20% BG film; 20% HA + 80% BG film		Wang et al. (2018)
Mehdikhani-Nahrkhalaji, M.2015	Tibial bone defect	New Zealand rabbit	Male	8–10 months	3–3.5 kg	Tibia	Pure titanium screws; diameter: 1.5 mm, length: 6 mm	20 for PBGHA nanocomposite coating, 20 without coating	20	Uncoated pure Ti	Coated with PBGHA nanocomposite/PBG nanocomposite	Mehdikhani-Nahrkhalaji et al. (2015)
van Oirschot,2014	Mandibular implantation	Beagle dogs	—	1–2 years old	10–12 kg	Right side of the mandible	Screw-type pure titanium implants; diameter: 3.4 mm, length: 10 mm	—	16 (48)	—	Coated with different ratios of HA and BG (HA, HABGLow, and HABGHigh)	van Oirschot et al. (2014)

(Continued on following page)

10.3389/fbioe.2023.1269223

TABLE 4 (*Continued*) Characteristics of animal experiments.

Study ID	Application field (surgery type)	Basic information about animals						Number (animal numbers/site numbers)		Intervention		Ref.
		Species	Sex	Age	Weight	Surgical site	Substrate material	Control group	Experimental group	Control group	Experimental group	
Soares2018	Mandibular implantation	Beagle dogs	Male	Approximately 1.5 years of age	—	Right and left mandible	Morse taper pure titanium implants; diameter: 3.5 mm, length: 7 mm	10 (20)	10 (20)	AE surface implants	Coated with AE surface functionalized with BSF18	Soares et al. (2018)
Klyui2021	Femoral bone defect	Wistar rats	Male	—	240 ± 15 g	Lower femur part	Pure Ti cylinders; diameter: 2 mm, length: 4 mm	Four for each group (24 in total)		1) Uncoated implant; 2) abrasive-surfaced implant with SiC powder; 3) with pure HA; 4) with HA composites; 5) with composite material—BG, 50 wt%; pure HA, 30 wt%; TCP, 20 wt%; 6) with composite material—BG, 65 wt%; HA combination, 35 wt%		Klyui et al. (2021)
Van Oirschot2016	Bone conduction chamber cassette model on the goat transverse process	Dutch Saanen milk goats	—	24 months	60 kg	Spinal transverse	Ti-6Al-4V rectangular samples; 12 × 9 × 1 mm, width: 0.5 mm	10 (40) for each group	10 (40)	Machined Ti, PLD HA, plasma-sprayed HA coating, and biomimetic HA coating	Coated with hydroxyapatite/bioactive glass	van Oirschot et al. (2016)
van Oirschot2016	Iliac bone defect, osteotomies	Saanen goats	Female	24 months	60 kg	Iliac crest	Cylindrical screw-type pure titanium implants; diameter: 4.0 mm, length: 12 mm	8 (32)/8 (32)	8 (32)	Uncoated with grit-blasted/acid-etched surface, coated with hydroxyapatite	Coated with hydroxyapatite/bioactive glass	van Oirschot et al. (2016)
Popa, A. C.2015	Mandibular implantation	Pigs	—	—	—	Mandibular bone	Ti6Al4V dental screws; diameter: 3.5 mm, length: 10 mm	—	—	Uncoated	RF-MS coating with BG/RF-MS BG coating + PDHT	Popa et al. (2015)

10.3389/fbioe.2023.1269223

TABLE 5 Characteristics of clinical trials.

Surgery type	Study ID	Study type	Patients				Interventions and comparisons			Outcome indicator	Ref.
			Surgical site	Number	Sex	Inclusion criteria	Substrate material	Control group	Experimental group		
Total hip arthroplasty	Orita2022	Retrospective study	Hip joint	99 patients (116 hips)	—	Received cementless implants, followed up for at least 10 years	Pure titanium hip implants	Uncoated pure titanium	Cementless glass-ceramics containing apatite and wollastonite (AW-GC)	1) Hip joint function; 2) stress shielding; 3) extent of osteolysis; 4) steady-state wear rate; 5) survival rate	Orita et al. (2022)
Dental implant in human jaws	Mistry2016	Prospective clinical trials	Incisor areas of anterior maxilla and mandible	62 patients (126 sites)	35 males and 27 females	Age limited to 18–58 years, and anterior incisor area allows for the same implants; minimal bone requirements of 6 mm in alveolar ridge width and 18 mm in ridge height	Ti6Al4V screw endosseous implant (size: 3.5 and 4 mm diameter × 11 and 13 mm length, respectively)	Uncoated Ti6Al4V; coated with HAp	Coated with BAG (SiO_2 59.1%, CaO 19.2%, P_2O_5 5.46%, B_2O_3 9.4%, TiO_2 1%, and Na_2O 22.24%)	1) New osseous tissue deposition; 2) bone loss; 3) plaque index; 4) gingival index; 5) probing pocket depth; 6) gingival recession	Mistry et al. (2016)

the osteoblast models. The pre-osteoblast MC3T3-E1 cell line is generated from mouse primary osteoblast culture (Nesabi et al., 2021), which displays similar behavior toward primary osteoblasts and, thus, shows better osteogenic differentiation (Ye et al., 2017). Mesenchymal matrix or stem cells, which are derived from a variety of tissues such as the bone marrow and adipose tissue, are multipotent adult cells (Zhang et al., 2016) and can differentiate into different cell lines. Adipose-derived mesenchymal stem cells (MSCs) are more frequently used because they are abundant and the collection process is simpler and does not cause great trauma (Chen et al., 2014), and this leads to their wide application prospects in regenerative medicine (Palangadan et al., 2014). Such MSCs can also be used to study the osteogenic differentiation potential of glass materials and to study the ability to synthesize certain specific proteins (Rau et al., 2020). Involved in granulation tissue formation, fibroblasts are connective tissue cells that synthesize collagen fibers and matrix components and are essential in the wound healing process (Avcu et al., 2018) and mediation of soft tissue integration (Patel et al., 2019). The test on fibroblasts can illustrate a material's potential application in soft tissue repair.

3.2.2 *In vivo* studies

For animal tests, the characteristics of the *in vivo* studies that were included are listed in Table 4. Many included studies have chosen New Zealand rabbits, and the included surgical sites were the femur, rabbit tibia, and mandible for dogs or pigs. Rabbits are the most commonly used animals due to their size and growth speed. Less soft tissue is found around rabbits' tibia, which is easy to operate on, while the femur has sufficient bone marrow cavity and is, thus, suitable for studying internal fixation of fractures (Guimarães et al., 2020). However, the small size of the bone has led to a reduction in the number and size of implants and, consequently, their style types are also reduced. Pig mandibles have a similar regeneration rate, morphology, and masticatory mechanics to that of humans, and human-sized dental implants are allowed (Zarghami et al., 2020). Even though mini pigs can overcome the problem of being overweight, they are very aggressive and difficult to tame. Dog mandibles are commonly used in dental implant models for assessing bone regeneration around implants (Zarghami et al., 2021). We can use human-sized dental implants in larger dogs that can actively cooperate with rehabilitation treatment programs (Guimarães et al., 2020). However, ethical issues deserve further discussion due to the harm of medical experiments to dogs.

3.2.3 Clinical studies

For clinical trials, BG-coated implants are mainly applied in orthopedics and stomatology, and the relative information is shown in Table 5. To date, clinical trials have revealed the effectiveness of BG-coated implants in total hip arthroplasty and dental implantation. In the 10-year retrospective studies carried out by Orita et al. (2022) through clinical evaluation and radiographic assessment after hip arthroplasty surgery, BG-coated implants were proven to have a better survival rate and wear resistance. In the prospective studies by Mistry et al. (2016), by comparing the osteogenesis around dental implants, the BG-coated dental implants contributed to new bone generation.

4 Coating manufacturing technology for BGs on Ti implant surface

4.1 Substrate pretreatment

Substrate pretreatment plays an important role in bio-interaction (Pattanaik et al., 2012), which can improve corrosion resistance (Kim et al., 1996) and osteointegration (Buser et al., 2012; Fischer and Stenberg, 2012). Surface roughness can also be increased as well as the adhesion between substrate and coating. Sandblasting is a simple, low-cost method (Zhou et al., 2016). Aluminum oxide and silicon carbon can be injected onto the substrate using high-speed compressed air, which improves the surface roughness. Sandblasting combined with acid etching forms a microporous structure and removes the residual abrasive particles (Pattanaik et al., 2012). Chemical pretreatments are also performed. Alkali and heat-treated implants, which apply hydroxide at high temperatures, form a titanate layer on the Ti surface. This improves the connection between the bone tissue and the implant and enables higher implant stability (Nishiguchi et al., 2003). The porous nanostructures can also increase the bond strength between coatings and substrates (Nesabi et al., 2021). Surface topology is an important surface structure that can effectively regulate the behavior of cells. Numerous studies have shown that rough or micro-/nano-sized topological structures can effectively improve cell behavior, thereby enhancing the integration ability between implants and bone interfaces (Geng et al., 2021a). Micro-arc oxidation can generate a uniform, rough, and porous oxide layer, which contributes to a tighter connection between substrate and coatings (Ma et al., 2016). Among the different coating technologies, polishing and sandblasting the titanium substrate to increase its surface roughness, followed by cleaning the substrate with distilled water, acetone, or ethanol, are the more common pretreatment procedures.

4.2 Pulsed laser deposition

PLD is performed under confined conditions. The schematic diagram is shown in Figure 3A. The pulsed molecular laser source can be used to sinter bioactive glass. In a physical coating preparation process, the precise ratio of the coating components can be guaranteed, and the prepared coatings are more uniformly attached. To ensure uniform adhesion and prevent laser single-point substrate surface corrosion, the target is usually coated in a rotary manner (Ma et al., 2016; Wang et al., 2018; Wang et al., 2020).

Table 6 shows the process parameters of the included studies. In the included studies, PLD was usually performed under an environmental temperature of 200°C–800°C. The substrate temperature mainly regulates crystal composition and physiochemical and biological properties by changing the alignments of the target material on the surface and the bonding level of the coating (Figure 4) (Serra et al., 2004; Wang et al., 2020). When the substrate temperature reaches 200°C, the BG coating gains the best mechanical properties and surface appearance and can best bond with the substrates (Serra et al., 2004; Zhao et al., 2008). However, another study has proven that coatings formed under 700°C have the best biological properties (Dhinasekaran et al., 2021). To reduce the overlap between the laser and vapor that it generates, the angle of incidence of the laser projection on the substrate is maintained at 45° (Shaikh et al., 2019).

Coatings formed by PLD have a dense surface, a better chemical composition ratio of BG (Ledda et al., 2016), and a microsphere (Palangadan et al., 2014). The nanostructure on the surface can help in implant osteointegration (Rau et al., 2020). PLD mixed with micro-arc oxidation enables the porous morphology of coatings, which results in a better surface appearance and structure (Ma et al., 2016).

4.3 Magnetron sputtering

Magnetron sputtering is usually performed under low-pressure conditions, where the deposition chamber is filled with gas, which usually comprises argon (Ar) (Figure 3B). Ar atoms are ionized to produce Ar^+ and new electrons, with the electronic field accelerating the electrons that bombard the targets and sputter the ions from the target atoms. After deposition, the substrate is heated to optimize the coatings (Shi et al., 2008).

The distance between the substrate and target may influence the deposition rate. A closer distance means a higher deposition rate. However, the increased momentum of the charged particles leads to an increase in the substrate temperature (Maximov et al., 2021). The acceleration voltage, heat treatment time, vacuum pressure, and filling gas also have an impact on the process (Wolke et al., 2005; Popa et al., 2017).

Magnetron sputtering makes the thickness of the coating uniform and adjustable and results in higher adhesion and purity of the coating (Shi et al., 2008), which makes it suitable for covering large areas of the substrate, and the technology is easily scalable to the industrial level under alternating current conditions (Popa et al., 2015).

4.4 Dip coating

Dip coating technology is usually combined with sol–gel, which is a process of preparing bioactive glass (Figure 5A). The glass precursor is obtained from a solution of metal alkoxides and nitrates in ethanol, which is subjected to sufficient hydrolysis and condensation reactions by stirring (Catauro et al., 2016), and the substrates are then immersed in gel. In other cases, the prepared glass is mixed into the solution and infiltrates the substrates. After dipping, drying and calcination are performed to remove excess material and stabilize the coating.

Various conditions such as the extraction speed, dipping times, viscosity of sol, and process of drying influence the coating formation (Brown, 1989). The extraction speed is directly related to the coating thickness. The slower the speed, the thinner the coating and the more the original shape of the substrate can be maintained.

When compared with others, dip coating can be performed under lower temperatures, and the process is cheaper and easier. The coatings are more uniform and have higher purity, which stabilizes the substrate's shape (Fu et al., 2011; Catauro et al., 2016; Fu et al., 2017a). Other components, such as nanoparticles, mesoporous

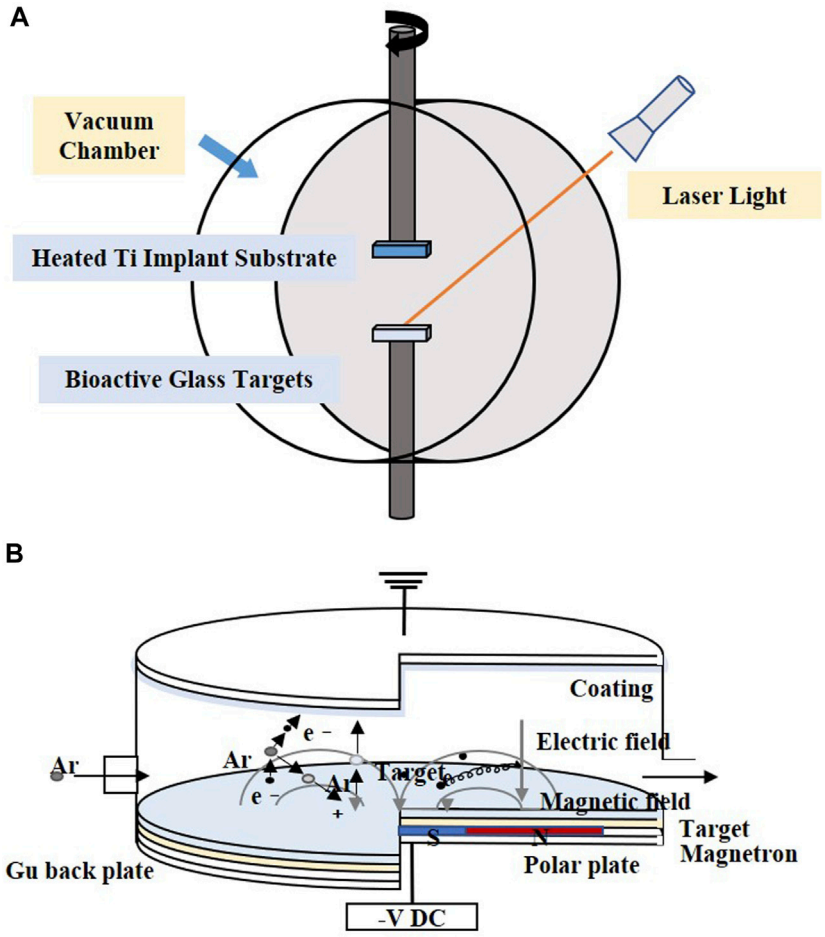

FIGURE 3
Coating manufacturing technologies of **(A)** PLD and **(B)** magnetron sputtering. The figures were redesigned based on other studies (Torrisi et al., 2007; Calderon Velasco et al., 2016).

agents, and antimicrobial agents added to the solution, may lead to complications in the coating structure and composition (Tian et al., 2016; Rivadeneira and Gorustovich, 2017).

4.5 Electrophoretic deposition

Electrophoretic deposition (EPD) forms a coating by applying a direct current or alternating current electric field between two electrodes, causing charged particles to be dispersed in suspension and move in the direction of the substrate electrode (Figure 5B). The particles are deposited in an orderly manner on the substrate (Wang et al., 2014; Sultana et al., 2021). Heat treatment at 800°C–900°C makes the coatings denser and more stable (Ananth et al., 2013; Khanmohammadi et al., 2020).

Table 7 shows the parameters in the process of EPD in the included studies. The factors affecting the properties of coatings prepared via EPD can be concluded as solutions' stability, conductivity (Zhitomirsky et al., 2009), and BG powder concentration. The distance between the electrodes, applied electric field voltage, deposition time, temperature, and pH all influence the deposited coatings. Changes in the BG concentration in the solution may increase the electrophoretic mobility, and adjustments made in the deposition parameters can make the coatings denser and more uniform (Jugowiec et al., 2017).

4.6 Hydrothermal deposition

Hydrothermal deposition is a multiphase reaction of dissolution and recrystallization of materials under high temperature and pressure with an aqueous solution as the reaction system in a closed autoclave, leading to the formation of precipitates (Pore et al., 2021). This method can be used for the preparation of powders and as a coating technique for materials.

The process essentially involves attaching thermocouples and pressure sensors to the reactor assembly, setting the parameters, and heating the reactor. Subsequently, pressure builds up and the coating is deposited on the sample in a supercritical environment (Ali et al., 2018).

The method is simple and inexpensive and can be used to synthesize coatings with uniform thickness, orientation, and shape directly in an aqueous solution (Valanezhad et al., 2015). The coating structure can be

TABLE 6 Parameters for pulsed laser deposition in the included studies.

Study ID	Chamber condition		Laser parameter					Deposition parameter			Ref.
	Gas	Pressure (Pa)	Emission wavelength	Repetition rate (Hz)	Pulse duration (ns)	Base distance (mm)	Deposition time h)	Substrate temperature (°C)	Laser fluence (J/cm^2)	
Ledda, M. 2016	Vacuum	1.5×10^{-4}	532	10	10	20	2	500	12	Ledda et al. (2016)
Ma 2016	Vacuum	1×10^{-4}	1,064	10	7	40	1	200	—	Ma et al. (2016)
Palangadan, R. 2014	Controlled oxygen atmosphere	10^{-1}	355	10	—	35	1	400	—	Palangadan et al. (2014)
Wang 2020	Argon gas	45	248	5	—	—	—	600/800	5	Wang et al. (2020)
Wang 2018	Vacuum	3×10^{-5}	248	5	20	—	1	600	—	Wang et al. (2018)
Ledda, 2015	—	—	532	10	10	20	2	500	12	Ledda et al. (2015)
Shaikh 2019	Vacuum	2×10^{-3}	532	10	6	50	1	RT to 200	—	Shaikh et al. (2019)
Dhinasekaran 2021	Vacuum	1×10^{-4}	355	10	—	—	—	200	—	Dhinasekaran et al. (2021)
Rau 2020	Vacuum	10^{-4}	532	10	7	20	5	—	12	Rau et al. (2020)

controlled by changing the synthesis parameters. However, with this method, it is not easy to control the crystal structure formed, and due to the environmental requirements of high temperature and high pressure, it is more dependent on the experimental equipment.

5 Biocompatibility and antibacterial properties

5.1 Cytotoxicity and cell activity

Cytotoxicity is the killing of cells by chemicals without involving the cellular mechanisms of apoptosis or necrosis. After implantology, ions that reach the cytotoxic concentration leach out of the glass coating and interact with the cells (Al-Noaman et al., 2012). As an important indicator to assess the safety of biological materials, cytotoxicity is assessed by *in vitro* studies that simulate the survival environment of cells. A lower cell survival rate indicates higher cytotoxicity, indicating clinical risk (Wataha et al., 1994). Cell viability above 70% is usually considered non-cytotoxic (Wei and Ding, 2017). The release of large amounts of alkaline ions can have adverse effects on living cells. The increase in pH at the implantation site is accompanied by the dissolution of bioactive glass, which increases by-products and ultimately leads to toxic effects on the surrounding tissues (Jones, 2013). The adverse effect causes tissue reactions such as inflammation, necrosis, induction of immunity, and carcinogenesis (Costa, 1991).

Cytotoxicity is influenced by the substance and doped content in the glass coating. BG doped with silver ions, cobalt oxide, and titanium dioxide has shown that the doping of cobalt oxide causes higher cytotoxicity than that of silver and titanium dioxide (Lung et al., 2021). This is mainly because cobalt ions induce oxidative stress and activate intracellular nicotinamide adenine dinucleotide phosphate (NADPH) oxidase to produce ROS, which causes oxidative damage to cells (Chattopadhyay et al., 2015) and affects cell morphology and viability (Fleury et al., 2006). A high level of silver in the coating increases the level of released nitrate and improves its cytotoxicity (Catauro et al., 2015).

Cell activity refers to the ability of cells to maintain or resume normal physiological activities, such as cell adhesion, proliferation, migration, differentiation, and metabolism (Patel et al., 2019), which is affected by environmental factors, such as cell culture parameters, attached drugs, and growth factors. Cell adhesion refers to the cellular ability to contact and bind to adjacent cells or the extracellular matrix (ECM) (Humphries et al., 2009). Cell spreading is the behavior of cells on the surface of a biomaterial, which is influenced by certain protein molecules (Cuvelier et al., 2007). Cell proliferation is the process of cell division by DNA replication and other reactions under the action of cycle regulators, resulting in an increase in cell numbers, which is the basis for normal tissue development and maintenance (Xynos et al., 2001). Cell migration is the movement of cells after receiving a certain signal or concentration gradient of a substance and is essential for proper immune response and wound repair (Trepat et al., 2012). The morphological and functional changes that occur because of the selective expression of cellular genes are defined as cell differentiation (Ponzetti and Rucci, 2021).

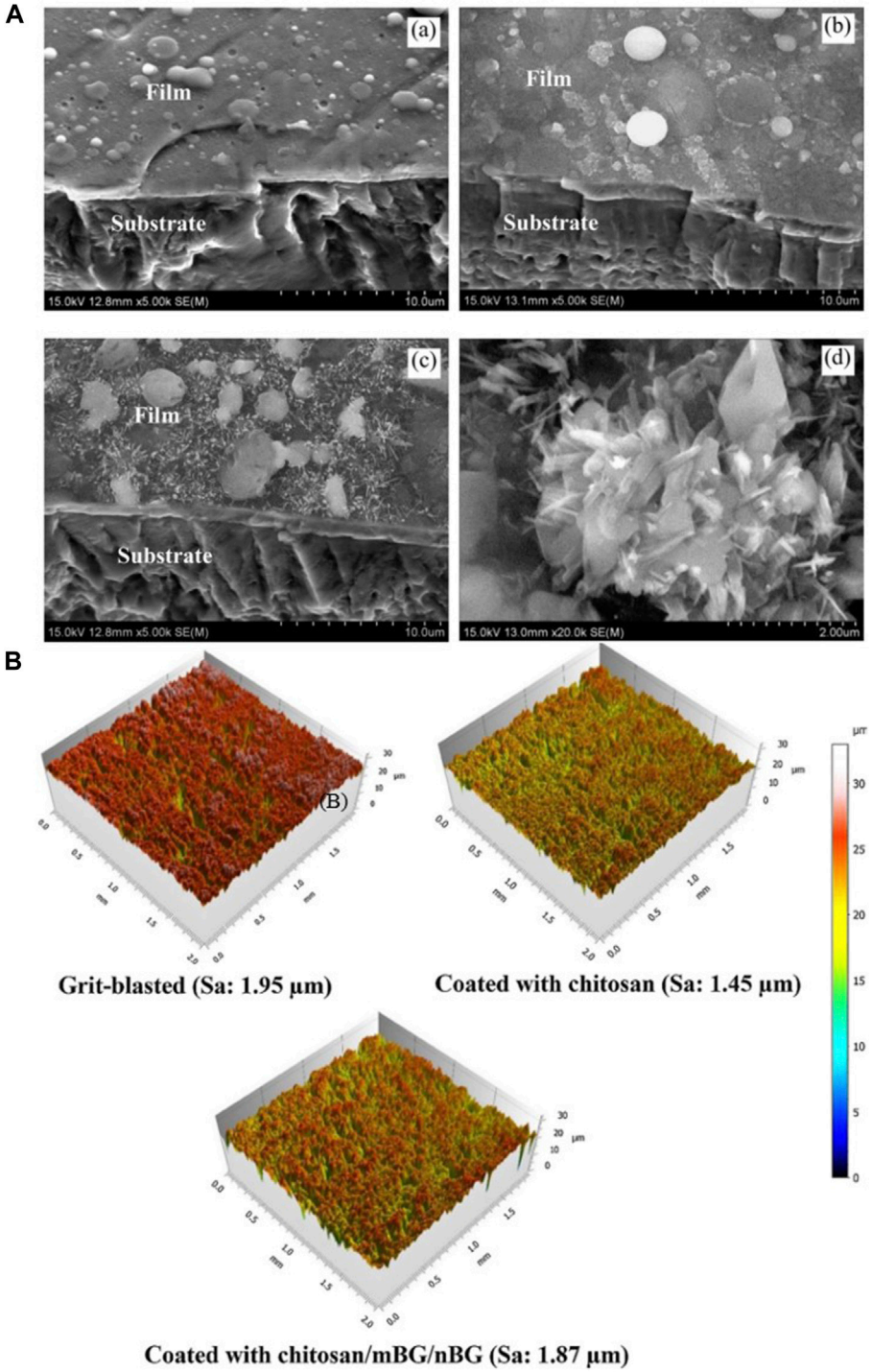

FIGURE 4
(A) SEM morphologies of films under different PLD process parameters: **(a)** 600°C; **(b)** 800°C; **(c,d)** 600°C + 800°C. **(B)** 3D surface topographies of the substrate and coatings. The figures were obtained with permission from Avcu et al. (2018) and Wang et al. (2020).

BG 45S5 is generally regarded as the gold standard for bioactive glass, and its ionic lysate induces adhesion and proliferation of cells (Abushahba et al., 2020). Calcium silicate-based materials release calcium and silicate ions, which induce osteoblast proliferation by gene activation (Catauro et al., 2016). Uniform coatings give the best cell metabolic, whereas inhomogeneous coatings, where some cells are in direct contact with the Ti matrix, are less biocompatible (Catauro et al., 2016). However, studies have shown that, when compared with HA coatings, BG-coated samples lead to the rupture and contraction of cells (Dhinasekaran et al., 2021). The surface roughness and profile of the coatings influence cell adhesion and proliferation

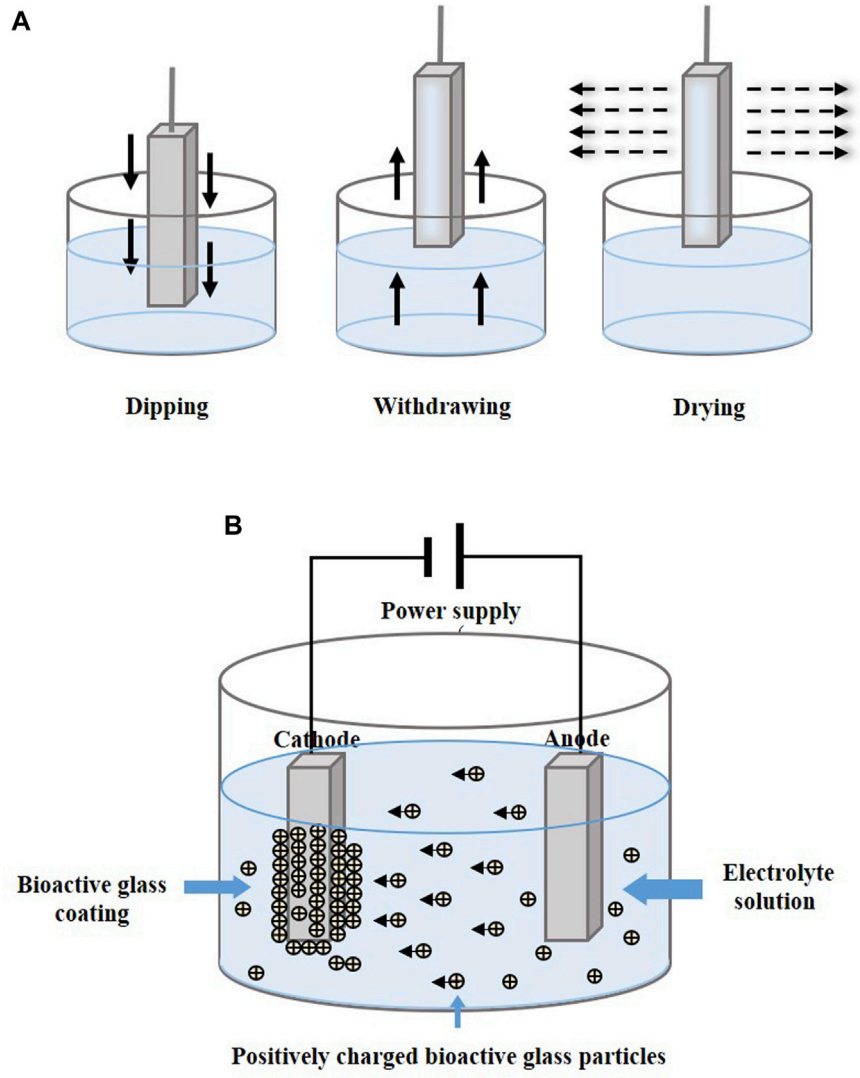

FIGURE 5
Coating manufacturing technologies of **(A)** dip coating and **(B)** EPD. The figures were redesigned based on other studies (Bohner and Lemaitre, 2009; Boccaccini et al., 2010; Bakhshandeh and Amin Yavari, 2018; Sultana et al., 2021).

(Gaweda et al., 2018). Fluorescence staining was performed on cells to observe the effect of BG coatings on the distribution of cytoskeleton, a typical sub-apical localization of the cytoskeleton around the cell membrane can be found. This phenomenon confirms the adhesion and proliferation ability of the cells and demonstrates that BG coatings contribute to the differentiation of the Caco-2 cell line [Figure 6A(a,b)] (Ledda et al., 2015). Doping zinc oxide into BG 45S5 stimulates osteoblasts proliferation and, thus, improves the combination between the implants and bone tissue (Ishikawa et al., 2002; Oki et al., 2004). BG-coated implants doped with Ag_2O increase cell viability. A large number of cells can be observed on the surface with Ag_2O in 0.008 % mol/mol, which may have resulted from the release of nitrate ions (Catauro et al., 2015). On the surface of composite coatings comprising chitosan and BG, more cell adhesion, a higher rate of proliferation, and an extended and expanded cytoskeleton can be observed (Patel et al., 2019; Zarghami et al., 2021). On the surface of yttria-stabilized zirconia (YSZ)-BG composite coatings, a large coverage of osteoblasts can be observed, with many filamentous adhesions between the cells and visible nodule formations, which is an early feature of cell differentiation [Figure 6A(c,d)]. However, increasing the relative content of YSZ in the coating decreases the cell activity, as more yttria Y^{3+} ions are released (Ananth et al., 2013).

In *in vivo* experiments, after the formation of HA on the surface, five stages of biological events occurred: 1) growth factors adsorption, 2) bone progenitor cells adhesion, 3) proliferation, 4) differentiation, and 5) production of the extracellular matrix, which enhances bone healing (Popa et al., 2015). The surface roughness contributes to a larger cell attachment area. It has been observed that cell density and bone healing in implants with rough surfaces are significantly better than in those with smooth surfaces (Klyui et al., 2021). Dissolved ions such as Ca, Mg, and Si can activate the expression of bone-related genes by regulating bone-related cell growth and metabolism (Taguchi et al., 2019; Zhang et al., 2021). The wettability and hydrophilicity of the surface also promote cell proliferation (Soares et al., 2018).

TABLE 7 Parameters for electrophoretic deposition in included studies.

Study ID	Coating method	Coating component	Solution	Anode	Cathode	Distance between the electrodes (mm)	Work voltage (V)	Time (min)	Temperature	pH	Coating thickness (μm)	Ref.
Ordikhani, F.2014	EPD	—	Chitosan (0.5 g/L), bioactive glass (0.5 g/L), vancomycin (1 g/L)	Titanium	Titanium	10	15	10	—	3	—	Ordikhani and Simchi (2014)
			Chitosan (0.5 g/L), bioactive glass (0.5 g/L)								55 ± 6	
Ordikhani2016		—	Chitosan (0.5 g/L), bioactive glass (0.5 g/L) in 1 vol% acetic acid in deionized water	Titanium	Titanium	10	15	10	Room temperature	3	—	Ordikhani et al. (2016)
			Chitosan (0.5 g/L), bioactive glass (0.5 g/L), vancomycin in 1 vol% acetic acid in deionized water				15	10				
			Chitosan (0.5 g/L), bioactive glass (0.5 g/L), vancomycin (0.5 g/L, 1 g/L, 1.5 g/L, 2 g/L) in 1 vol% acetic acid in deionized water				10 (for chitosan), 15 (for chitosan/bioactive glass composite)	20			128	
Ananth2013		$(Ca\ Mg)_3(PO_4)_2$, $CaSiO_3$, ZrO_2	1) 5 wt% YSZ [yttria-stabilized zirconia (YSZ)], 2) 1YSZ-2BG (5 wt% YSZ-10 wt% BG) in isopropanol [bioactive glass (BG)]	Platinum	Ti6Al4V	10	70	5	Room temperature	—	1) 4–5, 2) 12–15	Ananth et al. (2013)
			1) 10 wt% YSZ, 2) 2YSZ-2BG (10 wt% YSZ, 10 wt% BG) in isopropanol									
Patel2019		Mesoporous bioglass nanoparticles, chitosan	Mesoporous bioglass nanoparticles (0.25 g/L), chitosan (0.50 g/L)	Stainless steel	Pure titanium	10	25	1–5 min	—	3.5	—	Patel et al. (2019)
			Mesoporous bioglass nanoparticles (0.50 g/L), chitosan (0.50 g/L)									
			Mesoporous bioglass nanoparticles (0.75 g/L), chitosan (0.50 g/L)									

(Continued on following page)

10.3389/fbioe.2023.1269223

TABLE 7 (*Continued*) Parameters for electrophoretic deposition in included studies.

Study ID	Coating method	Coating component	Solution	Anode	Cathode	Distance between the electrodes (mm)	Work voltage (V)	Time (min)	Temperature	pH	Coating thickness (μm)	Ref.
Avcu2018		—	Chitosan (0.5 g/L), micro-45S5 bioactive glass (0.5 g/L), nano-bioglass (0.5 g/L), acetic acid (1 vol%), deionized water (20 vol %), ethanol (79 vol%)	Ti6Al4V alloy	Ti6Al4V	10	4, 6, 8, 10, 15, 20	3	Room temperature	4–5	—	Avcu et al. (2018)
			Chitosan (0.5 g/L), nano-bioglass (0.5 g/L), acetic acid (1 vol%), deionized water (20 vol %), ethanol (79 vol%)									
			Chitosan (0.5 g/L), micro-45S5 bioactive glass (0.5 g/L), acetic acid (1 vol%), deionized water (20 vol%), ethanol (79 vol%)									
Costa2020	PEO	SiO_2, CaO, $CaCO_3$, Na_2O, P_2O_5	$C_3H_7Na_2O_6P$ (0.0010 M), Na_2SiO_3-$5H_2O$ (0.014 M), $C_4H_6O_4Ca$ (0.20 M), $NaNO_3$ (0.50 M), $C_3H_7Na_2O_6P$ (0.0010 M), $Na_2EDTA{\cdot}2H_2O$ (0.025 M)	Pure Ti	Steel	—	500	7	23.0°C ± 1.5°C	—	23.42282	Costa et al. (2020)

10.3389/fbioe.2023.1269223

5.2 Hemocompatibility analysis

Hemocompatibility is the ability of blood to tolerate a material without causing significant adverse blood reactions when the material is in contact with blood (Nalezinkova, 2020). The main adverse blood reactions involve thrombosis. The absorbance of blood proteins on the surface of the materials triggers a series of cascade reactions, resulting in thrombosis, and the coagulation cascade spreads rapidly, leading to death in severe cases (Manivasagam et al., 2021). Hemolysis, which reflects hemocompatibility, is caused by adverse reactions to any toxic substance that comes in contact with blood (Dhinasekaran et al., 2021). The percentage of hemolysis (hemolysis%) is calculated on the basis of the following formula:

$$\text{Hemolysis\%} = \frac{\text{free hemoglobin concentration}}{\text{total hemoglobin concentration}} \times 100\%.$$

If the hemolysis% of a sample is <2%, it is non-hemolytic; a hemolysis% between 2% and 5% indicates that it is slightly hemolytic; if the hemolysis% >5%, it is considered hemolytic. Materials that are blood compatible are considered to have a hemolysis% less than 5%.

Studies have demonstrated that the hemolysis% of BG powders in all concentrations is lower than that of HA at the same concentrations, while more red blood cells (RBCs) are ruptured with BG coating. This may be due to the release of sodium ions from the BG coating, causing RBCs to rupture and, thus, exhibit hematotoxicity, which is corrected by washing after coating (Durgalakshmi et al., 2020; Dhinasekaran et al., 2021). Bargavi et al. (2022) found that BG coatings doped with various concentrations of alumina (Al) exhibited non-hemolytic properties and improved hemocompatibility when compared to pure BG coatings, where BG coatings doped with 10% Al had the best hemocompatibility. The hemocompatibility of BG coatings doped with zirconia (Zr) has also been investigated. With an increase in Zr concentration, the hemolysis% of the coating slightly decreased; while BG coatings doped with 5% and 10% Zr showed non-hemolysis, BG coatings doped with 15% Zr showed slight hemolysis (hemolysis % <2.5%) (Bargavi et al., 2020). Generally, BG-coated implants show great hemocompatibility.

5.3 Anti-inflammatory properties

Inflammation is an immune response of the body to resist harmful irritation, which helps maintain tissue homeostasis during injury or infection (Medzhitov, 2010; Wu et al., 2019; Chang and Xiong, 2020); however, excessive inflammatory responses form fibrous capsules that prevent implants' osteointegration. Therefore, superior anti-inflammatory property is critical for implant success.

There is no significant difference in the expression of anti-inflammatory factors in human amniotic mesenchymal stromal cells (hAMSCs) on RKKP glass-ceramic coating when compared with the control group, which indicates that the coating did not affect the expression of hAMSCs' anti-inflammatory factors (Ledda et al., 2016). Wu et al. (2014) found that bioactive $Sr_2MgSi_2O_7$ (SMS) ceramic coatings exhibited superior anti-inflammatory effects compared to HAp coatings, and their mechanism of inhibiting the inflammatory response may be due to the 1) inhibition of the Wnt5A/Ca^{2+} pathway, which enhances the inflammatory response by decreasing the Ca^{2+} concentration or 2) inhibition of inflammatory cytokine expressions by the Toll-like receptor (TLR) pathway, which induces an immune response by the release of Mg^{2+} and Sr^{2+} (Figures 7A a–c).

For *in vivo* experiments, the inflammatory response of the host to the implant is a normal bodily reaction, often manifested as a local inflammatory response and vascular congestion, which disappears after some time (Taguchi et al., 2019). The gingival index determines the inflammatory status by observing the gingival condition, while the periodontal pocket is a manifestation of the pathological inflammatory response (Löe, 1967; Donos, 2018). In clinical trials, in follow-up survey statistics, the gingival index and depth of periodontal pockets were smaller in BG-coated groups, which showed a higher success rate of implantology (Mistry et al., 2016).

5.4 Bioactivity properties

5.4.1 Osteointegration

Osteointegration, also known as osseointegration, mainly describes the level of direct connection between an artificial implant and bone tissue without an intermediate fibrous connective tissue layer (Brånemark et al., 1977; Goriainov et al., 2014). A good interface between the implant and bone is an important factor in the formation of dense new bone and, thus, for the osseointegration of both (Agarwal et al., 2015; Hu et al., 2019; Sang et al., 2022). The wettability and surface energy of a material can change the binding of implants to osteoblasts after implantation (Chen et al., 2011).

In animal experiments, BG coating improved implant wettability and enhanced cell viability in the early stages of bone healing, thus significantly increasing bone-to-implant contact (BIC) and bone mineral density (BMD) (Soares et al., 2018), with new bones being formed around the implant and closely combined with the bone tissue (Taguchi et al., 2019). Strontium-substituted bioactive glass (SrBG) coating can stimulate bone formation by releasing dissolved products, showing a superior bone fixation effect (Newman et al., 2014). Reparative osteogenesis formed around the BG/HA/TCP composite coating implants (Klyui et al., 2021), and a perfect fusion with the bone tissue could be observed around the HA/BG/wollastonite (WS) composite coating implant (Wang et al., 2020). However, some studies have also found that in HA/BG coatings, when the concentration of BG is increased, a faster dissolution rate of BG leads to new bone damage and limits the combination of implants and bone tissue (Wang et al., 2018). Only BG containing a certain weight percentage, that is, 40–60wt% SiO_2, can promote osteogenesis (van Oirschot et al., 2014).

In clinical trials, good bone ingrowth can be found near the implants in BG-coated hip implants (Orita et al., 2022). The bone regeneration around the oral implants is better, with osteoid formation and increased mineralization, which is specifically reflected in the higher median interface density (MID), discrete interface density (DID), and interface radiodensity (IFD) observed at 6 months (Mistry et al., 2016).

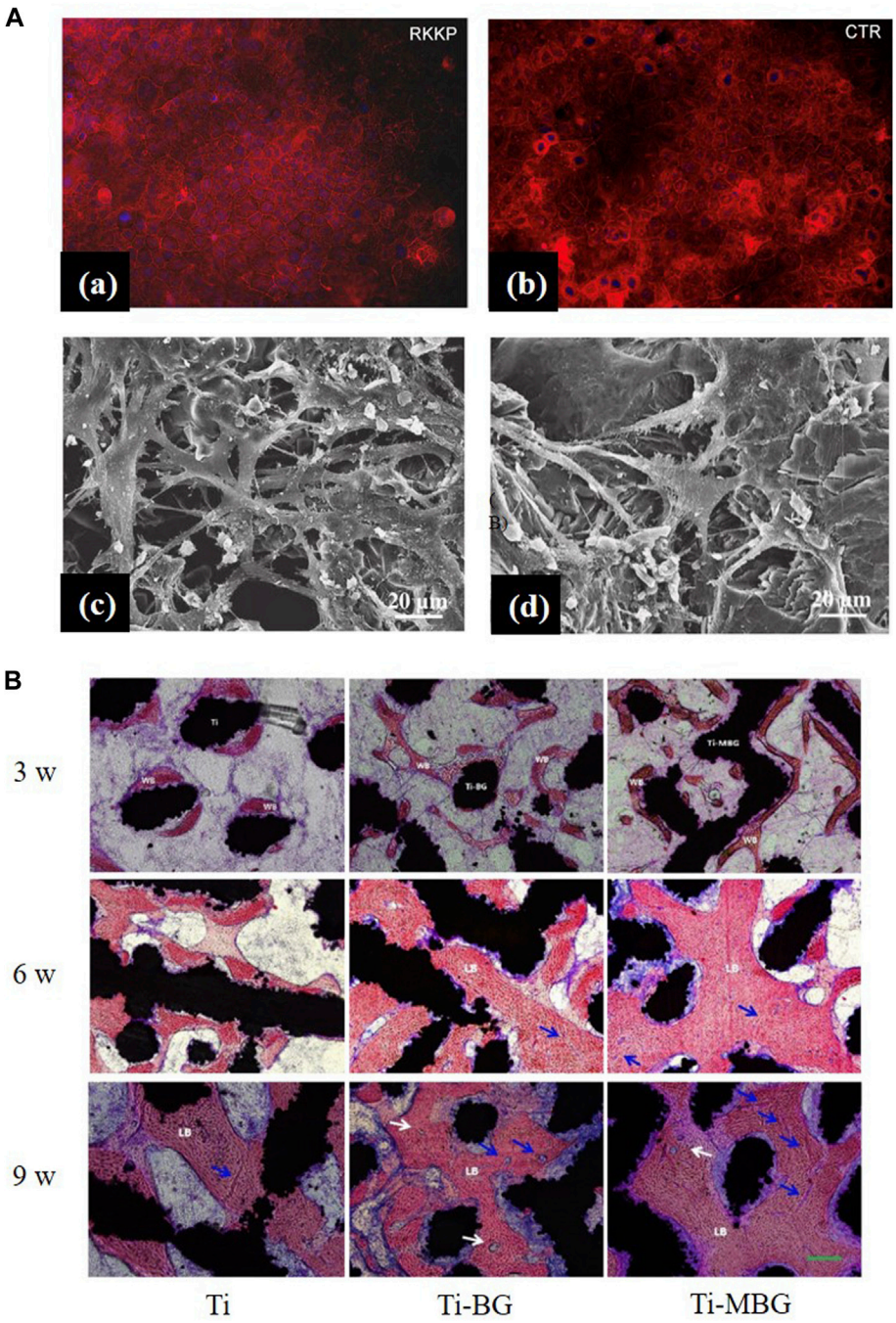

FIGURE 6
(A), **(a,b)** Actin distribution in the Caco-2 cell line: cells seeded on the RKKP film surfaces and plastic Petri dishes (CTR: critical temperature resister, a semiconductor ceramic material). **(c, d)** Morphological aspects of MG-63 osteoblast cells cultured on YSZ-BG-coated Ti6Al4V. **(c)** Cells on 1YSZ-2BG are similar, but the osteoblasts are well spread and present cytoplasmic extensions forming a continuous surface layer. **(d)** Cell morphology on 2YSZ-2BG coating is similar to **(c)**, but filopodial extensions are fewer. The figures were obtained with permission from Ananth et al. (2013) and Ledda et al. (2015). **(B)** Representative histological images of non-decalcified sections are obtained by methylene blue acid fuchsin staining. Blue arrows, neovascularization; white arrows, the Haversian system; WB, woven bone; LB, lamellar bone. The figures were obtained with permission from Zhang et al. (2021).

5.4.2 Osteogenesis

Osteogenesis refers to bone tissue formation, which is a complex procedure of osteo-development. Bone matrix mineralization and secretion are eternal procedures controlled by osteoblasts (Popa et al., 2015). Based on the included studies, osteogenesis mainly reflects on apatite formation in simulated body fluid (SBF), positive osteoblasts response, and rapid increase in new bone formation and mineralization *in vivo*.

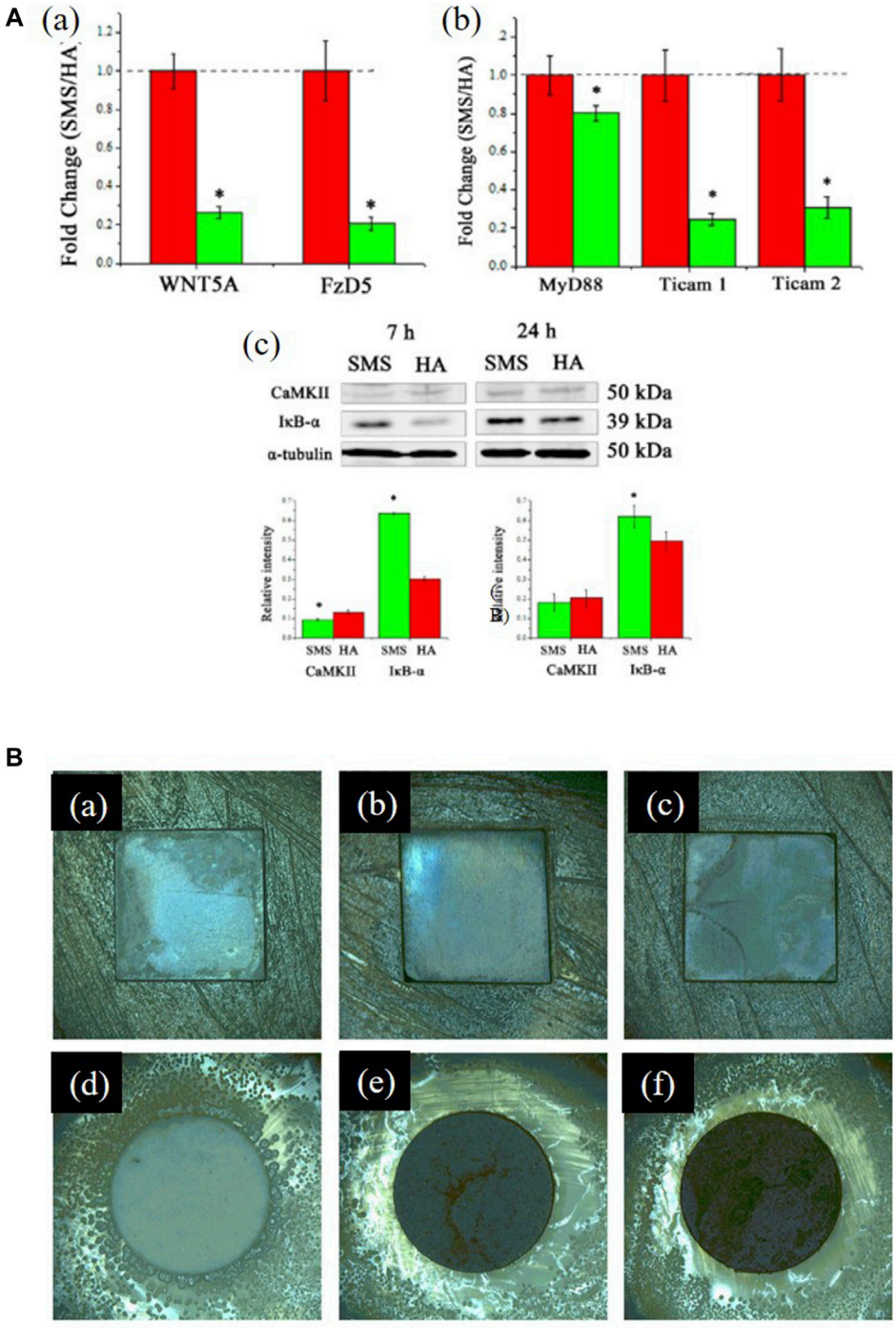

FIGURE 7
(A), (a) Fold changes of WNT5A/Ca2+ pathway-related genes: WNT5A and Fz5. **(b)** Fold changes of Toll-like pathway-related genes: MyD88, TICAM1, and TICAM2. **(c)** Western blotting analysis of CaMKII and IκB-α expression. *significant difference by comparing RAW 264.7 cells cultured in SMS coating with HA ($p < 0.05$). The figures were obtained with permission from Wu et al. (2014). **(B)** Typical optical images of antibacterial test results of the coated samples against *Staphylococcus aureus*: **(a)** 0 Ag, **(b)** 5 Ag, **(c)** 10 Ag, and **(d–f)** their corresponding glass wafer samples: 0 Ag, 5 Ag, and 10 Ag: Ag/Ca atomic ratios of 0%, 5%, and 10%, respectively. The figures were obtained with permission from Fu et al. (2017).

5.4.2.1 Apatite formation in SBF

BG and doped ions in the coating significantly affect apatite formation in SBF. Phosphate in BG can promote apatite formation in SBF (Li et al., 2021). Mesoporous bioactive glass (MBG) coatings with an ordered mesoporous structure exhibit more evident apatite deposition than BG coatings (Zhang et al., 2016).

Ananth et al. (2013) observed more calcium phosphate particle deposition by increasing the relative content of BG in YSZ-BG

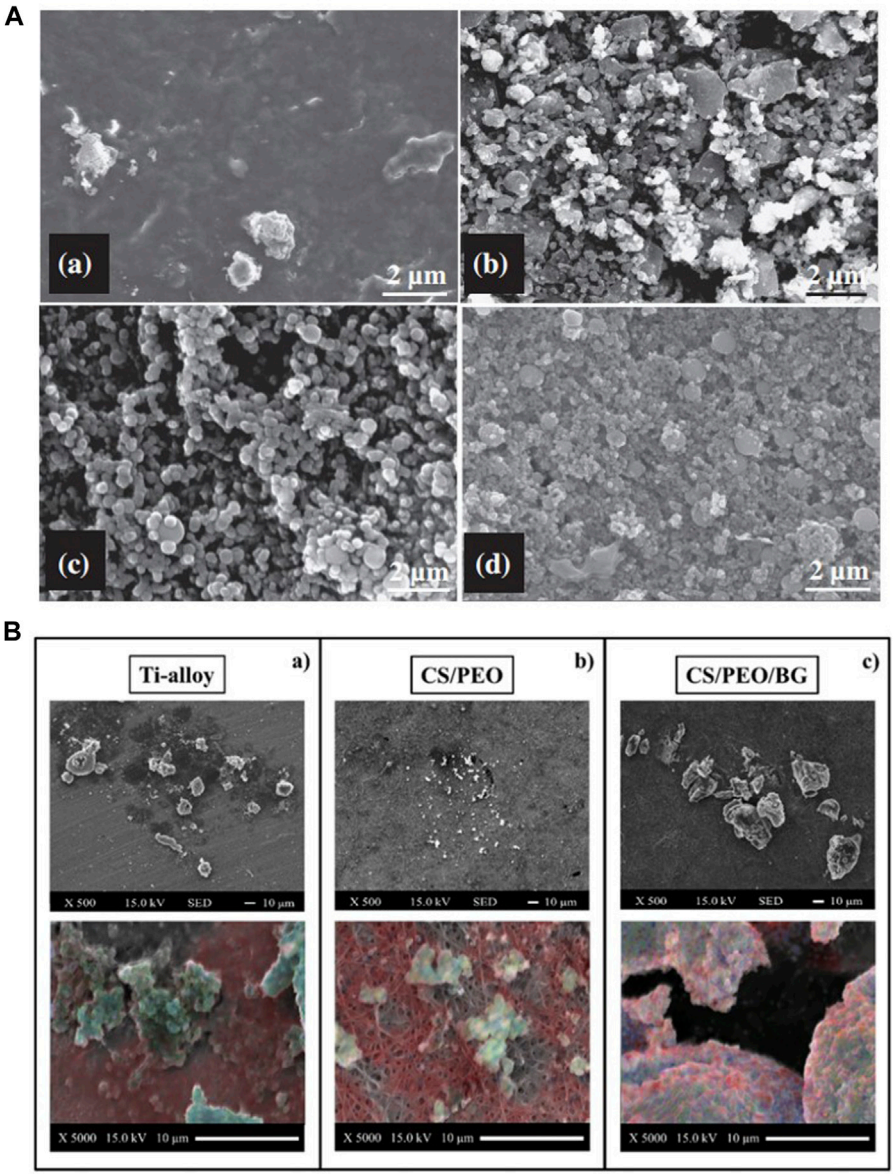

FIGURE 8
(A) SEM images of the 1YSZ-2BG–coated Ti6Al4V alloy, which was immersed in SBF for various time durations (days): **(a)** 3, **(b)** 7, **(c)** 14, and **(d)** 21. **(B)** SEM images of bone formation on the three substrates and EDX elemental maps labeled calcium (blue), carbon (red), and phosphorous (blue) to identify the presence of the mineral. The figures were obtained with permission from Ananth et al. (2013) and Boschetto et al. (2020).

composite coatings, which may be due to the promotion of apatite nucleation by the Si–OH group in the BG coating (Figure 8A). Increasing the BG content in chitosan/BG composite coatings also enhances the osteo-biological activity of the coating (Avcu et al., 2018). A high SiO_2 content reduces the dissolution rate of BG and influences surface apatite formation, which indicates that the formation of surface apatite can be improved by reducing the content of SiO_2 and doping an appropriate amount of Ag and Co (Lung et al., 2021). However, Ag^+ is smaller in size than Ca^{2+} and binds more firmly with unbridged oxygen, so high Ag content is not conducive to the formation of HA (Catauro et al., 2015). The BG-Al composite coating was created using the sol–gel method, and with an increase in Al concentration, the growth rate of apatite accelerated (Bargavi et al., 2022).

5.4.2.2 Osteocyte experiments

A material's influence on cellular behavior is essential in osteogenesis. The connection between the bone *in vivo* has two steps: first, the generation of a carbonate HA layer on the glass surface, to which the osteogenesis-related cells will subsequently respond. The dissolution products of BG modulate the proliferation and differentiation of cells to accelerate the integration of bone (Crush et al., 2021). *In vitro* cellular experiments reveal the production of intracellular osteogenic markers and assess the osteogenic activity of BG. The maturation of osteoblasts is categorized into proliferation, differentiation, and mineralization (Owen et al., 1990). In the proliferative stage, cells express genes that regulate the cell cycle

and growth and form the ECM. Alkaline phosphatase (ALP), which is expressed in the initial differentiation stage, and osteopontin (OPN), which is expressed in the initial mineralization stage, induce matrix maturation and mineralization, and their increased expressions in osteoblast markers promote mineral deposition (Saino et al., 2010).

Ions released by BG dissolution can stimulate gene expression (Hench et al., 2020), which indicates that glass components have a significant impact on cells' proliferation and differentiation. Si and Ca groups play a more important role in osteo-associated cells' differentiation and proliferation than P and Na groups (Su et al., 2019). Cell inoculation on BG-coated surface significantly increased the content of mineralized matrix deposition (Figure 8B) (Boschetto et al., 2020), markers of early differentiation such as ALP and RUNX2, and expression of osteocalcin (OCL), which is expressed in late differentiation (Ledda et al., 2016). It has also been shown that the mesoporous physical structure of glass promotes the effective release of Ca and Si ions, leading to a higher level of cell differentiation (Zhang et al., 2016; Ye et al., 2017). When compared with uncoated Ti and BG-coated implants, more collagens were released in osteoblasts co-cultured with zirconia-containing BG-coated implants because the BG-Zr composite mediates collagen synthesis by changing the pH through an ion-release mechanism (Bargavi et al., 2020). Meanwhile, a higher pH also favors bone formation processes, which include the cross-linking of collagen chains and subsequent deposition of HA (Wang et al., 2011; Bargavi et al., 2020).

5.4.2.3 *In vivo* trials

Osteogenesis in clinical trials contributes to the complete restoration and biomechanical properties of natural bone (Santos et al., 2009). Mechanical stabilization and appropriate host response are essential to ensure osteogenesis (Lavenus et al., 2015).

The intrinsic mechanism of osteogenesis is inextricably linked to the ion release process of the BG coating. The silica-rich layer on BG coatings leaches into the local tissue fluid, regulating the osteoblast cycle and allowing rapid osteogenesis and mineralization, which increases peri-implant osteogenesis and mineralization (Xynos et al., 2000; Hench and Greenspan, 2013). Ion dissolution products containing Ca, Mg, and Si bioactive glasses activate the expression of bone-related genes such as bone morphogenetic proteins (BMPs) and vascular endothelial growth factor (VEGF), stimulating osteogenesis and angiogenesis (Huang et al., 2009; Sun et al., 2009; Gu et al., 2011; Hoppe et al., 2011; Saffarian Tousi et al., 2013; Zhai et al., 2013; Henstock et al., 2015; Shamsi et al., 2017; Naseri et al., 2018; O'Neill et al., 2018; Zafar et al., 2019; Zhou et al., 2019).

In animal tests, BG-coated implants show active areas on the surface that serve as the origin of osteogenesis, forming bones with better morphology, maturity, quantity, and thickness than in control groups, and with more rapid and effective osteogenesis (Figure 6B) (Taguchi et al., 2019; Zhang et al., 2021). It has also been shown that a more mature new bone was observed around BG-coated implants in the early stages of bone healing, but as the healing time increased, the advantage of BG-coated implants was no longer evident, since surface roughness affects the adhesion, migration, and differentiation of osteoblasts and thereby the osteogenesis process (Soares et al., 2018).

Poly (co-glycolide propionate)/BG (PBG) nanocomposite coatings induce more than 85% in bone formations. On HA/BG/WS composite coatings, the formation of surface bone tissue has been observed (Wang et al., 2020), while BG composite coatings with 30 wt% HA (pure) and 20 wt% TCP (tricalcium phosphate) show a larger area of bone formation around the implant (Klyui et al., 2021). Furthermore, the peri-implant osteogenic capacity may be related to the implant site and animal species, and the bone quality and quantity at the implant site may interfere with possible significant differences between experimental groups (van Oirschot et al., 2014).

5.4.2.4 Clinical trials

In clinical trials, BG-coated groups show a higher success potential: the least marginal bone loss (MBL), the highest IFD in both low- and high-density bone tissue, and a better deposition and mineralization of new bone tissue around the implant (Mistry et al., 2016). Furthermore, BG-coated hip implants have better bone growth conditions with excellent survival rates and wear resistance (Orita et al., 2022).

5.4.3 Angiogenesis

Angiogenesis, also known as vascular regeneration, is the sprouting and remodeling of neovascularization in the original vascular network (Huang and Nan, 2019), which is essential for tissue repair after implantation (Mehdikhani-Nahrkhalaji et al., 2015; Nowak-Sliwinska et al., 2018; Klyui et al., 2021). The formation of vessels helps transport oxygen, nutrients, minerals, and osteoprogenitor cells over long distances, contributing to bone healing (Zhang et al., 2021). Cerium oxide and BG doped with 2% Zn nanocomposite coatings exhibit superior pro-vascular regenerative capacity and the mechanism is related to the regulation of the hypoxic response and structural reorganization of cells (Matter et al., 2021). Increasing the porosity of BG-coated porous scaffold, reducing the thickness of the coating, and improving the surface roughness all provide space for new bone formation, contributing to angiogenesis (Zhang et al., 2021).

5.4.4 Soft tissue adhesion

After implantation, soft tissue reaction leads to the formation of a fibrous capsule, which contacts the implant without adhesion, allowing relative movement between the implant and the surrounding tissue. Appropriate soft tissue adhesion holds the implant stably in the surrounding tissue (Lee et al., 2010), which limits hematoma and abscess formation and prevents infection (Lee et al., 2010; Zigterman et al., 2019).

Surface roughness, coating composition, and structural design of the implants are the main factors affecting soft tissue adhesion (Lee et al., 2010; Zigterman et al., 2019). The ceria and BG doped with 2% Zn nanocomposite coatings reduce the biomineralization behavior to adapt to soft tissue while inducing the generation of vascular endothelial cells without cytotoxicity to gingival fibroblasts. It can promote rapid wound healing and exhibit superior soft tissue regeneration abilities in subsequent scratch assays (Matter et al., 2021).

During oral implantology, the surrounding blood clot adheres firmly to BG-coated implants, indicating that BG-coated implants have higher wettability and stronger adhesion to the surrounding soft tissue than machined bare titanium implants (Mistry et al., 2016).

5.5 Antibacterial properties

Antibacterial properties are an essential characteristic in grafts implanted clinically, which refers to the grafts' ability to reduce microbial growth on their surfaces. The formation of a biofilm is the first stage of bacterial growth, which also inhibits the proliferation of osteoblasts.

Better antibacterial properties are reflected in larger bacterial inhibition zones, lower reduction rates, fewer colony-forming units, and lower minimum inhibitory concentrations. A study has shown that as the content of silver ions in the coating increased, the number of bacteria on the sample surface decreased significantly and the bacterial inhibition area on the surface became larger [Figures 7B(a–f)] (Fu et al., 2017b). The cobalt- and Ti-doped glass coatings have better antibacterial properties than traditional 58S glass (Lung et al., 2021). As more zirconium oxide is added to samples, they exhibit a higher ability to inhibit bacterial growth (Bargavi et al., 2020), whereas borate-based glass exhibits worse antibacterial properties (Rau et al., 2020). Glass composited with drugs can help eradicate bacteria (Zarghami et al., 2021). By observing bacteria in saliva on the implant surface, Costa et al. (2020) found that fewer pathogenic bacteria were observed on the surface.

The antibacterial property is mainly increased by doping silver and other metallic ions in the manufacturing of chitosan composted coatings and in combination with antibiotics like tetracycline and vancomycin. The inhibition of bacteria by silver ions is mainly due to direct contact, which results in the deformation of cell membranes (Lung et al., 2021) and ROS in bacteria (Fu et al., 2017b). The electrostatic effects leading to changes in cell membrane permeability, thereby influencing cell signal transduction and production of ROS, are the main reasons for antibacterial properties caused by metallic compounds (Lung et al., 2021). Due to the slow-release behavior, BG containing chitosan and vancomycin has higher bactericidal effects (Zarghami et al., 2020). Chitosan increases cell membrane permeability, leading to the release of intracellular substances and thus causing cell death (Ordikhani et al., 2016). The composite coating of bioactive glass as a drug carrier can also significantly improve antimicrobial properties. BG has a rougher surface (Matter et al., 2021) and creates a more alkaline biological environment (Echezarreta-López and Landin, 2013; Brauer, 2015) through dissolution and ion release, where bacteria grow poorly.

In *in vivo* experiments, the plaque index and gingival recession were assessed to evaluate the degree of oral hygiene (Silness and Löe, 1964; Kassab and Cohen, 2003). A clinical trial proved that patients with BG-coated implants have reduced plaque index and gingival recession and, therefore, reduced occurrence of oral disease (Mistry et al., 2016).

6 Conclusion and future prospects

Bioactive glasses are widely researched because of their good biological properties; however, poor mechanical properties limit their clinical applications. Suitable coating technologies are essential for the performance of glass coatings' relevant properties. This work systematically reviews the coating technology of BG on the surface of Ti and its alloys and summarizes the principles of the technology, relevant parameters, and their relative advantages, providing a reliable basis for coating technology selection. BG coatings exhibit excellent cell compatibility, antibacterial and anti-inflammatory properties, and higher levels of osseointegration and osteogenesis, which indicate that BG coatings on Ti and its alloys have excellent biocompatibility and bioactivity. The doping of ions and compounding with other substances significantly improve the coatings' performances.

However, BG-coated Ti and its alloy implants face many challenges nowadays. Adding antibacterial ions, such as Ag and Co, and compositing with drugs, such as tetracycline and vancomycin, can improve the antibacterial properties of metal implants. However, the overuse of metal ions may cause cytotoxicity and limit cell metabolism, which leads to negative tissue reactions. Therefore, the balance of antibacterial properties and cytotoxicity requires further study for coating optimization. In terms of physical properties, there are significant differences in the coefficients of thermal expansion between metals and glass materials that can lead to cracking and failure of coatings. Improving the compatibility of substrates and coatings also relies on further research.

In vitro experiments can filter suitable implant biomaterials in the first stage, which prevents excessive euthanization of laboratory animals and simplifies the quantification of experimental results. However, cellular metabolites cause peripheral tissue reactions, and *in vitro* studies cannot test the subsequent biological effects. Animal experiments can assess the influence of coated implants on the surrounding and distant organs while controlling different pathological models and loading conditions, making them important pre-clinical research. For BG-coated implants, advanced clinical applications require more animal experiments and clinical trials.

Data availability statement

The original contributions presented in the study are included in the article/Supplementary Material; further inquiries can be directed to the corresponding authors.

Author contributions

JL: conceptualization, data curation, resources, visualization, manuscript writing–original draft, and manuscript writing–review and editing; XL: Methodology, resources, software, visualization, and manuscript writing–original draft; XZ: methodology, resources, software, visualization, and manuscript writing–original draft; YL: formal analysis, investigation, resources, and manuscript

writing–original draft; XG: methodology, resources, visualization, and manuscript writing–original draft; KS: investigation, resources, visualization, and manuscript writing–original draft; HC: investigation, resources, and manuscript writing–original draft; QJ: investigation, resources, and manuscript writing–original draft; HJ: conceptualization, supervision, validation, and manuscript writing–review and editing; KL: conceptualization, supervision, and validation.

Funding

The author(s) declare financial support was received for the research, authorship, and/or publication of this article. This research was funded by [Shandong Provincial key research and development program] grant number [2019GSF108259].

Conflict of interest

The authors declare that the research was conducted in the absence of any commercial or financial relationships that could be construed as a potential conflict of interest.

Publisher's note

References

Abushahba, F., Tuukkanen, J., Aalto-Setala, L., Miinalainen, I., Hupa, L., and Narhi, T. O. (2020). Effect of bioactive glass air-abrasion on the wettability and osteoblast proliferation on sandblasted and acid-etched titanium surfaces. *Eur. J. Oral Sci.* 128 (2), 160–169. doi:10.1111/eos.12683

Agarwal, R., Gonzalez-Garcia, C., Torstrick, B., Guldberg, R. E., Salmeron-Sanchez, M., and Garcia, A. J. (2015). Simple coating with fibronectin fragment enhances stainless steel screw osseointegration in healthy and osteoporotic rats. *Biomaterials.* 63 (2015) 137–145. doi:10.1016/j.biomaterials.2015.06.025

Al-Noaman, A., Rawlinson, S. C. F., and Hill, R. G. (2012). The influence of CaF2 content on the physical properties and apatite formation of bioactive glass coatings for dental implants. *J. NON-CRYSTALLINE SOLIDS* 358 (15), 1850–1858. doi:10.1016/j.jnoncrysol.2012.05.039

Ali, A., Iqbal, F., Ahmad, A., Ikram, F., Nawaz, A., Chaudhry, A. A., et al. (2018). Hydrothermal deposition of high strength calcium phosphate coatings on magnesium alloy for biomedical applications. *Surf. Coatings Technol.* 357, 716–727. doi:10.1016/j.surfcoat.2018.09.016

Allan, I., Wilson, M., and Newman, H. (2002). Particulate Bioglass® reduces the viability of bacterial biofilms formed on its surface in an *in vitro* model. *Clin. Oral Implants Res.* 13 (1), 53–58. doi:10.1034/j.1600-0501.2002.130106.x

Ananth, K. P., Suganya, S., Mangalaraj, D., Ferreira, J. M. F., and Balamurugan, A. (2013). Electrophoretic bilayer deposition of zirconia and reinforced bioglass system on Ti6Al4V for implant applications: an *in vitro* investigation. *Mater. Sci. Eng. C-Materials Biol. Appl.* 33 (7), 4160–4166. doi:10.1016/j.msec.2013.06.010

Asif, I. M., Shelton, R. M., Cooper, P. R., Addison, O., and Martin, R. A. (2014). *In vitro* bioactivity of titanium-doped bioglass. *J. Mater. Sci. Mater. Med.* 25 (8), 1865–1873. doi:10.1007/s10856-014-5230-4

Avcu, E., Avcu, Y. Y., Bastan, F. E., Rehman, M. A. U., Ustel, F., and Boccaccini, A. R. (2018). Tailoring the surface characteristics of electrophoretically deposited chitosan-based bioactive glass composite coatings on titanium implants via grit blasting. *Prog. Org. Coatings* 123, 362–373. doi:10.1016/j.porgcoat.2018.07.021

Baino, F., and Verné, E. (2017). Glass-based coatings on biomedical implants: A state-of-the-art review. *Biomed. Glas.* 3 (1), 1–17. doi:10.1515/bglass-2017-0001

Bakhshandeh, S., and Amin Yavari, S. (2018). Electrophoretic deposition: a versatile tool against biomaterial associated infections. *J. Mater Chem. B* 6 (8), 1128–1148. doi:10.1039/c7tb02445b

Balamurugan, A., Balossier, G., Michel, J., and Ferreira, J. M. F. (2009). Electrochemical and structural evaluation of functionally graded bioglass-apatite composites electrophoretically deposited onto Ti6Al4V alloy. *Electrochimica Acta* 54 (4), 1192–1198. doi:10.1016/j.electacta.2008.08.055

Bargavi, P., Chandran, R. R., Durgalakshmi, D., Rajashree, P., Ramya, R., and Balakumar, S. (2022). Drug infused Al2O3-bioactive glass coatings toward the cure of orthopedic infection. *Prog. Biomater.* 11 (1), 79–94. doi:10.1007/s40204-022-00181-y

Bargavi, P., Chitra, S., Durgalakshmi, D., Radha, G., and Balakumar, S. (2020). Zirconia reinforced bio-active glass coating by spray pyrolysis: structure, surface topography, *in-vitro* biological evaluation and antibacterial activities. *Mater. Today Commun.* 25, 101253. doi:10.1016/j.mtcomm.2020.101253

Berbecaru, C., Alexandru, H. V., Stan, G. E., Marcov, D. A., Pasuk, I., and Ianculescu, A. (2010). First stages of bioactivity of glass-ceramics thin films prepared by magnetron sputtering technique. *Mater. Sci. Eng. B* 169 (1-3), 101–105. doi:10.1016/j.mseb.2010.01.007

Boccaccini, A. R., Keim, S., Ma, R., Li, Y., and Zhitomirsky, I. (2010). Electrophoretic deposition of biomaterials. *J. R. Soc. Interface* 7 (5), S581–S613. doi:10.1098/rsif.2010.0156.focus

Bohner, M., and Lemaitre, J. (2009). Can bioactivity be tested *in vitro* with SBF solution? *Biomaterials* 30 (12), 2175–2179. doi:10.1016/j.biomaterials.2009.01.008

Boschetto, F., Doan, H. N., Vo, P. P., Zanocco, M., Zhu, W. L., Sakai, W., et al. (2020). Antibacterial and osteoconductive effects of chitosan/polyethylene oxide (PEO)/Bioactive glass nanofibers for orthopedic applications. *Appl. Sciences-Basel* 10 (7), 2360. doi:10.3390/app10072360

Brånemark, P. I., Hansson, B. O., Adell, R., Breine, U., Lindström, J., Hallén, O., et al. (1977). Osseointegrated implants in the treatment of the edentulous jaw. Experience from a 10-year period. *Scand. J. Plast. Reconstr. Surg. Suppl.* 16, 1–132.

Brauer, D. S. (2015). Bioactive glasses—structure and properties. *Angew. Chem. Int. Ed.* 54 (14), 4160–4181. doi:10.1002/anie.201405310

Brown, P. (1989). *Sol-gel technology for thin films, fibers, preforms, electronics, and specialty shapes*: Edited by Lisa C Klein. Noyes Publications.

Buser, D., Janner, S. F. M., Wittneben, J. G., Bragger, U., Ramseier, C. A., and Salvi, G. E. (2012). 10-Year survival and success rates of 511 titanium implants with a sandblasted and acid-etched surface: a retrospective study in 303 partially edentulous patients. *Clin. IMPLANT Dent. Relat. Res.* 14 (6), 839–851. doi:10.1111/j.1708-8208.2012.00456.x

Calderon Velasco, S., Cavaleiro, A., and Carvalho, S. (2016). Functional properties of ceramic-Ag nanocomposite coatings produced by magnetron sputtering. *Prog. Mater. Sci.* 84, 158–191. doi:10.1016/j.pmatsci.2016.09.005

Cannillo, V., Colmenares-Angulo, J., Lusvarghi, L., Pierli, F., and Sampath, S. (2009). *In vitro* characterisation of plasma-sprayed apatite/wollastonite glass–ceramic biocoatings on titanium alloys. *J. Eur. Ceram. Soc.* 29 (9), 1665–1677. doi:10.1016/j.jeurceramsoc.2008.09.022

Catauro, M., Bollino, F., Papale, F., and Ciprioti, S. V. (2015). Investigation on bioactivity, biocompatibility, thermal behavior and antibacterial properties of calcium silicate glass coatings containing Ag. *J. Non-Crystalline Solids* 422, 16–22. doi:10.1016/j.jnoncrysol.2015.04.037

Catauro, M., Papale, F., and Bollino, F. (2016). Coatings of titanium substrates with xCaO·(1 – x)SiO 2 sol–gel materials: characterization, bioactivity and biocompatibility evaluation. *Mater. Sci. Eng. C-Materials Biol. Appl.* 58, 846–851. doi:10.1016/j.msec.2015.09.033

Chang, M. X., and Xiong, F. (2020). Astaxanthin and its effects in inflammatory responses and inflammation-associated diseases: recent advances and future directions. *Molecules* 25 (22), 5342. doi:10.3390/molecules25225342

Chattopadhyay, S., Dash, S. K., Tripathy, S., Das, B., Mandal, D., Pramanik, P., et al. (2015). Toxicity of cobalt oxide nanoparticles to normal cells; an *in vitro* and *in vivo* study. *Chemico-Biological Interact.* 226, 58–71. doi:10.1016/j.cbi.2014.11.016

Chen, L., McCrate, J. M., Lee, J. C. M., and Li, H. (2011). The role of surface charge on the uptake and biocompatibility of hydroxyapatite nanoparticles with osteoblast cells. *Nanotechnology* 22 (10), 105708. doi:10.1088/0957-4484/22/10/105708

Chen, Q., and Thouas, G. A. (2015). Metallic implant biomaterials. *Mater. Sci. Eng. R Rep.* 87, 1–57. doi:10.1016/j.mser.2014.10.001

Chen, X. C., Zhang, M. J., Pu, X. M., Yin, G. F., Liao, X. M., Huang, Z. B., et al. (2014). Characteristics of heat-treated plasma-sprayed CaO-MgO-SiO2-based bioactive glass-

ceramic coatings on Ti-6Al-4V alloy. *Surf. Coatings Technol.* 249, 97–103. doi:10.1016/j.surfcoat.2014.03.056

Cohrs, N. H., Schulz-Schonhagen, K., Mohn, D., Wolint, P., Meier Burgisser, G., Stark, W. J., et al. (2019). Modification of silicone elastomers with Bioglass 45S5® increases in ovo tissue biointegration. *J. Biomed. Mater Res. B Appl. Biomater.* 107 (4), 1180–1188. doi:10.1002/jbm.b.34211

Comesana, R., Quintero, F., Lusquinos, F., Pascual, M. J., Boutinguiza, M., Duran, A., et al. (2010). Laser cladding of bioactive glass coatings. *Acta Biomater.* 6 (3), 953–961. doi:10.1016/j.actbio.2009.08.010

Coraça-Huber, D. C., Fille, M., Hausdorfer, J., Putzer, D., and Nogler, M. (2014). Efficacy of antibacterial bioactive glass S53P4 against *S. aureus* biofilms grown on titanium discs *in vitro*. *J. Orthop. Res.* 32 (1), 175–177. doi:10.1002/jor.22463

Costa, M. (1991). Molecular mechanisms of nickel carcinogenesis. *Annu. Rev. Pharmacol. Toxicol.* 31, 321–337. doi:10.1146/annurev.pa.31.040191.001541

Costa, R. C., Souza, J. G. S., Cordeiro, J. M., Bertolini, M., de Avila, E. D., Landers, R., et al. (2020). Synthesis of bioactive glass-based coating by plasma electrolytic oxidation: untangling a new deposition pathway toward titanium implant surfaces. *J. Colloid Interface Sci.* 579, 680–698. doi:10.1016/j.jcis.2020.06.102

Crush, J., Hussain, A., Seah, K. T. M., and Khan, W. S. (2021). Bioactive glass: methods for assessing angiogenesis and osteogenesis. *Front. Cell. Dev. Biol.* 9, 643781. doi:10.3389/fcell.2021.643781

Cuvelier, D., Théry, M., Chu, Y. S., Dufour, S., Thiéry, J. P., Bornens, M., et al. (2007). The universal dynamics of cell spreading. *Curr. Biol.* 17 (8), 694–699. doi:10.1016/j.cub.2007.02.058

Dhinasekaran, D., Kaliaraj, G. S., Jagannathan, M., Rajendran, A. R., Prakasarao, A., Ganesan, S., et al. (2021). Pulsed laser deposition of nanostructured bioactive glass and hydroxyapatite coatings: microstructural and electrochemical characterization. *Mater. Sci. Eng. C-Materials Biol. Appl.* 130, 112459. doi:10.1016/j.msec.2021.112459

Donos, N. (2018). The periodontal pocket. *Periodontology* 76(1), 7–15. doi:10.1111/prd.12203

Drago, L., Toscano, M., and Bottagisio, M. (2018). Recent evidence on bioactive glass antimicrobial and antibiofilm activity: a mini-review. *Materials* 11 (2), 326. doi:10.3390/ma11020326

Durgalakshmi, D., Rakkesh, R. A., Aruna, P., Ganesan, S., and Balakumar, S. (2020). Bioactivity and hemocompatibility of sol–gel bioactive glass synthesized under different catalytic conditions. *New J. Chem.* 44 (48), 21026–21037. doi:10.1039/D0NJ02445G

Echezarreta-López, M. M., and Landin, M. (2013). Using machine learning for improving knowledge on antibacterial effect of bioactive glass. *Int. J. Pharm.* 453 (2), 641–647. doi:10.1016/j.ijpharm.2013.06.036

Escalas, F., Galante, J., Rostoker, W., and Coogan, P. (1976). Biocompatibility of materials for total joint replacement. *J. Biomed. Mater. Res.* 10 (2), 175–195. doi:10.1002/jbm.820100203

Estrada-Cabrera, E., Torres-Ferrer, L. R., Aztatzi-Aguilar, O. G., De Vizcaya-Ruiz, A., Meraz-Rios, M. A., Zarate-Triviño, D. G., et al. (2019). Chitosan-bioglass coatings on partially nanostructured anodized Ti-6Al-4V alloy for biomedical applications. *Surf. Coatings Technol.* 375, 468–476. doi:10.1016/j.surfcoat.2019.07.002

Fischer, K., and Stenberg, T. (2012). Prospective 10-year cohort study based on a randomized controlled trial (RCT) on implant-supported full-arch maxillary prostheses. Part 1: sandblasted and acid-etched implants and mucosal tissue. *Clin. IMPLANT Dent. Relat. Res.* 14 (6), 808–815. doi:10.1111/j.1708-8208.2011.00389.x

Fleury, C., Petit, A., Mwale, F., Antoniou, J., Zukor, D. J., Tabrizian, M., et al. (2006). Effect of cobalt and chromium ions on human MG-63 osteoblasts *in vitro*: morphology, cytotoxicity, and oxidative stress. *Biomaterials* 27 (18), 3351–3360. doi:10.1016/j.biomaterials.2006.01.035

Fu, T., Alajmi, Z., Shen, Y. G., Wang, L. J., Yang, S. Y., and Zhang, M. (2017b). Sol-gel preparation and properties of Ag-containing bioactive glass films on titanium. *Int. J. Appl. Ceram. Technol.* 14 (6), 1117–1124. doi:10.1111/ijac.12713

Fu, T., Liu, B. G., Zhou, Y. M., and Wu, X. M. (2011). Sol-gel titania coating on NiTi alloy with a porous titania film as interlayer. *J. SOL-GEL Sci. Technol.* 58 (1), 307–311. doi:10.1007/s10971-010-2392-5

Fu, T., Sun, J. M., Zhao, Y. T., Wang, L. J., Zhou, Y. C., and Ma, X. (2017a). Hydrothermally crystallized Sr-containing bioactive glass film and its cytocompatibility. *Ceram. Int.* 43 (16), 13689–13695. doi:10.1016/j.ceramint.2017.07.080

Gaweda, M., Jelen, P., Dlugon, E., Wajda, A., Lesniak, M., Simka, W., et al. (2018). Bioactive layers based on black glasses on titanium substrates. *J. Am. Ceram. Soc.* 101 (2), 590–601. doi:10.1111/jace.15202

Gebhardt, F., Seuss, S., Turhan, M. C., Hornberger, H., Virtanen, S., and Boccaccini, A. R. (2012). Characterization of electrophoretic chitosan coatings on stainless steel. *Mater. Lett.* 66 (1), 302–304. doi:10.1016/j.matlet.2011.08.088

Geng, Z., Ji, L., Li, Z., Wang, J., He, H., Cui, Z., et al. (2021b). Nano-needle strontium-substituted apatite coating enhances osteoporotic osseointegration through promoting osteogenesis and inhibiting osteoclastogenesis. *Bioact. Mater.* 6 (2021), 905–915. doi:10.1016/j.bioactmat.2020.09.024

Geng, Z., Li, X., Ji, L., Li, Z., Zhu, S., Cui, Z., et al. (2021a). A novel snail-inspired bionic design of titanium with strontium-substituted hydroxyapatite coating for promoting osseointegration. *J. Mater. Sci. Technol.* 79(2021) 35–45. doi:10.1016/j.jmst.2020.11.041

Geng, Z., Sang, S., Wang, S., Meng, F., Li, Z., Zhu, S., et al. (2022). Optimizing the strontium content to achieve an ideal osseointegration through balancing apatite-forming ability and osteogenic activity. *Biomater. Adv.* 133(2022) 112647. doi:10.1016/j.msec.2022.112647

Gomez-Vega, J. M., Hozumi, A., Saiz, E., Tomsia, A. P., Sugimura, H., and Takai, O. (2001). Bioactive glass–mesoporous silica coatings on Ti6Al4V through enameling and triblock-copolymer-templated sol-gel processing. *J. Biomed. Mater. Res.* 56(3): 382–389. doi:10.1002/1097-4636(20010905)56:3<382::AID-JBM1107>3.0

Goriainov, V., Cook, R., Latham, J. M., Dunlop, D. G., and Oreffo, R. O. C. (2014). Bone and metal: an orthopaedic perspective on osseointegration of metals. *Acta Biomater.* 10 (10), 4043–4057. doi:10.1016/j.actbio.2014.06.004

Gu, H., Guo, F., Zhou, X., Gong, L., Zhang, Y., Zhai, W., et al. (2011). The stimulation of osteogenic differentiation of human adipose-derived stem cells by ionic products from akermanite dissolution via activation of the ERK pathway. *Biomaterials* 32 (29), 7023–7033. doi:10.1016/j.biomaterials.2011.06.003

Guimarães, R. P., Xavier, L. G. O., Maltos, K. L. M., Sá, A. F., Domingues, R. Z., Carvalho, V. E., et al. (2020). Koh group influence on titanium surfaces and pure sol-gel silica for enhanced osteogenic activity. *J. Biomater. Appl.* 35 (3), 405–421. doi:10.1177/0885328220934323

He, D. H., Wang, P., Liu, P., Liu, X. K., Chen, X. H., Li, W., et al. (2019). Anodic voltage dependence of Ti-6Al-4V substrates and hydroxyapatite coating. *J. Nanosci. Nanotechnol.* 19 (9), 5700–5706. doi:10.1166/jnn.2019.16530

Hench, L. L., and Greenspan, D. (2013). Interactions between bioactive glass and collagen: a review and new perspectives. *J. Aust. Ceram. Soc.* 49 (2), 1–40.

Hench, L. L. (2006). The story of Bioglass®. *J. Mater. Sci. Mater. Med.* 17(11): 967–978. doi:10.1007/s10856-006-0432-z

Hench, L. L., Xynos, I. D., Edgar, A. J., Buttery, L. D. K., and Polak, J. M. (2020). Gene activating glasses. *Phys. Chem. GLASSES-EUROPEAN J. GLASS Sci. Technol. PART B* 61 (4), 155–162. doi:10.13036/17533562.61.4.Hench

Henstock, J. R., Canham, L. T., and Anderson, S. I. (2015). Silicon: the evolution of its use in biomaterials. *Acta Biomater.* 11, 17–26. doi:10.1016/j.actbio.2014.09.025

Herman, H., Sampath, S., and McCune, R. (2000). Thermal spray: current status and future trends. *MRS Bull.* 25 (7), 17–25. doi:10.1557/mrs2000.119

Hoppe, A., Güldal, N. S., and Boccaccini, A. R. (2011). A review of the biological response to ionic dissolution products from bioactive glasses and glass-ceramics. *Biomaterials* 32 (11), 2757–2774. doi:10.1016/j.biomaterials.2011.01.004

Hu, C., Ashok, D., Nisbet, D. R., and Gautam, V. (2019). Bioinspired surface modification of orthopedic implants for bone tissue engineering. *Biomaterials* 219, 119366. doi:10.1016/j.biomaterials.2019.119366

Huang, Y.-J., and Nan, G.-X. (2019). Oxidative stress-induced angiogenesis. *J. Clin. Neurosci.* 63, 13–16. doi:10.1016/j.jocn.2019.02.019

Huang, Y., Jin, X., Zhang, X., Sun, H., Tu, J., Tang, T., et al. (2009). *In vitro* and *in vivo* evaluation of akermanite bioceramics for bone regeneration. *Biomaterials* 30 (28), 5041–5048. doi:10.1016/j.biomaterials.2009.05.077

Humphries, M. J., Even-Ram, S., and Artym, V. (2009). *Extracellular matrix protocols*. Second Edition. Totowa, NJ: Humana Press, 203–210. doi:10.1007/978-1-59745-413-1_14Cell adhesion assays

Ishikawa, K., Miyamoto, Y., Yuasa, T., Ito, A., Nagayama, M., and Suzuki, K. (2002). Fabrication of Zn containing apatite cement and its initial evaluation using human osteoblastic cells. *Biomaterials* 23 (2), 423–428. doi:10.1016/S0142-9612(01)00121-1

Jones, J. R. (2013). Review of bioactive glass: from Hench to hybrids. *Acta Biomater.* 9 (1), 4457–4486. doi:10.1016/j.actbio.2012.08.023

Jugowiec, D., Lukaszczyk, A., Cieniek, L., Kot, M., Reczynska, K., Cholewa-Kowalska, K., et al. (2017). Electrophoretic, deposition and characterization of composite chitosan-based coatings incorporating bioglass and sol-gel glass particles on the Ti-13Nb-13Zr alloy. *Surf. Coatings Technol.* 319, 33–46. doi:10.1016/j.surfcoat.2017.03.067

Kargozar, S., Montazerian, M., Fiume, E., and Baino, F. (2019). Multiple and promising applications of strontium (Sr)-Containing bioactive glasses in bone tissue engineering. *Front. Bioeng. Biotechnol.* 7, 161. doi:10.3389/fbioe.2019.00161

Kassab, M. M., and Cohen, R. E. (2003). The etiology and prevalence of gingival recession. *J. Am. Dent. Assoc.* 134 (2), 220–225. doi:10.14219/jada.archive.2003.0137

Khanmohammadi, S., Ojaghi-Ilkhchi, M., and Farrokhi-Rad, M. (2020). Evaluation of bioglass and hydroxyapatite based nanocomposite coatings obtained by electrophoretic deposition. *Ceram. Int.* 46 (16), 26069–26077. doi:10.1016/j.ceramint.2020.07.100

Kim, H. M., Miyaji, F., Kokubo, T., and Nakamura, T. (1996). Preparation of functionally graded bioactive titanium and its alloys by chemical treatment. *J. Biomed. Mater Res.* 32 (3), 1102–1107. doi:10.2320/jinstmet1952.62.11_1102

Klyui, N. I., Chornyi, V. S., Zatovsky, I. V., Tsabiy, L. I., Buryanov, A. A., Protsenko, V. V., et al. (2021). Properties of gas detonation ceramic coatings and their effect on the osseointegration of titanium implants for bone defect replacement. *Ceram. Int.* 47 (18), 25425–25439. doi:10.1016/j.ceramint.2021.05.265

Lavenus, S., Poxson, D. J., Ogievetsky, N., Dordick, J. S., and Siegel, R. W. (2015). Stem cell behavior on tailored porous oxide surface coatings. *Biomaterials* 55, 96–109. doi:10.1016/j.biomaterials.2015.03.033

Ledda, M., De Bonis, A., Bertani, F. R., Cacciotti, I., Teghil, R., Lolli, M. G., et al. (2015). Interdisciplinary approach to cell-biomaterial interactions: biocompatibility and cell friendly characteristics of RKKP glass-ceramic coatings on titanium. *Biomed. Mater.* 10 (3), 035005. doi:10.1088/1748-6041/10/3/035005

Ledda, M., Fosca, M., De Bonis, A., Curcio, M., Teghil, R., Lolli, M. G., et al. (2016). Placenta derived mesenchymal stem cells hosted on RKKP glass-ceramic: a tissue engineering strategy for bone regenerative medicine applications. *Biomed Res. Int.* 2016, 1–11. doi:10.1155/2016/3657906

Lee, S., Goh, B. T., Wolke, J., Tideman, H., Stoelinga, P., and Jansen, J. (2010). Soft tissue adaptation to modified titanium surfaces. *J. Biomed. Mater. Res. Part A* 95A (2), 543–549. doi:10.1002/jbm.a.32849

Li, B., Li, Y., Li, J., Fu, X., Li, H., Wang, H., et al. (2014). Influence of nanostructures on the biological properties of Ti implants after anodic oxidation. *J. Mater Sci. Mater Med.* 25 (1), 199–205. doi:10.1007/s10856-013-5064-5

Li, Y., Chen, L., Chen, X., Hill, R., Zou, S., Wang, M., et al. (2021). High phosphate content in bioactive glasses promotes osteogenesis *in vitro* and *in vivo*. *Dent. Mater* 37 (2), 272–283. doi:10.1016/j.dental.2020.11.017

Löe, H. (1967). The gingival index, the plaque index and the retention index systems. *J. Periodontology* 38 (6), 610–616. doi:10.1902/jop.1967.38.6_part2.610

Long, M., and Rack, H. J. (1998). Titanium alloys in total joint replacement—A materials science perspective. *Biomaterials* 19 (18), 1621–1639. doi:10.1016/S0142-9612(97)00146-4

López, M. M. M., Fauré, J., Cabrera, M. I. E., and García, M. E. C. (2016). Structural characterization and electrochemical behavior of 45S5 bioglass coating on Ti6Al4V alloy for dental applications. *Mater. Sci. Eng. B* 206, 30–38. doi:10.1016/j.mseb.2015.09.003

Lung, C. Y. K., Abdalla, M. M., Chu, C. H., Yin, I., Got, S. R., and Matinlinna, J. P. (2021). A multi-element-doped porous bioactive glass coating for implant applications. *Materials* 14 (4), 961. doi:10.3390/ma14040961

Ma, J., Wang, C. Z., Ban, C. L., Chen, C. Z., and Zhang, H. M. (2016). Pulsed laser deposition of magnesium-containing bioactive glass film on porous Ti-6Al-4V substrate pretreated by micro-arc oxidation. *Vacuum* 125, 48–55. doi:10.1016/j.vacuum.2015.12.005

Mahlooji, E., Atapour, M., and Labbaf, S. (2019). Electrophoretic deposition of Bioactive glass - chitosan nanocomposite coatings on Ti-6Al-4V for orthopedic applications. *Carbohydr. Polym.* 226, 115299. doi:10.1016/j.carbpol.2019.115299

Manam, N. S., Harun, W. S. W., Awang Shri, D. N., Bin Che Ghani, S., Kurniawan, T., Ismail, M., et al. (2017). Study of corrosion in biocompatible metals for implants: a review. *J. Alloys Compd.* 701, 698–715. doi:10.1016/j.jallcom.2017.01.196

Manivasagam, V. K., Sabino, R. M., Kantam, P., and Popat, K. C. (2021). Surface modification strategies to improve titanium hemocompatibility: a comprehensive review. *Mater Adv.* 2 (18), 5824–5842. doi:10.1039/d1ma00367d

Marques, I. D., Barao, V. A., da Cruz, N. C., Yuan, J. C., Mesquita, M. F., Ricomini-Filho, A. P., et al. (2015). Electrochemical behavior of bioactive coatings on cp-Ti surface for dental application. *Corros. Sci.* 100, 133–146. doi:10.1016/j.corsci.2015.07.019

Massera, J., Fagerlund, S., Hupa, L., and Hupa, M. (2012). Crystallization mechanism of the bioactive glasses, 45S5 and S53P4. *J. Am. Ceram. Soc.* 95 (2), 607–613. doi:10.1111/j.1551-2916.2011.05012.x

Matter, M. T., Maliqi, L., Keevend, K., Guimond, S., Ng, J., Armagan, E., et al. (2021). One-Step synthesis of versatile antimicrobial nano-architected implant coatings for hard and soft tissue healing. *Acs Appl. Mater. Interfaces* 13 (28), 33300–33310. doi:10.1021/acsami.1c10121

Maximov, M., Maximov, O.-C., Craciun, L., Ficai, D., Ficai, A., and Andronescu, E. (2021). Bioactive glass—an extensive study of the preparation and coating methods. *Coatings* 11 (11), 1386. doi:10.3390/coatings11111386

Medzhitov, R. (2010). Inflammation 2010: new adventures of an old flame. *Cell.* 140 (6), 771–776. doi:10.1016/j.cell.2010.03.006

Mehdikhani-Nahrkhalaji, M., Fathi, M. H., Mortazavi, V., Mousavi, S. B., Akhavan, A., Haghighat, A., et al. (2015). Biodegradable nanocomposite coatings accelerate bone healing: *in vivo* evaluation. *Dent. Res. J. (Isfahan).* 12 (1), 89–99. doi:10.4103/1735-3327.150342

Mistry, S., Roy, R., Kundu, B., Datta, S., Kumar, M., Chanda, A., et al. (2016). Clinical outcome of hydroxyapatite coated, bioactive glass coated, and machined Ti6Al4V threaded dental implant in human jaws: a short-term comparative study. *Implant Dent.* 25 (2), 252–260. doi:10.1097/ID.0000000000000376

Moreira, C. D. F., Carvalho, S. M., Sousa, R. G., Mansur, H. S., and Pereira, M. M. (2018). Nanostructured chitosan/gelatin/bioactive glass *in situ* forming hydrogel composites as a potential injectable matrix for bone tissue engineering. *Mater. Chem. Phys.* 218, 304–316. doi:10.1016/j.matchemphys.2018.07.039

Nalezinkova, M. (2020). *In vitro* hemocompatibility testing of medical devices. *Thromb. Res.* 195, 146–150. doi:10.1016/j.thromres.2020.07.027

Naseri, S., Nazhat, S. N., and Ylänen, H. (2018). *Bioactive glasses*. Second Edition. Woodhead Publishing, 381–405. doi:10.1016/B978-0-08-100936-9.00019-814 - bioactive and soluble glasses for wound-healing applications

Nesabi, M., Valanezhad, A., Safaee, S., Odatsu, T., Abe, S., and Watanabe, I. (2021). A novel multi-structural reinforced treatment on Ti implant utilizing a combination of alkali solution and bioactive glass sol. *J. Mech. Behav. Biomed. Mater.* 124, 104837. doi:10.1016/j.jmbbm.2021.104837

Newman, S. D., Lotfibakhshaiesh, N., O'Donnell, M., Walboomers, X. F., Horwood, N., Jansen, J. A., et al. (2014). Enhanced osseous implant fixation with strontium-substituted bioactive glass coating. *Tissue Eng. Part A* 20 (13-14), 1850–1857. doi:10.1089/ten.TEA.2013.0304

Niinomi, M. (1998). Mechanical properties of biomedical titanium alloys. *Mater. Sci. Eng. A* 243 (1), 231–236. doi:10.1016/S0921-5093(97)00806-X

Nishiguchi, S., Fujibayashi, S., Kim, H. M., Kokubo, T., and Nakamura, T. (2003). Biology of alkali- and heat-treated titanium implants. *J. Biomed. Mater Res. A* 67 (1), 26–35. doi:10.1002/jbm.a.10540

Nowak-Sliwinska, P., Alitalo, K., Allen, E., Anisimov, A., Aplin, A. C., Auerbach, R., et al. (2018). Consensus guidelines for the use and interpretation of angiogenesis assays. *Angiogenesis* 21 (3), 425–532. doi:10.1007/s10456-018-9613-x

Oki, A., Parveen, B., Hossain, S., Adeniji, S., and Donahue, H. (2004). Preparation and *in vitro* bioactivity of zinc containing sol-gel–derived bioglass materials. *J. Biomed. Mater. Res. Part A* 69A (2), 216–221. doi:10.1002/jbm.a.20070

Oliver, J. N., Su, Y., Lu, X., Kuo, P. H., Du, J., and Zhu, D. (2019). Bioactive glass coatings on metallic implants for biomedical applications. *Bioact. Mater* 4, 261–270. doi:10.1016/j.bioactmat.2019.09.002

O'Neill, E., Awale, G., Daneshmandi, L., Umerah, O., and Lo, K. W. H. (2018). The roles of ions on bone regeneration. *Drug Discov. Today* 23 (4), 879–890. doi:10.1016/j.drudis.2018.01.049

Ordikhani, F., and Simchi, A. (2014). Long-term antibiotic delivery by chitosan-based composite coatings with bone regenerative potential. *Appl. Surf. Sci.* 317, 56–66. doi:10.1016/j.apsusc.2014.07.197

Ordikhani, F., Zustiak, S. P., and Simchi, A. (2016). Surface modifications of titanium implants by multilayer bioactive coatings with drug delivery potential: antimicrobial, biological, and drug release studies. *Jom* 68 (4), 1100–1108. doi:10.1007/s11837-016-1840-2

Orita, K., Goto, K., Kuroda, Y., Kawai, T., Okuzu, Y., Takaoka, Y., et al. (2022). Long-term outcome of primary total hip arthroplasty with cementless bioactive glass ceramic bottom-coated implants and highly cross-linked polyethylene: A minimum 10-year analysis. *J. Orthop. Sci.* 28 (2), 385–390. doi:10.1016/j.jos.2021.12.019

Owen, T. A., Aronow, M., Shalhoub, V., Barone, L. M., Wilming, L., Tassinari, M. S., et al. (1990). Progressive development of the rat osteoblast phenotype *in vitro*: reciprocal relationships in expression of genes associated with osteoblast proliferation and differentiation during formation of the bone extracellular matrix. *J. Cell. Physiol.* 143 (3), 420–430. doi:10.1002/jcp.1041430304

Palangadan, R., Sukumaran, A., Fernandez, F. B., John, A., and Varma, H. (2014). Pulsed laser deposition and *in vitro* characteristics of triphasic - HASi composition on titanium. *J. Biomaterials Appl.* 28 (6), 849–858. doi:10.1177/0885328213484545

Pantulap, U., Arango-Ospina, M., and Boccaccini, A. R. (2021). Bioactive glasses incorporating less-common ions to improve biological and physical properties. *J. Mater Sci. Mater Med.* 33 (1), 3. doi:10.1007/s10856-021-06626-3

Park Ridge, N. J. (1988). Price: $72.00 ISBN 0-8155-1154-X. *Mater. Res. Bull.* 24(3): 389. doi:10.1016/0025-5408(89)90225-0

Patel, K. D., Buitrago, J. O., Parthiban, S. P., Lee, J. H., Singh, R. K., Knowles, J. C., et al. (2019). Combined effects of nanoroughness and ions produced by electrodeposition of mesoporous bioglass nanoparticle for bone regeneration. *ACS Appl. Bio Mater* 2 (11), 5190–5203. doi:10.1021/acsabm.9b00859

Patel, K. D., El-Fiqi, A., Lee, H.-Y., Singh, R. K., Kim, D.-A., Lee, H.-H., et al. (2012). Chitosan–nanobioactive glass electrophoretic coatings with bone regenerative and drug delivering potential. *J. Mater. Chem.* 22 (47), 24945–24956. doi:10.1039/c2jm33830k

Pattanaik, B., Pawar, S., and Pattanaik, S. (2012). Biocompatible implant surface treatments. *Indian J. Dent. Res.* 23 (3), 398–406. doi:10.4103/0970-9290.102240

Pishbin, F., Mourino, V., Gilchrist, J. B., McComb, D. W., Kreppel, S., Salih, V., et al. (2013). Single-step electrochemical deposition of antimicrobial orthopaedic coatings based on a bioactive glass/chitosan/nano-silver composite system. *Acta Biomater.* 9 (7), 7469–7479. doi:10.1016/j.actbio.2013.03.006

Pishbin, F., Simchi, A., Ryan, M. P., and Boccaccini, A. R. (2011). Electrophoretic deposition of chitosan/45S5 Bioglass® composite coatings for orthopaedic applications. *Surf. Coatings Technol.* 205 (23-24), 5260–5268. doi:10.1016/j.surfcoat.2011.05.026

Ponzetti, M., and Rucci, N. (2021). Osteoblast differentiation and signaling: established concepts and emerging topics. *Int. J. Mol. Sci.* 22 (13), 6651. doi:10.3390/ijms22136651

Popa, A. C., Stan, G. E., Enculescu, M., Tanase, C., Tulyaganov, D. U., and Ferreira, J. M. (2015). Superior biofunctionality of dental implant fixtures uniformly coated with durable bioglass films by magnetron sputtering. *J. Mech. Behav. Biomed. Mater* 51, 313–327. doi:10.1016/j.jmbbm.2015.07.028

Popa, A. C., Stan, G. E., Husanu, M. A., Mercioniu, I., Santos, L. F., Fernandes, H. R., et al. (2017). Bioglass implant-coating interactions in synthetic physiological fluids with varying degrees of biomimicry. *Int. J. Nanomedicine* 12, 683–707. doi:10.2147/IJN.S123236

Pore, O. C., Fulari, A. V., Shejwal, R. V., Fulari, V. J., and Lohar, G. M. (2021). Review on recent progress in hydrothermally synthesized MCo2O4/rGO composite for energy storage devices. *Chem. Eng. J.* 426, 131544. doi:10.1016/j.cej.2021.131544

Rastegari, S., and Salahinejad, E. (2019). Surface modification of Ti-6Al-4V alloy for osseointegration by alkaline treatment and chitosan-matrix glass-reinforced nanocomposite coating. *Carbohydr. Polym.* 205, 302–311. doi:10.1016/j.carbpol.2018.10.082

Rau, J. V., De Bonis, A., Curcio, M., Schuhladen, K., Barbaro, K., De Bellis, G., et al. (2020). Borate and silicate bioactive glass coatings prepared by nanosecond pulsed laser deposition. *Coatings* 10 (11), 1105. doi:10.3390/coatings10111105

Rivadeneira, J., and Gorustovich, A. (2017). Bioactive glasses as delivery systems for antimicrobial agents. *J. Appl. Microbiol.* 122 (1365-2672), 1424–1437. (Electronic). doi:10.1111/jam.13393

Rizwan, M., Alias, R., Zaidi, U. Z., Mahmoodian, R., and Hamdi, M. (2018). Surface modification of valve metals using plasma electrolytic oxidation for antibacterial applications: a review. *J. Biomed. Mater Res. A* 106 (2), 590–605. doi:10.1002/jbm.a.36259

Safaee, S., Valanezhad, A., Nesabi, M., Jafarnia, S., Sano, H., Shahabi, S., et al. (2021). Fabrication of bioactive glass coating on pure titanium by sol-dip method: dental applications. *Dent. Mater J.* 40 (4), 949–956. doi:10.4012/dmj.2020-323

Saffarian Tousi, N., Velten, M. F., Bishop, T. J., Leong, K. K., Barkhordar, N. S., Marshall, G. W., et al. (2013). Combinatorial effect of Si4+, Ca2+, and Mg2+ released from bioactive glasses on osteoblast osteocalcin expression and biomineralization. *Mater. Sci. Eng. C* 33 (5), 2757–2765. doi:10.1016/j.msec.2013.02.044

Saino, E., Maliardi, V., Quartarone, E., Fassina, L., Benedetti, L., De Angelis, M. G., et al. (2010). *In vitro* enhancement of SAOS-2 cell calcified matrix deposition onto radio frequency magnetron sputtered bioglass-coated titanium scaffolds. *Tissue Eng. Part A* 16 (3), 995–1008. doi:10.1089/ten.TEA.2009.0051

Sang, S., Wang, S., Yang, C., Geng, Z., and Zhang, X. (2022). Sponge-inspired sulfonated polyetheretherketone loaded with polydopamine-protected osthole nanoparticles and berberine enhances osteogenic activity and prevents implant-related infections. *Chem. Eng. J.* 437 (2022), 135255. doi:10.1016/j.cej.2022.135255

Santos, M. I., Unger, R. E., Sousa, R. A., Reis, R. L., and Kirkpatrick, C. J. (2009). Crosstalk between osteoblasts and endothelial cells co-cultured on a polycaprolactone–starch scaffold and the *in vitro* development of vascularization. *Biomaterials* 30 (26), 4407–4415. doi:10.1016/j.biomaterials.2009.05.004

Sanz-Herrera, J. A., and Boccaccini, A. R. (2011). Modelling bioactivity and degradation of bioactive glass based tissue engineering scaffolds. *Int. J. Solids Struct.* 48 (2), 257–268. doi:10.1016/j.ijsolstr.2010.09.025

Sepulveda, P., Jones, J. R., and Hench, L. L. (2002). *In vitro* dissolution of melt-derived 45S5 and sol-gel derived 58S bioactive glasses. *J. Biomed. Mater. Res.* 61 (2), 301–311. doi:10.1002/jbm.10207

Serra, J., Liste, S., González, P., Serra, C., Borrajo, J. P., Chiussi, S., et al. (2004). The role of the temperature and laser fluence on the properties of PLD bioactive glass films. *Appl. Phys. A* 79 (4), 983–986. doi:10.1007/s00339-004-2610-5

Shaikh, S., Kedia, S., Majumdar, A. G., Subramanian, M., and Sinha, S. (2019). 45S5 bioactive glass coating on Ti6Al4V alloy using pulsed laser deposition technique. *Mater. Res. Express* 6 (12), 125428. doi:10.1088/2053-1591/ab7568

Shamsi, M., Karimi, M., Ghollasi, M., Nezafati, N., Shahrousvand, M., Kamali, M., et al. (2017). *In vitro* proliferation and differentiation of human bone marrow mesenchymal stem cells into osteoblasts on nanocomposite scaffolds based on bioactive glass (64SiO2-31CaO-5P2O5)-poly-l-lactic acid nanofibers fabricated by electrospinning method. *Mater. Sci. Eng. C* 78, 114–123. doi:10.1016/j.msec.2017.02.165

Shi, J. Z., Chen, C. Z., Yu, H. J., and Zhang, S. J. (2008). The effect of process conditions on the properties of bioactive films prepared by magnetron sputtering. *Vacuum* 83 (2), 249–256. doi:10.1016/j.vacuum.2008.05.019

Silness, J., and Löe, H. (1964). Periodontal disease in pregnancy II. Correlation between oral hygiene and periodontal condition. *Acta Odontol. Scand.* 22 (1), 121–135. doi:10.3109/00016356408993968

Soares, P. B. F., Moura, C. C. G., Chinaglia, C. R., Zanotto, E. D., Zanetta-Barbosa, D., and Stavropoulos, A. (2018). Effect of titanium surface functionalization with bioactive glass on osseointegration: an experimental study in dogs. *Clin. Oral Implants Res.* 29 (11), 1120–1125. doi:10.1111/clr.13375

Sola, A., Bellucci, D., Cannillo, V., and Cattini, A. (2011). Bioactive glass coatings: A review. *Surf. Eng.* 27 (8), 560–572. doi:10.1179/1743294410y.0000000008

Su, T. R., Chu, Y. H., Yang, H. W., Huang, Y. F., and Ding, S. J. (2019). Component effects of bioactive glass on corrosion resistance and *in vitro* biological properties of apatite-matrix coatings. *Bio-Medical Mater. Eng.* 30 (2), 207–218. doi:10.3233/bme-191045

Sultana, A., Zare, M., Luo, H., and Ramakrishna, S. (2021). Surface engineering strategies to enhance the *in situ* performance of medical devices including atomic scale engineering. *Int. J. Mol. Sci.* 22 (21), 11788. doi:10.3390/ijms222111788

Sun, J., Li, J., Liu, X., Wei, L., Wang, G., and Meng, F. (2009). Proliferation and gene expression of osteoblasts cultured in DMEM containing the ionic products of dicalcium silicate coating. *Biomed. Pharmacother.* 63 (9), 650–657. doi:10.1016/j.biopha.2009.01.007

Taguchi, T., Yanagi, Y., Yoshimaru, K., Zhang, X.-Y., Matsuura, T., Nakayama, K., et al. (2019). Regenerative medicine using stem cells from human exfoliated deciduous teeth (SHED): a promising new treatment in pediatric surgery. *Surg. Today* 49 (4), 316–322. doi:10.1007/s00595-019-01783-z

Tian, B., Chen, W., Dong, Y. F., Marymont, J. V., Lei, Y., Ke, Q. F., et al. (2016). Silver nanoparticle-loaded hydroxyapatite coating: structure, antibacterial properties, and capacity for osteogenic induction *in vitro*. *RSC Adv.* 6 (11), 8549–8562. doi:10.1039/c5ra25391h

Torrisi, L., Borrielli, A., and Margarone, D. (2007). Study on the ablation threshold induced by pulsed lasers at different wavelengths. *Nucl. Instrum. Methods Phys. Res. Sect. B Beam Interact. Mater. Atoms* 255 (2), 373–379. doi:10.1016/j.nimb.2006.12.144

Trepat, X., Chen, Z., and Jacobson, K. (2012). Cell migration. *Compr. Physiol.* 2 (4), 2369–2392. doi:10.1002/cphy.c110012

Valanezhad, A., Tsuru, K., and Ishikawa, K. (2015). Fabrication of strongly attached hydroxyapatite coating on titanium by hydrothermal treatment of Ti–Zn–PO4 coated titanium in CaCl2 solution. *J. Mater. Sci. Mater. Med.* 26 (7), 212. doi:10.1007/s10856-015-5548-6

van Oirschot, B. A., Alghamdi, H. S., Närhi, T. O., Anil, S., Al Farraj Aldosari, A., van den Beucken, J. J., et al. (2014). *In vivo* evaluation of bioactive glass-based coatings on dental implants in a dog implantation model. *Clin. Oral Implants Res.* 25 (1), 21–28. doi:10.1111/clr.12060

van Oirschot, B. A., Meijer, G. J., Bronkhorst, E. M., Närhi, T., Jansen, J. A., and van den Beucken, J. J. (2016). Comparison of different surface modifications for titanium implants installed into the goat iliac crest. *Clin. Oral Implants Res.* 27 (2), e57–e67. doi:10.1111/clr.12529

van Oirschot, B., Eman, R. M., Habibovic, P., Leeuwenburgh, S. C. G., Tahmasebi, Z., Weinans, H., et al. (2016). Osteophilic properties of bone implant surface modifications in a cassette model on a decorticated goat spinal transverse process. *Acta Biomater.* 37, 195–205. doi:10.1016/j.actbio.2016.03.037

Vuornos, K., Ojansivu, M., Koivisto, J. T., Hakkanen, H., Belay, B., Montonen, T., et al. (2019). Bioactive glass ions induce efficient osteogenic differentiation of human adipose stem cells encapsulated in gellan gum and collagen type I hydrogels. *Mater Sci. Eng. C Mater Biol. Appl.* 99, 905–918. doi:10.1016/j.msec.2019.02.035

Wang, D. G., Chen, C. Z., Yang, X. X., Ming, X. C., and Zhang, W. L. (2018). Effect of bioglass addition on the properties of HA/BG composite films fabricated by pulsed laser deposition. *Ceram. Int.* 44 (12), 14528–14533. doi:10.1016/j.ceramint.2018.05.069

Wang, D. G., Xiao, F. H., Li, Y., Ming, X. C., Zhai, J. Q., and Chen, C. Z. (2020). Properties of HA-based composite films fabricated by pulsed laser deposition with an *in-situ* heat treatment. *Surf. Coatings Technol.* 394, 125863. doi:10.1016/j.surfcoat.2020.125863

Wang, G., Liu, X., Zreiqat, H., and Ding, C. (2011). Enhanced effects of nano-scale topography on the bioactivity and osteoblast behaviors of micron rough ZrO2 coatings. *Colloids Surf. B Biointerfaces* 86 (2), 267–274. doi:10.1016/j.colsurfb.2011.04.006

Wang, Z., Zhang, X., Gu, J., Yang, H., Nie, J., and Ma, G. (2014). Electrodeposition of alginate/chitosan layer-by-layer composite coatings on titanium substrates. *Carbohydr. Polym.* 103, 38–45. doi:10.1016/j.carbpol.2013.12.007

Wataha, J. C., Hanks, C. T., Strawn, S. E., and Fat, J. C. (1994). Cytotoxicity of components of resins and other dental restorative materials. *J. Oral Rehabil.* 21 (4), 453–462. doi:10.1111/j.1365-2842.1994.tb01159.x

Wei, C. K., and Ding, S. J. (2017). Dual-functional bone implants with antibacterial ability and osteogenic activity. *J. Mater. Chem. B* 5 (10), 1943–1953. doi:10.1039/c7tb00173h

Wolke, J. G. C., Vandenbulcke, E., van Oirschot, B., and Jansen, J. A. (2005). A study to the surface characteristics of RF magnetron sputtered bioglass - and calcium phosphate coatings. *Key Eng. Mater.* 284-286, 187–190. doi:10.4028/www.scientific.net/kem.284-286.187

Wu, C. T., Chen, Z. T., Yi, D. H., Chang, J., and Xiao, Y. (2014). Multidirectional effects of Sr-Mg-and Si-containing bioceramic coatings with high bonding strength on inflammation, osteoclastogenesis, and osteogenesis. *Acs Appl. Mater. Interfaces* 6 (6), 4264–4276. doi:10.1021/am4060035

Wu, M.-S., Aquino, L. B. B., Barbaza, M. Y. U., Hsieh, C.-L., De Castro-Cruz, K. A., Yang, L.-L., et al. (2019). Anti-inflammatory and anticancer properties of bioactive compounds from Sesamum indicum L.—a review. *Molecules* 24 (24), 4426. doi:10.3390/molecules24244426

Xynos, I. D., Edgar, A. J., Buttery, L. D. K., Hench, L. L., and Polak, J. M. (2001). Gene-expression profiling of human osteoblasts following treatment with the ionic products of Bioglass® 45S5 dissolution. *J. Biomed. Mater. Res.* 55 (2), 151–157. doi:10.1002/1097-4636(200105)55:2<151::aid-jbm1001>3.0.co;2-d

Xynos, I. D., Edgar, A. J., Buttery, L. D. K., Hench, L. L., and Polak, J. M. (2000). Ionic products of bioactive glass dissolution increase proliferation of human osteoblasts and induce insulin-like growth factor II mRNA expression and protein synthesis. *Biochem. Biophysical Res. Commun.* 276 (2), 461–465. doi:10.1006/bbrc.2000.3503

Yanovska, A., Kuznetsov, V., Stanislavov, A., Danilchenko, S., and Sukhodub, L. (2011). Synthesis and characterization of hydroxyapatite-based coatings for medical implants obtained on chemically modified Ti6Al4V substrates. *Surf. Coatings Technol.* 205 (23), 5324–5329. doi:10.1016/j.surfcoat.2011.05.040

Ye, X., Leeflang, S., Wu, C., Chang, J., Zhou, J., and Huan, Z. (2017). Mesoporous bioactive glass functionalized 3D Ti-6Al-4V scaffolds with improved surface bioactivity. *Mater. (Basel)* 10 (11), 1244. doi:10.3390/ma10111244

Zafar, M. S., Farooq, I., Awais, M., Najeeb, S., Khurshid, Z., Zohaib, S., et al. (2019). *Chapter 11 - bioactive surface coatings for enhancing osseointegration of dental implants. Biomedical, therapeutic and clinical applications of bioactive glasses*. Woodhead Publishing, 313–329. doi:10.1016/B978-0-08-102196-5.00011-2

Zarghami, V., Ghorbani, M., Bagheri, K. P., and Shokrgozar, M. A. (2021). Prevention the formation of biofilm on orthopedic implants by melittin thin layer on chitosan/bioactive glass/vancomycin coatings. *J. Mater. Science-Materials Med.* 32 (7), 75. doi:10.1007/s10856-021-06551-5

Zarghami, V., Ghorbani, M., Bagheri, K. P., and Shokrgozar, M. A. (2020). Prolongation of bactericidal efficiency of chitosan - bioactive glass coating by drug controlled release. *Prog. Org. Coatings* 139, 105440. doi:10.1016/j.porgcoat.2019.105440

Zhai, W., Lu, H., Wu, C., Chen, L., Lin, X., Naoki, K., et al. (2013). Stimulatory effects of the ionic products from Ca–Mg–Si bioceramics on both osteogenesis and angiogenesis *in vitro*. *Acta Biomater.* 9 (8), 8004–8014. doi:10.1016/j.actbio.2013.04.024

Zhang, G., Zhao, P., Lin, L., Qin, L., Huan, Z., Leeflang, S., et al. (2021). Surface-treated 3D printed Ti-6Al-4V scaffolds with enhanced bone regeneration performance: an *in vivo* study. *Ann. Transl. Med.* 9 (1), 39. doi:10.21037/atm-20-3829

Zhang, J., Lynch, R. J. M., Watson, T. F., and Banerjee, A. (2019). Chitosan-bioglass complexes promote subsurface remineralisation of incipient human carious enamel lesions. *J. Dent.* 84, 67–75. doi:10.1016/j.jdent.2019.03.006

Zhang, Y. L., Chen, L., Shi, M. C., Zhai, D., Zhu, H. Y., Chang, J., et al. (2016). Mesoporous bioactive glass nanolayer-modified zirconia coatings on Ti-6Al-4V with improved *in vitro* bioactivity. *Int. J. Appl. Glass Sci.* 7 (2), 216–228. doi:10.1111/ijag.12210

Zhao, Y., Song, M., Chen, C., and Liu, J. (2008). The role of the pressure in pulsed laser deposition of bioactive glass films. *J. Non-Crystalline Solids* 354 (33), 4000–4004. doi:10.1016/j.jnoncrysol.2008.05.019

Zhitomirsky, D., Roether, J. A., Boccaccini, A. R., and Zhitomirsky, I. (2009). Electrophoretic deposition of bioactive glass/polymer composite coatings with and without HA nanoparticle inclusions for biomedical applications. *J. Mater. Process. Technol.* 209 (4), 1853–1860. doi:10.1016/j.jmatprotec.2008.04.034

Zhou, J. C., Yang, Y. Y., Frank, M. A., Detsch, R., Boccaccini, A. R., and Virtanen, S. (2016). Accelerated degradation behavior and cytocompatibility of pure iron treated with sandblasting. *ACS Appl. Mater. INTERFACES* 8 (40), 26482–26492. doi:10.1021/acsami.6b07068

Zhou, Y., Wu, C., and Chang, J. (2019). Bioceramics to regulate stem cells and their microenvironment for tissue regeneration. *Mater. Today* 24, 41–56. doi:10.1016/j.mattod.2018.07.016

Zigterman, B. G. R., Van den Borre, C., Braem, A., and Mommaerts, M. Y. (2019). Titanium surface modifications and their soft-tissue interface on nonkeratinized soft tissues-A systematic review (Review). *BIOINTERPHASES* 14 (4), 040802. doi:10.1116/1.5113607

frontiers | Frontiers in Bioengineering and Biotechnology

TYPE Original Research
PUBLISHED 04 April 2024
DOI 10.3389/fbioe.2024.1381685

OPEN ACCESS

EDITED BY
Xiubo Zhao,
Changzhou University, China

REVIEWED BY
Kui Xu,
Anhui University of Chinese Medicine, China
Zhennan Deng,
Wenzhou Medical University, China

*CORRESPONDENCE
Ling Guo,
372083745@qq.com

RECEIVED 04 February 2024
ACCEPTED 22 March 2024
PUBLISHED 04 April 2024

CITATION
You X, Wang Z, Wang L, Liu Y, Chen H, Lan X and Guo L (2024), Graphene oxide/ε-poly-L-lysine self-assembled functionalized coatings improve the biocompatibility and antibacterial properties of titanium implants.
Front. Bioeng. Biotechnol. 12:1381685.
doi: 10.3389/fbioe.2024.1381685

Graphene oxide/ε-poly-L-lysine self-assembled functionalized coatings improve the biocompatibility and antibacterial properties of titanium implants

Xiaoxiao You[1,2,3,4,5], Zhongke Wang[1,2,3,4], Li Wang[1,2,3,4], Youbo Liu[1,2,3,4], Hongmei Chen[1], Xiaorong Lan[2,3,4] and Ling Guo[1,2,3,4]*

[1]Department of Oral Prosthodontics, The Affiliated Stomatological Hospital, Southwest Medical University, Luzhou, China, [2]Institute of Stomatology, Southwest Medical University, Luzhou, China, [3]School of Stomatology, Southwest Medical University, Luzhou, China, [4]Luzhou Key Laboratory of Oral & Maxillofacial Reconstruction and Regeneration, Luzhou, China, [5]The Public Platform of Zebrafish Technology, Public Center of Experimental Technology, Southwest Medical University, Luzhou, China

The construction of an antibacterial biological coating on titanium surface plays an important role in the long-term stability of oral implant restoration. Graphene oxide (GO) has been widely studied because of its excellent antibacterial properties and osteogenic activity. However, striking a balance between its biological toxicity and antibacterial properties remains a significant challenge with GO. ε-poly-L-lysine (PLL) has broad-spectrum antibacterial activity and ultra-high safety performance. Using Layer-by-layer self-assembly technology (LBL), different layers of PLL/GO coatings and GO self-assembly coatings were assembled on the surface of titanium sheet. The materials were characterized using scanning electron microscope (SEM), Fourier transform infrared spectroscopy (FTIR), X-ray photoelectron spectroscopy (XPS) and contact angle test. The antibacterial properties of Porphyromonas gingivalis (*P.g.*) were analyzed through SEM, coated plate experiment, and inhibition zone experiment. CCK-8 was used to determine the cytotoxicity of the material to MC3T3 cells, and zebrafish larvae and embryos were used to determine the developmental toxicity and inflammatory effects of the material. The results show that the combined assembly of 20 layers of GO and PLL exhibits good antibacterial properties and no biological toxicity, suggesting a potential application for a titanium-based implant modification scheme.

KEYWORDS

graphene oxide, ε-poly-L-lysine, antibacterial, biocompatibility, layer-by-layer self-assembly

1 Introduction

Implant restoration has become a crucial method for replacing missing teeth due to its excellent function and aesthetic effects (Jiang et al., 2020; Li et al., 2022b). However, 42%–43% patients will suffer from peri-implant mucositis after oral implant restoration, and 20%–22% patients will suffer from peri-implantitis (Lee et al., 2017; Onclin et al., 2022; Suzuki et al., 2023). What is more concerning is that peri-implant mucositis can further develop into peri-implantitis (Herrera et al., 2023). Peri-implantitis is a progressive

inflammatory disease that causes irreversible damage to the soft and hard tissues around the implant, threatening the long-term survival of implants (Schwarz et al., 2018; Cai et al., 2019). Research has shown that the accumulation and colonization of bacterial biofilms around implants are an important cause of peri-implant inflammation (Cai et al., 2019; Qian et al., 2020), and once colonized, bacteria become difficult to remove (Yu et al., 2022). The long-term survival of implants requires that implant materials possess excellent osteogenesis, antibacterial properties, and biocompatibility (Shao et al., 2022). While titanium is widely used in the production of dental implants (Souza et al., 2019), it lacks osteogenic and antibacterial properties (Ji et al., 2023). Therefore, an increasing number of researchers are beginning to modify the implant surface to prevent peri-implant diseases.

Graphene oxide (GO) is a new type of two-dimensional carbon material that holds significant potential in the field of biomedicine (Yousefi et al., 2017; Gusev et al., 2019). GO possesses a unique amphiphilic structure that can interact with cells or growth/differentiation factors, accelerating the adhesion, growth and differentiation of bone marrow stem cells (Wei et al., 2017), neural stem cells (Lin et al., 2020), and induced pluripotent stem cells (Saburi et al., 2019; Ricci et al., 2022). Studies have reported that when GO is used as a scaffold or coating material, it can enhance the regeneration of bone and cartilage (Li et al., 2022b). Additionally, direct contact of GO with bacteria can activate mechanisms such as nano-knife (Sun et al., 2020), encapsulation or capture (Du et al., 2022), oxidative stress (Liu et al., 2011), and has an evident antibacterial effect on both Gram-negative and Gram-positive bacteria (Pulingam et al., 2019). However, the inhibitory ability of GO to planktonic bacteria around the implant is limited (Pandit et al., 2023). Furthermore, the antibacterial activity of GO is concentration-dependent, meaning that at high concentrations, GO may induce biotoxicity. To address the issue of low bactericidal efficiency of GO with non-biotoxic concentrations, consideration was given to loading ε-poly-L-lysine (PLL) onto the titanium surface.

ε-poly-L-lysine (PLL) is a cationic polypeptide polymerized from 25–35 L-lysine (Wang et al., 2021). Presently, it finds extensive applications in the fields of food preservation and medicine (Zhang et al., 2018a). PLL exhibits high antibacterial activity and broad-spectrum effects. Studies have confirmed its efficacy against various Gram-negative bacteria, Gram-positive bacteria, fungi, and viruses (Bankar and Singhal, 2010). Additionally, PLL possesses water solubility, biodegradability, and shows no human or environmental toxicity, demonstrates extremely high safety (Wang et al., 2021). Consequently, PLL is considered to be a safe agent by the United States Food and Drug Administration, and is approved for food preservation in the United States, China, Japan, and other countries (Zhang et al., 2018a; Li et al., 2022a).

To effectively control the deposition amount of PLL and GO, layer-by-layer self-assembly technology (LBL) demonstrates significant technical advantages due to its simple process and mild preparation conditions (Zhang et al., 2018b). LBL utilizes electrostatic interactions to alternately adsorb positively/negatively charged polyelectrolytes on the surface of materials, forming composite multilayer films where the biological activities of the components do not interfere with each other (Lv et al., 2014; Alkekhia et al., 2020). Moreover, LBL offers the advantage of accurately controlling the thickness of the film on a nano-scale and can delay the release of drugs while maintaining sustained antibacterial ability, making it a promising coating method (Gentile et al., 2015). Numerous studies have demonstrated that biologically active coatings containing GO, constructed using LBL techniques, exhibit significant effects in areas such as cardiovascular stents and bone implants. Research by Xu et al. (Xu et al., 2021) illustrates that polydopamine/GO/type I collagen nanofilms exhibit strong capabilities for controlled release of bioactive substances, enhancing not only protein adsorption but also promoting osteogenic differentiation of rat bone marrow-derived mesenchymal stem cells. Furthermore, studies indicate that the greater the number of nanofilm layers, the more pronounced the osteogenic differentiation effect (Xu et al., 2021). Studies by Gao et al. indicate that chitosan/heparinized GO multilayer films can promote adhesion and proliferation of endothelial cells, demonstrating good blood compatibility and corrosion resistance, thus providing new insights for the development of cardiovascular stent materials.

The objective of this study is to assemble PLL and GO on the surface of a titanium sheet to enhance antibacterial properties. The optimal number of assembly layers with good biocompatibility was determined through *in vivo* and *in vitro* experiments. This study introduces novel approaches to address peri-implant diseases and enhance the long-term retention of implants.

2 Materials and methods

2.1 Materials

PLL was procured from Shanghai Aladdin Biochemical Technology Co., Ltd. The sheet diameters of GO, carboxylated graphene oxide (GO-COOH) and aminated graphene oxide (GO-NH_2) are all less than 500 nm and these materials were obtained from Jiangsu Xianfeng Nanomaterials Technology Co., Ltd. Titanium sheets (purity 99.99%) were supplied by Taizhou Senno Material Technology Co., Ltd. Preosteoblasts MC3T3-E1 used in the experiment were obtained from ATCC. Luzhou Keyang Biotechnology Co., Ltd. provided Porphyromonas gingivalis, as well as culture media and reagents for cell and bacterial experiments. The zebrafish and breeding materials used in the experiment were obtained from the zebrafish technology platform of the Public Experimental Technology Center of Southwest Medical University.

2.2 Fabrication of composite coatings on titanium surface

Pure titanium sheets were processed into circular samples with a diameter of 15 mm and a thickness of 1 mm, and their surfaces were polished with #800, #1200, and #2000 silicon carbide paper under running water. Then, they were ultrasonically cleaned in acetone, ethanol, and deionized water for 15 min and dried at 60°C for 24 h. As shown in Figure 1 (Figure 1 was drawn by Figdraw), to obtain active titanium sheets (ATi), the samples were soaked in 5 M sodium hydroxide (NaOH) solution at 60°C for 24 h, then rinsed with

10.3389/fbioe.2024.1381685

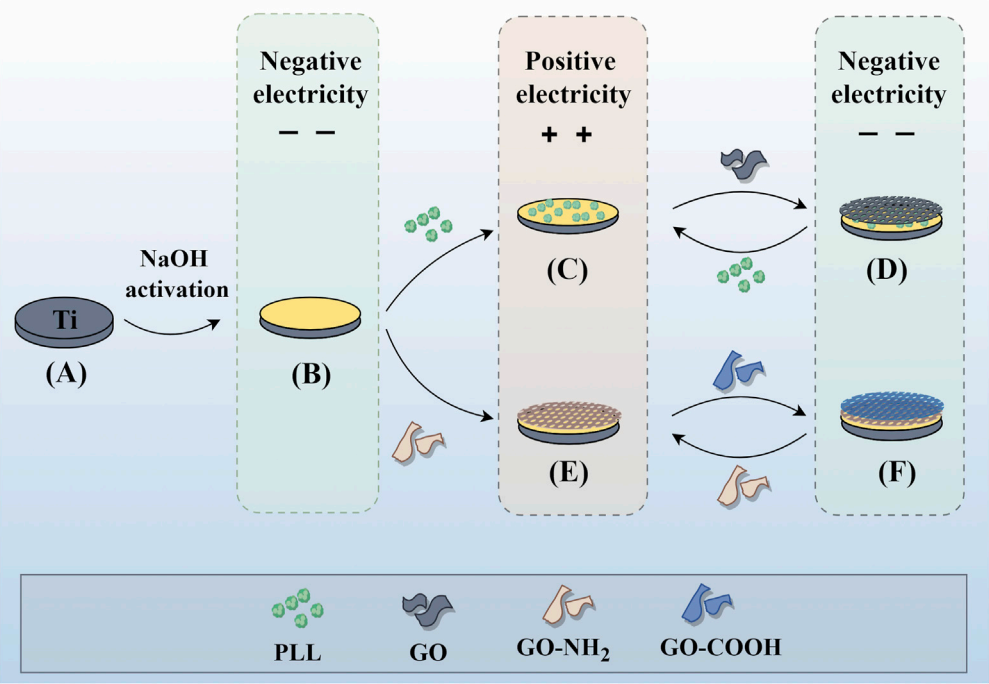

FIGURE 1
Individual assembly of GO and combined assembly of GO and PLL on the titanium surface. Assembly process of P/G and G/G on the titanium surface. **(A)** Pure titanium. **(B)** Titanium surface with negative charge after alkali activation. **(C)** Deposition of positively charged PLL. **(D)** Deposition of negatively charged GO. **(E)** Deposition of positively charged GO-NH_2. **(F)** Deposition of negatively charged GO-COOH. Repeat (C) (D) or (E) (F) to achieve the desired number of layers.

distilled water 3 times and dried for use. Half of the samples were soaked in 1 mg/mL PLL for 10 min, rinsed with deionized water, followed by nitrogen drying. Subsequently, they were immersed in 1 mg/mL GO for 10 min, rinsed, and dried, thereby constructing a bilayer membrane structure. The above steps were repeated to obtain multilayer samples with different layers, labeled as $(P/G)_{10}$, $(P/G)_{20}$, $(P/G)_{30}$. Similarly, the other half of the samples were alternately immersed in 1 mg/mL of GO-COOH and 1 mg/mL of GO-NH_2, and the film assembly process was repeated to obtain $(G/G)_{10}$, $(G/G)_{20}$, $(G/G)_{30}$.

2.3 Characterization of samples

As shown in Figure 2A (Figure 2 was drawn by Figdraw), the surface morphology of the samples was characterized by scanning electron microscopy (SEM, Thermo Fisher, USA), and the chemical composition of the samples was collected and analyzed by energy dispersive X-ray spectroscopy (EDS, AMETEK,USA). The chemical composition of the modified surface was analyzed using the attenuated total reflection attachment (ATR) of Fourier transform infrared spectroscopy (FTIR, Beifen-Ruili, China) and X-ray photoelectron spectroscopy (XPS, Thermo Fisher ScientificK-Alpha, USA). Three samples were selected for each group, and 5 μL of deionized water droplets were placed on the surface of the sample at room temperature. The water contact angle was measured by contact angle measuring instrument (KRUSS, DSA25, Germany) and photographed.

2.4 Evaluation of antibacterial ability

2.4.1 Observation of bacterial morphology

P.g was anaerobically cultured in BHI broth at 37°C to logarithmic growth stage, and the concentration of bacterial suspension was adjusted to 1.0×10^6 CFU/mL for later use. Samples from each group were placed face up in a 12-well plate, 200 μL of bacterial suspension was applied to the surface of the sterilized sample and carefully transferred to an anaerobic incubator for 2 h of cultivation. After stable bacterial adhesion, 0.8 mL of BHI medium was added to each well for further cultivation. The sample was co-cultured with bacteria for 24 h, then, the surface of the sample was washed with aseptic PBS twice to remove unattached bacteria. Subsequently, 2.5% glutaraldehyde was fixed for 20 min, rinsed with PBS, followed by ethanol gradient dehydration and drying. The surface of the sample was sprayed with gold, and the microscopic morphology of *P.g* on the surface of each group was observed by SEM.

2.4.2 Antibacterial rate

The bacterial suspension was co-cultured with the samples for 24 h. After washing off the suspended bacteria, the samples were placed in 1 mL PBS and vortexed for 10 min to collect the adhered bacteria on the surface of the sample. The concentration of bacterial suspension was adjusted to 1.0×10^3 CFU/mL. A 100 μL bacterial suspension was evenly spread on BHI solid medium, and after

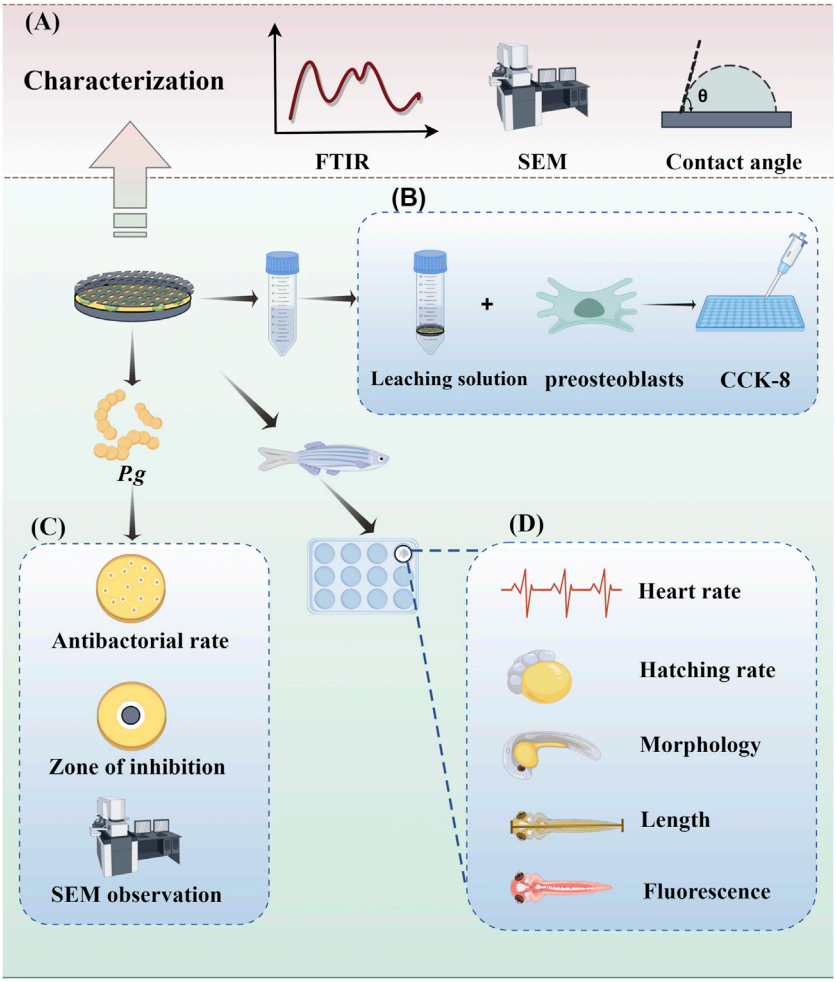

FIGURE 2
Experimental operation diagram. **(A)** Characterization of samples. **(B)** Evaluation of antibacterial ability. **(C)** Cytotoxicity assays. **(D)** *In vivo* toxicity assessment.

anaerobic culture for 48 h, the antibacterial rate was calculated using the following formula.

$$\text{Antibacterial rate}\,(\%) = \frac{CFU\ (Control) - CFU\ (\text{Experimental})}{CFU\ (Control)}$$

2.4.3 Inhibition zone test

A 100 μL bacterial suspension was uniformly inoculated on the surface of the BHI solid medium. After sterilization, each sample was carefully placed face down in BHI medium and anaerobically cultured for 48 h. The inhibition of each sample against the surrounding bacteria was recorded.

2.5 Cytotoxicity assays

MC3T3-E1 cells were incubated with α-MEM medium containing 10% fetal bovine serum (FBS), 100 U/mL penicillin and 100 ug/mL streptomycin in a 5% CO_2 incubator at 37°C. The culture medium was changed every 2 days and passaged at a ratio of 1:3. After sterilization, the samples of each group were immersed in α-MEM medium for 1 week, and 1 mL of leaching solution was collected for each sample. The extraction medium was prepared with different leaching solutions instead of α-MEM and FBS in a 9:1 ratio. Well-grown cells were cleaned with PBS, digested by pancreatic enzymes, and then centrifuged to produce a 1×10^4/mL cell suspension. A 100 μL cell suspension was inoculated into 96-well plates with three compound wells in each group. After culture for 24 h, the previous medium was discarded, and the prepared extraction medium was added. After another 24 h, 100 μL medium containing 10% CCK-8 was added to each well. After incubation for 2 h, the absorbance was determined at the wavelength of 450 nm using an enzyme labeling instrument.

2.6 *In vivo* toxicity assessment

The zebrafish involved in the experiment were sourced from the Zebrafish technology platform of the Public Experimental Technology Center of Southwest Medical University. Wild-type AB zebrafish were fed with newly hatched harvest insects twice a day in a zebrafish culture system with a constant temperature of 28°C and a light-dark

10.3389/fbioe.2024.1381685

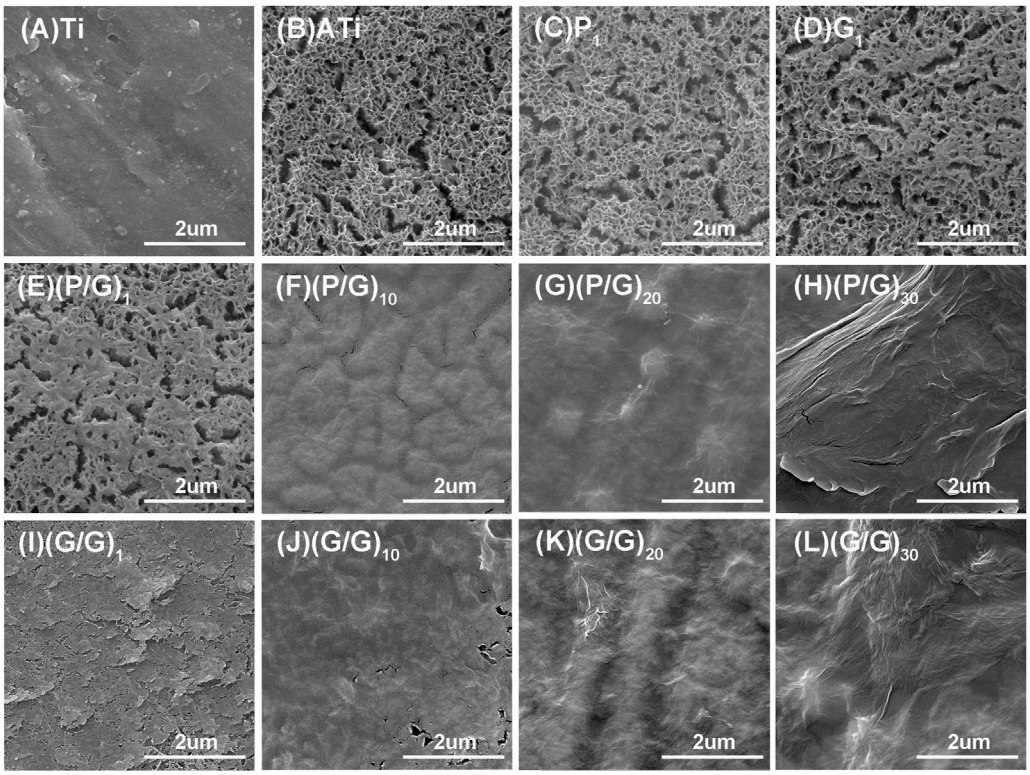

FIGURE 3
SEM morphology observation of titanium sheet surface. **(A)** The surface of pure Ti is smooth and dense. **(B)** After alkali activation, numerous mesh pores and cracks appear. **(C)** After depositing a layer of PLL, the surface of the titanium sheet is covered with extremely small PLL, presenting a foggy appearance. **(E)** After depositing a layer of P/G, some pores are blocked by the material. **(F) (G) (H)** After assembling 10, 20, and 30 layers of P/G, the pores and cracks are gradually filled and leveled. **(D)** After depositing a layer of GO-COOH, most of the pores are blocked. **(I–L)** After assembling 1, 10, 20, and 30 layers of G/G, the surface pores and cracks disappear with the increasing number of layers.

TABLE 1 Elemental compositions of the different samples.

Samples	Atomic concentration (at%)			
	C	N	O	Ti
Ti	-	-	-	100
ATi	-	-	43.31	56.69
$(P/G)_{10}$	13.96	3.14	37.79	45.11
$(P/G)_{20}$	15.55	2.86	40.07	41.52
$(P/G)_{30}$	27.31	2.11	32.26	38.32
$(G/G)_{10}$	18.46	2.37	35.97	43.2
$(G/G)_{20}$	28.74	2.23	29.98	39.05
$(G/G)_{30}$	37.95	0.8	27.67	33.58

photoperiod of 14:10 h. After reaching the adult stage, healthy male and female fish of similar size were selected for mating and egg laying. The fertilized eggs were sorted under the microscope (Nikon, Japan). Sodium hypochlorite disinfectant (0.003%) and sterilized embryo culture water containing 0.3 × Danien's buffer were alternately added to the culture plate for 5 min each. The disinfectant should completely submerge the embryos, and the plate should be gently shaken to ensure full contact. Subsequently, the disinfectant was filtered, and sterilized embryo culture water was added and washed twice to ensure complete removal of sodium hypochlorite. Samples were placed in a 12-well plate, and embryos 6 h after fertilization were directly exposed to the surface of the test material. There were 10 embryos in each group, and the experiment was conducted twice. The embryos were incubated in a constant-temperature incubator. At 72 hpf, the incubation and mortality of the embryos were observed and recorded under a stereomicroscope. At 120 hpf, the heart rate, body length and developmental morphology of zebrafish were observed and recorded under 0.1% (w/v) tricaine solution anesthesia. After the experiment is completed, embryos are euthanized by freezing at −20°C for ≥24 h. All experimental procedures were conducted under the approval of the Ethics Committee of Southwest Medical University (License Number: 20220819–006).

2.7 Immunotoxicity assessment

The potential inflammatory and myelotoxic (neutropenia) effects of GO and PLL-modified titanium sheets were investigated using transgenic Tg (lyz:DsRed2) zebrafish embryos expressing red fluorescent protein (GFP) in neutrophils. This enabled direct observation of the impact of the study material on the emergence and accumulation of neutrophils in exposed tissues or internal organs.

The transgenic zebrafish were bred to the adult stage following the feeding methods described above. Embryos were exposed to the test material at 36 hpf, then incubated at 28°C. At 120 hpf, the exposed embryos were imaged under a fluorescence microscope (Leica, Wetzlar, Germany), and the ImageJ program was used to assess the presence of neutrophils relative to the control group (based on fluorescence intensity). The experiment was performed twice, using five embryos in each group. The experimental procedures have been approved by the Ethics Committee of Southwest Medical University. Statistical analysis.

2.8 Statistical analysis

All data were presented as the mean ± standard deviation. Group comparisons were conducted using one-way ANOVA with Tukey's test in GraphPad Prism (GraphPad Software, United States). Statistical significance was determined at $^*p < 0.05$.

3 Results and discussion

3.1 Synthesis and morphology of materials

Implant restoration has greatly improved the quality of life of patients, and the growing sophistication of implantation technology has led to an increasing number of implant restorations. However, peri-implant disease remains a serious complication that jeopardizes the long-term survival of implants (Rokaya et al., 2020). This is due to the lack of real periodontal ligaments and blood supply around the implant, bacteria are more likely to invade the surrounding tissue, and inflammation progresses more rapidly (Herrera et al., 2023). The chemical composition of the implant surface can influence the adhesion of proteins and bacteria (Yu et al., 2022). Therefore, proper modification of titanium surface to inhibit bacterial adhesion and growth is a method worth considering (Suzuki et al., 2023).

LBL technology has found extensive application in the functionalization of biomaterials. It has the capability to alter the surface properties of the substrate, thereby improving or enhancing tissue function. Recently, LBL technology has been introduced into the manufacturing of implant coatings (Gentile et al., 2015; Liu et al., 2022). PLL and GO-NH_2 in aqueous solution are positively charged, while GO and GO-COOH are negatively charged, which makes it possible to deposit GO and PLL functional films on titanium surface by LBL technology (Guo et al., 2021). In order to make GO and PLL firmly combine on the surface of titanium sheet, firstly, the surface of titanium sheet was treated with 5 mol/L NaOH to make it full of negative charges (Kokubo and Yamaguchi, 2015). As depicted in Figure 3, the surface of pure titanium sheet is relatively smooth and dense, with the surface elements predominantly composed of titanium. After alkali activation treatment, the content of oxygen increased to 43.31%, the surface has a honeycomb grid structure and there are a lot of cracks, which was consistent with the phenomenon observed by He et al. (Kokubo and Yamaguchi, 2015; He et al., 2022; Jiang et al., 2023). After loading a layer of PLL, the bottom and surface of the fissure groove seem to be covered with fog, which is a very small PLL deposition. After completing the assembly of a PLL/GO, some cellular grids are blocked by materials. By alternately assembling different layers, the control of GO dosage is realized, which intuitively shows that with the increase of assembly layers, the pores and cracks on the surface of titanium sheet are gradually filled up. In Groups $(P/G)_{10}$ and $(G/G)_{10}$, although only a few cracks are not completely blocked by materials, the direction of the cracks at the bottom can be clearly seen. The surface gaps in the $(P/G)_{20}$ and $(G/G)_{20}$ groups were completely filled, while the surfaces of the $(P/G)_{30}$ and $(G/G)_{30}$ groups slightly protruded, exhibiting an appearance similar to that of crumpled paper. After PLL and GO are assembled, C and N elements begin to appear, C is provided by PLL and GO, and N comes from PLL. In the GO self-assembly groups, the presence of C and N elements indicates the successful assembly of GO-COOH and GO-NH_2, where N comes from GO-NH_2 (Table 1).

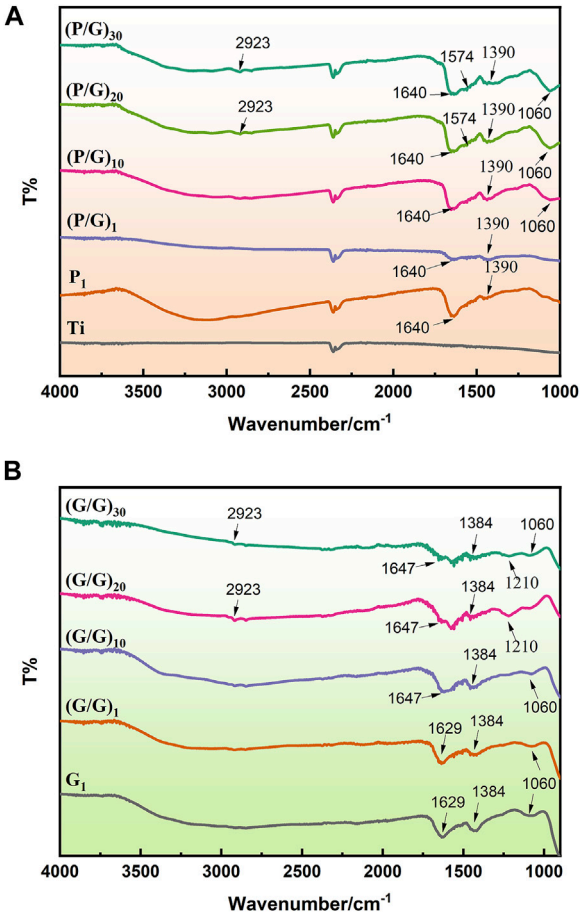

FIGURE 4
(A) FTIR spectra of the P/G group. **(B)** FTIR spectra of the G/G group.

3.2 FTIR

The samples deposited with PLL exhibit a C=O stretching vibration peak at 1,640 cm^{-1}, and an NH bending vibration peak at 2,923 cm^{-1}, confirming the successful bonding of PLL to the sample surface (Guo et al., 2021). On the surface of the sample adsorbed with GO, characteristic peaks of oxygen-containing functional groups such as C=O (1,640 cm^{-1}), C-OH (1,390 cm^{-1}) and C-O-C (1,060 cm^{-1}) appear, confirming the presence of GO coating on the modified material (Suo et al., 2019) (Figure 4). The sample assembled from GO-NH2 and GO-

10.3389/fbioe.2024.1381685

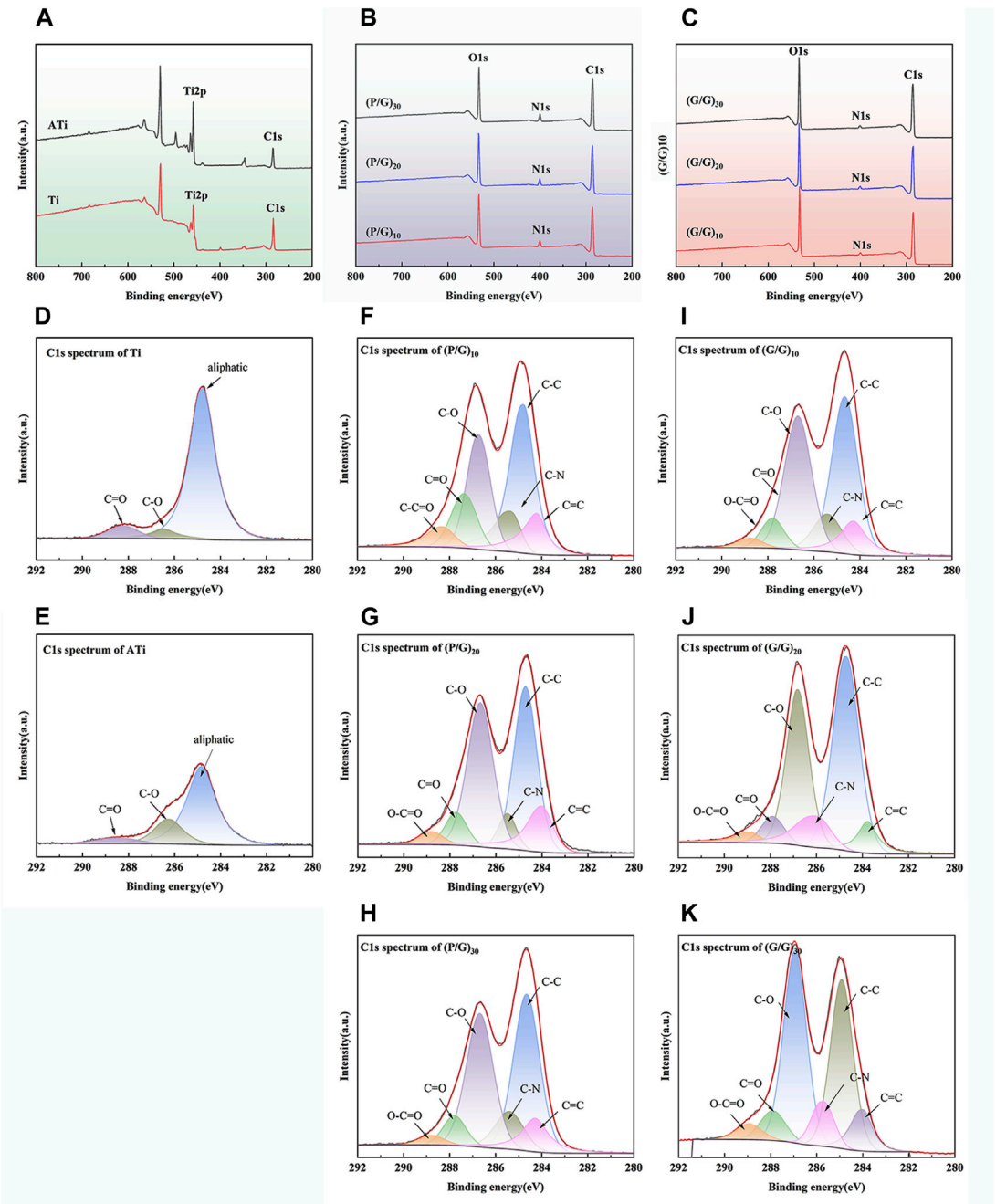

FIGURE 5
Surface chemical characteristics of different titanium samples: **(A)** XPS spectra of Ti and ATi surfaces; **(B)** XPS measurement spectra of $(P/G)_{10}$, $(P/G)_{20}$, $(P/G)_{30}$ surfaces; **(C)** XPS measurement spectra of $(G/G)_{10}$, $(G/G)_{20}$, $(G/G)_{30}$ surfaces; **(D–K)** High-resolution C1 peak fitting of surfaces of different titanium samples.

COOH shows characteristic peaks of GO, such as C-C (1,647 cm^{-1}), C=C (cm^{-1}), C-O-C (1,060 cm^{-1}), and C-OH (1,390 cm^{-1}). Additionally, characteristic peaks of carboxyl groups, C=O (1,640 cm^{-1}), and amino groups, N-H (1,574 cm^{-1}), as well as C-N (1,210 cm^{-1}) peaks, are observed on the surface, indicating the success of the self-assembly. Moreover, with the number of assembly layers exceeding 10, the intensity of the C-O-C vibration peak of GO and the CH_2 vibration peak of PLL also increase, indicating an increase in the relative content of PLL and GO (Figure 4A).

3.3 XPS analysis

The surface chemical composition of samples was thoroughly analyzed using XPS technology. As shown in Figure 5A, three primary characteristic signals, Ti, C, and O, can be clearly identified in Ti and ATi samples, with the C and O signals originating from contaminant amino acids that were not completely removed from the sample surfaces. It is noteworthy that the XPS analysis results reveal that the O signal on the titanium

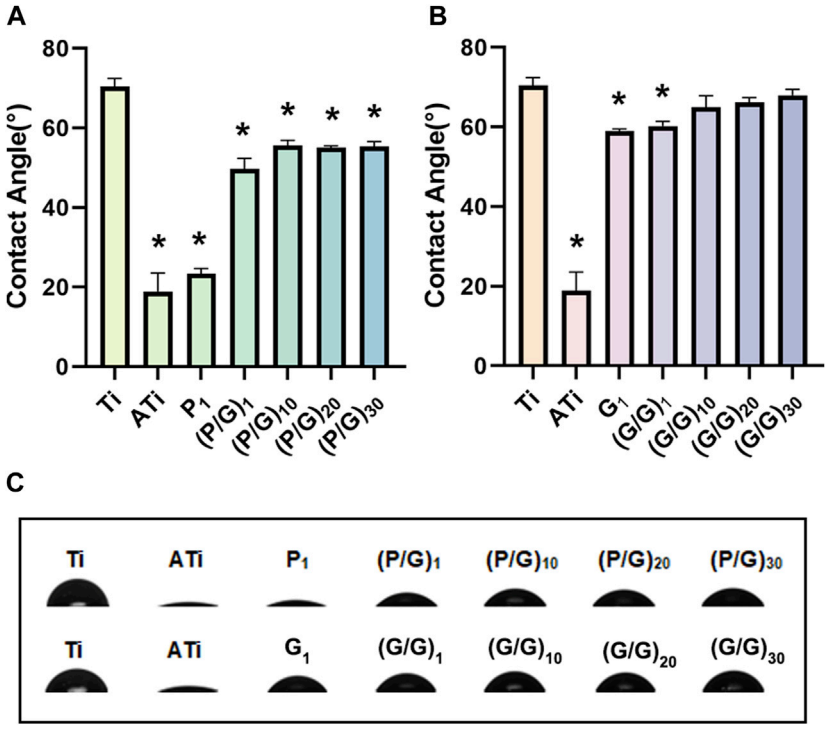

FIGURE 6
(A) Statistical analysis of water contact angles for the P/G group (n = 3). **(B)** Statistical analysis of water contact angles for the G/G group (n = 3). **(C)** Morphology of water droplets on different surfaces. (*$p < 0.05$).

surface increased after alkaline activation. Furthermore, on all samples treated with self-assembly, the characteristic Ti signal was no longer present, and only signals corresponding to C, N, and O were observed, with the C signal intensity being significantly higher than that on the Ti and ATi surfaces (Figures 5B,C). This phenomenon indicates that GO and PLL were uniformly deposited on the pure titanium surface, and its thickness exceeded the detection range of XPS. As shown in Figures 5F–I, samples such as $(P/G)_{10}$, $(P/G)_{20}$, $(P/G)_{30}$, $(G/G)_{10}$, $(G/G)_{20}$, and $(G/G)_{30}$ exhibited extremely similar high-resolution C1s spectra. The C1s spectrum contained six main peaks, corresponding to O-C=O (289.1 eV), C=O (287.9 eV), C-O (286.6 eV), C-N (285.5 eV), C=C (289.1 eV), and C-C (284.7 eV) chemical states. The nitrogen in these peaks originated from PLL and GO-NH2, while the carbon originated from PLL and GO-COOH.

3.4 Contact angle measurement

The water contact angle on the surface of titanium sheet is approximately 70.47° ± 1.95°. After alkali activation, the surface becomes super-hydrophilic, with a contact angle of about 18.87° ± 4.7°, significantly different from that of the pure titanium surface (Figure 6A). This difference is attributed to the abundant hydroxyl (-OH) groups generated after alkali activation, interacting with water molecules to form hydrogen bonds, facilitating the spreading of water droplets on the titanium surface. With the layer-by-layer assembly of PLL and GO, the water contact angle gradually increases but remains significantly lower than that of pure titanium. We hypothesize that the hydroxyl groups on the titanium sheet surface are gradually consumed, and the van der Waals force produced by the interaction of carboxyl, amine, hydroxyl and other polar functional groups on the newly deposited PLL and GO surface is weak. Unfortunately, although a significant decrease in contact angle was observed when GO self-assembled a layer, the 10, 20 and 30 layers observed in the experiment all showed contact angles similar to those of pure titanium (Figure 6B). Studies have shown that hydrophilic surfaces with water contact angles less than 60° exhibit better cell binding and diffusion rates than hydrophobic surfaces (Jurak et al., 2021). Li et al. also pointed out that a rough hydrophilic titanium surface can reduce the production of pro-inflammatory factors by neutrophils (Abaricia et al., 2020). It can be observed that the biocompatibility of PLL and GO modified titanium tablets is better than that of pure titanium and GO modified titanium sheet alone, resulting in less tissue irritation and inflammation.

3.5 Antibacterial activity

3.5.1 SEM morphology of bacteria

P.g is considered to be the main periodontal pathogen associated with peri-implantitis (Pérez-Chaparro et al., 2016; Alves et al., 2022). After 24 h of co-cultivation with P.g, the number and morphology of bacteria on the titanium sheet surface were observed using SEM (Figures 6, 7). *P.g* on the surface of Ti and ATi titanium sheets grew well, covering almost the entire material surface, with smooth

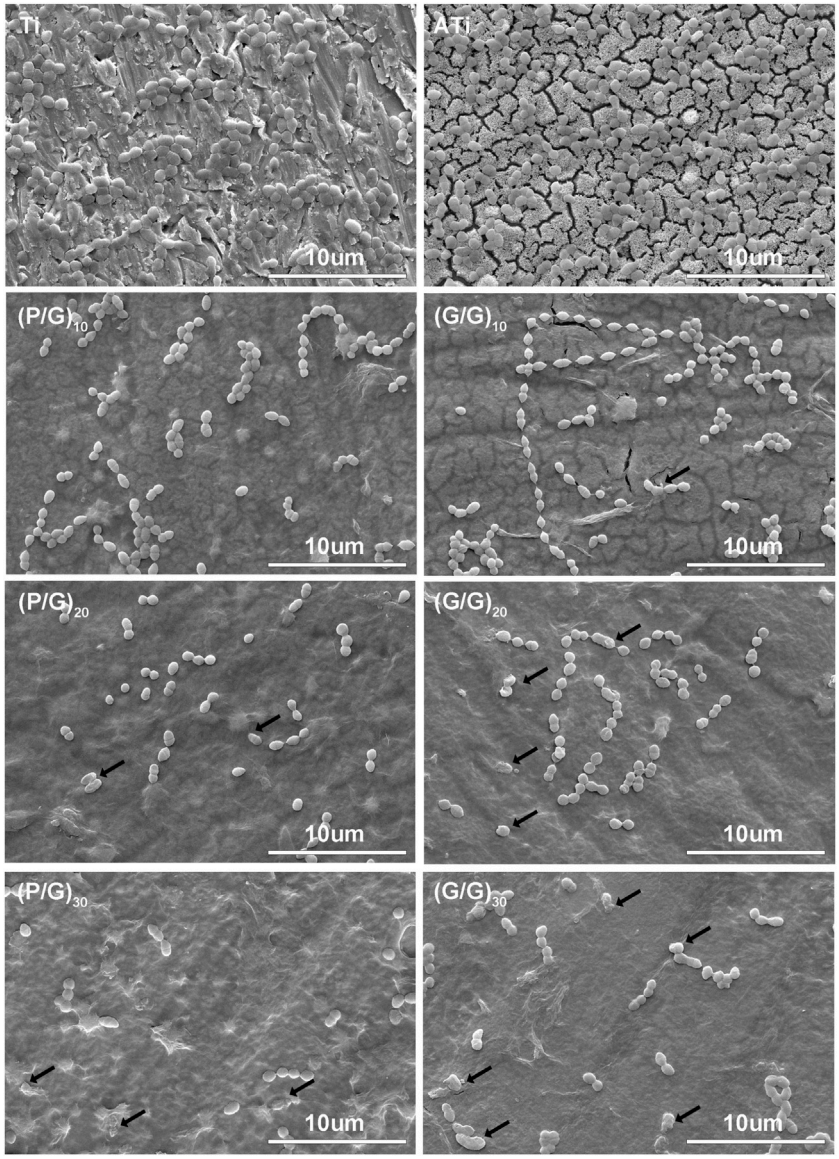

FIGURE 7
SEM image of bacteria. The black arrow shows ruptured and deformed bacteria.

bacteria displaying neat edges and an oval shape. In both the P/G and G/G groups, it was observed that with the increase of loading layers, *P.g* grew from chain-like head-to-tail connection to sporadic form, and bacterial rupture and deformation became ubiquitous (shown by black arrows). Interestingly, compared to the P/G group with the same number of layers, the G/G group showed more bacterial rupture and deformation, although the number of bacteria was relatively higher. GO can produce ROS damage cellular components through oxidative stress, but it is in the state of suspension (Shi et al., 2016). In this experiment, GO tended to cause physical damage to the bacterial membrane by exerting membrane stress through its sharp edges.

3.5.2 Inhibition zone test

The ZOI method was employed to assess the inhibitory ability of the material on the growth of *P.g*. As shown in Figure 8A, only a tiny circular area free of bacteria was observed around the G/G group with all layers, showing no significant difference compared to the pure Ti group. On the contrary, obvious bacteriostatic ring appeared around the P/G modified titanium sheet, and the diameter of bacteriostatic ring increased with the increase of loading layers. This indicates that GO has difficulty diffusing from titanium sheet, while PLL can smoothly diffuse around the titanium sheet smoothly and effectively inhibit the growth of *P.g*. Literature has pointed out that PLL can not only act on cell wall and cell membrane system, but also target genetic materials, enzymes and functional proteins, causing disruptions in material, energy and information transmission within cells and ultimately leading to cell death (Wang et al., 2021).

3.5.3 Antibacterial rate

The bacteriostatic rate of P.g was evaluated by plate counting method. The antibacterial rate of the control group was defined as 0,

10.3389/fbioe.2024.1381685

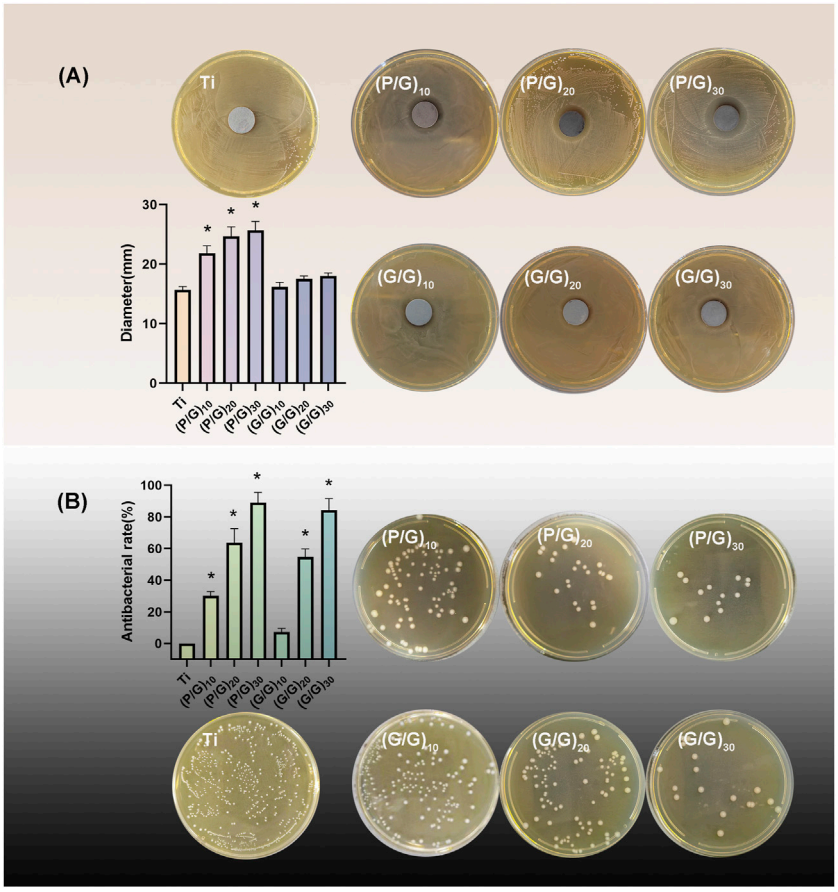

FIGURE 8
(A) Inhibition zone test and statistical analysis of each group (n = 3); **(B)**Colony count and inhibition rate statistics (n = 3). (*$p < 0.05$).

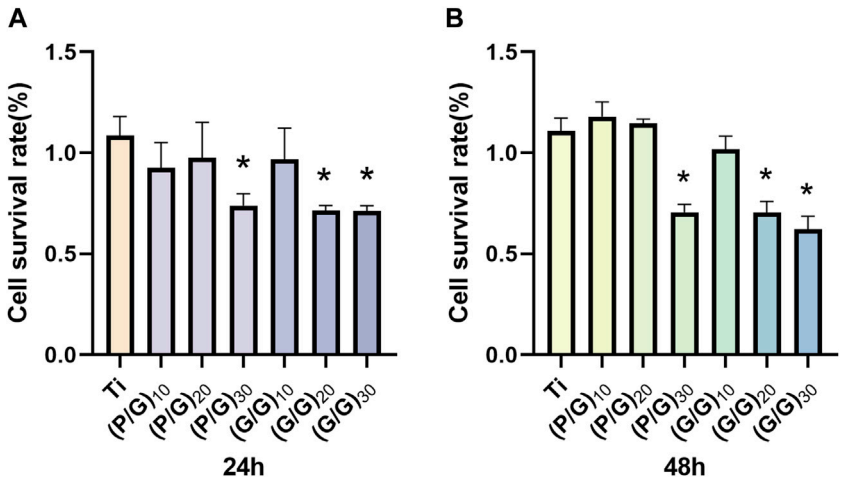

FIGURE 9
(A) The cell survival rate of MC3T3-E1 cells in each group at 24 h (n = 3). **(B)** The cell survival rate of MC3T3-E1 cells in each group at 48 h (n = 3). (*$p < 0.05$).

and the results revealed that the bacteriostatic rates of $(P/G)_{10}$, $(P/G)_{20}$, $(P/G)_{30}$ were 30.1% ± 2.69%, 63.5% ± 8.92%, 88.99% ± 6.43%, $(G/G)_{10}$, $(G/G)_{20}$, $(G/G)_{30}$ were 7.26% ± 2.33%, 54.5% ± 5.03%, 84.15% ± 7.44%, respectively (Figure 8B). GO has bacteriostatic ability either alone or in combination with PLL, but the bacteriostatic effect is limited when the content is low. At the

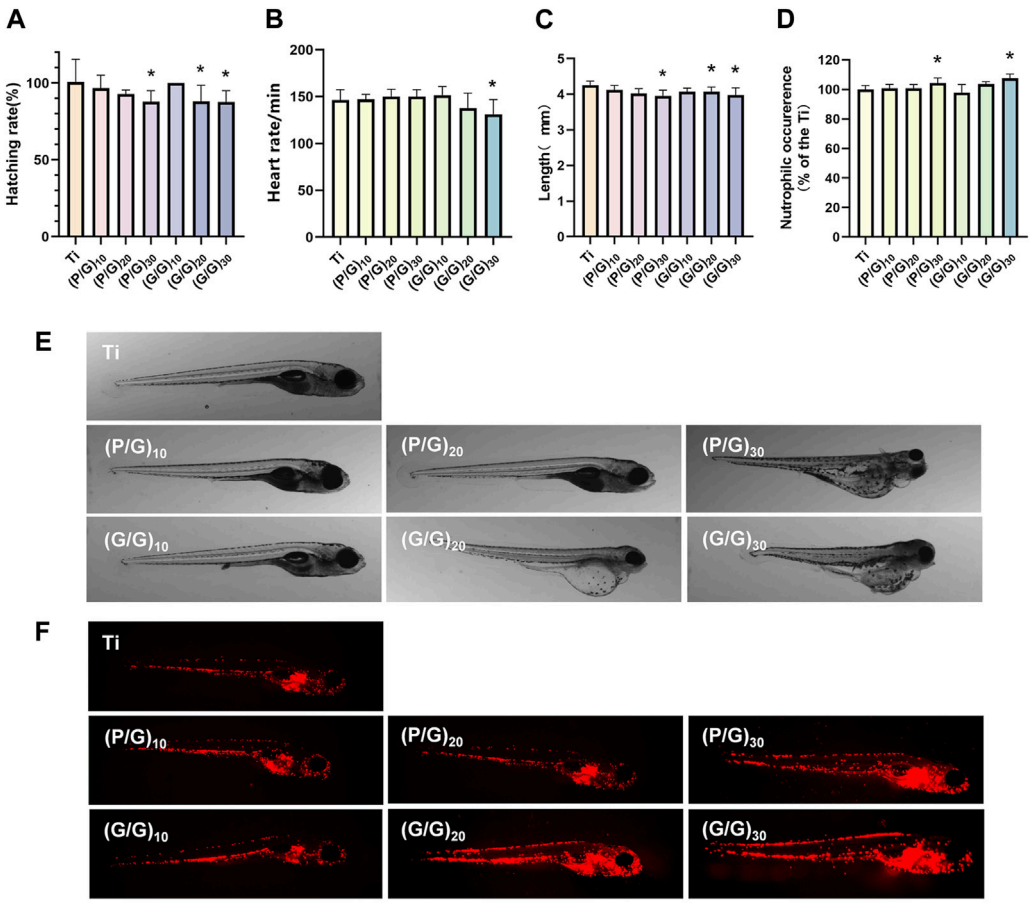

FIGURE 10
(A) Zebrafish embryo hatching rate (n = 3). **(B)** Zebrafish heart rate (n = 10). **(C)** Body length of zebrafish in each group (n = 15). **(D)**growth and development morphology of zebrafish in each group. **(E)** Analysis of neutrophil fluorescence intensity in transgenic zebrafish. **(F)** Appearance of neutrophils under fluorescence microscope (n = 10). (*$p < 0.05$).

same number of layers, the bacteriostatic ability of the group P/G was better than that of the group G/G, which indicated that the combined self-assembly of GO and PLL is a more effective antibacterial strategy. This approach can exert an antibacterial effect on the bacteria adhered to the implant surface as well as those suspended around the implant.

3.6 Cytotoxicity assays

Osteoblasts play a crucial role in osseointegration. They adhere, spread, proliferate, and differentiate on the surface of implant materials, ultimately mineralizing into bone and forming a solid union with the bone implants. The murine-derived osteoblast cell line MC3T3-E1 is commonly employed for studying the biocompatibility of bone implants (Czekanska et al., 2012). As can be seen from Figure 9, with an increase in the number of film layers, the cell survival rate of the experimental group showed a decreasing trend compared with the control group. The cell viability of groups $(P/G)_{20}$, $(G/G)_{20}$ and $(G/G)_{30}$ showed a significant decrease at both 24 h and 48 h. A large number of studies (Pang et al., 2017; Pulingam et al., 2020) have shown that cytotoxicity is positively correlated with the concentration of graphene oxide. This is because PLL itself can be degraded into essential amino acids for the human body, suggesting that cytotoxicity comes from GO and is concentration-dependent. Moreover, as long as the assembly of PLL and GO does not reach 30 layers, it remains relatively safe for MC3T3-E1 cells and can be used in oral implant repair.

3.7 *In vivo* toxicity assessment

Zebrafish have up to 70% genomic homology compared to the human genome (Howe et al., 2013; Miyawaki, 2020). Moreover, zebrafish possess excellent characteristics such as *in vitro* fertilization and development, embryo transparency, and easy breeding. Hence, it stands out as an exceptional model organism for evaluating the biocompatibility and therapeutic efficacy of new biological materials (Feng et al., 2022). When wild type (AB) zebrafish were co-cultured with titanium sheets during the highly material sensitive early embryonic stage (6 hpf), there was no significant increase in embryo mortality in all experimental groups compared with the control group. Under normal conditions, most embryos would break through the chorions to complete incubation at 72 hpf, however, there was a delay in

hatching (Figure 10A) observed in the $(P/G)_{30}$, $(G/G)_{20}$, and $(G/G)_{30}$ group. This is consistent with the results of Chen et al., they confirmed that GO will adsorb on the surface of the chorion, blocking the pores between the chorionic processes, and gradually form an anoxic environment in the embryo, which leads to the delay of hatching (Chen et al., 2020). In addition, studies have shown that GO induces edema in the pericardium and yolk sac, which disrupts the activity of hatching enzymes and may be another reason for delayed hatching (Chen et al., 2016). The heart is the earliest organ that occurs and functions in the process of embryonic development, and the heart rate is the most intuitive reaction of the normal function of the heart (Chen et al., 2020). However, when the embryos developed to 120 hpf, the heart rate decreased in $(G/G)_{30}$ groups (Figure 10B), the body surface of zebrafish in $(G/P)_{30}$, $(G/G)_{20}$, $(G/G)_{30}$ groups was no longer smooth (Figure 10E), There seems to be floc shedding and adhesion, and there are many developmental deformities, including pericardial edema, yolk sac edema, and tail deformity. In addition, a reduction in body length was observed in the $(P/G)_{30}$, $(G/G)_{20}$, and $(G/G)_{30}$ group (Figure 10C). In the study by Chen et al., zebrafish embryos exposed to 1 mg/L GO also showed a significant reduction in heart rate (Chen et al., 2016). This suggests that high concentrations of GO may produce certain cardiotoxicity to zebrafish, which in turn affects growth and development.

3.8 Immunotoxicity assessment

Taking advantage of the transparent nature of zebrafish embryos, the neutrophils of transgenic zebrafish Tg (lyz:DsRed2) are labeled red by fluorescent proteins, which can be used to evaluate the early inflammatory response and immunotoxicity that we are very concerned about when planting. After 120 hpf direct exposure, $(P/G)_{30}$ and $(G/G)_{30}$ groups showed a significant increase in neutrophils (Figure 10D), and the fluorescence was mainly concentrated in the yolk sac, heart and periocular area (Figure 10F). It has been reported that once GO enters the embryo, it will selectively locate the yolk sac, heart, eye and tail, affecting the early development of the embryo, and the incidence of early malformation increases with the increase of GO concentration.

4 Conclusion

This study successfully performed separate assemblies of 10, 20, and 30 layers of GO on the titanium surface, as well as combined assemblies of GO and PLL. The results indicate that self-assembly of GO with more than 10 layers exhibits good antibacterial performance, and the joint assembly of GO and PLL demonstrates superior antibacterial efficacy under the same layer conditions. Additionally, assemblies of P/G with less than 30 layers and G/G with less than 20 layers exhibit safe biological properties, without causing cytotoxicity, developmental toxicity, and immunotoxicity. Considering the balance between antibacterial performance and biological toxicity, the combined assembly of GO and PLL with 20 layers presents a promising choice for designing and optimizing titanium-based implants.

Data availability statement

The raw data supporting the conclusions of this article will be made available by the authors, without undue reservation.

Ethics statement

The animal study was approved by The Ethics Committee of Southwest Medical University. The study was conducted in accordance with the local legislation and institutional requirements.

Author contributions

XY: Conceptualization, Writing–original draft, Writing–review and editing. ZW: Data curation, Formal Analysis, Writing–original draft. LW: Investigation, Methodology, Writing–original draft. YL: Investigation, Methodology, Project administration, Writing–original draft. HC: Software, Resources, Validation, Writing–original draft. XL: Writing–review and editing, Software, Supervision. LG: Funding acquisition, Validation, Visualization, Writing–review and editing.

Funding

The author(s) declare that financial support was received for the research, authorship, and/or publication of this article. This work was supported by Luzhou Science and Technology Bureau (Grant number 2022-RCM-170; 2022-GYF-11); Sichuan Science and Technology Program (2022YFS0634; 2022YFS0634-B4).

Conflict of interest

The authors declare that the research was conducted in the absence of any commercial or financial relationships that could be construed as a potential conflict of interest.

Publisher's note

Supplementary material

The Supplementary Material for this article can be found online at: https://www.frontiersin.org/articles/10.3389/fbioe.2024.1381685/full#supplementary-material

References

Abaricia, J. O., Shah, A. H., Musselman, R. M., and Olivares-Navarrete, R. (2020). Hydrophilic titanium surfaces reduce neutrophil inflammatory response and NETosis. *Biomater. Sci.* 8 (8), 2289–2299. doi:10.1039/c9bm01474h

Alkekhia, D., Hammond, P. T., and Shukla, A. (2020). Layer-by-Layer biomaterials for drug delivery. *Annu. Rev. Biomed. Eng.* 22, 1–24. doi:10.1146/annurev-bioeng-060418-052350

Alves, C. H., Russi, K. L., Rocha, N. C., Bastos, F., Darrieux, M., Parisotto, T. M., et al. (2022). Host-microbiome interactions regarding peri-implantitis and dental implant loss. *J. Transl. Med.* 20 (1), 425. doi:10.1186/s12967-022-03636-9

Bankar, S. B., and Singhal, R. S. (2010). Optimization of poly-epsilon-lysine production by Streptomyces noursei NRRL 5126. *Bioresour. Technol.* 101 (21), 8370–8375. doi:10.1016/j.biortech.2010.06.004

Cai, Z., Li, Y., Wang, Y., Chen, S., Jiang, S., Ge, H., et al. (2019). Antimicrobial effects of photodynamic therapy with antiseptics on *Staphylococcus aureus* biofilm on titanium surface. *Photodiagnosis Photodyn. Ther.* 25, 382–388. doi:10.1016/j.pdpdt.2019.01.024

Chen, Y., Hu, X., Sun, J., and Zhou, Q. (2016). Specific nanotoxicity of graphene oxide during zebrafish embryogenesis. *Nanotoxicology* 10 (1), 42–52. doi:10.3109/17435390.2015.1005032

Chen, Z., Yu, C., Khan, I. A., Tang, Y., Liu, S., and Yang, M. (2020). Toxic effects of different-sized graphene oxide particles on zebrafish embryonic development. *Ecotoxicol. Environ. Saf.* 197, 110608. doi:10.1016/j.ecoenv.2020.110608

Czekanska, E. M., Stoddart, M. J., Richards, R. G., and Hayes, J. S. (2012). In search of an osteoblast cell model for *in vitro* research. *Eur. Cell. Mater* 24, 1–17. doi:10.22203/ecm.v024a01

Du, T., Huang, B., Cao, J., Li, C., Jiao, J., Xiao, Z., et al. (2022). Ni nanocrystals supported on graphene oxide: antibacterial agents for synergistic treatment of bacterial infections. *ACS Omega* 7 (22), 18339–18349. doi:10.1021/acsomega.2c00508

Feng, Z., Ducos, B., Scerbo, P., Aujard, I., Jullien, L., and Bensimon, D. (2022). The development and application of opto-chemical tools in the zebrafish. *Molecules* 27 (19), 6231. doi:10.3390/molecules27196231

Gentile, P., Carmagnola, I., Nardo, T., and Chiono, V. (2015). Layer-by-layer assembly for biomedical applications in the last decade. *Nanotechnology* 26 (42), 422001. doi:10.1088/0957-4484/26/42/422001

Guo, J., Cao, G., Wang, X., Tang, W., Diwu, W., Yan, M., et al. (2021). Coating CoCrMo alloy with graphene oxide and epsilon-poly-L-lysine enhances its antibacterial and antibiofilm properties. *Int. J. Nanomedicine* 16, 7249–7268. doi:10.2147/IJN.S321800

Gusev, A., Zakharova, O., Vasyukova, I., Muratov, D. S., Rybkin, I., Bratashov, D., et al. (2019). Effect of GO on bacterial cells: role of the medium type and electrostatic interactions. *Mater Sci. Eng. C Mater Biol. Appl.* 99, 275–281. doi:10.1016/j.msec.2019.01.093

He, X., Yamada, M., Watanabe, J., Tiskratok, W., Ishibashi, M., Kitaura, H., et al. (2022). Titanium nanotopography induces osteocyte lacunar-canalicular networks to strengthen osseointegration. *Acta Biomater.* 151, 613–627. doi:10.1016/j.actbio.2022.08.023

Herrera, D., Berglundh, T., Schwarz, F., Chapple, I., Jepsen, S., Sculean, A., et al. (2023). Prevention and treatment of peri-implant diseases-The EFP S3 level clinical practice guideline. *J. Clin. Periodontol.* 50 (Suppl. 26), 4–76. doi:10.1111/jcpe.13823

Howe, K., Clark, M. D., Torroja, C. F., Torrance, J., Berthelot, C., Muffato, M., et al. (2013). The zebrafish reference genome sequence and its relationship to the human genome. *Nature* 496 (7446), 498–503. doi:10.1038/nature12111

Ji, Z., Wan, Y., Wang, H., Yu, M., Zhao, Z., Wang, T., et al. (2023). Effects of surface morphology and composition of titanium implants on osteogenesis and inflammatory responses: a review. *Biomed. Mater* 18 (4), 042002. doi:10.1088/1748-605X/acd976

Jiang, P., Zhang, Y., Hu, R., Shi, B., Zhang, L., Huang, Q., et al. (2023). Advanced surface engineering of titanium materials for biomedical applications: from static modification to dynamic responsive regulation. *Bioact. Mater* 27, 15–57. doi:10.1016/j.bioactmat.2023.03.006

Jiang, X., Yao, Y., Tang, W., Han, D., Zhang, L., Zhao, K., et al. (2020). Design of dental implants at materials level: an overview. *J. Biomed. Mater Res. A* 108 (8), 1634–1661. doi:10.1002/jbm.a.36931

Jurak, M., Wiącek, A. E., Ładniak, A., Przykaza, K., and Szafran, K. (2021). What affects the biocompatibility of polymers? *Adv. Colloid Interface Sci.* 294, 102451. doi:10.1016/j.cis.2021.102451

Kokubo, T., and Yamaguchi, S. (2015). Bioactive titanate layers formed on titanium and its alloys by simple chemical and heat treatments. *Open Biomed. Eng. J.* 9, 29–41. doi:10.2174/1874120701509010029

Lee, C. T., Huang, Y. W., Zhu, L., and Weltman, R. (2017). Prevalences of peri-implantitis and peri-implant mucositis: systematic review and meta-analysis. *J. Dent.* 62, 1–12. doi:10.1016/j.jdent.2017.04.011

Li, S., Mao, Y., Zhang, L., Wang, M., Meng, J., Liu, X., et al. (2022a). Recent advances in microbial ε-poly-L-lysine fermentation and its diverse applications. *Biotechnol. Biofuels Bioprod.* 15 (1), 65. doi:10.1186/s13068-022-02166-2

Li, X., Liang, X., Wang, Y., Wang, D., Teng, M., Xu, H., et al. (2022b). Graphene-based nanomaterials for dental applications: principles, current advances, and future outlook. *Front. Bioeng. Biotechnol.* 10, 804201. doi:10.3389/fbioe.2022.804201

Lin, L., Zhuang, X., Huang, R., Song, S., Wang, Z., Wang, S., et al. (2020). Size-Dependent effects of suspended graphene oxide nanoparticles on the cellular fate of mouse neural stem cells ;/p>. *Int. J. Nanomedicine* Volume 15, 1421–1435. doi:10.2147/ijn.S225722

Liu, S., Zeng, T. H., Hofmann, M., Burcombe, E., Wei, J., Jiang, R., et al. (2011). Antibacterial activity of graphite, graphite oxide, graphene oxide, and reduced graphene oxide: membrane and oxidative stress. *ACS Nano* 5 (9), 6971–6980. doi:10.1021/nn202451x

Liu, Y. F., He, L. B., Li, J. S., Luo, J., Liang, K. N., Yin, D. R., et al. (2022). Mussel-inspired organic-inorganic implant coating based on a layer-by-layer method for anti-infection and osteogenesis. *Industrial Eng. Chem. Res.* 61 (35), 13040–13051. doi:10.1021/acs.iecr.2c01646

Lv, H., Chen, Z., Yang, X., Cen, L., Zhang, X., and Gao, P. (2014). Layer-by-layer self-assembly of minocycline-loaded chitosan/alginate multilayer on titanium substrates to inhibit biofilm formation. *J. Dent.* 42 (11), 1464–1472. doi:10.1016/j.jdent.2014.06.003

Miyawaki, I. (2020). Application of zebrafish to safety evaluation in drug discovery. *J. Toxicol. Pathol.* 33 (4), 197–210. doi:10.1293/tox.2020-0021

Onclin, P., Slot, W., Vissink, A., Raghoebar, G. M., and Meijer, H. J. A. (2022). Incidence of peri-implant mucositis and peri-implantitis in patients with a maxillary overdenture: a sub-analysis of two prospective studies with a 10-year follow-up period. *Clin. Implant Dent. Relat. Res.* 24 (2), 188–195. doi:10.1111/cid.13071

Pandit, S., Jacquemin, L., Zhang, J., Gao, Z., Nishina, Y., Meyer, R. L., et al. (2023). Polymyxin B complexation enhances the antimicrobial potential of graphene oxide. *Front. Cell. Infect. Microbiol.* 13, 1209563. doi:10.3389/fcimb.2023.1209563

Pang, L., Dai, C., Bi, L., Guo, Z., and Fan, J. (2017). Biosafety and antibacterial ability of graphene and graphene oxide *in vitro* and *in vivo*. *Nanoscale Res. Lett.* 12 (1), 564. doi:10.1186/s11671-017-2317-0

Pérez-Chaparro, P. J., Duarte, P. M., Shibli, J. A., Montenegro, S., Lacerda Heluy, S., Figueiredo, L. C., et al. (2016). The current weight of evidence of the microbiologic profile associated with peri-implantitis: a systematic review. *J. Periodontol.* 87 (11), 1295–1304. doi:10.1902/jop.2016.160184

Pulingam, T., Thong, K. L., Ali, M. E., Appaturi, J. N., Dinshaw, I. J., Ong, Z. Y., et al. (2019). Graphene oxide exhibits differential mechanistic action towards Gram-positive and Gram-negative bacteria. *Colloids Surf. B Biointerfaces* 181, 6–15. doi:10.1016/j.colsurfb.2019.05.023

Pulingam, T., Thong, K. L., Appaturi, J. N., Nordin, N. I., Dinshaw, I. J., Lai, C. W., et al. (2020). Synergistic antibacterial actions of graphene oxide and antibiotics towards bacteria and the toxicological effects of graphene oxide on human epidermal keratinocytes. *Eur. J. Pharm. Sci.* 142, 105087. doi:10.1016/j.ejps.2019.105087

Qian, W., Qiu, J., and Liu, X. (2020). Minocycline hydrochloride-loaded graphene oxide films on implant abutments for peri-implantitis treatment in beagle dogs. *J. Periodontol.* 91 (6), 792–799. doi:10.1002/JPER.19-0285

Ricci, A., Cataldi, A., Zara, S., and Gallorini, M. (2022). Graphene-oxide-enriched biomaterials: a focus on osteo and chondroinductive properties and immunomodulation. *Mater. (Basel)* 15 (6), 2229. doi:10.3390/ma15062229

Rokaya, D., Srimaneepong, V., Wisitrasameewon, W., Humagain, M., and Thunyakitpisal, P. (2020). Peri-implantitis update: risk indicators, diagnosis, and treatment. *Eur. J. Dent.* 14 (4), 672–682. doi:10.1055/s-0040-1715779

Saburi, E., Islami, M., Hosseinzadeh, S., Moghadam, A. S., Mansour, R. N., Azadian, E., et al. (2019). *In vitro* osteogenic differentiation potential of the human induced pluripotent stem cells augments when grown on Graphene oxide-modified nanofibers. *Gene* 696, 72–79. doi:10.1016/j.gene.2019.02.028

Schwarz, F., Derks, J., Monje, A., and Wang, H. L. (2018). Peri-implantitis. *J. Periodontol.* 89 (Suppl. 1), S267-S290–S290. doi:10.1002/JPER.16-0350

Shao, H., Ma, M., Wang, Q., Yan, T., Zhao, B., Guo, S., et al. (2022). Advances in the superhydrophilicity-modified titanium surfaces with antibacterial and pro-osteogenesis properties: a review. *Front. Bioeng. Biotechnol.* 10, 1000401. doi:10.3389/fbioe.2022.1000401

Shi, L., Chen, J., Teng, L., Wang, L., Zhu, G., Liu, S., et al. (2016). The antibacterial applications of graphene and its derivatives. *Small* 12 (31), 4165–4184. doi:10.1002/smll.201601841

Souza, J. C. M., Sordi, M. B., Kanazawa, M., Ravindran, S., Henriques, B., Silva, F. S., et al. (2019). Nano-scale modification of titanium implant surfaces to enhance osseointegration. *Acta Biomater.* 94, 112–131. doi:10.1016/j.actbio.2019.05.045

Sun, N., Yin, S., Lu, Y., Zhang, W., and Jiang, X. (2020). Graphene oxide-coated porous titanium for pulp sealing: an antibacterial and dentino-inductive restorative material. *J. Mater Chem. B* 8 (26), 5606–5619. doi:10.1039/d0tb00697a

Suo, L., Jiang, N., Wang, Y., Wang, P., Chen, J., Pei, X., et al. (2019). The enhancement of osseointegration using a graphene oxide/chitosan/hydroxyapatite composite coating on titanium fabricated by electrophoretic deposition. *J. Biomed. Mater Res. B Appl. Biomater.* 107 (3), 635–645. doi:10.1002/jbm.b.34156

Suzuki, K., Iwatsu, M., Mokudai, T., Furuya, M., Yokota, K., Kanetaka, H., et al. (2023). Visible-light-enhanced antibacterial activity of silver and copper Co-doped titania formed on titanium via chemical and thermal treatments. *Molecules* 28 (2), 650. doi:10.3390/molecules28020650

Wang, L., Zhang, C., Zhang, J., Rao, Z., Xu, X., Mao, Z., et al. (2021). Epsilon-poly-L-lysine: recent advances in biomanufacturing and applications. *Front. Bioeng. Biotechnol.* 9, 748976. doi:10.3389/fbioe.2021.748976

Wei, C., Liu, Z., Jiang, F., Zeng, B., Huang, M., and Yu, D. (2017). Cellular behaviours of bone marrow-derived mesenchymal stem cells towards pristine graphene oxide nanosheets. *Cell. Prolif.* 50 (5), e12367. doi:10.1111/cpr.12367

Xu, K., Zhou, M., Chen, W., Zhu, Y., Wang, X., Zhang, Y., et al. (2021). Bioinspired polydopamine/graphene oxide/collagen nanofilms as a controlled release carrier of bioactive substances. *Chem. Eng. J.* 405, 126930. doi:10.1016/j.cej.2020.126930

Yousefi, M., Dadashpour, M., Hejazi, M., Hasanzadeh, M., Behnam, B., de la Guardia, M., et al. (2017). Anti-bacterial activity of graphene oxide as a new weapon nanomaterial to combat multidrug-resistance bacteria. *Mater. Sci. Eng. C* 74, 568–581. doi:10.1016/j.msec.2016.12.125

Yu, J., Zhou, M., Zhang, L., and Wei, H. (2022). Antibacterial adhesion strategy for dental titanium implant surfaces: from mechanisms to application. *J. Funct. Biomater.* 13 (4), 169. doi:10.3390/jfb13040169

Zhang, J. H., Zeng, X., Chen, X. S., and Mao, Z. G. (2018a). Metabolic analyses of the improved ε-poly-L-lysine productivity using a glucose-glycerol mixed carbon source in chemostat cultures. *Bioprocess Biosyst. Eng.* 41 (8), 1143–1151. doi:10.1007/s00449-018-1943-y

Zhang, S., Xing, M., and Li, B. (2018b). Biomimetic layer-by-layer self-assembly of nanofilms, nanocoatings, and 3D scaffolds for tissue engineering. *Int. J. Mol. Sci.* 19 (6), 1641. doi:10.3390/ijms19061641

Frontiers in
Bioengineering and Biotechnology

Accelerates the development of therapies, devices, and technologies to improve our lives

A multidisciplinary journal that accelerates the development of biological therapies, devices, processes and technologies to improve our lives by bridging the gap between discoveries and their application.

Discover the latest Research Topics

See more →

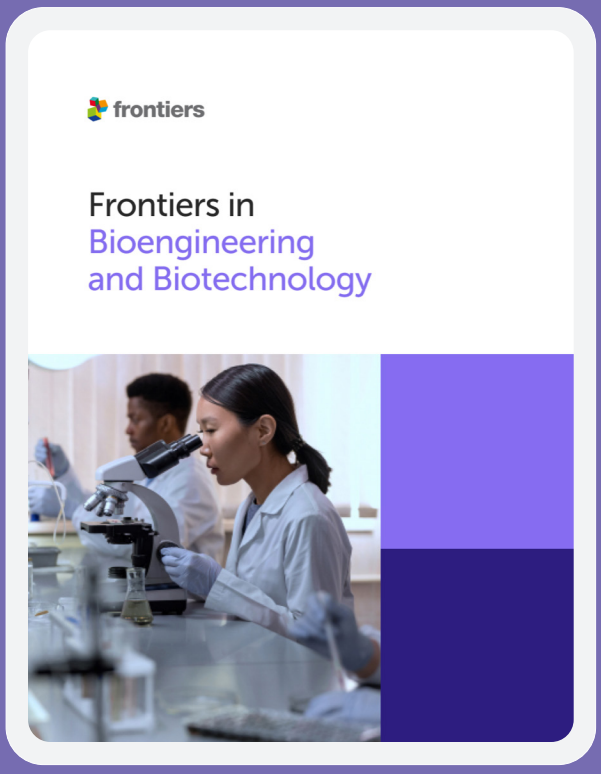

Frontiers

Avenue du Tribunal-Fédéral 34
1005 Lausanne, Switzerland
frontiersin.org

Contact us

+41 (0)21 510 17 00
frontiersin.org/about/contact